COLLEGE SCIENCES
DOCTORAL DE LA MER
BRETAGNE ET DU LITTORAL

Université de Bretagne Occidentale

Ifremer

emso

iAtlantic
INTEGRATED ASSESSMENT OF ATLANTIC MARINE ECOSYSTEMS IN SPACE AND TIME

THESE DE DOCTORAT DE

L'UNIVERSITE
DE BRETAGNE OCCIDENTALE

ECOLE DOCTORALE N° 598
Sciences de la Mer et du littoral
Spécialité : Ecologie marine

Par
Loïc VAN AUDENHAEGE

Étude par l'imagerie de la distribution spatio-temporelle multi-échelles des communautés benthiques associées au champ hydrothermal Lucky Strike

Thèse présentée et soutenue à Plouzané, le 9 janvier 2023
Unité de recherche : Unité Biologie et Ecologie des Ecosystèmes Marins Profonds (Université de Bretagne Occidentale, CNRS, Ifremer, UMR6197 BEEP)

Rapporteurs avant soutenance :

Katleen ROBERT Assistant Professor, Fisheries and Marine Institute, Memorial University of Newfoundland, St. John's
Canada Research Chair in Ocean Mapping
Jon COPLEY Professor, University of Southampton

Composition du Jury :

Président :	François LE LOC'H	Directeur de recherche, Université de Bretagne Occidentale, CNRS, IRD, Ifremer, UMR6539 LEMAR
Examinateurs :	Katleen ROBERT	Assistant Professor, Fisheries and Marine Institute, Memorial University of Newfoundland, St. John's, Canada Research Chair in Ocean Mapping
	Jon COPLEY	Professor, University of Southampton
	Valérie CHAVAGNAC	Directrice de Recherche, Université de Toulouse, CNRS, IRD, UMR5563 GET
	Olivier GAUTHIER	Maître de Conférences, Université de Bretagne Occidentale, CNRS, IRD, Ifremer, UMR6539 LEMAR
Dir. de thèse :	Jozée SARRAZIN	Cadre de recherche, Université de Bretagne Occidentale, CNRS, Ifremer, UMR6197 BEEP

Invitée
Co-dir. de thèse : Marjolaine MATABOS Cadre de recherche, Université de Bretagne Occidentale, CNRS, Ifremer, UMR6197 BEEP

Remerciements

Trois ans ont filé depuis mon arrivée à Brest. Trois années remplies de rencontres, de découvertes et de très bons moments qui ne s'effaceront pas d'aussitôt de ma mémoire. Mes encadrantes ont pu le remarquer à maintes reprises : j'ai du mal à être concis. Néanmoins, je ne compte pas m'abstenir pour cette section qui mérite d'être développée sans retenue.

Mes premiers remerciements sont destinés à mes encadrantes de thèse, Jozée Sarrazin et Marjolaine Matabos. Merci pour votre suivi jusqu'au bout de cette aventure. Votre accompagnement sans relâche fut d'une précieuse aide pour l'aboutissement de ces travaux, bien que parsemés d'embûches parfois imprévues, notamment suite à la pandémie du COVID-19. Vous m'avez permis de grandir scientifiquement parlant ainsi que de gagner en maturité sur beaucoup d'aspects professionnels qui n'étaient pas acquis au départ. Les jeux de données sur lesquels vous m'avez offert l'opportunité de travailler étaient uniques et ambitieux. Ils furent stimulants à traiter et je suis très heureux que l'on y soit arrivé. Je remercie également mes deux encadrantes pour l'autonomie qu'elles m'ont offerte dans la réalisation de mes travaux, mais aussi pour la liberté à présenter ces derniers. Qui plus est, leur soutien inconditionnel à ma participation dans divers congrès eut l'effet d'un catalyseur pour mes recherches. Je ne me serais sûrement pas exposé à de tels événements de par ma propre initiative. D'autre part, je tiens à les remercier pour leur confiance, notamment allouée à ma participation à diverses opportunités qui m'ont permis d'agréger un panel de connaissances générales, ainsi que de profiter des nombreux événements de médiation qui définissent le caractère unique de la dynamique de la recherche marine en Bretagne.

Je tiens à remercier les membres de mon jury de thèse, pour leur leur participation constructive à cette défense, leur intérêt ainsi que l'évaluation de mes travaux. Mes remerciements vont aussi à Katleen Robert et Jon Copley pour leur efficace révision du manuscrit de thèse qui s'en est vu grandement amélioré. Je tiens d'autre part à remercier les membres de mon comité de suivi individuel Lénaïck Menot, Pierre Legendre, Mathilde Cannat et Pierre-Marie Sarradin qui m'ont accompagné durant ces trois années. Leurs conseils avisés et leur sens critique extérieur m'ont permis de moduler judicieusement la trajectoire de cette thèse.

Je remercie immensément le projet iAtlantic dirigé par Murray Roberts pour m'avoir offert le soutien financier afin de réaliser cette thèse. iAtlantic fut aussi au centre de divers événements de partage de connaissances auxquels j'ai pu prendre part et même organiser. En outre, je tiens à remercier les différents organismes responsables des événements auxquels j'ai pu participer, et notamment le programme eCoast pour le financement de ma venue à un workshop d'identification des coraux au Brésil. Je tiens aussi à remercier toutes les personnes qui ont permis de mettre sur pied l'observatoire fond de mer EMSO-Açores, avant 2007 jusqu'à ce jour. Il est important de se rappeler que ce projet de longue haleine met en œuvre des moyens financiers et humains considérables. Bien que je n'aie pas pu rencontrer tout ce monde, mes remerciements vont notamment à l'équipe RDT et particulièrement Laurent et Julien, à la flotte océanographique française et aux pilotes de Victor et du Nautile. Je remercie particulièrement les embarquants de la mission MoMARSAT2020 avec qui j'ai eu la chance de voir mes premières sources hydrothermales. Outre les activités professionnelles, la quarantaine et les transits ont permis de renforcer nos liens et de façonner cette mission comme une expérience impérissable.

Je remercie aussi grandement les collaborateurs de mes diverses études : Catherine Borremans, Mathilde Cannat, Benjamin Wheeler, Anik Brind'Amour, Pierre-Marie Sarradin, Pierre

Legendre, Agathe Laes pour leur temps alloué à la discussion des analyses, à la collection des données ainsi qu'à la rédaction de ces différents articles.

Mes remerciements vont à l'équipe du LEP qui m'a accueilli dans un cadre convivial, de partage et d'entraide, de sourires et de rigolades, de mots croisés autour d'un café. Je ne pourrai pas citer tout le monde avec qui ces belles rencontres ce seront façonnées, mais je remercie l'ensemble de l'équipe pour ce bel environnement de travail. Je tiens aussi à remercier Daniela Zeppilli et Annaig Wittische, pour leur proximité ainsi que leur bienveillance.

Un grand merci aux stagiaires que j'ai eu le plaisir d'encadrer et qui m'ont significativement aidé à terminer mes travaux, notamment Jonathan Drugmand, Annah Ramière et Marin Marcillat. Sur ce point, je remercie l'appui que Garance Perrois et Pedro Soto ont pu donner aux différents cas d'étude. Mes remerciements à l'équipe de Toulon, pour leur écoute à trouver des solutions concernant la production de modèles 3D, Aurélien Arnaubec, Maxime Ferreira, Clémentin Boittiaux. Ma gratitude va à Pierre-Antoine Simkat et Loïc le Sage, qui m'ont intensément soutenu et conseillé au travers de cette thèse et de rigolades. Pour ces mêmes raisons, je remercie Mélissa la pro' de la taxo, l'infatigable escaladeur Julien Van Damme et le dernier venu, Riwan, policier des déchets sauvages, qui ont donné quotidiennement vie à ce petit bureau que nous avons partagé. Nos longues discussions sérieuses ou parfois complétement loufoques m'ont permis de trouver du soutien et du réconfort pour ma thèse. Je citerai aussi Mathilde L., Adriana S., Camille P., Simon G., Cas C., Elodie L., Maurane R., Elena B., Valentine F., Alicia V., Diego C., Alberto G. et Jean-Romain L. même si bien d'autres ont contribué à mon épanouissement sur Brest. Mes pensées vont aussi à la célèbre et festive coloc de la Rue Saint-Malo, Léo, Théo, Alex, Tommy. Nous avons grandi ensemble pendant deux ans et notre amitié franco-belge restera à jamais gravée dans le marbre, bien que parfois houleuses en terme footbalistique. Je remercie également Manu S., Jody G., Max, Armelle M., Lucas V., Marion M., Ines N., Marion L., Léonard H., Léonard P., Silvia F., Mariane M., Alizé pour ces bons moments passés ensemble. Je remercie du fond du cœur mes amis de Belgique que j'aime revoir à chaque retour et qui m'ont encouragé jusqu'au bout. Certains sont même venus jusqu'ici danser avec Billy sur l'Île Vierge : Clémence J., Clémence C., Blaise M., Kenzo F., Antoine Z., Quentin S., Alex H. et Pierre-Philippe L.

J'ai une pensée émue pour mes grands-parents, Andrée Martin et Géry Van Audenhaege, qui n'auront pas pu assister à la fin de ma thèse mais qui auront toujours été fiers de leurs petits enfants. Je remercie ma famille, mes cousins et cousines, mon papa Stéphane, ma maman Annick et mes deux sœurs Alice et Julie pour leur soutien apporté. Je remercie mon papa et Valérie pour m'avoir accueilli au plat pays et pour nos longues discussions autour de l'étang. Alice, je te soutiendrai inconditionnellement dans ce dur labeur que tu as aussi entrepris. Je remercie Julie pour m'avoir ouvert les yeux sur la vie et pour son courage que j'admire. Je remercie ma maman, ainsi que Gildas, pour ces incessants allers-retours vers la Bretagne pour venir écouter le cri des goélands. Ces visites m'ont apporté une bouffée d'air frais, mais surtout, beaucoup de bonheur (et de fruits de mer).

Finalement, je remercie ma douce Elise. Son soutien sans faille a été un pilier pour mener à bien ce long travail dans les moments difficiles comme heureux, comme lors de l'adoption de notre cher Mr Le Gall (aka Zissou). Je me suis régalé de ces siestes sur les plages bretonnes ensoleillées et de notre découverte aventureuse de la France, du Nord au Sud et d'Ouest en Est. Let's do it again in Hampshire!

Table of contents

*In French

List of figures

Chapter I

Chapter II

Chapter III

Chapter IV

Chapter V

Chapitre VI

List of Tables

Chapter I

No table in this chapter

Chapter II

Chapter III

Chapter IV

Chapter V

No table in this chapter

Chapitre VI

No table in this chapter

Avant-propos

La connaissance sur les dynamiques fauniques acquise au travers de cette thèse repose sur une stratégie de recherche initiée avant 2010 (Sarrazin and Sarradin 2006; Sarrazin et al. 2007). En effet, les données et travaux présentés dans ce manuscrit sont le fruit d'un travail de longue date s'étalant depuis la conceptualisation, l'installation en 2010 et la maintenance et le développement de l'observatoire EMSO-Açores (Cannat et al. 2016) permis par le consortium European Multidisciplinary Seafloor and water column Observatory (EMSO; Grant agreement No. 731036) financé par l'European Research Infrastructure Consortium (ERIC). L'observatoire est maintenu chaque année grâce à la flotte océanographique française armée par Genavir et opérée par l'Ifremer durant les campagnes MoMARSAT (Cannat and Sarradin 2010). J'ai pu notamment prendre part à la mission MoMARSAT 2020 et participer activement à la collecte de données et au déploiement d'instruments.

Cette thèse réalisée au centre de Brest de l'Ifremer de 3 ans et 3 mois a été financée par le projet iAtlantic (Grant agreement no. 818123) soutenu par le programme European Union's Horizon 2020 (H2020). Cette thèse a abouti à la publication d'un article en premier auteur dans une revue international *Progress in Oceanography* (voir la liste détaillée ci-dessous, section [1]). D'autre part, j'ai participé à divers rapports et déliverables pour EMSO Açores et iAtlantic. De plus, ce séjour au BEEP m'a permis de participer à la publication d'autres recherches [2]. Grâce, notamment, à l'observatoire EMSO Açores, j'ai eu la chance de collaborer avec des chercheurs venant de milieux scientifiques souvent différents de celui de l'écologie hydrothermale. Cette multidisciplinarité s'est avérée essentielle pour mes différents travaux et riche en terme d'expérience professionnelle. Par exemple, j'ai participé à la publication de divers jeux de données [3]. Durant mon séjour, j'ai pu profiter de l'opportunité de présenter mes travaux et de rencontrer des chercheurs du monde entier, durant les différents congrès ou meetings intra- et internationaux auxquels j'ai pu assister [4]. J'ai moi-même pu participer à la réalisation d'un workshop pour le projet iAtlantic, à la mise sur pied d'une session 'hands-on' pour le Marine Imaging Workshop 2022 et ai assisté à un workshop de taxonomie des coraux pour lequel mon déplacement au Brésil été financé par eCOST [5]. En plus de cours donnés aux étudiants du Master Sciences de la Mer (Institut Universitaire Européen de la Mer), j'ai eu la chance d'encadrer des étudiants de tous niveaux qui m'ont aidé dans ma tâche de collecte et d'analyse de données [6]. En outre, grâce au programme de thèse soutenu par l'école doctorale des sciences de la mer (EDSML), j'ai pu compléter et diversifier mes compétences par des

formations n'ayant pas spécialement trait à la recherche en milieu profond [7]. Finalement, ma mission scientifique ne s'arrêtant pas aux portes du laboratoire, j'ai participé à divers événements de médiation scientifique à destination du grand public, mission que j'affectionne particulièrement [8]. Ces expériences m'ont permis d'ouvrir les yeux sur la perception qu'a le grand public sur le milieu scientifique et de réaliser l'importance de lui partager nos recherches.

[1] Articles revus par des paires :

- Van Audenhaege, L., Matabos, M., Brind'Amour, A., Drugmand, J., Laës-Huon, A., Sarradin, P.-M., Sarrazin, J. (2022). Long-term monitoring reveals unprecedented stability of a vent mussel assemblage on the Mid-Atlantic Ridge. Progress in Oceanography. 204, 102791. https://doi.org/10.1016/j.pocean.2022.102791

[2] Autres articles réalisés ou projets d'articles :

- Van Audenhaege L, Broad E, Hendry KR and Huvenne VAI (2021) High-Resolution Vertical Habitat Mapping of a Deep-Sea Cliff Offshore Greenland. Front. Mar. Sci. 8:669372.doi: 10.3389/fmars.2021.669372
- Versteegh, E.A.A., Van Dover, C.L., Van Audenhaege, L., Coleman, M., 2022. Multiple nutritional strategies of hydrothermal vent shrimp (*Rimicaris hybisae*) assemblages at the Mid-Cayman Rise. Deep. Res. Part I Oceanogr. Res. Pap. 103915. https://doi.org/10.1016/j.ddsr.2022.103915
- Boittiaux, C., Ferrera, M., Arnaubec, A., Dune, C., Marxer, R., Matabos, M., Van Audenhaege, L., Hugel, V. In prep. Eiffel Tower: A Deep-Sea Underwater Dataset for Long-Term Visual Localization
- Soto Vega, P., Papadakis, P., Matabos, M., Van Audenhaege, L., Ramière, A., Sarrazin J., da Costa, G. A. O. P. In prep. Hydrothermal Vents Substrate Classification using Convolutional Neural Networks.
- Marcillat, M., Van Audenhaege, L., Menot, L. In prep. 3D reprojection for optimal 2D annotation and georeferencing.

[3] Jeux de données publiés :

- Van Audenhaege Loic, Matabos Marjolaine, Gautier Laurent, Legrand Julien, Sarradin Pierre-Marie, Sarrazin Jozee (2022). Feature-matching based overlay of 7 years of high-resolution imagery collected by the TEMPO ecological module (EMSO-Azores observatory). SEANOE https://doi.org/10.17882/87389
- Van Audenhaege Loic, Matabos Marjolaine, Courant Valentin, Jaulin Emmanuel, Raffault Clarisse, Le Goffic Léa, Drugmand Jonathan, Brind'Amour Anik, Laes Agathe, Sarradin Pierre-Marie, Sarrazin Jozée (2022). Compilation of image annotations and environmental data of 7 years of monitoring of hydrothermal assemblages using the TEMPO ecological module (EMSO-Azores observatory). SEANOE https://doi.org/10.17882/84672
- Van Audenhaege, L et al. (2021): High-Resolution Vertical of a Deep-Sea Cliff offshore Greenland and the Associated Epibenthic fauna. *PANGAEA*, https://doi.pangaea.de/10.1594/PANGAEA.931687 *(dataset in review)*

- Matabos Marjolaine, Sarradin Pierre-Marie, Legrand Julien, Van Audenhaege Loic, Moreau Bertrand, Cannat Mathilde (2021). Thermistor chain temperature data from the EMSO-Azores observatory, 2020-2021. SEANOE. https://doi.org/10.17882/84226
- Matabos Marjolaine, Rodier Philippe, Van Audenhaege Loic, Sarradin Pierre-Marie, Cannat Mathilde (2021). Autonomous ibuttons temperature data from the EMSO-Azores observatory, 2020-2021. SEANOE. https://doi.org/10.17882/8395
- Matabos Marjolaine, Rodier Philippe, Van Audenhaege Loic, Sarrazin Jozee, Sarradin Pierre-Marie, Cannat Mathilde (2021). Autonomous ibuttons temperature data from the EMSO-Azores observatory, 2019-2020. SEANOE. https://doi.org/10.17882/80042
- Sarrazin Jozee, Matabos Marjolaine, Sarradin Pierre-Marie, Legrand Julien, Van Audenhaege Loic, Gautier Laurent, Moreau Bertrand, Chauvet Adrien, Cannat Mathilde (2021). SMOOVE, video data from EMSO-Azores observatory, 2020-2021. SEANOE. https://doi.org/10.17882/83948
- Cannat Mathilde, Matabos Marjolaine, Van Audenhaege Loic, Gayet Nicolas, Wheeler Benjamin, Souradeep Mahato, Sarradin Pierre-Marie, Sarrazin Jozee, Legrand Julien (2021). Array of Ocean Bottom Tilt Current Meters: data from the EMSO-Azores observatory, 2019-2021. SEANOE. https://doi.org/10.17882/76001
- Submission of a stable isotope dataset in Michel, L., Bell, J., Dubois, S., Le Pans, M., Lepoint, G., Olu, K., Reid, W., Sarrazin, J., Schaal, G. and Hayden, B. (2020). DeepIso-a global open database of stable isotope ratios and elemental contents for deep-sea ecosystems. SEANOE doi: 10.17882/76595

[4] Congrès ou meetings intra- et internationaux :

- Van Audenhaege L, Matabos M, Sarrazin J. Multi-scale investigation of spatio-temporal dynamics of vent fauna at Lucky Strike: a general overview of approaches used in my thesis. Journée imagerie de l'Ifremer (Nantes, 11-12/12/2019).
- Attendance to iAtlantic General Assembly 2020 (online, 11-14/05/20).
- Van Audenhaege L, Matabos M, Drugmand J, Laes-Huon A, Sarradin PM, Sarrazin J. Monitoring temporal dynamics of microbial mats at hydrothermal vents with the EMSO-Azores observatory (Lucky Strike vent field, Mid-Atlantic Ridge). eDSBS (online, 19-21/08/20).
- Van Audenhaege L, Matabos M, Drugmand J, Laes-Huon A, Sarradin PM, Sarrazin J. TEMPO: 10 years of ecological observations. IMOVE InterRidge workshop (online, 23-25/11/20).
- Van Audenhaege L, Matabos M, Drugmand J, Laes-Huon A, Sarradin PM, Sarrazin J. Monitoring 10 years of temporal dynamics using deep-sea image observatory. Journée imagerie de l'Ifremer (online, 08-09/02/21)
- Van Audenhaege L, Matabos M, Drugmand J, Laes-Huon A, Sarradin PM, Sarrazin J. 7-year monitoring of the spatio-temporal evolution of hydrothermal assemblages at the centimeter-scale of a diffuse-flow habitat. DSBS, September 2021, presentation available on demand
- Van Audenhaege L, Matabos M, Sarrazin J. Multi-scale spatio-temporal distribution of faunal assemblages on the Lucky Strike hydrothermal vent field (-1700 m). iAtlantic General Assembly 2021 (online, 21-24/09/20)
- Van Audenhaege l, Sarrazin J, Perrois G, Legendre P, Cannat M, Matabos M. Pluri-annual and high-resolution monitoring of vent assemblages at the Eiffel Tower

hydrothermal edifice. Imaging the Ocean, UN Ocean Decade satellite event (online https://www.iatlantic.eu/imaging-the-ocean-event/, 11/05/22)

- Van Audenhaege L, Matabos M, Sarrazin J. An automated workflow designed for space-time data processing of deep-sea imagery observatory. Marine Imaging Workshop (Océanopolis, 03/10/22)
- Van Audenhaege L, Sarrazin J, Perrois G, Legendre P, Cannat M, Matabos M. Deep-sea vent assemblage dynamics revealed by a pioneer time series of 3D reconstructions of a hydrothermal edifice. Work Package 3 Plenary session, iAtlantic General Assembly 2022 (Florianopolis, 10-14/10/2022)
- Van Audenhaege L, Matabos M, Sarrazin J. From the centimeter to 100s of metre: the use of high-resolution imaging techniques to investigate scale patterns of faunal dynamics at deep-sea vents. Innovation and Exploitation Examples Session, iAtlantic General Assembly 2022 (Florianopolis, 11-14/10/2022)

[5] Workshop :

- WP3 workshop iAtlantic, time series data analyses, co-organisation with Henry L.-A., Matabos M., Legendre P., Perrois G., Vad J. (online, 15-18/06/21) https://www.iatlantic.eu/events-calendar/wp3-timeseries-workshop/
- 2022 COBRA Early Career Fellowship and Deep-Sea Expedition Planning Master Class and Fellowship (03-06/2022)
- Kernec M, Van Audenhaege L, Borremans C, Matabos M. Hands-on session: The ImmerSea LAB. Marine Imaging Workshop (Océanopolis, 05/10/22)
- Coral Taxonomy Workshop – eCost (2000 € grant; 17-19/10/2022)

[6] Enseignement et encadrement :

- UE Environnements Profonds (IUEM), theoretical lecture (2h x 2; 21/10/20 & 04/10/21)
- Ramière A. (2022). Master 2, Université de Bretagne Occidentale, France. Caractérisation de la distribution spatiale de la mégafaune benthique au champ hydrothermal de Lucky Strike (ride médio-Atlantique). Matabos, M., Sarrazin J., Van Audenhaege, L.
- Pablo Richou (2022). License 2, Université catholique de l'Ouest, France. Stage d'observation. Annotation de l'ichthyofaune sur les vidéos du module caméra TEMPO (observatoire EMSO-Açores, champ hydrothermal de Lucky Strike). Encadrants : Van Audenhaege, L., Borremans, C., Matabos, M.
- Villers Maïlys (2021). Master 1, Université de Bretagne Occidentale, France. Étude des comportements de la macrofaune au sein d'un assemblage de modioles *Bathymodiolus azoricus* à 1700 m de profondeur sur le champ hydrothermal Lucky Strike. Rapport de Master en biologie et écosystèmes marins. Encadrants : Matabos, M., Sarrazin, J., Van Audenhaege, L.
- Drugmand Jonathan (2020). Master 2, Université de Louvain, Belgique. Étude à long terme de la dynamique infra-annuelle des mattes microbiennes et de l'habitat d'une zone de diffusion, à l'aide de l'observatoire EMSO-Açores, au sein du champ hydrothermal Lucky Strike sur la dorsale médio-Atlantique. Rapport de Master en biologie des organismes et écologie. Encadrants : Matabos, M., Sarrazin, J., Van Audenhaege, L.
- Raffault Clarisse (2020). License 3, Université de La Rochelle, France. Caractérisation des déplacements de la modiole Bathymodiolus azoricus à proximité d'une source

hydrothermale diffuse grâce au module d'observation biologique TEMPO (champ Lucky Strike, dorsale médio-Atlantique). Rapport de Licence Science de la Vie. Parcours Biologie des Ecosystèmes marins. Encadrants : Matabos, M., Sarrazin, J., Van Audenhaege, L.

- Le Goffic Léa (2020). Master 1, Université de Bretagne Occidentale, France. Étude de la variabilité d'un assemblage de modioles sur le champ hydrothermal de Lucky Strike. Rapport de Master en biologie et écosystèmes marins. Encadrants : Matabos, M., Sarrazin, J., Van Audenhaege, L.

[7] Formations comptabilisées (Total = 136h) :

- ETH-EDD-05 – Intégrité scientifique et données de la recherche (2h)
- PP-EDSML – Réseaux professionnels - Comprendre les fondamentaux des réseaux professionnels (4h)
- EDSML – How to pitch? – Journées EDSML (3h)
- FCv2-598-0290346U-16673-8466 – Atelier apprentissage au deep learning ALLOHa (6h)
- Atelier ASMA Modélisation multi-échelles de processus spatiaux (12h)
- SML Autre formation - Ocean Hackaton 2020 (10h)
- MGT-SML - Fête de la science, nuit des chercheurs, café scientifique (10h)
- ST-SML - MarDATA block course (30h)
- ST-SML - Campagne Océanographique - MoMARSAT 2020 (7h)
- ST-SML - Organisation et participation à l'iAtlantic ocean time series workshop (30h)
- PP-SML – Entreprenariat et Innovation - Emporia4kt (4h)
- MGT-SML – Participation manifestation vulgarisation scientifique - Journée professionnel IUEM (5h)
- SML Interventions en Lycée, L ou M – présentation liée au doctorat - UE Table ronde (3h)
- MGT SML – Participation manifestation vulgarisation scientifique - Science en Theizh (10h)

[7] Médiation scientifique :

- iAtlantic « *Follow the Fellows* » (presentation available upon request)
- Press release in the iAtlantic newsletter 2: MoMARSAT2020: "The technical maintenance of a deep-sea observatory during a technically restrictive pandemic."
- Exposition Capucins (1/2 journée)
- RadioU interview, Episode #1 Marines, https://www.radio-u.org/Marines-1-Ecosystemes-profonds-Loic-Van-Audenhaege.html
- Nuit des chercheurs Océanopolis 2020, 2021, 2022
- Science en Theizh 2021
- Journées IUEM: Q&A with MSc students and with Secondary school students
- Journées EDSML 2021

Chapter I

Introduction

I.1 Ecological background

I.1.1 Observing natural variability

The elaboration of a comprehensive ecological model requires identifying the patterns and sources of variability observed in natural communities and their responsible drivers (Levin 1992). This approach provides the opportunity to infer the underlying processes of changes, identify the mechanisms associated with community responses and describe keystone features structuring communities (Tews et al. 2004). While experimental studies aim to isolate the effect of one or more factors, they must be complemented by observations under realistic natural conditions. This can be achieved by first characterising the spatial distribution of communities. Indeed, living organisms are suited to occupy and develop in a particular set of conditions or " fundamental niches" based on their specific needs and tolerance thresholds linked to a particular location or "habitat" (Hutchinson 1957). Habitat complexity can have strong implications on community structure, allowing species co-existence and maintaining biodiversity (MacArthur and Wilson 1967; Tews et al. 2004). However, the actual occupancy called the "realised niche", reflects the effect of other factors that limit the establishment of a species within its fundamental niche, such as biotic interactions (e.g. competition, predation; Malanson et al. 1992). Assessing patterns of habitat occupancy in relation to the spatial arrangement of abiotic conditions and biotic components is fundamental to acquire knowledge on the mechanisms allowing species to maintain into particular niches and communities.

Understanding patterns of ecological variability can also be derived from temporal dynamics that interplay with spatial variability, and produce the observed distribution patterns. Communities evolve in a dynamic environment that can strongly affect their spatial arrangement and structure over time (Levin and Paine 1974; Connell 1978; Paine and Levin 1981). Depending on their predictability, intensity, selectivity and spatial extent (Sousa 1984a; Pickett and White 1985), the natural regime of disturbances of both biotic and environmental origins allows co-existence of species and regulates competition (e.g. Connell, 1978). These factors are primary drivers in a variety of ecosystems including intertidal zones, forests, savannas, lakes and abyssal plains (Brooks and Dodson 1965; Loucks 1970; Dayton 1971; Dayton and Hessler 1972; Menge and Sutherland 1976; Sousa 1979, 1984b; Parr and Brockett 1999; Parr and Andersen 2006). The temporal heterogeneity of the environment may also directly constrain the availability and diversity of resources (Rosenberg and Freedman 1994). Typically, environmental disturbances have been classified as "exogenous" as they are driven

by external forces (Sousa 1984a). Exogenous factors from destructive events can modify or even reset local assemblages. “Endogenous” factors of change can also take place within assemblages in relation to biotic interactions that may facilitate colonisation or, on the contrary, cause species exclusion (Watt 1947; Pickett and White 1985; Pickett et al. 1987). Often referred to as “foundation” or “ecosystem-engineer species”, the importance of organisms modifying and stabilising their habitats is key for structuring their associated communities (Dayton 1971; Bruno and Bertness 2001).

The continuum of exogenous and endogenous factors of changes constrain and shape the structure of communities over time, through a so-called “trajectory” (Pickett and White 1985). Those trajectories can be characterised by looking at predominant patterns of assemblage replacement and associated mechanisms (Pickett et al. 1987). First introduced by Clements (1916) and later reviewed by Connell and Slatyer (1977), community succession has been conceptualised as an ordered and directional process of community change involving modifications of the physical environment and tending to naturally evolve towards a stabilised ‘climax’ ecosystem (Odum 1969). That concept of succession claims that a likely sequence of distinctive communities follows a predictable temporal pattern (McIntosh 1981; Platt and Connell 2003). Knowing the disturbance regime and assemblage succession are therefore an asset to elucidate the functioning and dynamics of ecosystems of interest and predict their behaviour. At last, predicting trajectory of communities is fundamental for conservation and management purposes.

I.1.2 Handling scales in ecology

Observational studies are strongly constrained by logistical aspects (e.g. technology, time invested) needed to extract information from natural ecosystems. These constraints considerably restrict our perception of the natural variability to limited windows of observation in space and time (Steele 1978; Zajac et al. 1998). Therefore, the scale of description practically conditions the perception of processes acting at different scales in ecosystems (i.e. resolution and extent; Levin 1992). For instance, it is assumed that the larger the scale, the larger habitat heterogeneity and the pool of species will be (Underwood et al. 2005). Moreover, depending on the scale of investigation, the effect of one driver can predominate on another. For example, Zajac et al. (1998) reviewed the influence of biotic interactions for marine soft-sediment infauna and showed that they prevail at short term and small scales while environmental filtering applies

at larger scales. As we are capable to observe natural variability only over a limited range of scales due to time and technology constrains, data are acquired at distinct scales among studies, hence fragmenting the outcome of the results. This emphasises the difficulty to capture a full and integrated representation of the functioning of natural systems. Levin (1992) explains, '*One must recognize that the description of the system will vary with the choice of scales; that each species, including the human species, will sample and experience the environment on a unique range of scales; and that, rather than trying to determine the correct scale, we must understand simply how the system description changes across scales*'. Hence, building a comprehensive understanding of the behaviour of an ecosystem must be achieved by coupling insights provided by investigations performed at multiple scales. *In fine,* this allows to investigate how the influence of a factor of change propagates across scales. As recommended by Levin (1992), '*The essence of modelling is, in fact, to facilitate the acquisition of this understanding, by abstracting and incorporating just enough detail to produce observed patterns*'. As a contextual example, the emergence of the "patch dynamics" approach in intertidal ecology has demonstrated practical usefulness to emphasise the role of factors of change across scales (Pickett and Thompson 1978). The interplay of spatial heterogeneity, biotic interactions and simultaneously, temporal disturbances, produces complex mosaicking of natural communities over a wide range of scales. Although variability affects a given level of biological organisation (e.g. a local patch), those patterns of change may not apply at larger organisational scales (e.g. a mosaic of patches; Pickett et al., 1989). Indeed, the established species have evolved to maintain themselves at higher organisational levels in order to cope with the regime of change occurring within those levels (Levin 1992). Understanding how variable the system is across scales is therefore an asset to produce simple and meaningful ecological knowledge.

Patch monitoring has been typically performed following repetitive visits of study sites especially in the intertidal zone (e.g. Paine and Levin 1981). These patches represent smaller units of biological organisation evolving in a broader landscape (Watt 1947; Wiens 1976, 1997; Bormann and Likens 1979; Pickett and White 1985; Levin 1992; Parr and Brockett 1999). This approach has been particularly useful to understand the maintenance of patterns of intertidal assemblages despite the small-scale patchiness that remains challenging to link with driving factors (Paine and Levin 1981; Dethier 1984; Sousa 1984b). Such approach could be applied to vent communities exhibiting similar mosaicking of assemblage distribution (Sarrazin et al. 1997). However at vents, the lack of appropriate sampling methods has considerably limited our understanding of factors and mechanisms driving such fine-scale mosaic patterns (Gauthier

et al. 2010). More generally, undertaking multi-scale and high-resolution investigations have remained challenging in remote environments such as for deep-sea vent ecosystems because of the difficulty to perform high-resolution and extensive characterisation of natural systems.

I.1.3 Imaging deep-sea hydrothermal vents

The characterisation of remote deep-sea biological communities can be performed with the use of physical sampling or via imaging technology operated by underwater vehicles. Collection of samples is efficient at describing a large array of organism sizes, from the meio- to the megabenthos. The accumulation of samples have enabled to investigate the effect of spatial heterogeneity within and across vent sites (Van Dover and Doerries 2005; Sarrazin et al. 2015, 2020). However, early investigations have rapidly diagnosed the destructive impact of sampling on vent assemblages which could modify natural patterns in those patchy communities (Tunnicliffe 1990; Sarrazin et al. 1997). As a result, biologists have conscientiously worked towards reducing the effect of sampling activities at vent ecosystems (Tyler et al. 2005). Photo transects have been early used to describe the spatial distribution and temporal dynamics of hydrothermal vent assemblages in a non-destructive manner and over larger spatial extents (Fustec et al. 1987; Hessler et al. 1988; Chevaldonné and Jollivet 1993). Furthermore, the deployment of time-lapse cameras has enabled high-frequency *in situ* observation to monitor biotic interactions and changes over a few months (Tunnicliffe and Juniper 1990; Copley et al. 1999). More recently, deep-sea observatories provided new insights on high-resolution small scale variability of vent assemblages, highlighting the significant role of tidal variations (Cuvelier et al. 2014b; Sarrazin et al. 2014; Matabos et al. 2015; Lelièvre et al. 2017). While imaging capabilities have proven to be reliable and cost-efficient means to perform quantitative description of benthic communities, there remains a considerable gap of knowledge on how scales apply to the vent environment as those studies do not often bridge each other due to the different scales considered (Juniper et al. 1998; Cuvelier et al. 2012). With the constant technological development of underwater platforms and optical imaging, remote sensing has become an asset for high-resolution, quantitative ecological investigations over an array of nested spatial and temporal scales (Fisher 1995; Lutz et al. 2002; Matabos et al. 2016; Thornton et al. 2016; Huvenne et al. 2018; Feng et al. 2022). For the past decade, underwater vehicles and observatories have gathered extensive image sets in time and space that require the

development of new methods for extracting high-resolution information and understand how it propagates into larger spatial and temporal scales.

I.2 Hydrothermal vent ecosystems

I.2.1 Mid-Ocean Ridges – Genesis and characteristics

The surface of the Earth is composed of a solid shell called "lithosphere" divided into plates lying and moving on the "asthenosphere'", a more ductile region located beneath. As diverging plates spread and decompression occurs, the ascent of melted asthenosphere material takes place. As accretion of the material proceeds, faulting and magmatism provides the setting for hydrothermal processes to occur at Mid-ocean ridges (MORs). MORs are spreading centres forming elongated chains of underwater mountains, faults and axial valleys shearing the Earth seafloor (Figure I.1). Other tectonic settings displaying hydrothermal activity include converging plate boundaries, where the lithosphere material is conveyed back to the asthenosphere by subduction. However, these formations called "back-arc spreading centres" are much shorter than MORs.

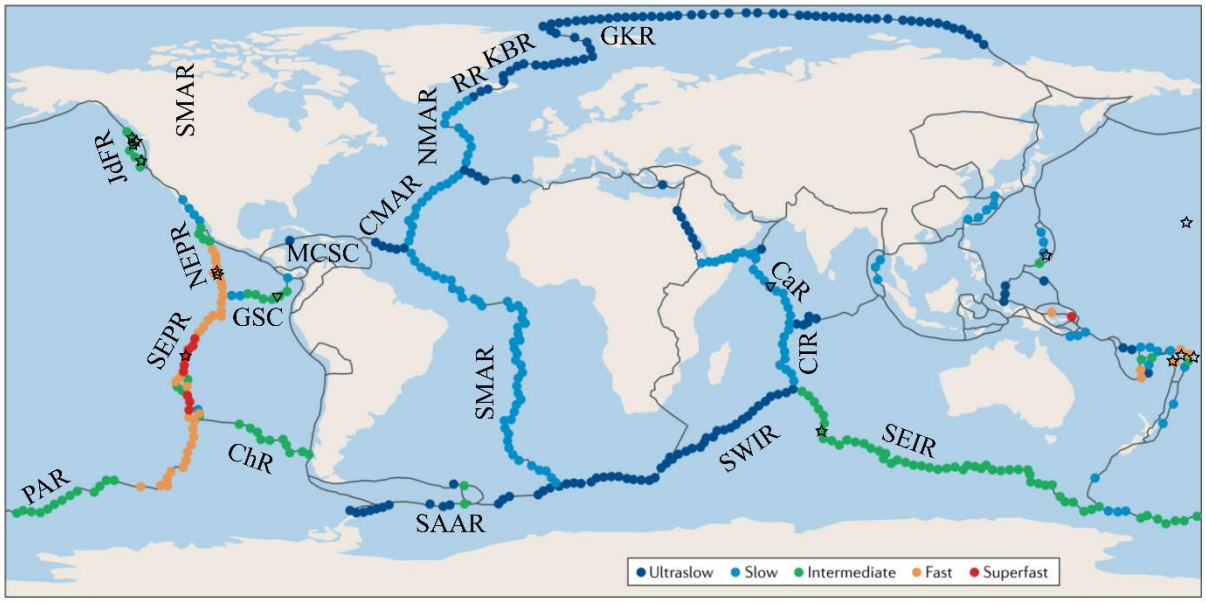

Figure I.1. Map locating the global ridge crest based on the InterRidge database (Beaulieu and Szafranski 2020). Colours inform on the spreading rates of ridges categorised from ultraslow (dark blue; < 20 mm/yr), slow (light blue; 20-50 mm/yr), intermediate (green; 50-80 mm/yr), to fast (orange; 80-140 mm/yr). Black lines delimit tectonic plate boundaries forming oceanic ridges: CaR: Carlsberg Ridge; ChR: Chile Ridge; CIR: Central Indian Ridge; CMAR: Central Mid-Atlantic Ridge; GKR: Gakkel Ridge, GSC: Galápagos Spreading Centre; JDFR: Juan de Fuca Ridge; KBR: Kolbeinsey Ridge; NEPR: North East Pacific Rise; NMAR: North Mid-Atlantic Ridge; MCSC: Mid-Cayman Spreading Centre; PAR: Pacific Antarctic Ridge; RR: Reykjanes Ridge; SAAR: South America-Antarctic Ridge;

SEIR: South East Indian Ridge; SEPR: South East Pacific Rise; SMAR: South Mid-Atlantic Ridge; SWIR: South West Indian Ridge. Stars and triangles indicate respectively confirmed and likely (i.e. detected remotely) records of deep-sea eruptions from historically active volcanoes (< 500 yrs; Rubin et al. 2012) respectively. modified after Dick (2019).

MORs widen at different pace, categorised from ultraslow (e.g. < 20 mm/year) to superfast (e.g. > 140 mm/year; Figure I.1; Karson et al. 2015) spreading ridges. Magmatic and tectonic events and plume anomalies have been commonly detected at MORs after swarms of earthquakes (Rubin et al. 2012; Figure I.1). These events are more frequent on fast-spreading than on slow MORs where they are very rare (~ 1000 years; Perfit and Chadwick 1998). In fact, repetitive eruptions have been observed at 9°50'N in the fast-spreading North-East Pacific Rise (NEPR) in 1991 and 2005/2006 and at the Axial Volcano of the intermediate-spreading Juan de Fuca Ridge (JDFR) in 1998, 2011 and 2015 (Haymon et al. 1993; Embley et al. 1999; Tolstoy et al. 2006; Chadwick et al. 2012; Wilcock et al. 2016; Figure I.1).

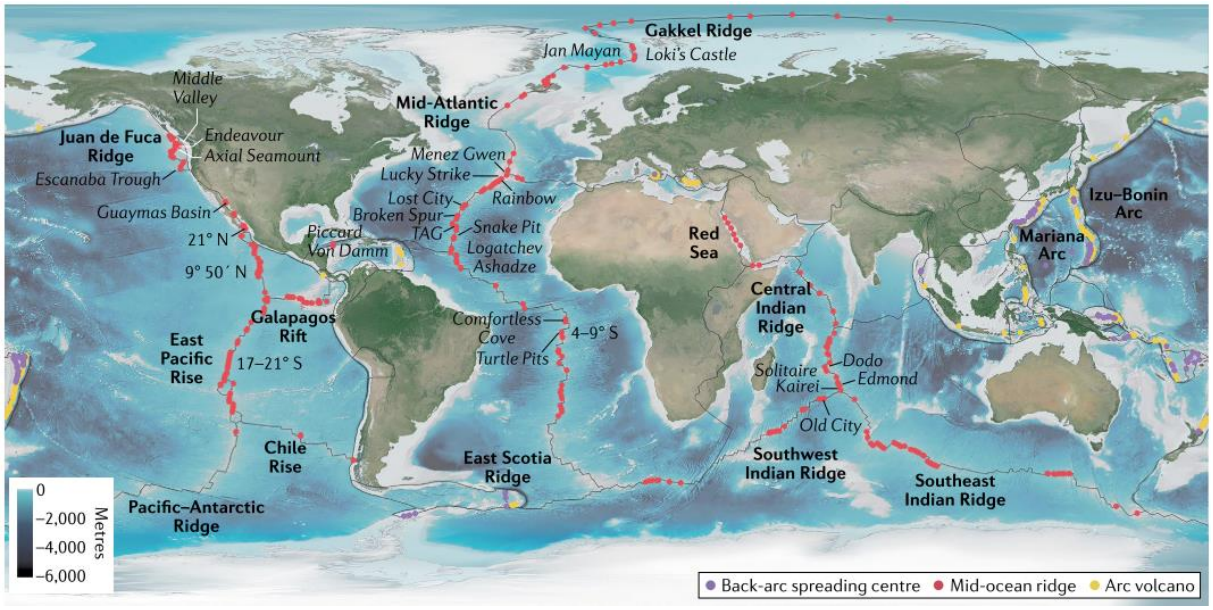

Figure I.2. Map of the global ridge system and hydrothermal vent fields that are known or inferred from water-column studies, located with a dot. Dot colour refers to the type of tectonic setting of the hydrothermal vent field, purple stands for back-arc spreading centre (22% of known vent fields), red for Mid-ocean ridge (MOR; 65%) and yellow for arc volcanos (12%). Data from the InterRidge data base (Beaulieu and Szafranski 2020). The bathymetry is shown with a gradient from light to dark blue. Map adapted from the Center of Environmental Visualization of the University of Washington by Früh-Green et al. (2022).

Magmatic and tectonic activities generate hydrothermal circulation cells that force the release of hydrothermal vent fluids at particular areas of the seabed areas. Known areas of hydrothermal activity are reported in the international global database of active submarine hydrothermal vent fields (Beaulieu and Szafranski 2020; Figure I.2). Spread out along the axial valleys of the MORs and back-arc basins and volcanic arcs, the so-called "hydrothermal vent fields" are

defined as the domain of hydrothermal discharge at a given location of a ridge (Baker and German 2004; Figure I.2).

I.2.2 Hydrothermal circulation – Creation of a peculiar habitat

Hydrothermal processes result from the convective circulation of sea water within the oceanic crust to its release at the seafloor (Jamieson et al., 2016; Tivey, 2007). The water enters the seafloor a few tens of metre away from venting (Becker et al. 1996; Salmi et al. 2014), or through normal faults especially at slow-spreading centres (Wilcock and Delaney 1996; Lowell and Yao 2002). By flowing down in the recharge zone, the seawater is incrementally heated up in contact with the magma chamber located for instance ~ 3 to 7 kilometres beneath the seafloor (e.g. Detrick et al. 1987; Singh et al. 2006; Figure I.3). Changes in thermal and pressure conditions displace chemical equilibria and force a panel of reactions to occur (Figure I.3). Higher temperatures trigger the precipitation of magnesium, calcium and sulphates forming anhydrite precipitates between 150 and 300°C ($CaSO_4$). Above 300°C, the low pH triggers the reduction of sulphate into sulphides.

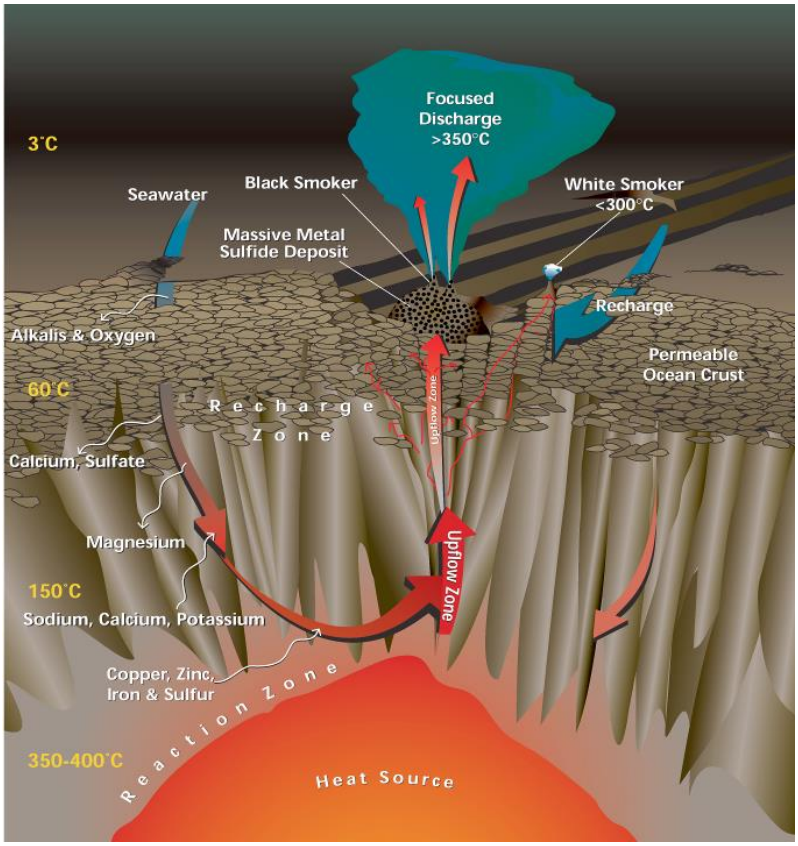

Figure I.3. Schematic description of hydrothermal circulation from a cross-section perspective of the lithosphere. The hydrothermal circulation typically takes place in four distinct zones of i. recharge, ii.

reaction, iii. upflow and iv. discharge. The chemical reactions and emission settings occurring throughout the hydrothermal circulation process are denoted. Figure from Humphris and McCollum (1998).

When the fluid reaches the reaction zone that constitutes the boundary with impermeable and ductile layer, it interacts and alters the magmatic rocks. Therefore, heat, protons, sulphur, metals (Fe, Mn, Zn and Cu) as well as rare elements are transferred to the fluid (Figure I.3). Exchanges of volatile components also occur (He, CO_2, CH_4, H_2; Tivey 2007). Additionally, if supercritical conditions are encountered, the fluid is separated in a dense brine and vapour phases in the reaction zone (Delaney et al. 1987; Von Damm 1988; Fontaine and Wilcock 2006). As buoyancy and viscosity decrease, the fluid rises in the upflow zone through conduits at temperatures up to ~ 400 °C (Coumou et al. 2008; Figure I.3).

Sustained vent fluid supply can lead to the formation of large and vertical sulphide structures also called "edifices" reaching up to 45 m high as they mature (Robigou et al. 1993; Hannington et al. 1995;). Hydrothermal emissions strongly varies within a sulphide edifice and adjacent areas in terms of kinetics as well as chemical and thermal properties (Tivey 2007; Barreyre et al. 2014; Figure I.4A). Such variability depends on the mixing of the rising vent fluid with seawater from the permeable upflow zone.

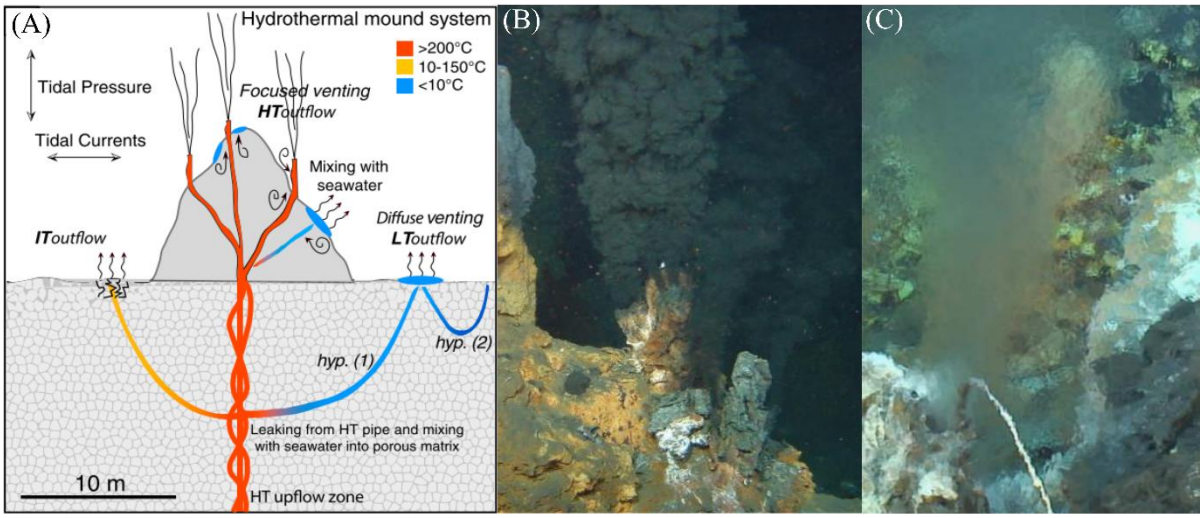

Figure I.4. Schematic description from Barreyre et al. (2014) of a mature edifice forming a sulphide talus (Hannington et al. 1995) and hydrothermal circulation from the end of the upflow zone to emission at the seabed of the Lucky Strike vent field (NMAR). The different colours indicate hypothesised pathways of circulation from focused high-temperature (HT) outflows fed by internal pipes, intermediate-temperature (IT) outflows redirected to cracks and diffuse low-temperature (LT) outflows. (B) Black plume typical of a focused high-temperature outflow emanating from several small hydrothermal chimneys at Rainbow (NMAR; Photo credit: EXOMAR 2005, Ifremer) and (C) shimmering waters linked to diffuse low-temperature venting at Lucky Strike (NMAR; Photo credit: MoMARSAT 2011, Ifremer). Note the presence of a high-temperature probe in Figure I.4C.

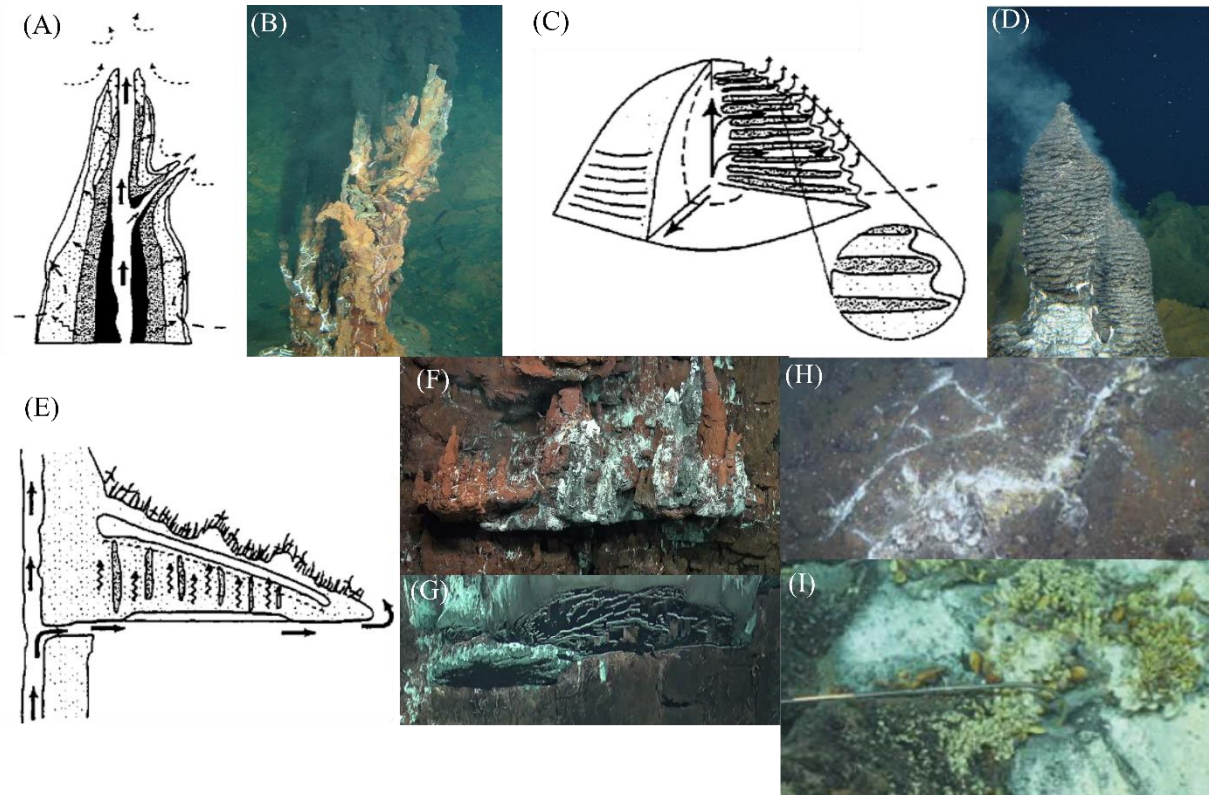

Figure I.5. Different patterns of hydrothermal outflow and associated structure modified from Hannington et al. (1995). (A) Cross-section of the conduit of a chimney associated with focused outflow. (B) Chimney from which focused vent emanates at the Rainbow vent field (NMAR; Photo credit: EXOMAR 2005, Ifremer). (C) Cross-section of a porous diffuser whose internal structure allows the mixing of the vent fluid. (D) Example of a typical porous diffuser forming a beehive structure from which a white vent fluid is released at the Rainbow vent field (Photo credit: EXOMAR 2005, Ifremer). (E) Lateral release of vent fluid building a horizontal outcrop called flange. Fluid can accumulate under the flange because. (F) Example of a flange forming an outcrop at the Capelinhos edifice of the Lucky Strike vent field (NMAR; Photo credit: MoMARSAT 2020, Ifremer). (G) View from underneath the flange of Figure I.5F showing accumulation of vent fluid (Photo credit: MoMARSAT 2020, Ifremer). (H) Example of vent fluid emanating from cracks in the periphery of the White Castle edifice of the Lucky Strike vent field (Photo credit: MoMARSAT 2016, Ifremer). (I) Example of diffusion of vent fluid percolating through sandy area near sulphide-indurated slab near the White Castle edifice. Note the white microbial mats and the presence of hydrothermal vent mussels (Photo credit: MoMARSAT 2017, Ifremer). All arrows from Figure I.5A-C-E describe the pattern of vent fluid circulation within the hydrothermal feature.

Vent emissions are typically classified based on outflow temperature measurements (Johnson et al. 1988b). Discrete or focused venting discharges high-temperature vent fluids from a narrow conduit at high speed (Figure I.4B). That turbulent venting usually occurs on sulphide edifices that isolate the main conduit from subsurface mixing with percolated seawater (Mittelstaedt et al. 2012; Barreyre et al. 2014). The fluid harbours a black to grey colour that reflects an increasing dilution with seawater, hereafter called “black” (> 300 °C) and “white” (150 to 300 °C) smokers (Figure I.4B). Black smoker releases end-member (i.e. fully

transformed) fluids that are warm, acidic, loaded with reduced elements (e.g. sulphides), metals and depleted in calcium, oxygen and sulphates (Charlou et al. 2000; Douville et al. 2002; Tivey 2007). As the fluid encounters the cold and alkaline seawater, precipitation occurs to form structures with different morphologies: vertical chimneys that can grow from a few centimetres to a decimetre within a day (Tunnicliffe and Juniper 1990; Figure I.5A-B), bulbous and porous diffusers (Figure I.5C-D) and lateral flanges emerging from cracks in the edifice (Hannington et al. 1995; Tivey 2007; Figure I.5E-F-G). Diffuse venting usually occurs in specific areas (e.g. cracks, porous rock and sediment; Barreyre et al., 2012; Figure I.5H-I). They are characterised by low-velocity release of low-temperature shimmering waters (<150 °C; Figure I.4C). Their formation may result from the leaking of high-temperature mixing with seawater or from conductive heating of seawater that seeped in the upflow zone (Cooper et al. 2000; Barreyre et al. 2014). After exiting, the vent fluid propagates vertically and horizontally in the water column (Mittelstaedt et al. 2012). A gradual dilution allowing metal partitioning and sulphur speciation contributes to the modification of vent fluid composition along a spatial gradient (Tivey 2007; Sarradin et al. 2009; Jamieson et al. 2016a; Cotte et al. 2020).

I.3 Ecology of vent communities

The discovery of hydrothermal vents at the Galapagos spreading centre (GSR) in 1976 led to the first images of unexpected aggregations of clams and anemones concentrating in the vicinity of hydrothermal deposits (Lonsdale 1977). In 1977, scientists diving in the human-occupied vehicle (HOV) *Alvin* stumbled on luxuriant communities of undescribed mussels, limpets and giant tubeworms (Corliss and Ballard 1977; Grassle et al. 1979). Their high densities contrasted with the assumption of declining biomass with depth (Sanders et al. 1972; Figure I.6). The possibility that life can abound in the deep sea has been neglected because of the scarcity of food, absence of light, coldness and high ambient pressure. As a result, the discovery of hydrothermal vents profoundly changed our understanding of this environment and transformed our knowledge and vision of life adaptations on Earth and potentially elsewhere. Hydrothermal vents were the first identified deep-sea ecosystems where primary productivity was predominantly supported by a community of chemoautolithotrophic microorganisms (Jannasch 1985). These microorganisms are able to oxidise an array of reduced elements such as H_2S, CH_4, NH_4^+, Fe^{2+} present in the vent fluid to harvest the chemical energy subsequently stored in adenosine triphosphate (ATP) molecules. As the vent fluid propagates, at depth or over the seafloor, it dilutes with seawater loaded of O_2, a by-product of photosynthesis, and NO_3^- or SO_4^-

used as electron receptors. That mixing provides a redox interface at which a diversity of metabolic pathways may be used to perform chemosynthesis (Jannasch 1995; Karl 1995).

These microorganisms can be free, living within the water column or attached to the substratum or in symbiosis with invertebrate species (Dick 2019). They constitute the base of the vent trophic web (Tunnicliffe 1991). As hydrothermal vent exploration proceeded, scientists discovered a number of symbiotic relationships (i.e. holobionts) involving vent endemic invertebrates as hosts all over the world oceans (Figure I.6). Such recurrent adaptations were described for many taxa including bathymodiolin mussels (e.g. *Bathymodiolus* spp. and *Idas* spp.), alvinocaridid shrimps (e.g. *Rimicaris* spp.), vesicomyid clams (e.g. *Calyptogena* spp. and *Vesicomya* spp.), gastropods (e.g. *Ifremeria nautilei*, *Alviniconcha* spp., *Chrysomallon squamiferum*), siboglinid tubeworms (e.g. *Riftia pachyptila*, *Ridgeia piscesae*, *Tevnia jerichonana*, *Lamellibrachia spp.*; Cavanaugh et al. 2006; Desbruyeres et al. 2006; Dubilier et al. 2008; Sogin et al. 2020; Figure I.6). They usually perform intracellular endosymbiosis as they house bacteria such as in their enlarged gills for clams, mussels and snails or in their trophosome for tubeworms. Ectosymbiosis occurs when symbionts remain outside the host's tissue (e.g. *Rimicaris exoculata* shrimps, *Kiwa tyleri* crabs; Goffredi 2010). These large ecosystem-engineer invertebrates provide habitat complexity (e.g. 3D substratum) that structures the community, allowing the coexistence of multiple associated species and contributes to increasing local biodiversity and abundance (Govenar et al. 2005; Govenar and Fisher 2007; Govenar 2010, 2012; Rybakova and Galkin 2015).

Although symbiotic invertebrates usually visually dominate at vents, their biomass seems poorly transferred to the rest of the community (Fisher et al. 1994; Van Dover and Fry 1994; Colaço et al. 2002; Levesque et al. 2006; Bergquist et al. 2007; De Busserolles et al. 2009; Lelièvre et al. 2018; Portail et al. 2018; Van Audenhaege et al. 2019). Vent trophic webs remain in general short, with two to three levels of consumers (Govenar 2012). Most of the vent community predominantly relies on the consumption of microbial communities and their detritus (Van Dover and Fry 1994; Limén et al. 2007; Portail et al. 2018). Few endemic polynoid, crabs and, in the Pacific, zoarcid species have specialised on preying selectively on vent fauna (Colaço et al. 2002; Micheli et al. 2002; Sancho et al. 2005). In the periphery, vent primary productivity is thought to support communities of non-vent organisms including suspension-feeding taxa and visiting predators making incursion within vent assemblages (Fisher et al. 1994; Colaço et al. 2002; Erickson et al. 2009; Gebruk et al. 2010; Fabri et al. 2011; Kim and Hammerstrom 2012; Marsh et al. 2012; Sen et al. 2016; Van Audenhaege et al.

2019). Both specialist and generalist species occur in feeding guilds (Bergquist et al. 2007) although specialists appear to predominate, hence favouring species co-existence (Levesque et al. 2003; Lelièvre et al. 2018).

I.4 Dynamics of the vent fauna

I.4.1 Spatial distribution

The vent fauna lives in relative proximity to the release of vent fluids. They occupy hard or soft substratum located at the interface between the anoxic and reduced vent emissions and the cold, oxygenated seawater. Firstly, the degree of exposure to the vent fluid directly influences the level of stress organisms experience due to the dispersion of noxious compounds and the presence of anoxic conditions. Secondly, primary productivity performed by chemoautolithotrophic bacteria is influenced by the concentrations in basal chemicals defining the local redox conditions, directly affected by the mixing between vent fluid (i.e. typically H_2S, Fe, CH_4, H_2) and surrounding oxidative seawater (O_2, CO_2). As a result, the environmental gradient that results from the vent fluid dilution creates a myriad of microhabitats that species will colonise depending on their tolerance threshold and trophic requirements (e.g. Vismann 1991; Levesque et al. 2003; Bates et al. 2005; Henry et al. 2008; Lelièvre et al. 2018; Sigwart and Chen 2018).

Typically, the habitat a species occupy is characterised with local measurements of temperature and concentrations of sulphide, iron and oxygen (Fisher et al. 1988; Sarradin et al. 1999; Sarrazin et al. 1999; Desbruyères et al. 2001; Le Bris et al. 2006b; Matabos et al. 2008; Moore et al. 2009; Podowski et al. 2010; Marsh et al. 2013). The hydrothermal conditions an organism experiences originally depends on the setting and composition of vent emissions located nearby. Moreover, the porosity of the substratum can locally facilitate vent fluid exits through preferential pathways. At JDFR, different assemblages were related to distinct substratum mineralogy that influence the vigorousness of the vent outflow (Sarrazin et al. 2002). Large ecosystem engineers additionally modify exposure to vent fluids at fine scales, by diverting and consuming associated sulphides as hypothesized for *Bathymodiolus thermophilus* on the East Pacific Rise (EPR; Johnson et al. 1994). Exposure to the vent fluid remains influenced by the mixing rate and its dispersion, often estimated with the distance from the vent outflow (Cuvelier et al. 2009; Kim and Hammerstrom 2012; Marsh et al. 2012; Gerdes et al. 2019a; Figure I.7).

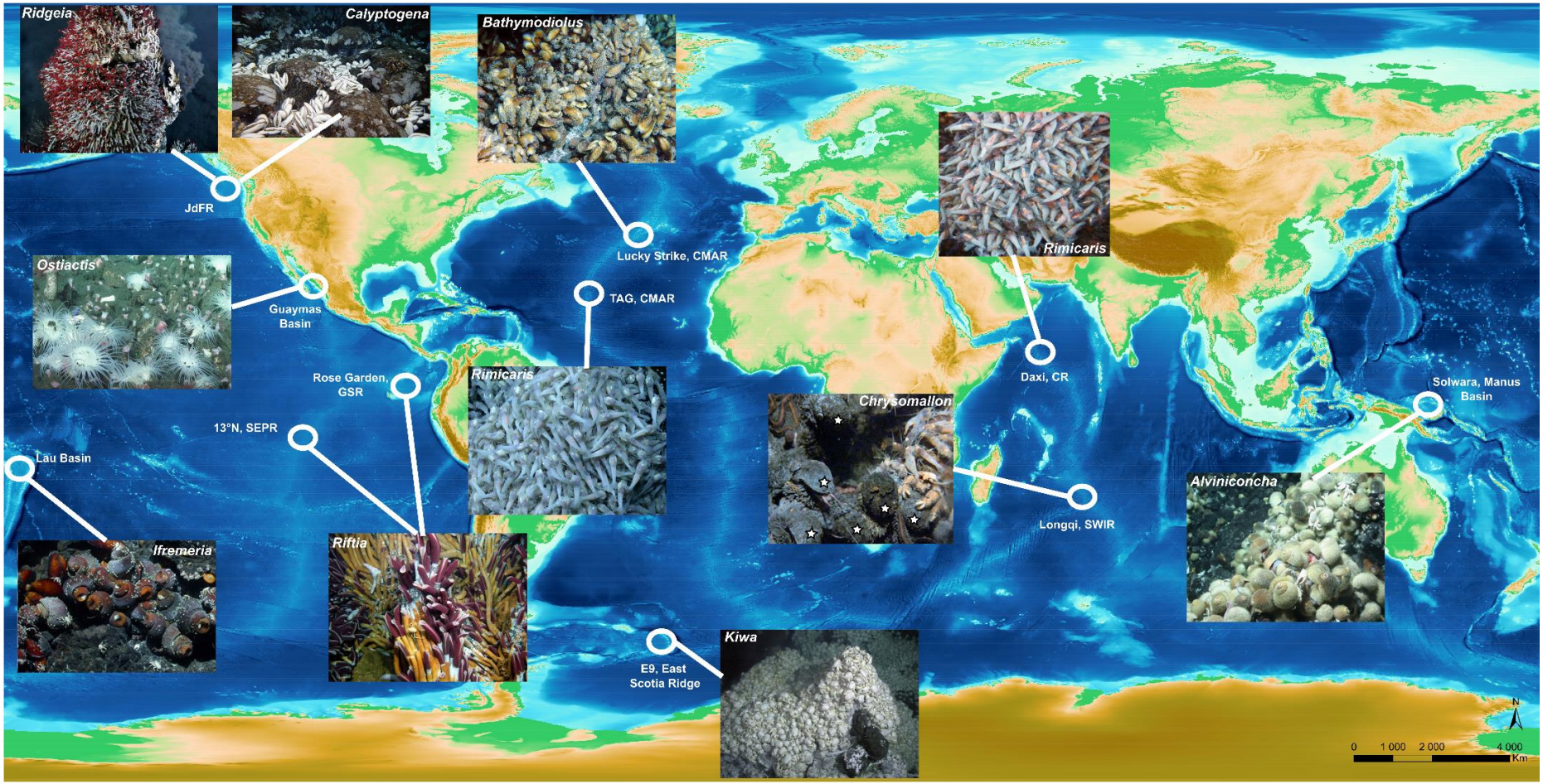

Figure I.6. Large endemic invertebrates at hydrothermal vents. All of them are symbiotic and create dense assemblages. From left to right, from top to bottom: *Ridgeia piscesae* (photo credit : Neptune Canada), *Ostiactis pearseae* (photo credit: Goffredi et al. 2021), *Ifremeria nautilei* (photo credit: MARUM), *Calyptogena magnifica* (photo credit: T. Shank and R. Lutz), bush of *Riftia pachyptila* (photo credit : Ifremer), bed of *Bathymodiolus azoricus* (photo credit: Ifremer), swarm of *Rimicaris exoculata* (photo credit: Ifremer), *Chrysomallon squamiferum* pointed with a white star (photo credit: Copley et al. 2016), *Kiwa tyleri* (photo credit: Rogers et al. 2012), *Rimicaris kairei* (photo credit: Zhou et al. 2022), *Alviniconcha boucheti* (photo credit: C. Fisher/Ridge 2000). Bathymetric map provided by GEBCO (2019). At the genus level, the global distribution is not exclusive as shown by *Rimicaris* shrimps present in the Atlantic and Indian oceans. The genus *Bathymodiolus* is found in the Atlantic, Indian and Pacific oceans but not necessarily at all vent fields of the MAR (e.g. TAG). *Alviniconcha* gastropods can be found in the back-arc basins of the West Pacific and the Indian oceans.

Bottom currents are additional drivers of vent fluid dispersion, primary productivity and larval export as well as resuspension of dissolved and particulate organic matter over scales of tens to hundreds of meters (Cannon et al. 1991; Khripounoff et al. 2008). On sulphide edifices, local interactions with the vertical topography leads to enhanced hydrodynamics which may significantly increase fine-scale habitat heterogeneity and the spatial extent of particle redistribution (Girard et al. 2020a). Over hundreds of metres, a few studies have however demonstrated the importance of the substratum properties and distance from venting for influence on the spatial distribution of non-vent communities (Arquit 1990; Milligan and Tunnicliffe 1994; Boschen et al. 2016; Levin et al. 2016a; Sen et al. 2016; Gerdes et al. 2019b).

Insight from image-based cartography of vent faunal assemblages pictured patterns of concentric zonation linked to the vent fluid dilution gradient as a response to the above detailed processes (Fustec et al. 1987; Shank et al. 1998; Gebruk et al. 2000; Podowski et al. 2010; Tokeshi 2011; Kim and Hammerstrom 2012; Marsh et al. 2012; Figure I.7). High-resolution cartography at sulphide edifices refined these models and demonstrated a mosaic zonation of assemblages rather than a linear gradient pattern linked to the spatial heterogeneity of the habitat, also interplaying with temporal dynamics (Sarrazin et al. 1997; Sarrazin and Juniper 1999; Marsh et al. 2013; Gerdes et al. 2019a; Girard et al. 2020a).

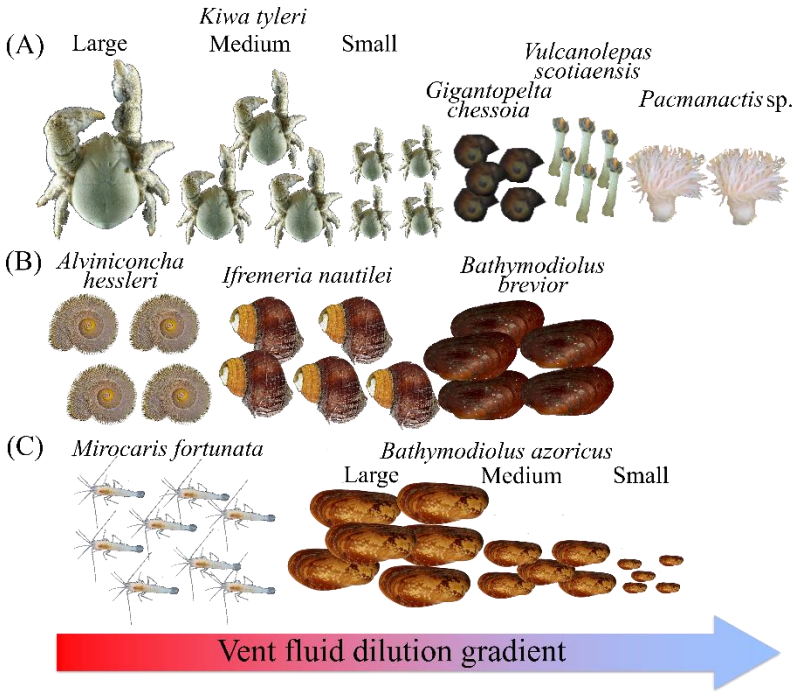

Figure I.7. Typical spatial zonation pattern observed among assemblages dominated by large invertebrates at (A) the E9 vent field (East Scotia Ridge; Marsh et al. 2012), (B) at the Lau back-arc basin (Kim and Hammerstrom 2012; Sen et al. 2013) and (C) at the Lucky Strike vent field (NMAR; Cuvelier et al. 2009). The zonation can be interspecific and intraspecific (size based in that case). The

relative position of the fauna is presented along the vent fluid dilution gradient from warmer to colder habitats indicated with the red-to-blue arrow.

At the field scale, a few studies have demonstrated the importance of substratum properties and distance from venting on the spatial distribution of non-vent communities (Arquit 1990; Milligan and Tunnicliffe 1994; Boschen et al. 2016; Levin et al. 2016a; Sen et al. 2016; Gerdes et al. 2019b).

Biotic interactions can also contribute to shape the observed spatial distribution of vent species '*Biotic interactions occur when organisms living in the same community directly or indirectly influence one another*' (Fraser et al. 2021). Depending on the mechanisms, they can be subdivided into inhibitory interactions, often referred as negative, and facilitative interactions, often referred to as positive (Benedetti-Cecchi 2000).

Inhibitory interactions (e.g. competition, predation) can have negative effects and limit species co-existence. For example, on the EPR, *Bathymodiolus thermophilus* can fully replace the siboglinid *R. pachyptila* through sulphide consumption and physical displacement (Hessler et al. 1988; Johnson et al. 1988b, 1994; Shank et al. 1998). On the JDFR *Paralvinella sulfincola* exhibits aggressive territorial behaviour towards conspecifics therefore influencing their distribution pattern (Grelon et al. 2006). Intra- and interspecific competition for food in dense alvinellid assemblages may negatively affect their size and the breadth of their trophic niche (Levesque et al. 2003; Grelon et al. 2006). Species recruitment can also be inhibited through the "bulldozer effect" of mobile grazers (Micheli et al. 2002; Marcus et al. 2009) or larviphagy by filter feeders (Lenihan et al. 2008). On the EPR, the selective consumption of *Lepetodrilus elevatus* by the zoarcid fish *Thermarces cerberus* creates a positive feedback allowing the recruitment of sessile organisms, normally inhibited by gastropod grazing activities (Micheli et al. 2002; Sancho et al. 2005). Despite having negative effect at the organism level, it is generally assumed that persistent biological disturbance has ecological implications at higher organisational levels by regulating community structure and distribution, preventing resource monopolisation and competition which possibly enhances diversity (e.g. Connell 1961; Ayling 1981; Shurin et al. 2001). Facilitation is a positive biotic interaction that includes the modification of the physical environment favouring the settlement of other organisms (Bruno and Bertness 2001). In fact, aggregations of large engineer species contribute to enhance the heterogeneity and the stability of the habitat by providing a panel of physical and trophic niches through the retention of organic matter, sulphide consumption and provide surface for colonization and microbial film growth which is of importance for colonisation (Johnson et al.

1994; Govenar et al. 2005; Le Bris et al. 2006a; Marcus et al. 2009; Lelièvre et al. 2018). On the JDFR, the biomineralisation of marcasite crusts by the early-colonist *Paralvinella sulfincola* contributes to decrease substratum porosity which in turn reduces the exposure to vent fluid and allows the colonisation of the less tolerant *P. palmiformis* (Juniper et al. 1992; Sarrazin et al. 2002). The intensity of biotic interactions may not be distributed evenly along the vent fluid dilution gradient. While inhibitory interactions seems to increase with denser assemblages in warmer habitats, the intensity of facilitative interactions seems to increase away from vent fluid exits in low temperature areas (Mullineaux et al. 2003). Similarly to the intertidal (Benedetti-Cecchi 2000), as productivity and density declines along the environmental gradient, so does the intensity of negative interactions to gain access to resources (Mullineaux et al. 2003).

I.4.2 Spatio-temporal dynamics

Temporal investigation at vents can be classified following the frequency of data acquisition ranging from infra-daily (e.g. Cuvelier et al. 2014; Lelièvre et al. 2017) to pluri-annual (e.g. Sarrazin et al. 1997; Shank et al. 1998). As those studies take place over a limited range of spatial and temporal scales, their setting will influence the observed regime of variability, associated processes of changes and the resulting dynamics of the fauna (Figure I.8). Temporal monitoring can be performed with repeated video/photographic surveys (e.g. Hessler et al. 1988; Juniper et al. 1992; Sarrazin et al. 1997), deployment of substratum for colonisation (e.g. Micheli et al. 2002; Mullineaux et al. 2003) or clearance of a patch followed by repeated samplings (e.g. Marticorena et al. 2021).

Large-scale disturbance – Magmatic eruptions can have dramatic consequences on vent communities at large scales, as resurgent lava can eradicate them (Desbruyères 1998; Lutz et al. 2001; Shank et al. 2003; Nees et al. 2008; Marcus et al. 2009) or activate new sites that possibly cease a few years later (Tunnicliffe et al. 1997). Post-eruptive monitoring were performed at GSR (Shank et al. 2003), twice at 9°50'N EPR (Shank et al. 1998; Nees et al. 2008; Mullineaux et al. 2020) and on JDFR, at Coaxial segment (Tunnicliffe et al. 1997), North Cleft Segment (Tsurumi and Tunnicliffe 2001) and Axial Volcano (Marcus et al. 2009). Most authors evaluated that two-third of the species returned within three years. This suggests the high recovery potential of vent populations in order to subsist in the ephemeral habitats of fast spreading ridges (Lutz et al. 1994; Tunnicliffe et al. 1997; Shank et al. 1998; Tsurumi and Tunnicliffe 2001; Marcus et al. 2009).

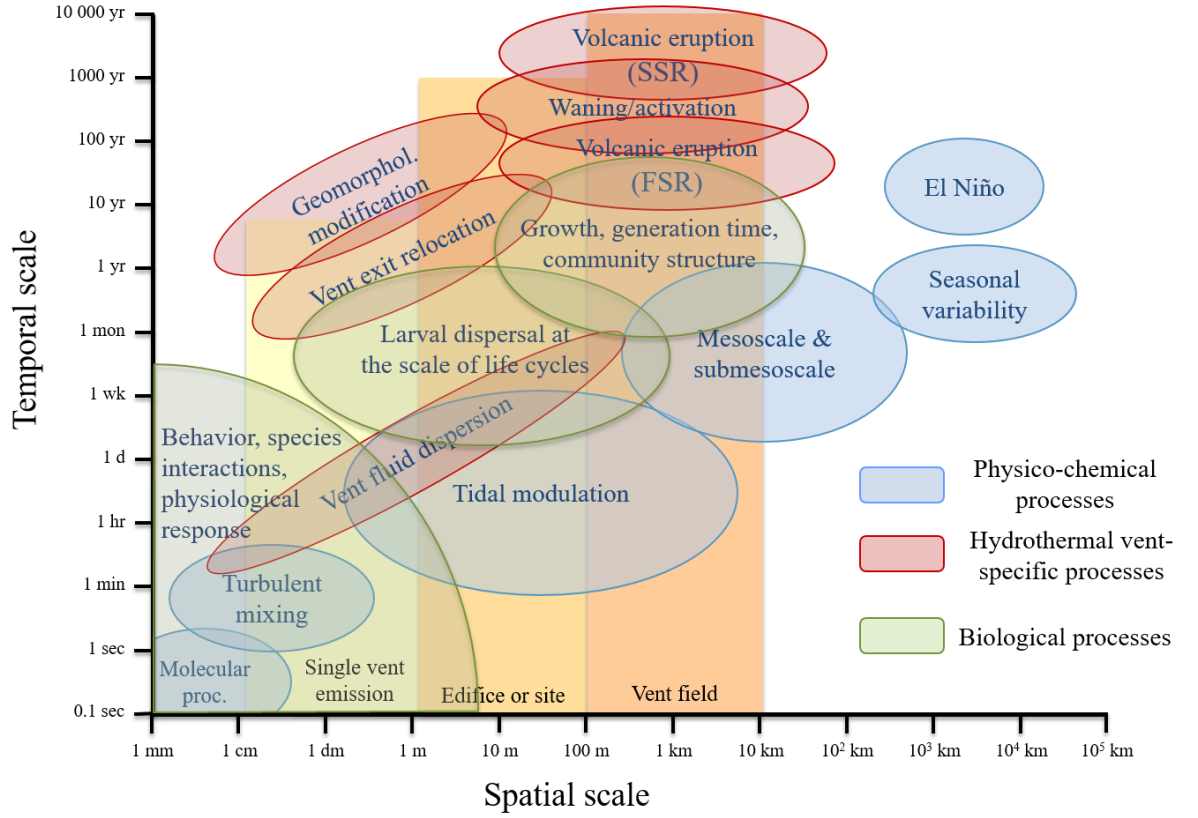

Figure I.8. Review of the abiotic and biotic drivers of variability of the vent habitat and fauna. Drivers of variability are plotted according to the range of spatial and temporal logarithmic scales at which those processes occur and at which they could potentially impact the dynamics of the associated fauna. Note for volcanic eruption: FSR = fast-spreading ridge, SSR = slow-spreading ridge.

No recovery potential has been estimated after eruptive events at slow-spreading features. Compared to fast-spreading ridges where eruptions occur at decadal frequency, eruptive events may occur at time scales of a millennium at slow-spreading ridges (Perfit and Chadwick 1998; Rubin et al. 2012; Figure I.8). For instance, to our knowledge they have never been witnessed in the deep sea along the Mid-Atlantic Ridge. In that case, inter-annual case studies have been conducted under continuous venting activity (Desbruyères 1998; Glover et al. 2010). In contrast with the dynamics observed at fast-spreading features of the Pacific ocean, they have revealed the high stability of venting and associated communities on time scales from a few years to decades: at the MAR (Copley et al. 1997, 2007; Gebruk et al. 2010; Cuvelier et al. 2011b), at the SWIR (Zhou et al. 2018) and the back-arc spreading centres of the Southwest Pacific Ocean (Sen et al. 2014, 2016; Du Preez and Fisher 2018).

Temporal changes at active vent sites: ecological succession – Successional models at vents are typically ordered by predominant patterns of transition, from the opening of a new habitat or the removal of the established assemblage following a disturbance, to the closing through the decline of venting activity monitored with sulphide measurements (Sarrazin et al. 1997;

Shank et al. 1998; Marcus et al. 2009). Sources of habitat change include level of venting activity, creation of new habitats by edifice growth, fluctuations and redistribution of fluid flow and more anecdotally, structural collapse (Fustec et al. 1987; Hessler et al. 1988; Sarrazin et al. 1997; Desbruyères 1998; Copley et al. 2007; Gebruk et al. 2010; Cuvelier et al. 2011b; Du Preez and Fisher 2018; Figure I.8). As a new habitat is made available, "pioneer" species with usually high tolerance to vent exposure and rapid colonisation capability (either through rapid recruitment or mobility) colonise the open area (Chevaldonne and Jollivet 1993; Sarrazin et al. 1997; Shank et al. 1998; Marcus et al. 2009; Mullineaux et al. 2012; Sen et al. 2014; Marticorena et al. 2021). Most studies have shown the importance of the gradual decline of sulphide concentrations to allow succession to proceed, conceptually ending when venting ceases and signals the senescence of the assemblage. As hydrothermal mineral precipitates, the porosity of the substratum may decrease and progressively clog the fluid exit. As a result, mineral accumulation may contribute to redirect the focused vent fluid to adjacent areas (Tivey 1995). At larger scales, precipitation inside the plumbing of a sulphide edifice could also redirect the vent fluid to the sides and switch the hydrothermal outflows from focused to more diffuse emissions that may be redirected to the base of the edifice (Sarrazin et al. 1997; Cuvelier et al. 2011b; Zhou et al. 2018; Figure I.8). Biotic interactions also play a role in this succession by influencing the transition from one successional stage to another (Sarrazin et al. 1997; Shank et al. 1998; Marcus et al. 2009; see section I.3.3.1). In case of waning, progressive replacement of declining chemosynthetic species (i.e. senescent) by less tolerant species such as scavengers was observed (Hessler et al. 1988; Gebruk et al. 2010; Sen et al. 2016).

Finally, successional models are a general summary of the predominant processes along the vent fluid dilution gradient and among study settings (Mullineaux et al. 2003, 2012). While models are ordered from habitat opening to senescence, successions can equally go backward as venting can undergo intensification (Sarrazin et al. 1997; Marcus et al. 2009). In reality, chronic regime of small-scale disturbances with varying intensity is more likely to shape successional patterns following a random scheme, therefore contributing to fragment the spatial arrangement of assemblages at the scale of the edifice and create mosaics (Sarrazin et al. 1997).

Infra-annual investigation – The development of autonomous cameras and deep-sea observatories has unlocked information on the sub-annual variability of faunal distribution in relation to changes in the physical habitat. In general, that variability modulates the activity and the microdistribution of vent organisms. Studies conducted this last decade highlighted the role of seasonal storms, internal waves and barotropic tides on the behaviour and distribution of the

vent fauna. For instance, using instrumentation deployed on the Ocean Networks Canada observatory along the Juan de Fuca Ridge, Lelièvre et al. (2017), found that decimetre-scale variability in the position of pycnogonids and polynoids living in a siboglinid tubeworm assemblage coincided with inertial current oscillation frequencies, possibly linked with seasonal surface storms. These storms generate inertial waves that can propagate to water masses at great depth causing low-frequency inertial oscillations that affect bottom currents (Thomson et al. 1990; Cannon et al. 1991; Figure I.8). These inertial currents constrain the dissipation of the plume as observed with oscillations in local temperature and plume velocities (Cannon and Thomson 1996; Xu et al. 2013). Disturbance in the vent habitat on the JDFR (spire collapse) was shown to strongly influenced the mortality of vent polychaetes (44%; Tunnicliffe et al. 1990).

At infra-daily scales, time series of temperature at vents have shown semi-diurnal variability of temperatures in the order of a few degrees within a day (Chevaldonné et al. 1991; Sarrazin et al. 2014; Lee et al. 2015; Figure I.8). This variability in vent fluid exposure can constrain the spatial distribution and/or activity of vent organisms (Bates et al. 2013; Lee et al. 2015). For example, at periodic intervals, the tide periodically modulates the hydrostatic pressure exerted by the water column. This modifies the permeability of the seafloor and pressure gradient impacting subseafloor mixing which ultimately modifies permeability and emission characteristics (e.g. velocity, chemical properties; Crone and Wilcock, 2005; Davis and Becker, 1999; Pruis and Johnson, 2004). In addition, tides cause the infra-daily change of bottom current direction and velocity therefore influencing the dispersion of the vent fluid (Scheirer et al. 2006; Xu et al. 2013; Barreyre et al. 2014). A number of recent studies showed the influence of tides on vent species physiology and behaviour. In the Pacific, growth of *B. thermophilus* mussels was shown to be constrained by tidal modulation of the vent mixing (Nedoncelle et al. 2015). Moreover, tidal cycles appear to strongly influence the transcriptome and physiology of *B. azoricus* (Mat et al. 2020). High-resolution video sequences acquired with deep-sea observatories showed that a few symbiotic and non-symbiotic species adapt their behaviour to change in the environment occurring at the tidal frequency, including the extension and retraction of sessile tubeworms at JDFR (Cuvelier et al. 2014b; also with time-lapse camera: Tunnicliffe et al. 1990), the opening and closing of mussel valves at NMAR (Mat et al. 2020), and the repositioning of pycnogonids and polynoids along tubeworms at JDFR (Lelièvre et al. 2017). At TAG (MAR), a time-lapse camera also revealed tidal variation in the micro-distribution of *R. exoculata* (Copley et al. 1999). These periodic behavioural responses may

help the organisms to avoid temporarily unsuitable conditions or may be linked to access on food supply. However, it remains unclear how that variability contributes to structure faunal dynamics at the scale of the assemblage.

I.5 Threats to hydrothermal vents

Deep-sea vent environments have remained inspiring for scientific research and cultural aspects and valuable for the ecosystem services they provide (Turner et al., 2019). The discovery of hydrothermal vents was also partially motivated by economic speculation on polymetallic sulphides first sampled in the Red Sea (Tooms 1970; Bignell et al. 1974). Described in 1979, seafloor massive sulphide deposits (SMS) are geological formations enriched in polymetallic sulphides including Fe, Cu, Zn, Pb (Spiess et al. 1980). They can be found at active and extinct vent sites. They correspond to the seafloor layer formed at the surface or under sulphide edifices through the deposition of precipitates from hydrothermal circulation (Jamieson et al. 2014; Murton et al. 2019; Graber et al. 2020; Sánchez-Mora et al. 2022). The growing demand in mineral resources and advances in underwater technology keep attracting the interest of industries despite technological difficulties for deep ore extraction (Hoagland et al. 2010; Van Dover 2011). As a result, the International Seabed Authority (ISA) has issued licenses to seven contractors for the exploration of polymetallic sulphides on the Mid-Atlantic Ridge and Indian Ocean (ISA 2022). The first trials have been undertaken within the national jurisdiction of Japan, but only a preliminary environmental impact assessment is available (Okamoto et al. 2019).

As deep-sea mining may represent a major threat to the fauna inhabiting in or near hydrothermal vents, it opened new room for ecological investigations of vent communities in order to define conservation guidelines (Van Dover 2011). As the large-scale effect of mining remains difficult to evaluate (Levin et al. 2016b), understanding the mechanisms of vent faunal responses to natural regime of disturbances can be used as a proxy for predicting the resilience of these faunal communities (Van Dover 2014). The impacts of natural disturbance known to occur at vents, has been primarily inferred from *in situ* observations during 45 years of research activities (Van Dover 2014; Juniper et al. 2019). However, the observed variability is only meaningful at particular scales of spatial, temporal and biological organisation at which the data and the knowledge have been collected (Pickett et al. 1989; Levin 1992). The deep-sea mining context motivates the identification of the scales at which we can identify natural drivers of

vent faunal distribution patterns, in order to disentangle their implication with investigations at different scales.

I.6 The Lucky Strike vent field: an *in situ* laboratory

Our review on processes and mechanisms shaping vent fauna distribution and dynamics demonstrated the extensive knowledge gathered over 45 years of scientific investigation. However, this knowledge remains highly fragmented across study sites with distinct communities and across scales of ecological investigation. In addition, the difference of observational scales among disciplines (e.g. geology vs. biology) make it difficult to determine the driving factors and processes at stake. This prevents embedding ecological insights into an integrated model of comprehension of the ecosystem (Levin 1992). There is a need to combine pluri-disciplinary large-scale cartography and time series acquisition on particular sites in order to provide a scale-integrated knowledge. Such intense effort of characterisation has been provided at a few hydrothermal vent fields that were repeatedly visited, and more especially where seafloor observatories have been deployed for the past decade (Matabos et al. 2022). Seafloor observatories are connected or autonomous infrastructures that power instruments deployed permanently in an area of interest and that can perform near-real time measurements (Favali et al. 2010; Delaney et al. 2016; Matabos et al. 2016). The extensive acquisition of multidisciplinary knowledge at the Lucky Strike hydrothermal vent field, boosted with the deployment of the EMSO-Azores deep-sea observatory for the past decade, makes it an ideal study site to investigate ecological patterns under multiple scales (Matabos et al. 2022).

Deployed since 2010, the EMSO-Azores is a multidisciplinary autonomous seafloor observatory monitoring the long-term environmental and biological dynamics of vent systems with high-frequency measurements within the Lucky Strike vent field (LS, NMAR; Cannat et al. 2011; Figure I.9). It aims at understanding the links between the geological, physical and chemical processes as well as their effects on the dynamics of the vent fauna considering a panel of spatial and temporal scales.

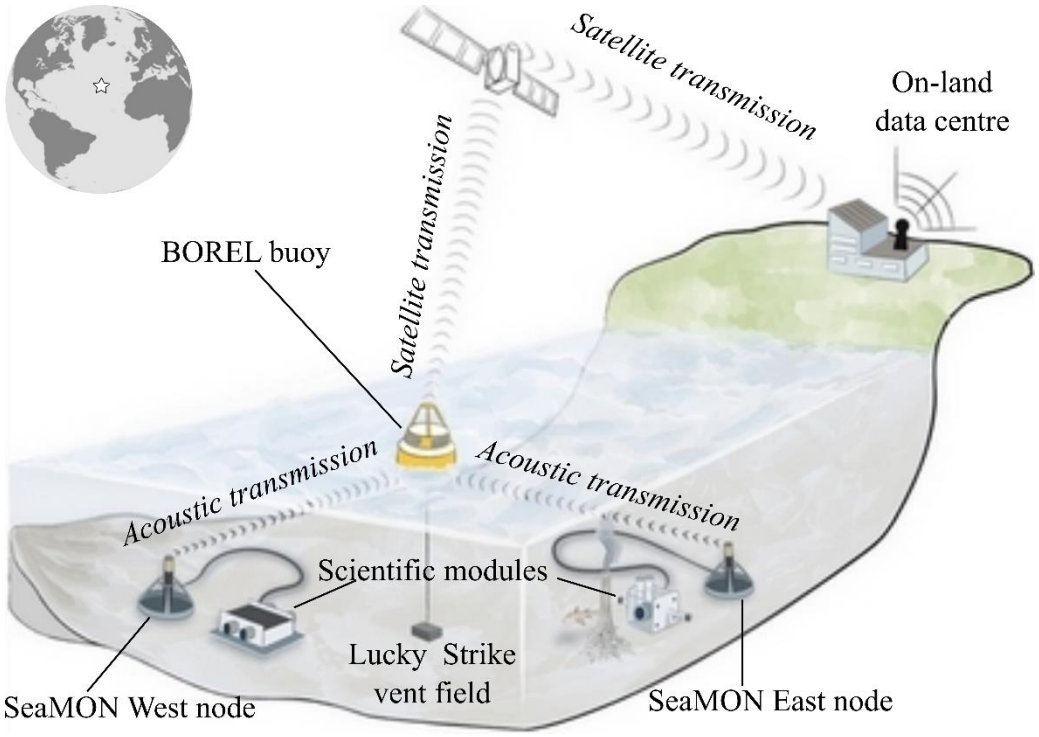

Figure I.9. The deep seafloor and non-cabled EMSO-Azores observatory. Plain lines represent cabled connection. Orientation of semi-circular waves show the directional transmission of data through signals. The upper-left inset repositions the Lucky Strike vent field (white star) over the Atlantic Ocean. Modified from Copyright: Capsule Graphik.

The infrastructure consists in two autonomous nodes providing data storage and energy to an array of multidisciplinary scientific equipment. The SeaMON nodes relay the data via acoustic relays to a surface buoy that in turn transmits them to the Ifremer centre by satellite communication (Blandin et al. 2010). The SeaMON West node is dedicated to the study of geophysical processes and is instrumented with a seismometer and a pressure gauge. The SeaMON East node is dedicated to the multi-disciplinary ecological investigation of the Eiffel Tower active edifice. Imagery monitoring with the TEMPO ecological module (Sarrazin et al. 2007) connected to SeaMON East has enabled to record at infra-daily frequency the high-resolution dynamics of mussel assemblages. In addition, the yearly maintenance cruises enable ancillary faunal sampling and physico-chemical characterisation, the deployment of experimental setups, and image acquisition over a wider spatial range using repeated transects with underwater vehicles. These sampling programs and ecological studies have brought a number of insights into the functioning and dynamics of the LS vent system that are reviewed below.

I.6.1 Geological and hydrothermal settings

LS discovery dates back to 1992 during the US-French FAZAR expedition when fragments of sulphides and vent organisms were recovered with a dredge haul. In 1993, hydrothermal activity was confirmed with dives of the HOV *Alvin* (Langmuir et al. 1993). The 65-km long Lucky Strike segment is located ~ 200 km south of the Azores Islands, on the slow-spreading North Mid-Atlantic Ridge (NMAR; ~ 20.3 mm/yr; Gripp and Gordon, 2002; Figure I.10A). In the central part of a 15-km wide rift is located a heavily-faulted central volcano rising ~ 400 m above the seafloor. It harbours a basalt-hosted hydrothermal vent field on its summit (Ondréas et al. 1997; Cannat et al. 1999; Figure I.10A). LS expands between three volcanic cones surrounding a ~ 1730 m deep depression identified as a fossil lava lake suggesting an ancient reactivation of the vent field (Fouquet et al. 1994; Langmuir et al. 1997; Figure I.10A-B).

The hydrothermal activity at LS is sustained by a 3-4 km wide axial magmatic chamber located ~ 3 km under the seafloor (Singh et al. 2006; Combier et al. 2015). Based on seismicity time series, it has been suggested that the hydrothermal circulation at LS is fed by two major cells located north and south (Crawford et al. 2013). As the hydrothermal fluid reaches the upflow zone, diking and cracking greatly enhances permeability and facilitates their vertical rise (Escartin et al. 2014; Fontaine et al. 2014). Vent fluids are channelled through along-axis permeable faults and released in venting clusters (or sites) located around the impermeable lava lake (Humphris et al. 2002; Crawford et al. 2013; Escartin et al. 2015). From seafloor observation and bathymetry, active sites were delimited in four to five areas harbouring aggregations of discrete venting outflows notably on sulphide edifices, and surrounded by large areas of diffuse venting (Ondréas et al. 2009; Barreyre et al. 2012; Figure I.10B).

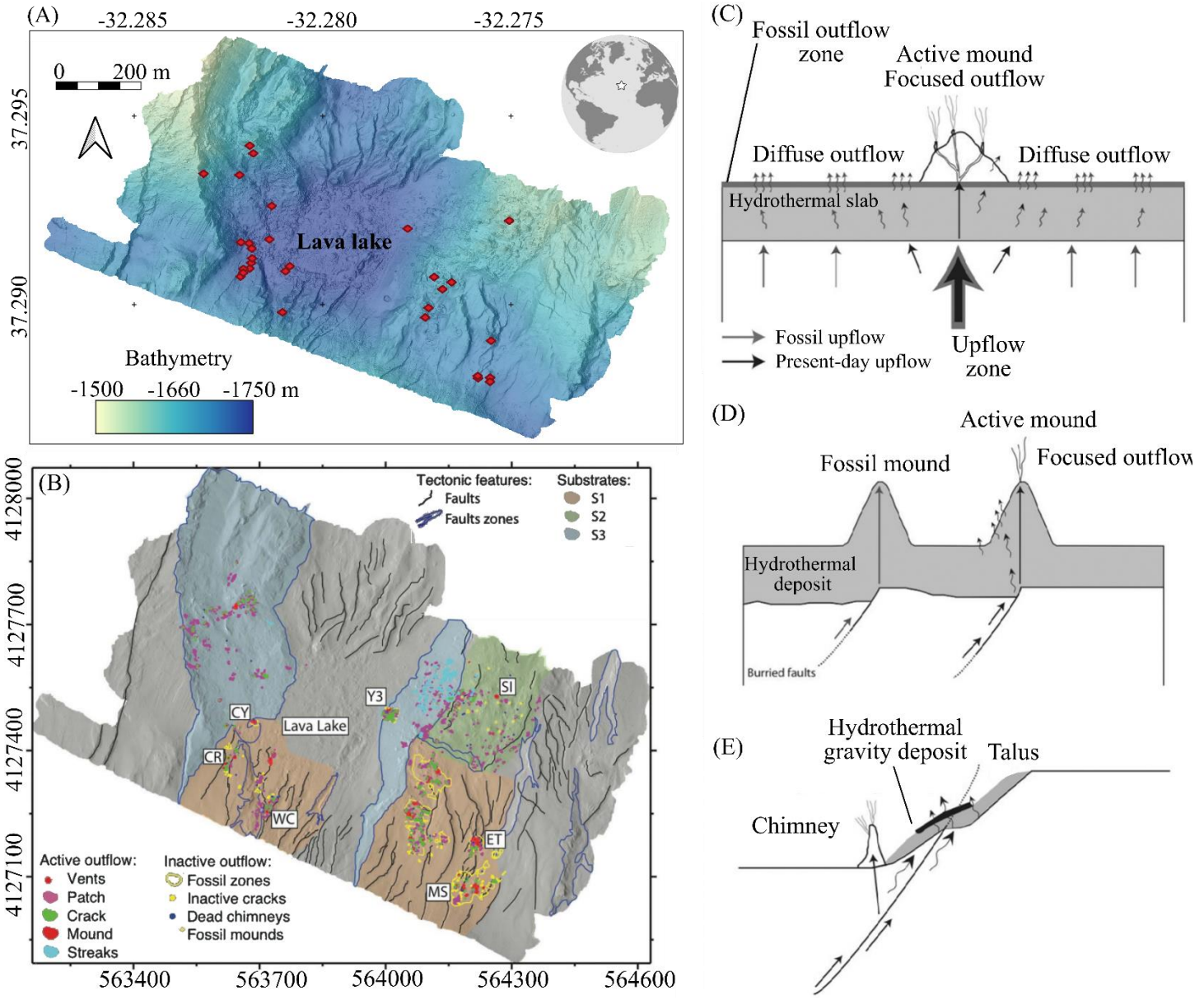

Figure I.10. Bathymetry and hydrothermal setting of the Lucky Strike vent field (LS). (A) Bathymetry with a colour gradient from beige to dark blue. The Globe repositions LS (white star) over the Atlantic Ocean. (B) Cartography of the Lucky Strike vent field. The position of a non-exhaustive list of active sulphide edifices is presented: (from left to right, top to bottom) CR: Crystal, CY: Cyprès, WC: White Castle, Y3, MS: Montségur, ET: Eiffel Tower, SI: Sintra. The legend in the upper right corner refers to the spatial distribution of active and inactive outflows, tectonic features and the presence of three types of venting substrata as inferred from photomosaics and acoustic bathymetry of the seabed. Schematic representation of the three types of venting substrata (C) S1: slab lacking complex topography, (D) S2: hydrothermal deposits with buried faults, (E) S3: hydrothermal gravity deposits at fault scarps. Figure I.10B-C-D-E modified from Barreyre et al. (2012).

Venting patterns and spatial arrangement strongly differ among those areas because of various seafloor substratum and geological settings (e.g. faults and scarps) of the vent field (Figure I.10C-D-E). For instance, the presence of an impermeable slab layer (i.e. hydrothermally cemented breccia) usually results in the presence of focused outflows on sulphide mounds located within fossil hydrothermal areas (Figure I.10C). Additionally, Chavagnac et al. (2018) detected the presence of five major chemistry domains coinciding with the spatial clusters delimited by Barreyre et al. (2012; Figure I.10B). Such differences may be linked with the residence time of the vent fluid influencing in-depth thermodynamic processes and alteration reaction with rocks which in turn, affects the end-member composition among vent sites. For instance, the discovery in 2013 of the Capelinhos active edifice approximately 1.5 km east of LS suggested the presence of a deep fault that allows the fast transit of an iron-enriched vent fluid (Escartin et al. 2015; Chavagnac et al. 2018).

I.6.2 Biological communities

Communities structure – In total, 78 species of macrofauna and meiofauna were collected so far at the Lucky Strike vent field (Alfaro-Lucas et al. 2020) and several still need to be identified at the species level. LS biological communities are largely dominated by the symbiont-bearing mussel *Bathymodiolus azoricus* that can constitute up to 90% of the biomass of active edifices (Husson et al. 2017). Three types of faunal assemblages have been described on the vent field (Cuvelier et al. 2009; Sarrazin et al. 2015, 2020): i) those dominated by *Mirocaris fortunata* shrimp that aggregate in the close vicinity of hydrothermal outflows, ii) those dominated by the gastropod *Peltospira smaragdina* also located in warm areas (Sarrazin et al. 2022), and iii) those dominated by *B. azoricus* mussels found in colder habitats (Cuvelier et al. 2009). *B. azoricus* assemblages can be further divided in three sub-assemblages from small, to medium and large mussels (Cuvelier et al. 2009). They are widely distributed over the vent field and can thrive in a wide range of environmental niches (Husson et al. 2017). The spatial distribution of *B. azoricus* exhibits a size-based segregation coinciding with the dilution gradient of the vent fluids (Cuvelier et al. 2009; Girard et al. 2020a). Large individuals (ranging from 2 to 6 cm length) inhabited more exposed and variable habitats compared to smaller individuals (Comtet and Desbruyères 1998; Sarradin et al. 1999; Cuvelier et al. 2011a; Husson et al. 2017). This size segregation and colonisation success could be linked to their nutrition mode. Indeed, large individuals mostly rely on sulphur and methane-oxidising Gammaproteobacteria

endosymbionts hosted in their gills (Fiala-Médioni et al. 2002; Duperron et al. 2006). However, they are also able to filter-feed (Riou et al. 2010); this nutritional mode being more common in smaller individuals (Martins et al. 2008; De Busserolles et al. 2009). *B. azoricus* mussels are considered as "ecosystem engineers" as their aggregation form 3D structures, contributing to enhance habitat complexity, providing surface for biofilm growth and ensuring detritus retention (Van Dover and Trask 2000; Rybakova and Galkin 2015; Sarrazin et al. 2015). As a result they provide shelter and resources to a variety of smaller macrofaunal species (Cuvelier et al. 2011a; Husson et al. 2017). A recent compilation of samples collected over 4 edifice of LS demonstrated the high share of mussel-associated macrofaunal taxa among sites, especially between Eiffel Tower and other active edifices including Cypress, Y3 and the neighbouring Montségur edifice (Sarrazin et al. 2020; Figure I.10A) supporting the representativeness of Eiffel Tower communities compared to other edifices. As edifices strongly vary in sizes and shapes, the extensive vent assemblages present over this sulphide edifice has provided an ideal study setting to refine the characterization of biological communities (Sarradin et al. 1999). Local variability in habitat conditions predominantly modulates most of the compositional differences as observed along thermal habitats occupied differently by the 79 taxa found at Eiffel Tower (Husson et al. 2017; Sarrazin et al. 2020). As observed elsewhere (Sarrazin et al. 1997), distributional patterns of assemblages of Eiffel Tower arrange in a mosaic of patches as a result of the complexity of the edifice setting and other driving factors (Cuvelier et al. 2009; Girard et al. 2020a).

Microbial mats often cover mussels and bare substratum (Cuvelier et al. 2009, 2011a). Those microbial communities are dominated with thiotrophic *Beggiatoa* sp. (Crépeau et al. 2011) and are often found in areas with no temperature anomaly. Recent studies have suggested that their distribution would be related to lateral inputs from the black smoker plumes transported by bottom currents (Girard et al. 2020a). However little is known on their ecology and factors controlling their distribution remains to be determined.

Dense zoanthid assemblages occupy colder habitats in the immediate vicinity of vent mussels (Husson et al. 2017; Girard et al. 2020a). No study to date have actually investigated peripheral fauna, its distribution or associated environmental drivers. Only a recent study using a metabarcoding approach showed a much higher diversity of eukaryotes in the vent peripheral area than on active edifice (Cowart et al. 2020).

Trophic web – The trophic web of Eiffel Tower has been investigated with stable isotope analyses (Colaço et al. 2002; De Busserolles et al. 2009; Portail et al. 2018). As generally observed at vents (Govenar 2012), the vent community predominantly relies on chemosynthetic primary production that sustain different trophic guilds. Secondary consumers can be symbiotrophic such as for *B. azoricus* hosting endosymbionts in their enlarged gills (Trask and Van Dover 1999; Von Cosel et al. 1999; Le Bris and Duperron 2010). Smaller mussels occupying colder niches would predominantly be suspension feeders (Portail et al. 2018). However, the mussel biomass remains poorly transferred to the rest of the food web (De Busserolles et al. 2009), except towards one parasitic/commensal polynoid *Branchipolynoe seepensis* (Bebianno et al. 2018). Most macrofaunal species are bactivorous including gastropod, polychaete, amphipod and copepod taxa (Portail et al. 2018). In addition to detritus and mucus, those primary consumers sustain a few scavengers and predators. The variable isotopic signatures of *M. fortunata* shrimp may reflect a flexible diet, from predator to bacterivore depending on their habitats (De Busserolles et al. 2009; Portail et al. 2018). The endemic *Segonzacia mesatlantica* crab seems to be an opportunistic predator/scavenger (Colaço et al. 2002; De Busserolles et al. 2009). The most common species appear to have a high trophic flexibility and the trophic web structures vary little along the environmental gradient and among habitats (Portail et al. 2018). The role of microbial mats in the trophic network is not established yet, despite suggestion that they may be a food source for several grazers. Nutritional resources on which the zoanthids feed remain to be studied, although chemosynthetic derived organic matter is suspected to be an important source of carbon (Girard et al. 2020a). The high abundance of the fauna at vents may be linked to the high productivity allowing species co-existence through higher functional richness (Alfaro-Lucas et al. 2020). In comparison, vent peripheral habitats may be food depleted which may induce low functional richness (Alfaro-Lucas et al. 2020).

Temporal dynamics – The pluri-annual dynamics of faunal assemblages at the scale of the Eiffel Tower edifice was assessed over 14 years (1994-2008) with images from the *Nautile* and *Victor6000*, (Cuvelier et al. 2011b). Annotations on 2D mosaics depicted the high stability of faunal assemblages despite local variability resulting from subtle variations in the distribution of vent outflows. Cuvelier et al. (2011b) also noticed a progressive succession from small to large mussel individuals, following sequential processes starting from settlement, to growth, migration and mortality. From this evident stability, the authors suggested that *B. azoricus* assemblages may constitute a “climax” community at Lucky Strike. Microbial mat dynamics

were more variable during that period and an abrupt change appeared to be influenced by the dike intrusion observed in 2001 (Dziak et al. 2004).

In the absence of magmatic or tectonic events that re-set communities, natural recolonisation processes and associated successional patterns are less understood at vents along slow spreading ridges such as the MAR. Natural recolonisation of newly open spaces was assessed using experimental approaches. Results from a small scale disturbance experiment conducted at the Montségur edifice were used to propose the first conceptual model of ecological succession from initial colonisation to climax community (Marticorena et al. 2021; Figure I.11). Marticorena et al. (2021) showed that pioneer species such as *M. fortunata* mobile shrimps arrived the first year followed by gastropod grazers the second year. Surprisingly, *B. azoricus* mussels did not recolonize the cleared surface in the two year period of the study. This may be due to predation pressure, limiting their recovery but also to the restricted time window of observations (Marticorena et al. 2021). However, recent observations 5 years after the disturbance still show the lack of recovery of the mussel assemblages in most quadrats (JS, MM pers. obs).

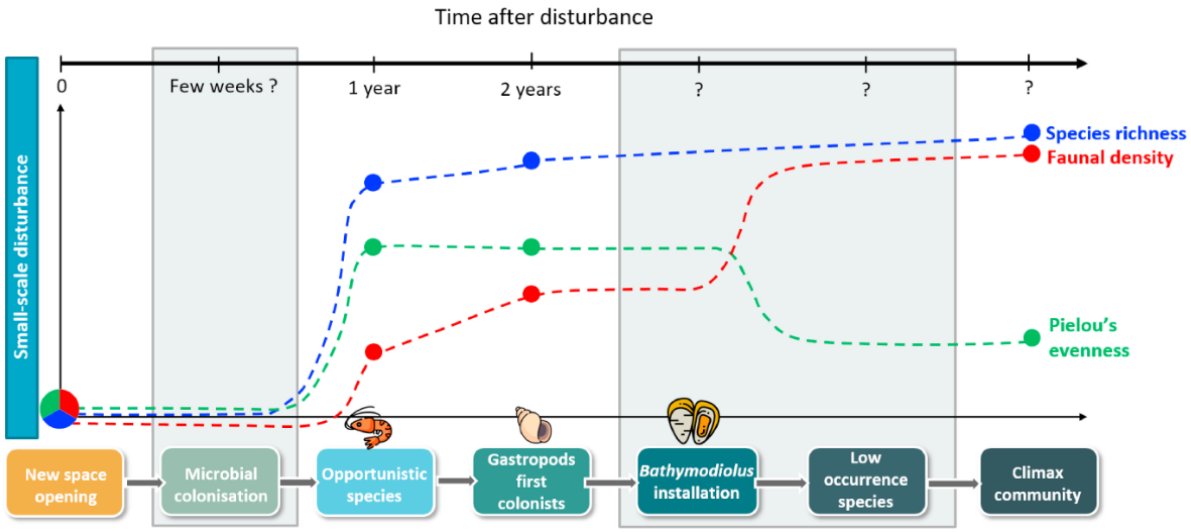

Figure I.11. Conceptual model of colonisation and ecological succession until climax after clearance of *B. azoricus* mussel assemblages. The evolution of species richness, faunal densities and Pielou's evenness index during the recovery were based on the main results of our disturbance experiment (solid dots) or inferred from the literature (grey boxes). Figure from Marticorena et al. (2021).

Colonisation experiments with different types of substrata were also used to better understand factors driving colonisation processes at LS. Results revealed the predominance of local environmental conditions and presence of *B. azoricus* assemblages in shaping patterns of community colonisation (Ivanenko et al. 2011; Cuvelier et al. 2014a) and lower influence of substratum characteristics (Zeppilli et al. 2015; Plum et al. 2017; Baldrighi et al. 2018). The

substratum played a more important role on the structure of communities at the periphery (Alfaro-Lucas et al. 2020).

The deployment of the EMSO-Azores observatory also brought new insights on communities' variations at infra-annual time scales. Two studies performed with the TEMPO ecological module that monitored a mussel assemblage (< 1 m²) over short periods of time (48 and 23 days respectively) showed low variability in *B. azoricus* cover as well as stable abundances of *M. fortunata* and *S. mesatlantica.* On the contrary, microbial mat cover exhibited a high variability (Sarrazin et al. 2014; Cuvelier et al. 2017). Monthly observation over 8 months confirmed steady abundances of *M. fortunata* and *S. mesatlantica* in the same area (Matabos et al. 2015) and emphasised the lack of interaction of predators on *B. azoricus* (Matabos et al. 2015).

At infra-annual scales, sensors detected a semi-diurnal periodic signal in temperature time-series at both the assemblage and over the vent field scales (Khripounoff et al. 2008; Sarrazin et al. 2014; Cuvelier et al. 2017). Later, images captured with TEMPO highlighted the influence of tides on *B. azoricus* behaviour with the detection of semi-diurnal periodicity in their opening/closing activity. Tidal influence was also shown to predominate mussel gene expression and their physiology (Mat et al. 2020).

I.7 Thesis objectives

Two decades of observational studies at LS have allowed to characterise spatial and temporal patterns of vent assemblages over a wide range of scales from the assemblage -with infra-daily images extending over a few months- to the scale of the edifice -with pluri-annual photomosaics over 14 years. However, mechanisms involved in faunal responses to change are still poorly understood. In addition, those insights are difficult to integrate to reach a comprehensive understanding of communities dynamics as the temporal extent and spatial resolution do not necessarily overlap. For instance, the pluri-annual local variability of faunal assemblages observed over the entire Eiffel Tower edifice (Cuvelier et al. 2011b) contrasts with the high infra-annual stability observed in a single mussel assemblage (Sarrazin et al. 2014; Cuvelier et al. 2017). The acquisition of high-resolution images over several years is thus essential to unravel the processes and mechanisms shaping small-scale dynamics of vent assemblages. However, the integration of ecological insights produced at fragmented spatial and temporal scales remains a challenge. Finally, ecological investigations at LS in the past years have

overlooked the distribution of the non-vent megafauna as well as the scales and processes shaping the sphere of hydrothermal influence at the vent-field scale.

The long-term deployment of the EMSO-Azores observatory has now enabled to aggregate data over a decade which may help to disentangle the role of environmental and biological processes at various scales, bridging gaps among study scales. Furthermore, this dataset is completed by all of the information acquired during the yearly maintenance MoMARSAT cruises. Indeed, these cruises supported the regular acquisition of imagery data over spatial scales that cannot be resolved with deep-sea observatories solely (Sarrazin and Sarradin 2006; Cannat and Sarradin 2010).

In this context, this thesis will rely on the extensive monitoring and sampling effort conducted over the last 10 years to enhance our understanding on the functioning of Lucky Strike vent ecosystems (Cannat et al. 2016; Matabos et al. 2022). Along with the recent development of computer vision tools and underwater platforms capable of meticulous tasks (Simeoni et al. 2007), this PhD project aims at characterising vent communities dynamics and disentangling the environmental drivers over spatial scales ranging from the individual to the vent field, and over several temporal scales (from hours to decade). This approach will ultimately help to bridge the ecological knowledge gaps across scales of investigation.

The overarching hypothesis of this thesis is defined by the postulate that, as the study scale increases, the nature of the factors driving the observed spatial distribution will also vary. This PhD is divided into three objectives aiming to investigate, with the use of innovative nested image sets, i) the long-term, small-scale (~ 0.5 m^2) dynamics of a vent assemblages monitored at a high frequency (~ daily to monthly) to identify the processes contributing to the observed variability, ii) the long-term dynamics of vent assemblages and environmental conditions at the scale of a vent edifice (~ 450 m^2) with pluri-annual high-resolution cartography and iii) the large-scale spatial distribution of vent and peripheral assemblages over the entire vent field (~1 km^2) to characterise the sphere of influence of hydrothermal activity over various habitat settings. Each of the objective is separated into a chapter summarised below. Each chapter is or will be published in peer-reviewed journals.

Chapter II provides the first pluri-annual monitoring of vent assemblages (~ 0.5 m^2) inhabiting a diffuse outflow at the base of the Eiffel Tower hydrothermal edifice using infra-daily video sequences collected over 7 years. In this study, we investigate the spatial and temporal scales

characterising the dynamics of *B. azoricus* mussels, microbial mats and zoanthid sp. assemblages and we attempt to link the observed changes with biotic and abiotic factors.

This chapter has been published as Van Audenhaege, L., Matabos, M., Brind'Amour, A., Drugmand, J., Laës-Huon, A., Sarradin, P.-M., Sarrazin, J., 2022. Long-term monitoring reveals unprecedented stability of a vent mussel assemblage on the Mid-Atlantic Ridge. Prog. Oceanogr. 204, 102791. https://doi.org/10.1016/j.pocean.2022.102791

Chapter III represents one of the first pluri-annual monitoring making use of 3D reconstructions. It ambitions to assess vent assemblage dynamics over the Eiffel Tower edifice (~ 450 m²) over 5 years. High-resolution observations of changes in habitats and faunal cover were compiled and compared with the results the 2D study of Cuvelier et al. (2011b). We provide quantitative insights on the natural regime of change of vent faunal assemblages and corroborate scales of biological modifications with those of environmental disturbance.

This chapter will soon be submitted in Limnology and Oceanography.

Chapter IV uses high-resolution downward-looking seafloor imagery to assess the spatial distribution of vent and peripheral communities at the scale of Lucky Strike (~ 1 km²). The distribution of the fauna and hydrothermal activity were mapped over the entire vent field. Moreover, the use of topographical descriptors and bottom current characteristics enabled to further explore the influence of substratum and hydrothermal activity on faunal distribution.

This chapter is being prepared for publication.

Chapter V integrates the insights made at multiple scales to develop our comprehension of the spatio-temporal dynamics of the benthic fauna. It also looks at limitations and gives an overview of the technological and methodological achievements made during this thesis. It also suggests different research perspectives to follow up on this thesis. This chapter has been translated to French in **Chapitre VI**.

Chapter II

Long-term monitoring of hydrothermal vent assemblages at infra-annual frequency

Long-term monitoring reveals unprecedented stability of a vent mussel assemblage on the Mid-Atlantic Ridge

Loïc Van Audenhaege[1]* (loic.van.audenhaege@ifremer.fr), Marjolaine Matabos[1] (marjolaine.matabos@ifremer.fr), Anik Brind'Amour[2] (anik.brindamour@ifremer.fr), Jonathan Drugmand[1,3] (jonathan.drugmand@uclouvain.be), Agathe Laës-Huon[4] (agathe.laes@ifremer.fr), Pierre-Marie Sarradin[1] (pierre.marie.sarradin@ifremer.fr), Jozée Sarrazin[1] (jozee.sarrazin@ifremer.fr)

[1] *Univ Brest, CNRS, Ifremer, UMR6197 BEEP, F-29280 Plouzané, France*

[2] *DECOD (Ecosystem Dynamics and Sustainability), IFREMER, INRAE, Institut Agro, Nantes, France*

[3] *Université catholique de Louvain, Ecole de biologie, B-1348 Louvain-la-Neuve, Belgique*

[4] *Ifremer, REM/RDT/LDCM, F-29280 Plouzané, France*

***Corresponding author**: loic.van.audenhaege@ifremer.fr

Keywords: Hydrothermal ecology, Ecosystem functioning, Deep-sea observatory, Underwater imagery, *Bathymodiolus azoricus*, Species behaviour, Habitat monitoring, Multidisciplinary research; Long-term dynamics

Reference: Van Audenhaege, L., M. Matabos, A. Brind'Amour, J. Drugmand, A. Laës-Huon, P.-M. Sarradin, and J. Sarrazin. 2022. Long-term monitoring reveals unprecedented stability of a vent mussel assemblage on the Mid-Atlantic Ridge. Prog. Oceanogr. 204: 102791. doi:10.1016/j.pocean.2022.102791

Abstract

Understanding scales and drivers of ecological variability is essential to a full understanding of ecosystem functioning. At remote deep-sea hydrothermal vents, infra-annual dynamics remain poorly described. This study aims to characterise the factors that drive the dynamics of a vent faunal assemblage dominated by *Bathymodiolus azoricus* mussels from infra-daily to monthly time steps. We analysed a 7-year time series of images and environmental data collected at 1695 m depth at the base of the active Eiffel Tower edifice in the Lucky Strike vent field (Mid-Atlantic Ridge). Using images acquired by the TEMPO ecological module connected to the EMSO-Azores observatory, we assessed the dynamics of key species inhabiting the faunal assemblage in relation to changes in environmental conditions monitored daily.

Our results show that habitat conditions were generally stable over the 7-year period, with small-scale variability related to tidal periodicity and local temperature anomalies. Likewise, the mussel and zoanthid assemblages exhibited remarkable stability. Changes in fluid exposure and substratum instability induced decimetre-scale movements of the mussel assemblage. Microbial mats displayed infra-annual changes characterised by aperiodic growth and decline. Their development patterns could not be entirely attributed to environmental conditions, because other factors, including biotic interactions, appeared to be involved. The crab population preferentially occupied the mussel habitat, but no predation was observed. Scales of variation and driving factors were compared with those governing intertidal zones. The outcomes question the assumption that vent fauna experience extreme and highly variable conditions. On the MAR, mussel assemblages appear to experience relatively stable and mild environmental conditions compared with their coastal counterparts.

II.1 Introduction

Hydrothermal vents result from the emission of superheated fluids that are released on the seafloor through the advection of cold seawater in the oceanic crust where a variety of mixing and reactive processes occur. These fluids are enriched with reduced chemicals that are used by chemoautotrophic organisms to sustain exceptionally dense faunal communities in a generally food-deprived deep sea. A variety of microhabitats are spread along a dilution gradient between hot hydrothermal fluids and cold oxygenated seawater (Jannasch 1985). Despite the presence of environmentally stressful conditions, vent ecosystems sustain luxuriant communities of endemic species, often dominated by large endosymbiotic invertebrates (Tunnicliffe 1991; Childress and Fisher 1992; Léveillé et al. 2005). Vent species are distributed according to their nutritional needs as well as their physiological tolerance to environmental conditions (Vismann 1991). Their habitats are characterised by steep centimetre- to metre-scale gradients of physico-chemical conditions that can vary through time due to tidal and hydrodynamic forcing (Johnson et al. 1988a; Chevaldonné et al. 1991; Le Bris et al. 2006a; Podowski et al. 2009; Lee et al. 2015). Biotic interactions also influence the spatial distribution of the vent fauna (Micheli et al. 2002; Mullineaux et al. 2003; Sancho et al. 2005; Lenihan et al. 2008). At longer time scales, succession mechanisms are also controlled by changes in venting activity, habitat modifications and stochastic events (Fustec et al. 1987; Tunnicliffe et al. 1990, 1997; Sarrazin et al. 1997, 2002; Shank et al. 1998; Marcus et al. 2009). Although we are beginning to understand the spatial distribution of vent assemblages, resolving the scales of ecological variability and underlying mechanisms is paramount to reaching a fuller understanding of vent ecosystem functioning (Levin 1992; Wiens et al. 1993).

Discovered in 1993, Lucky Strike (LS) is a basalt-hosted vent field located in the Azores Triple Junction on the slow-spreading Mid-Atlantic Ridge, at a depth of ~ 1700 m (Langmuir et al. 1993). This large hydrothermal field (~ 1 km²) lies at the summit of a seamount that harbours a central fossilised lava lake surrounded by three volcanic cones (Fouquet et al. 1994; Langmuir et al. 1997; Cannat et al. 1999; Figure II.1A). More than 20 active hydrothermal sites have been discovered (Von Damm et al. 1998; Charlou et al. 2000; Ondréas et al. 2009; Barreyre et al. 2012), all fed by a unique source (Pester et al. 2012; Chavagnac et al. 2018) fuelled by an axial magmatic chamber (Singh et al. 2006). Differences in hydrothermal fluid composition occur among vent sites due to varying geological settings and permeability of the upflow zone (Charlou et al. 2000; Leleu et al. 2015; Chavagnac et al. 2018). Eiffel Tower (ET), located east of the lava lake, is the most studied hydrothermal edifice of the vent field, and its ecology has

been thoroughly investigated for over 20 years (e.g. Sarradin et al. 1999; Desbruyères et al. 2001; Cuvelier et al. 2009, 2011a; b; De Busserolles et al. 2009; Crépeau et al. 2011; Martins et al. 2011; Sarrazin et al. 2015, 2020; Husson et al. 2017; Girard et al. 2020a; Figure II.1B). This 11 m edifice consists of a massive sulphide deposit of ~ 452 m² (Girard et al. 2020a) surrounded by a peripheral zone extending more than 20 m from the summit (Cuvelier et al. 2009). Hydrothermal activity occurs on the main sulphide tower and at the periphery through focused releases, flanges and diffuse outflows (Cuvelier et al. 2009; Mittelstaedt et al. 2012).

Similar to several edifices of LS, ET diffusion zones are dominated by the symbiont-bearing mussel *Bathymodiolus azoricus* Cosel & Comtet, 1999 and the shrimp *Mirocaris fortunata* Martin & Christiansen, 1995 forming two main assemblages: those found in warmer and more variable habitats (5.2-9.5°C) and visually dominated by *M. fortunata* and those visually dominated by *B. azoricus* in colder habitats (4.4-6.1°C; Cuvelier et al. 2011a; Sarrazin et al. 2015, 2020; Husson et al. 2017). The biomass of ET is largely dominated by *B. azoricus* mussels (~ 90%, Husson et al. 2017), which can thrive in a wide range of trophic niches. For their nutrition, they mostly rely on sulphur and methane-oxidising *Gammaproteobacteria* endosymbionts hosted in their gills (Fiala-Médioni et al. 2002; Duperron et al. 2006). However, they are also able to filter-feed (Riou et al. 2010); this nutritional mode is more common in smaller individuals (Martins et al. 2008; De Busserolles et al. 2009). *B. azoricus* is considered an engineer species, because the 3D structure of their aggregations provides shelter, feeding grounds and various microhabitats. At ET, over 79 species of macro- and meiofauna composed of grazers, predators and detritivores have been identified in these assemblages (review by Husson et al. 2017). Mussels can be further subdivided into distinct assemblages, corresponding to different microhabitats and various shell sizes (Cuvelier et al. 2009; Sarrazin et al. 2015; Husson et al. 2017). Faunal diversity varies along the mixing gradient between vent fluids and ambient seawater (~ 4.4°C), with higher densities and richness in lower temperature habitats (Sarrazin et al. 2015). Dense colonies of unidentified zoanthid colonise the bare substratum in the periphery of the ET sulphide edifice (Husson et al. 2017; Girard et al. 2020a). The most mobile taxa, such as *M. fortunata* shrimp and the crab *Segonzacia mesatlantica* Williams, 1998, occupy a wide range of temperature niches (Husson et al. 2017). Both species occupy the highest level of the trophic network (De Busserolles et al. 2009), either as predators or scavengers. Moreover, *S. mesatlantica* shows territorial behaviour and is occasionally observed feeding on mussels (Matabos et al. 2015). The ichthyofauna consists of a few visiting species (Cuvelier et al. 2009, 2017). To complete the picture, microbial communities form visible mats

that cover all kinds of hard substrata including mussel shells (Cuvelier et al. 2009; Crépeau et al. 2011). These microbial mats are dominated by *Gammaproteobacteria* sulphur-oxidisers such as *Beggiatoa* spp. which give them a white filamentous aspect (Crépeau et al. 2011). They are found in low-temperature areas (< 6°C, Cuvelier et al. 2011a) that benefit from hydrothermal particles conveyed by bottom currents (Girard et al. 2020a). Although the factors explaining the spatial distribution of these assemblages have been identified and niches of dominant species characterised, much less is known about their infra-annual temporal dynamics.

Compared with vent fields located on faster spreading ridges, catastrophic events at LS rarely occur (review in Glover et al. 2010). In fact, only one major seismic event — a dike intrusion in 2001 — has been recorded (Dziak et al. 2004). At ET, a temporal study based on imagery reported the stability of vent communities and environmental conditions over 14 years and suggested that faunal communities may have reached a climax state (Cuvelier et al. 2011b). Some authors have suggested that in conditions of low environmental stress and relative stability, biotic factors may play a crucial role in the structure of hydrothermal communities (Sarrazin et al. 1997; review in Glover et al. 2010). Negative interactions including predation, larviphagy, physical disturbance, grazing activities (Johnson et al. 1988b; Micheli et al. 2002; Sancho et al. 2005; Lenihan et al. 2008; Marticorena et al. 2021), as well as facilitation (Sarrazin et al. 1997, Mullineaux et al. 2003) influence faunal distribution. However, the absence of long-term, high-frequency observations has restricted our ability to determine the relative roles of biotic and abiotic factors in shaping vent communities (Tunnicliffe et al. 1990; Grelon et al. 2006; Matabos et al. 2015; Cuvelier et al. 2017). The long-term acquisition of high-resolution infra-annual time series of faunal and environmental changes is therefore essential to gain further knowledge on factors driving community dynamics in these ecosystems. The development of deep-sea observatories now offers this possibility (Matabos et al. 2016).

In 2010, after many years of scientific cruises at LS, a multidisciplinary observatory — EMSO-Azores — was installed to monitor the long-term dynamics of physical, chemical and geophysical factors and evaluate their impact on faunal communities (Cannat et al. 2011, 2016). Two Sea MOnitoring Nodes (SeaMON) are the energy suppliers and communication relays for a variety of sensors deployed on the seafloor (Figure II.1A). Data is acoustically transferred to a surface buoy (BOREL) that ensures the relay between the nodes and an IFREMER SISMER data centre on land via satellite (Blandin et al. 2010). The SeaMON East node is dedicated to ecological studies and includes, among others, the TEMPO ecological observation module

(Sarrazin et al. 2007, Figure II.1C-D). Equipped with a camera and environmental sensors, TEMPO records high-resolution images as well as physico-chemical conditions (temperature, dissolved oxygen and iron concentrations) within the field of view of the camera (Figure II.2). The area chosen to study long-term vent faunal assemblage dynamics is located at the base of Eiffel Tower and is colonised by a dense *B. azoricus* assemblage.

A pilot study using TEMPO imagery in this area provided the first insights into the day-to-day variations in the mussel assemblage for the 48 days during which the video camera was operational (Sarrazin et al. 2014). Daily observations showed that the assemblage was quite stable, reflecting the relative stability of environmental conditions during this period. *B. azoricus* mussels thrived in habitats with very limited hydrothermal fluid input and significantly influenced by ocean tidal signals (Sarrazin et al. 2014). Temporal variation in species abundance was observed, but — with the exception of *M. fortunata* shrimp — no link could be established with measured environmental factors (Sarrazin et al. 2014; Cuvelier et al. 2017). Although these imagery studies did not indicate a clear tidal influence on LS mussel assemblages, Mat et al. (2020) recently showed that the physiology and behaviour of *B. azoricus* were significantly influenced by these periodic variations. Nevertheless, questions about the processes influencing long-term variations remain. What are the underlying mechanisms acting on mussel assemblage dynamics over a period of several years? Can we observe biological processes such as interactions, settlement, mortality, reproduction? From infra-daily to pluri-annual time scales, which environmental drivers explain habitat variability? Can any stochastic events be linked with biological responses? These questions will be addressed by analysing the spatio-temporal variability of biological processes and environmental conditions in the monitored diffuse-flow habitat. Imagery recorded between 2012 and 2019 by the TEMPO biological observatory module at ET will be combined with *in situ* measurements to address the following hypotheses: (H1) local environmental conditions vary at scales of minutes to days, but generally remain stable over a long period of several years; (H2) mussel cover and (H3) microbial mat cover similarly remain stable over a period of several years; (H4) zoanthid abundance does not vary significantly over long time periods, (H5) the spatial distribution of fauna is linked to particular environmental conditions and/or substratum types and (H6) biotic interactions (e.g. facilitation, predation, competition) have a significant influence on faunal/microbial distribution.

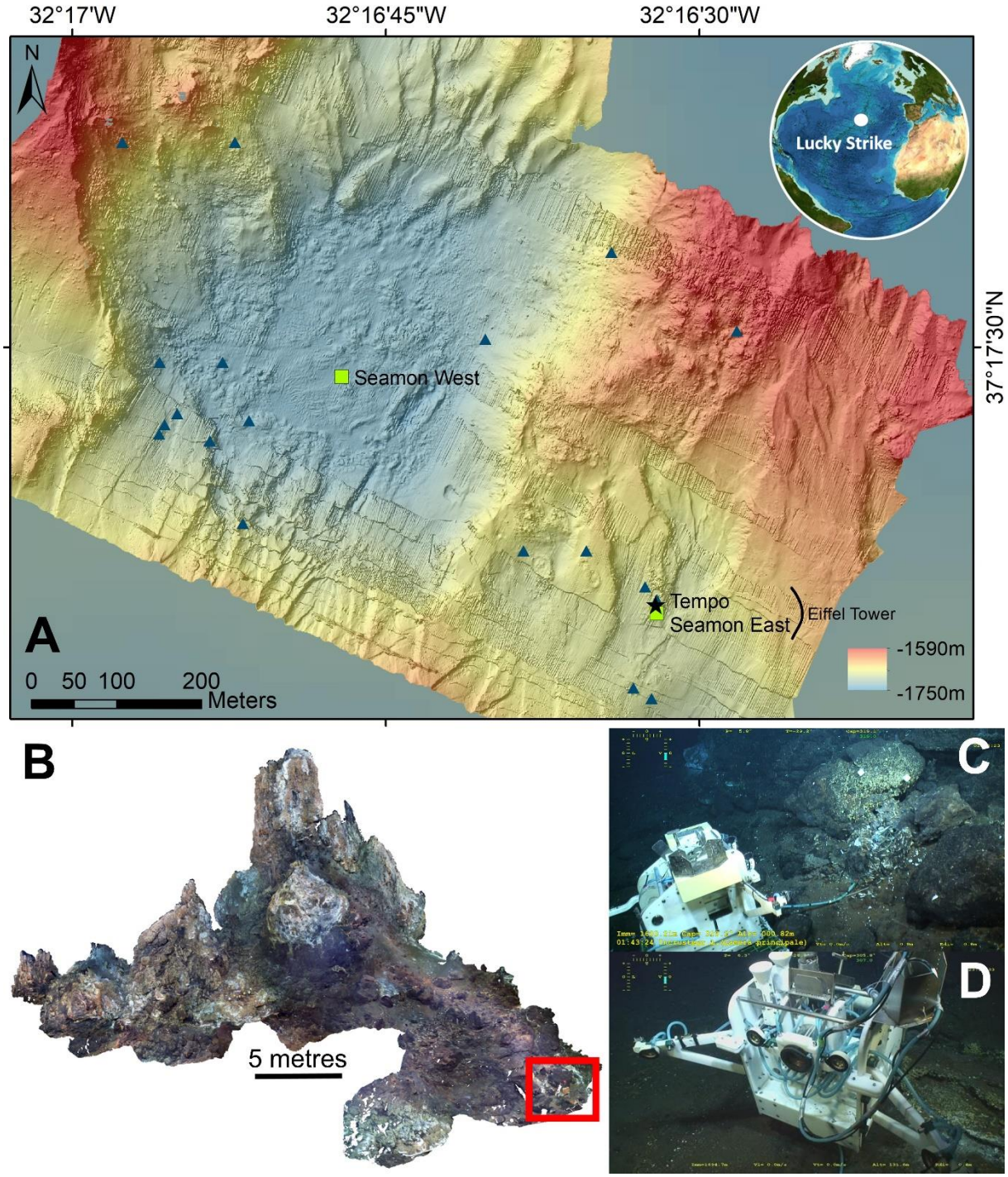

Figure II.1. (A) Map of the Lucky Strike vent field (northern Mid-Atlantic Ridge). The colour gradient corresponds to the bathymetry (Ondréas et al. 2009). Active vent sites are indicated with blue triangles. Green squares indicate the location of the SeaMON nodes. The TEMPO ecological module location is shown by a black star. (B) 3D reconstruction of the Eiffel Tower edifice (ET; Matabos and Arnaubec 2015). The red box indicates the monitoring area, located 30 metres away from the summit of ET. (C) Side view of the TEMPO ecological module monitoring a mussel assemblage in a diffuse-flow habitat. The blue cable on the seabed links the CHEMINI iron *in situ* analyser and the sampling inlet deployed in the field of view. (D) Front view of the TEMPO ecological module. The central porthole is the camera. The yellow subtext in Figure II.1C-D is the submersible's navigation information encrusted in the images and should not be considered by the reader.

II.2 Material and methods

II.2.1 Data acquisition and pre-processing

Since 2010, the TEMPO ecological module (Figure II.1B) has been capturing high-resolution daily video sequences of a bathymodiolin mussel assemblage inhabiting a diffuse-flow habitat at the base of the ET sulphide edifice (Sarrazin et al. 2014; Matabos et al. 2015). Two types of images are available depending on the zoom level and two acquisition strategies were adopted as a trade-off between the scientific questions and the limited energy supply. Between 2012 and 2015, zoomed-out videos were acquired four times a day to study the role of tidal oscillations on species behaviour and assemblage dynamics (Cuvelier et al. 2017; Mat et al. 2020). In 2015, we changed our acquisition strategy because we did not observe major changes in species distribution at a daily scale. From then on, zoomed-out sequences were recorded only once a week (2015-2016) and then only once every 10 days (2016-2019). In this study, we only considered zoomed-out sequences. Screenshots were extracted from imagery using FFmpeg libraries.

Every year, TEMPO is recovered and redeployed with an underwater vehicle (i.e. HOV *Nautile* or ROV *Victor6000*) for maintenance; therefore, its position varies slightly between recording time intervals (hereafter called "period"). In addition, currents may cause slight displacement of the bottom-deployed module. As a result, the image time series does not always capture exactly the same scene, making it challenging to conduct long-term quantitative assessments of changes in assemblage dynamics. A routine was developed in Python (v.3.7.4) to overlay the different snapshots on a common spatial system (available upon request). This overlay routine is based on the common features between image pairs, selected with a combination of 1) automatic detection by the Speeded-Up Robust Features detection algorithm (SURF; Bay et al. 2006; OpenCV library v.4.1.2.30; Howse 2013) on images pre-processed for contrast enhancement with the OpenCV CLAHE algorithm, and 2) manual annotations using Hugin software (v.2019.2.0; d'Angelo 2005). Finally, a RANSAC regression over distances between paired detection points determined the optimal homography transformation matrix computed for each image, within and among periods (Agarwal et al. 2005; Supplementary Video II.1). The dimensions of any object observable in the pictures were averaged to scale the images (0.65 mm/pixel) assuming a 2D and planar field of view (FoV). The surface areas of the different FoVs over time varied from 94.9 to 210.2 dm^2 among image acquisition periods. After homography transformation, two FoVs representing the area captured in 2012-2015 and 2012-

2019 respectively were defined. The FoVs considered for long-term monitoring included a large FoV (78.85 dm², 2012-2015) and a smaller one (35.66 dm², 2012-2019) which was comprised within the 2012-2015 FoV (Figure II.2).

The TEMPO ecological module is equipped with an environmental module that measured temperature and oxygen concentrations in the FoV every 15 minutes (Aanderaa Data Instruments Inc., TD 218 3830), and iron concentrations ([Fe(II)+ Fe(III)]) with the CHEMINI chemical analyser every 24 h (12 h for 2018-2019) with 2 to 4 replicates depending on the period (Vuillemin et al. 2009; Laes-Huon et al. 2016; Figure II.2; Table II.1). For the oxygen optode calibration, salinity was pre-set to 3.5% following the manufacturer's recommendations. Moreover, oxygen concentrations were depth-compensated according to the manufacturer's instructions to account for 3.2% of the lower response of the sensing foil per 1000 m depth. Between 2012 and 2015, the *in situ* CHEMINI iron analyser was calibrated daily. Given that these calibrations were very stable during the whole deployment time, the *in situ* calibration was extended to once a week from 2015 to 2019. The inlet nozzle of the chemical analyser was associated with a MISO temperature probe.

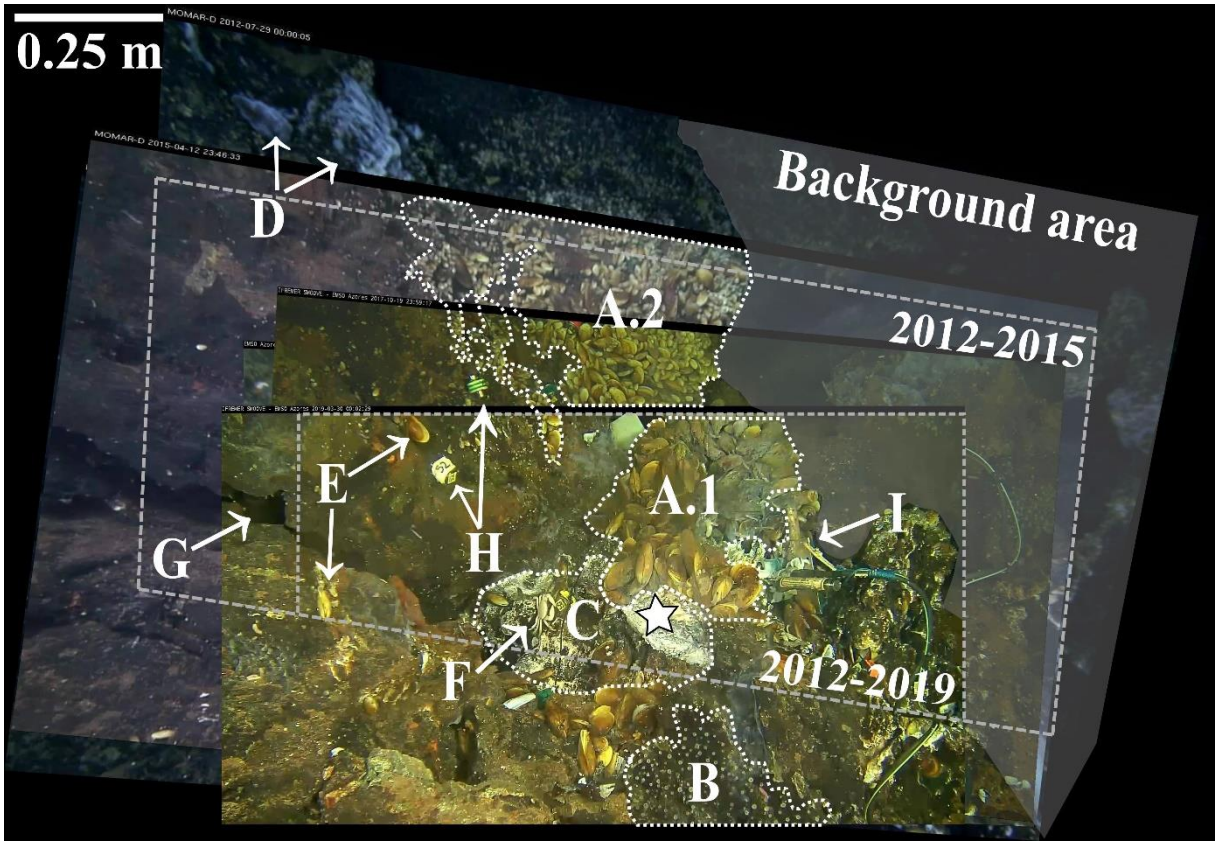

Figure II.2. Field of view (FoV) recorded by the TEMPO module and capturing the evolution of a diffuse-flow habitat over 7 years at the base of the Eiffel Tower (ET) edifice (Lucky Strike, Mid-Atlantic Ridge). The white star shows the locations of shimmering water in video sequences. Image overlay was

achieved using homography based on a combination of manual and automatic feature detection. Two FoVs are delineated by grey dashed boxes and were determined as the common area for two temporal windows: 2012-2015, comprised in the 2012-2019 window. The grey shaded section represents the background area, parts of that sections in the FOVs were discarded for image analysis. Various elements are delineated in the image. (A) *Bathymodiolus azoricus* mussel assemblage displaying size-based zonation: (A.1) a lower portion with densely packed large mussels and (A.2) an upper portion with sparse patches of small(er) mussels. (B) Patch of zoanthids located on a hard substratum. (C) White material where a small flange was observed growing on the outcrop on the right side of that area. This material extends behind that small outcrop, but it was not visible in the FoV. (D) White filamentous microbial mats. (E) *B. azoricus* individuals for which displacement can be tracked. (F) A *Segonzacia mesatlantica* crab. (G) Crevice in the bare substratum. (H) iButton® probes in titanium casings. They are separated by ~ 20 cm and tied together with a fine string. (I) TEMPO Environmental module with two temperature probes, a CHEMINI dissolved iron analyser and an optode.

Additionally, since 2014, up to four arrays of five autonomous sensors (Thermochron iButton®; ± 0.5°C) placed in titanium casings tied with a fine string that maintains them up to 20 cm apart, were deployed each year in the FoV to record hourly temperatures within the diffuse-flow habitat (Figure II.2; Table II.1). iButton® position was annotated monthly in images and a temperature average over a week was assigned to each position. The physico-chemical characterisation of the habitat was done during yearly maintenance cruises with the submersible high-temperature probe and an *in situ* CHEMINI chemical analyser operated by the submersible that measured total sulphide (ΣS; $H_2S+HS^-+S^{2-}$) and dissolved iron Fe(II) concentrations from 2014 to 2019. CHEMINI measurements were conducted on each iButton® temperature and at additional points on distinct biological features and substrata (Figure II.2). The detection limits were set to three times the standard deviation recorded using a blank solution measurement while on the seafloor. The detection limits for iron and total sulphide concentrations were on average 0.31 and 0.56 µmol/L, respectively, and CHEMINI concentrations lower than the dive-specific detection limits were set to 0. For a better understanding of the time series, the temporal coverage of each data type is detailed in Table II.1 (see Supplementary Figure II.1). Monitoring of background environmental parameters was performed with a turbidity sensor (ECO-BBRTD, WET labs, Inc.) deployed on the SeaMON East station (Figure II.1) and by an autonomous probe (MISO; Fornari et al. 1998) placed on the TEMPO module away from hydrothermal activity and measuring ambient seawater temperature.

II.2.2 Extraction of biological data through image processing

Three dominant visible taxa, including the ecosystem-engineer mussel *B. azoricus*, the crab *S. mesatlantica* and an unidentified zoanthid species, as well as white filamentous microbial mats

were studied here (Figure II.2). Cover was annotated as polygon features (mussels and mats), and individual organisms (crabs and zoanthids) were annotated as points. All annotations were determined with ImageJ® (Rasband 1997). Coordinates (in pixels) were then transformed in the new common image system and scaled as defined in Section II.2.1 for further comparison over time. Investigating long-term dynamics requires a trade-off between minimising the processing time and maximising the amount of information gained. If possible, the frequency of data extraction was adapted to reduce annotation time (Table II.1).

Cover dynamics - Cover dynamics were investigated for *B. azoricus* and microbial mats. As image spatial extents were not identical across all periods, analyses were separated into the two FoVs delimited by masks computed in the homography correction workflow. The poorly visible background area (Figure II.2) and the TEMPO environmental module, which partly occupied the FoV (8.85 dm², Figure II.2), were discarded from analyses. For mussels and microbial mats, the observer's reproducibility (Schoening et al. 2016) was evaluated by replicating three cover annotations of eight random images from which the variation coefficient was determined (Table II.1). In addition, movements of mussels or mats that may influence cover variability at short time scales were studied. For mussels, they can be due to changes in mussel shell orientation within a single day (authors' pers. obs.), but we assumed that they do not affect the total surface covered over the long term (Cuvelier et al. 2017). For microbial mats, infra-daily variability may be linked to the flapping movements of the microbial filaments induced by variability in bottom currents. Therefore, 15 randomly chosen patches from three video sequences were annotated on three screenshots taken randomly within the original video sequence (Table II.1). The final annotation error was estimated by summing the maximum coefficient of variation of both annotation errors (i.e. observer's reproducibility and infra-daily variability) and set to ± 5% for *B. azoricus* cover and ± 30% for microbial mat cover.

Mussel cover - Preliminary weekly and daily observations showed *B. azoricus* cover to be stable at the scale of weeks and only changing gradually over time (authors' pers. obs.). Given that these observations were also consistent with previous results at ET (Sarrazin et al. 2014; Cuvelier et al. 2017), we selected a monthly time step to characterise mussel assemblage dynamics in the present study (Table II.1). In addition, *B. azoricus* individuals were tracked to

Table II.1. Parameters of (1) environmental data acquired from *in situ* measurements recorded by the TEMPO ecological module (EMSO-Azores observatory) and during yearly visits with a submersible from July 2012 to June 2019, and (2) biological data extracted from images. Sampling frequency may vary among periods of data acquisition. FoV: Field of view. n is the number of measurements for environmental data or images/video sequences for biological data. See Section II.2.1 for details on video data acquisition as recorded *in situ*.

(1) Environmental data				
	Variable	**Data acquisition parameters**		**Data analysis**
Hydrothermal vent fluid characteristics	Dissolved iron [Fe(II)+ Fe(III)] concentration [µmol/L]	*In situ* chemical analyser CHEMINI. 1 to 2 measurements per day.	n = 1160 for 2013-2015 and 2016-2019	Time series plot (for all) Whittaker-Robinson periodograms (for all)
	Oxygen concentration [µmol/L] and temperature [°C]	Optode. 1 measurement every 15 to 30 min.	n = 186,862 for 2012-2019	
	Temperature [°C]	Autonomous probe on the CHEMINI analyser. 1 measurement every 2 to 15 min	n = 286,145 for 2012-2013, 2014-2015, 2016-2019	
Background environmental parameters	Turbidity [NTU]	Turbidity sensor on SeaMON East. 1 measurement every 15 min.	n = 168,959 for 2015-2018	Time series plot (for all) Whittaker-Robinson periodograms (for all)
	Temperature [°C]	Autonomous probe attached on the LED projectors of TEMPO. 1 measurement every 2 to 15 min.	n = 516,125 for 2012-2014 and 2016-2019	
Habitat heterogeneity	Temperature [°C]	iButtons® visible in the TEMPO FoV. 1 measurement every 1-2 hours. Values summarised as the average over 1 week centred on the end of the month	n = 21,988 for 2014-2019 (32 temperature sensors deployed)	Whittaker-Robinson periodograms Spatio-temporal empirical orthogonal function (EOF)** analysis (n = 25, p = 99 grid cells) based on monthly linear regressions (R^2, *p*-value) on iButton® temperatures according to the distance from the warmest recordings (only for iButton®).
	Temperature [°C]	*In situ* submersible probe from an average temperature over 1 minute. Yearly measurements with a submersible in the TEMPO FoV	n = 87 for 2014-2019 except for the 2015 expedition	
	Dissolved iron [Fe (II)] concentration [µmol/L]	*In situ* chemical analyser CHEMINI on the submersible. Yearly measurements with a submersible in the TEMPO FoV	n = 77 for 2014-2019	
	Total sulphide ($\Sigma S=H_2S+HS^-+S^{2-}$) concentration [µmol/L]	*In situ* chemical analyser CHEMINI on the submersible. Yearly measurements with a submersible in the TEMPO FoV	n = 99 for 2014-2019	
(2) Biological data				
Variable	**Taxon**	**Data extraction parameters**		**Data analyses**
Cover	*Bathymodiolus azoricus*	1 image per month	n = 29 for 2012-2015 n = 67 for 2012-2019	Total cover time series & linear regression (R^2, *p*-value) Maps of mean occurrence* Spatio-temporal empirical orthogonal function (EOF) analysis** (2012-2015: p = 627 grid cells, 2012-2019: p = 253 grid cells)
	Microbial mat	1 daily image	n = 93 for 3 months of 2012-2013	Total cover time series
		1 image per 7 days (2015-2016) and 10 days (all other periods)	n = 80 for 2012-2015 n = 170 for 2012-2019	Total cover time series Maps of mean occurrence* Spatio-temporal empirical orthogonal functions (EOF) analysis** (2012-2015: p = 627 grid cells, 2012-2019: p = 253 grid cells)

Error of cover annotation	Observer's reproducibility: *Bathymodiolus azoricus*, microbial mat	3 annotation replicates	n = 8 random images	Coefficient of variation
	Infra-daily variability: Microbial mat	3 annotation of individual patch of microbial mat at different moment within a video (2012-2013)	n = 15 patches	Coefficient of variation
Tracks of individual displacements	*Bathymodiolus azoricus*	Individual positioning every 6 hours	n = 36 individuals, over 4140 images for 2011-2015	Trajectory of displacement Mann-Whitney U test for trajectory differences
Density (counts)	Zoanthid	Automated detection: daily (2014-2015), weekly (2015-2016), 10 days (2017-2018, 2018-2019) Manual annotation: 3 replicates every 3 months	n = 280 n = 16	Linear regression
	Segonzacia mesatlantica	One image every 6 h for 2012-2015, weekly for 2015-2016, 10 days for 2016-2019	n = 3120	Whittaker-Robinson periodograms for periods of 2012-2015
		One image every 7 (2015-2016) or 10 days (2012-2015, 2016-2019)	n = 119 for 2012-2015 FoV n = 202 for 2012-2019 FoV	Friedman test and Wilcoxon-Nemenyi-McDonald-Thompson post-hoc test
Interactions & predatory activity	*Segonzacia mesatlantica* & fishes	Video sequences: 4 x 2 min a day in 2012-2015, 5 min/week in 2015-2016, 8 min/10 days in 2016-2019	122.5 h viewed	Observation of interspecific interactions

***Maps of mean occurrence were built by summing the presence (= 1) over the whole time series in each pixel **EOFs are the equivalent of a principal component analysis (PCA) performed on space (each pixel representing a "species") and time (each date represents an "observation/site") matrix for each response variable (biological component or temperature)**

assess the role of mobility on assemblage dynamics using video screenshots from 2011 to 2015 (Table II.1). Positions of these mussels were recorded every 6 h and only if they were traceable over more than one image. Three scenarios were possible: individuals were either leaving the assemblage, entering the image FoV from the bare substratum on the left or moving within the assemblage (Figure II.2). The final displacement rate was then standardised to the total number of mussels forming the main assemblage.

Microbial mat cover - For microbial mat dynamics, daily annotations were first carried out over a continuous 3-month image series (i.e. 27 July 2012 to 27 October 2012). Daily variability in microbial mat cover was lower than the annotation precision, and growth and decrease occurred progressively over several weeks (Supplementary Figure II.2). Therefore, their long-term dynamics were evaluated using the shortest image acquisition time step common to each time series (7 days for 2015-2016 and 10 days for 2012-2015 and 2016-2019; Table II.1).

Zoanthid density - Zoanthid assemblage dynamics were investigated for periods of at least 3 months when image quality allowed the quantification of single individuals (Table II.1). Regions of interest (ROIs) were delimited to exclude areas with microbial mats that interfered with zoanthid detection. Cnidarian individuals were counted automatically at daily to 10-day intervals (Table II.1) using an .IMJ image segmentation routine (ImageJ®; Rasband 1997) involving smoothing and contrast-enhancing filters on the image's green channel. Individuals were isolated by subtracting a period-calibrated threshold value from a binary image. The ImageJ® particle analyser plug-in (Ferreira and Rasband 2012) was then used on resulting images to automate the count of individuals. As suggested by Aron et al. (2013), manual individual counts were replicated three times in images with a 3-month interval to validate the results from the automatic detection Table II.1. Zoanthid abundances were transformed to density over dm^2. Temporal trends in the automated and manual detection methods were similar, validating the automated detection workflow.

Individual observations - Individual crabs were counted on all snapshots with support of video sequences for movement detection (Figure II.2; Table II.1). Their position was recorded using ImageJ®. To investigate preferential substratum occupancy, hydrothermal features, crevices and the TEMPO environmental module were delimited. The area not delimited by polygons was inferred to be "bare substratum". Predatory activities and interactions with crabs and visiting fishes were investigated by watching the entire sequence of each video at 16x speed. In total, this accounted for 122.5 h of video sequences (Table II.1).

II.2.3 Data analyses

Environmental conditions - Whittaker-Robinson periodograms were used to assess tidal periodicity in environmental parameters. They were performed on the residuals from least-square linear regressions of the environmental time series (i.e. temperature, dissolved oxygen and iron concentrations) to remove any linear trends in the data (Legendre and Legendre 2012; Table II.1). Permutations were used to estimate the associated *p*-values (n=499, Legendre 2012). We selected periodogram outputs considering the periods nearest in time to 12.5 h and 25 h corresponding to the semi-diurnal and diurnal tidal signals usually detectable in temperatures collected at LS (Khripounoff et al. 2008; Sarrazin et al. 2014).

Temporal dynamics in biological variables - Dynamics of biological variables were investigated by plotting either the total cover (mussels, microbial mats) or density (zoanthids) computed from annotations over time. Slopes of linear regressions were used to investigate temporal trends in the data. A Shapiro-Wilk test (1965) was performed to verify that the residuals were normally distributed. When this assumption was met and the slope significant, adjusted R^2 was used to assess data dispersion.

Spatio-temporal distribution of *Bathymodiolus azoricus* and microbial mats - The general spatial distribution of mussels and microbial mats over time was investigated by summing up the presence/absence (i.e. 1 and 0) in each pixel individually throughout the time series (Table II.1). The mean occurrence of mussels or microbial mats was then estimated over the time series by dividing the total occurrence in each pixel by the total number of images considered in each FoV. This procedure was used to build maps of mean occurrence in each FoV.

To investigate spatio-temporal dynamics within the FoV, each image (i.e. an observation in time) was split over space by dividing the FoV in grid cells of 5 x 5 cm, to which local percentages of cover were assigned based on the presence/absence of mussels or mats in the corresponding pixels (5929 pixels in each grid cell; Table II.1). A time x space matrix was constructed and used in subsequent analyses, with each row corresponding to one image (i.e. a vector of grid cells), and each column being a date in the time series. Empirical orthogonal functions (EOFs) were computed on that time x space matrix to highlight the spatial structure of the temporal variability in mussel and microbial mat cover (Preisendorfer and Mobley 1988; review in Hannachi et al. 2007). Similar to a principal component analysis (PCA), an EOF analysis decomposes the signals by determining the set of orthogonal functions that minimise the residual variance in the data. Eigenvectors were computed from the covariance of the time

x space matrix and only EOFs explaining at least 10% of the variance were selected. The temporal structure of each biological component was then relayed by drawing each eigenvector over time, by plotting the coordinates of each observation (i.e. image) along the EOF of interest. To characterise the spatial structure of the temporal variability represented by the first EOFs, the factor loadings (FL) were projected on the FoV for each EOF (see Rubio et al. 2020). They were calculated as the correlation between the cover within a grid cell for each EOF and can range from -1 to +1. The resulting map shows the contribution of each grid cell to the different scales of temporal variability, where high coverage (i.e. positive grid cells) correspond to years with positive coordinates. Negative grid cells correspond to higher coverage to the time scales with negative values.

Finally, statistics on the migration of mussel individuals were computed. The distance travelled by moving mussel individuals was extracted from their initial and final positions on the substratum. Additionally, average mussel speed was estimated by dividing their travelling distance with the time elapsed between two observations. Cosines and sines were derived from the vector of the distance travelled. As we suspected different patterns of migration between mussels moving from the assemblage to the bare substratum to those staying within the initial assemblage, the two groups were separated for the statistical analysis. A Mann-Whitney U test was applied on the sines and cosines of their trajectories to test for differences in direction (Table II.1).

***Segonzacia mesatlantica* spatio-temporal distribution** - Whittaker-Robinson periodograms (n = 499) were used to screen for tidal periodicity in infra-daily crab abundance after removal of the linear trend in the data (2012-2015; Table II.1). To identify occupancy differences across substrata, infra-daily observations from 2012 to 2015 were subsampled at a 10-day time interval to fit the observation time step of the years 2015 to 2019 (Table II.1). A Friedman non-parametric test (Mack and Skillings 1980) was used to compare mean crab densities among substratum types. If significant, a Wilcoxon-Nemenyi-McDonald-Thompson post-hoc test was performed between pairs of substratum types (Hollander and Wolfe 1999). The influence of substratum type on the distribution of this mobile species was evaluated by calculating the average nearest distance of individuals from the different substrata.

Environmental conditions of assemblages/substrata - Physico-chemical data were used to characterise species niches and environmental conditions on the different substrata. Annotations in the FoV were linked with the closest — in space and time — iButton® recording, using a circular buffer zone of 5 cm in radius. In addition, *in situ* CHEMINI and

temperature measurements were assigned to each assemblage and substratum. Distinction was made between ‘densely packed mussels’ and ‘sparsely packed mussels’, because these two assemblages were shown to colonise different habitats (Cuvelier et al. 2009; Husson et al. 2017). ‘Dense’ mussels were defined as large individuals entirely occupying a surface (no bare substratum visible), and ‘sparse’ mussels were more spread out with some substratum visible between individuals (Figure II.2A).

Role of temperature on faunal cover - To assess the role of temperature on local changes in mussel and mat cover over time, we computed the spatial distribution of temperatures every month. The data provided by the iButton® probes (± 0.5°C) were used to model the dilution gradient from the main vent orifice to different areas in the FoV (5 x 5 cm grid cells). We assumed the size of these cells to be accurate enough to map the dilution gradient of the vent fluid as observed by Podowski et al. (2009). iButton® probes located on the right side of the FoV were discarded due to their lack of visibility. To model the dilution gradient in a dynamic way, least-square linear regressions were performed every month based on the distance of each sensor to the warmest temperature point measured during the whole time series. The mean temperature for each grid cell was extracted (5929 pixels). The lower limit of temperatures in the dilution model was set to 4.7°C (mean temperature on the TEMPO ecological module). EOFs were computed on this new interpolated temperature dataset. To determine the role of changes in temperature on the spatio-temporal distribution of biological components, these EOFs were compared with those of *B. azoricus* and microbial mat cover using the Pearson correlation coefficient (Rubio et al. 2020). All figures and analyses were performed in Python (v. 3.7) and R (v. 3.3.2.; R Core Team 2016). Details on the results of EOF correlations are available in the Supplementary Table II.1.

II.3 Results

II.3.1 Scene description and evolution

The FoV was separated into several zones corresponding to the presence of fauna, microbial mats or substratum types (Figure II.2). Biological features included a distinct assemblage of *B. azoricus* mussels, zoanthid patches and microbial mats. The mussel assemblage extended more than 1 m upward on a vertical wall above the active hydrothermal diffusion zone. Mussel size varied with increasing distance from the vent orifice, with larger individuals forming a denser patch closer to the vent (Figure II.2). The dark substratum was identified as hydrothermal slab

of breccia (Pelleter E., pers. comm.). The slab substratum was either bare or covered by white material of unknown nature. One main active source of translucent fluid and secondary small diffusing zones were identified within the FoV (Figure II.2). Starting from 2015, the centre of the image featured the growth of a thin spire which repeatedly collapsed and regrew, before eventually being colonised by a few large mussel individuals (Supplementary Figure II.3). We also observed the growth of a lateral outcrop in March 2016, resulting in a ~ 10-cm diameter flange by the end of the 2018-2019 period (Supplementary Figure II.4). Finally, no major change in the FoV was observed over the entire study period, except for a slab rock of roughly 1 m that broke into two pieces and slid horizontally towards the mussel assemblage between April 2015 and September 2016 (Supplementary Figure II.5).

II.3.2 Long-term dynamics of the fauna and microbial mats

II.3.2.1 Bathymodiolus azoricus

Occupancy and temporal changes - The area that mussels occupied reached a maximum of 37.4% of the total area in 2012-2015 (large FoV) and 51.8% in 2012-2019 (small FoV). The mussel cover recorded in the large FoV from 2012-2015 was stable, ranging between 19.25 and 22.14 dm^2 (Figure II.3A). The smaller area captured by the full image set from 2012 to 2019 displayed more changes, with cover varying between 5.89 and 11.62 dm^2 (Figure II.3B).

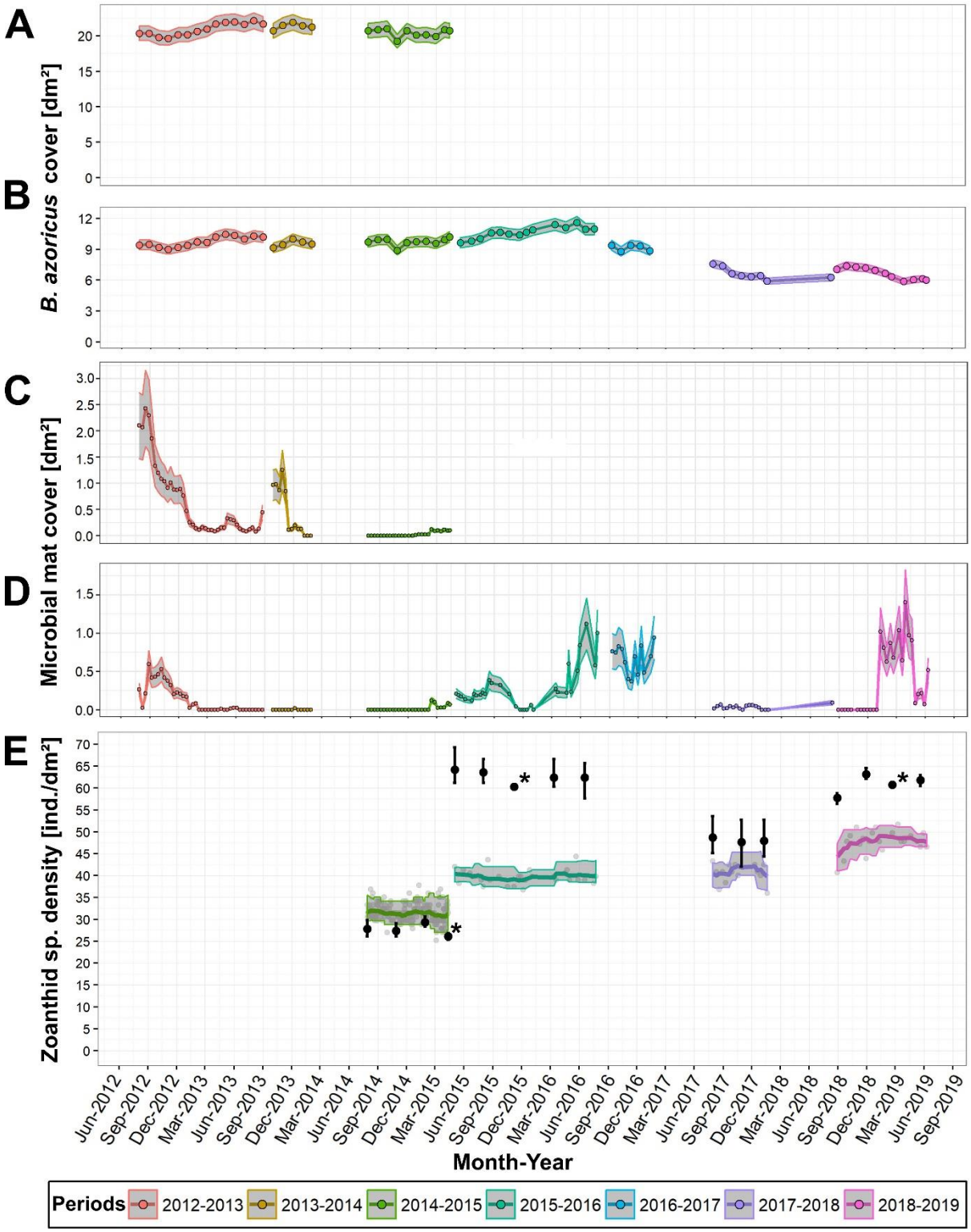

Figure II.3. Total cover annotated for (A-B) the mussel *Bathymodiolus azoricus* (monthly; e.g. Figure II.2A), (C-D) microbial mats (7 to 10 days; e.g. Figure II.2D) using different fields of view (FoVs): (A-C) the large FoV, recorded from 2012 to 2015 (75.85 dm²), comprising (B-D) the small FoV, recorded from 2012 to 2019 (35.66 dm²; see Figure II.2). Colours refer to periods delimited by the deployment and recovery of the TEMPO ecological module at the base of the active Eiffel Tower edifice (Lucky Strike vent field, Mid-Atlantic Ridge). Grey areas depict the intervals of annotation errors estimated for total mussel cover (± 5%) and microbial mat cover (± 30%). E. Zoanthid density plotted over time (e.g.

Figure II.2B). Lines refer to automated density data averaged over a monthly period. Grey areas refer to the associated 5-95th percentiles. Grey circles represent density values extracted from automatic detection. Black circles and bars represent the mean density and range, respectively, for three-replicate manual annotations for validation of the automated detection routine. Asterisks indicate that annotation replicates gave the same density values.

Table II.2. Results of least-square linear regressions applied on periods of mussel total cover recorded in two fields of view (FoVs; Figure II.3A-B). Only slope values are given with their associated adjusted R^2, degrees of freedom (df) and F-statistics. Significant slopes are indicated with asterisks (*p*-value: * < 0.05, ** < 0.01, *** < 0.001). [1]Only 6 months of data from 30 July 2017 to 19 January 2018 and from 29 September 2018 to 30 March 2019.

FoV	Period	Slope [dm²/month]	Adjusted R^2	df	F-statistic
2012-2015	2012-2013	+ 0.19***	0.74	12	36.85
	2013-2014	+ 0.10	- 0.15	3	0.46
	2014-2015	- 0.03	- 0.11	8	0.14
2012-2019	2012-2013	+ 0.10***	0.66	12	26.20
	2013-2014	+ 0.10	0.00	3	1.01
	2014-2015	+ 0.03	- 0.05	8	0.54
	2015-2016	+ 0.11***	0.72	12	34.58
	2016-2017	- 0.06	-0.21	3	0.30
	2017-2018	- 0.10	0.35	6	4.75
	2018-2019	- 0.16	0.82	9	46.24
	2017-2018 [1]	- 0.27**	0.84	5	31.75
	2018-2019 [1]	- 0.26***	0.92	5	73.83

A significant linear increase in *B. azoricus* cover occurred during the 2012-2013 period in both FoVs (Table II.2, Figure II.3A-B). Variations in 2013-2014 and 2014-2015 were smaller than the annotation error (± 5%) and no significant trend was detected (Figure II.3B). From 2015 to 2016, the cover significantly increased (Table II.2) and started decreasing in September 2016 until the end of the time series. Two periods were particularly noteworthy, with major cover loss: (1) August 2017 to mid-January 2018 with -0.27 dm²/month (Table II.2) and (2) October 2018 to April 2019 with -0.26 dm²/month (Table II.2).

The small and large FoVs are both occupied by a highly variable zone around the main vent orifice (WM in Figure II.4B). The large FoV also contains a portion of the mussel assemblage that is not present in the small FOV (UM in Figure II.4A) and that only exhibited minor changes (Figure II.3A). Given that EOFs computed for the large 2012-2015 FoV captured the same spatio-temporal structure as the small 2012-2019 FoV (Figure II.4D), only the results of the latter are presented because it covers a longer time period (Supplementary Figure II.6). The first three EOFs computed for the 2012-2019 FoV accounted for 58% of the total variance in spatial mussel cover (Figure II.4C). FLs described a poor correlation between local mussel cover and

all three EOFs (FLs ranging from -0.24 to 0.26, Figure II.4D). EOF1 explained 32% of the variance and showed a progressive change in cover distribution from mid-2015 until 2019.

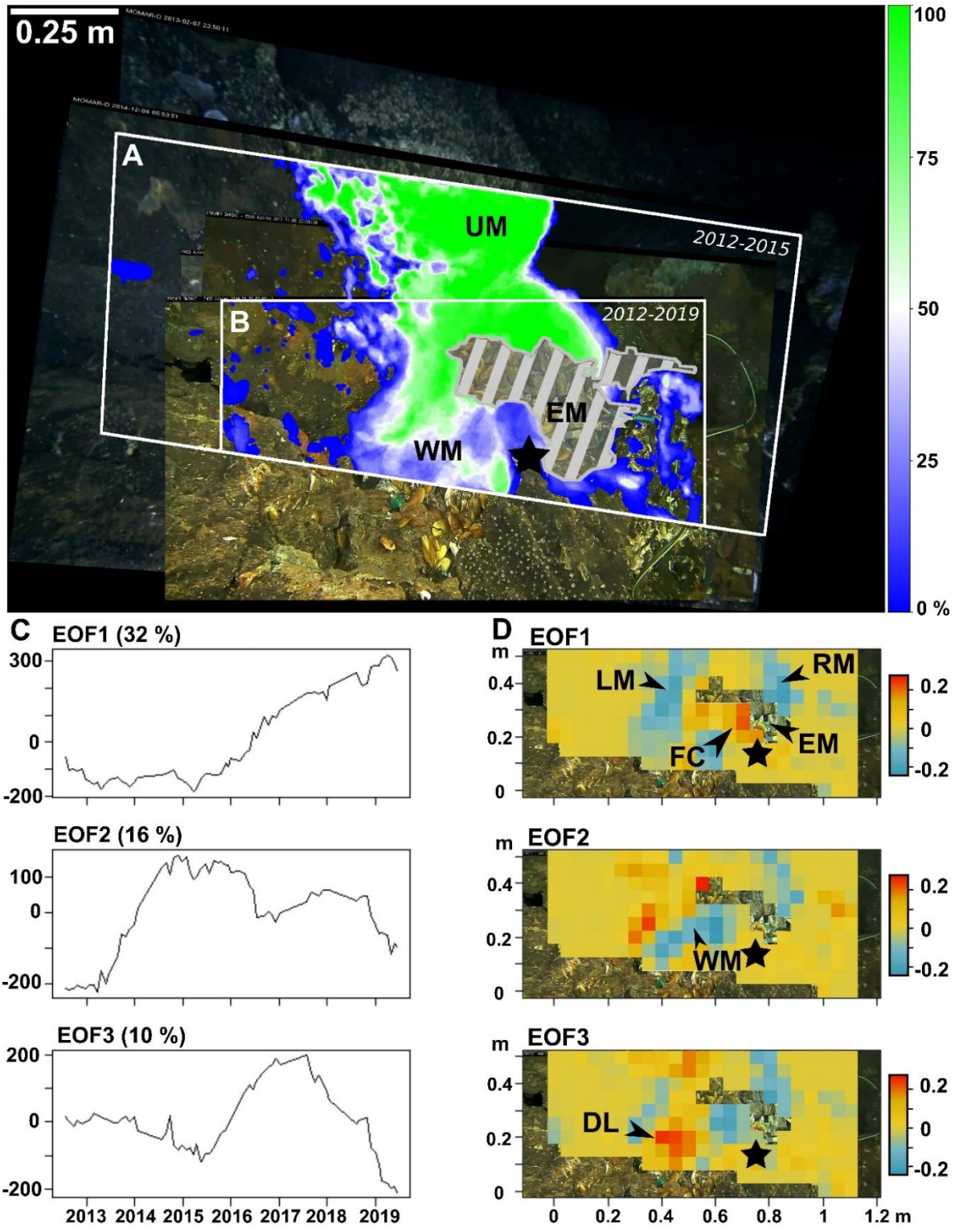

Figure II.4. (A-B) Maps of mean occurrence showing Bathymodiolus azoricus mussel cover distribution through time. The area occupied by the environmental module during the whole time series is hatched in grey. The colour gradient refers to the percentage of images displaying mussel cover at a given pixel (0% means full transparency): (A) for the large field of view (FoV) from 2012 to 2015 and (B) for the

small FoV from 2012 to 2019. The white scale bar indicates an estimated length of 0.25 m. (C-D) Results of the empirical orthogonal function (EOF) analysis to identify areas with different temporal patterns of variability. It was undertaken on a time x space matrix where space (i.e. 2012-2015 FoV) is divided in multiple cells of 5 x 5 cm. (C) Time series representing the coordinates of each observation date on the first 3 EOFs (variance explained = 58%). (D) Spatial projection of the factor loadings (FL) of each EOF. The grid cells are coloured according to the degree of correlation between the mussel cover of each grid cell and the given EOF time series. Red cells (positive values in Figure II.4D) indicate spatial patterns in years with positive coordinates (Figure II.4C), whereas blue cells (negative values) indicate other spatial patterns mainly observable in years with negative values. All metadata related to data acquisition and extraction are presented in Table II.1. UM: upper mussel assemblage, EM: Environmental module, WM: white material, LM: left mussel assemblage, RM: right mussel assemblage, FC: flange colonisation, DL: downward loss. Black star: vent orifice.

As supported by observation in images (Supplementary Video II.1), this change corresponded to (i) a 15-cm displacement of the mussel assemblage to the right starting from 2015 (negative FLs, LM in Figure II.4D), (ii) the disappearance of patches of small mussels that had settled in October 2013 in 2016-2017 (negative FLs, LM in Figure II.4D) and (iii) the colonisation of an area of 2.98 dm² on top of a growing flange by large mussels, from January 2017 to June 2019 (positive FLs, FC in Figure II.4D; Supplementary Figure II.3). The variability observed at the upper right edge of the mussel assemblage (RM in Figure II.4D) and captured by all EOFs corresponds to a loss of mussel cover (negative FLs; Figure II.4D). Visual variability of mussel cover in the white material coincided with EOF2-3 explaining part of the remaining variance (26%). This variability highlights frequent changes in cover distribution in this area (WM in Figure II.4B-D). EOF3 identified a decrease in a patch of large mussels initially located on the white material (DL in Figure II.4D), which corresponds to a decrease in cover in July 2017 (Figure II.3B).

Migration – Thirty-six mussel individuals were observed migrating onto the bare substratum, which represented ~ 12% of the assemblage population counted in the large FoV (~ 300 individuals, 2012-2015; see examples in Supplementary Figure II.7). Of the 28 individuals that were first observed on the slab substratum, 5 reached the main assemblage. Of the 8 individuals that left the mussel assemblage for the bare substratum, 6 returned to the assemblage. Significant differences in the horizontal direction displacement (i.e. cosines) suggested that mussels isolated on the bare substratum moved preferentially to the right, towards the main assemblage (Mann-Whitney U, $W = 614$, $p = 0.038$; mean cosine ± SD = 0.39 ± 0.72), compared with the 24 mussels located in the assemblage that favoured vertical movements (mean cosine ± SD = 0.14 ± 0.63). Mussel tracking showed that 11.25% of the displacements were greater than 10 cm in 6 h with a maximum average speed of 4.66 cm/h.

II.3.2.2 Microbial mats

Microbial mat cover varied from null to 2.43 dm² in the large 2012-2015 FoV and were present over a continuous period representing 77.5% of the images (Figure II.3C). Two main periods characterised by mat cover exceeding 0.5 dm² were identified and both lasted at least 2.5 months. The total microbial mat cover underwent a progressive decrease from September 2012 and stabilised around 0.1 dm² by the end of January 2013 (Figure II.3C). A new peak was recorded for 3 months between the end of August and the beginning of November 2013, after which the microbial mat cover declined at an average rate of -0.07 dm²/day. Cover was null by the beginning of January 2014 and the absence of microbial mats lasted until mid-December 2014 (Figure II.3C). When considering the small 2012-2019 FoV, total mat cover varied from null to 1.4 dm². During this period, 41.2% of the 170 images analysed did not show any microbial mat cover (Figure II.3D). Four episodes of increase (in 2012, 2015, 2016 and 2019) varying in duration and separated by null cover periods were identified with covers ranging from 0.4 dm² to 1.4 dm² (Figure II.3D). The most abrupt rates of change reached in average 0.08 dm²/day for two episodes of growth in January and March 2019 and for a decline in April 2019 (Figure II.3D). Overall, microbial mats were mainly observed on the left side of the FoV in the vicinity of the mussel assemblage (VM in Figure II.5A-B).

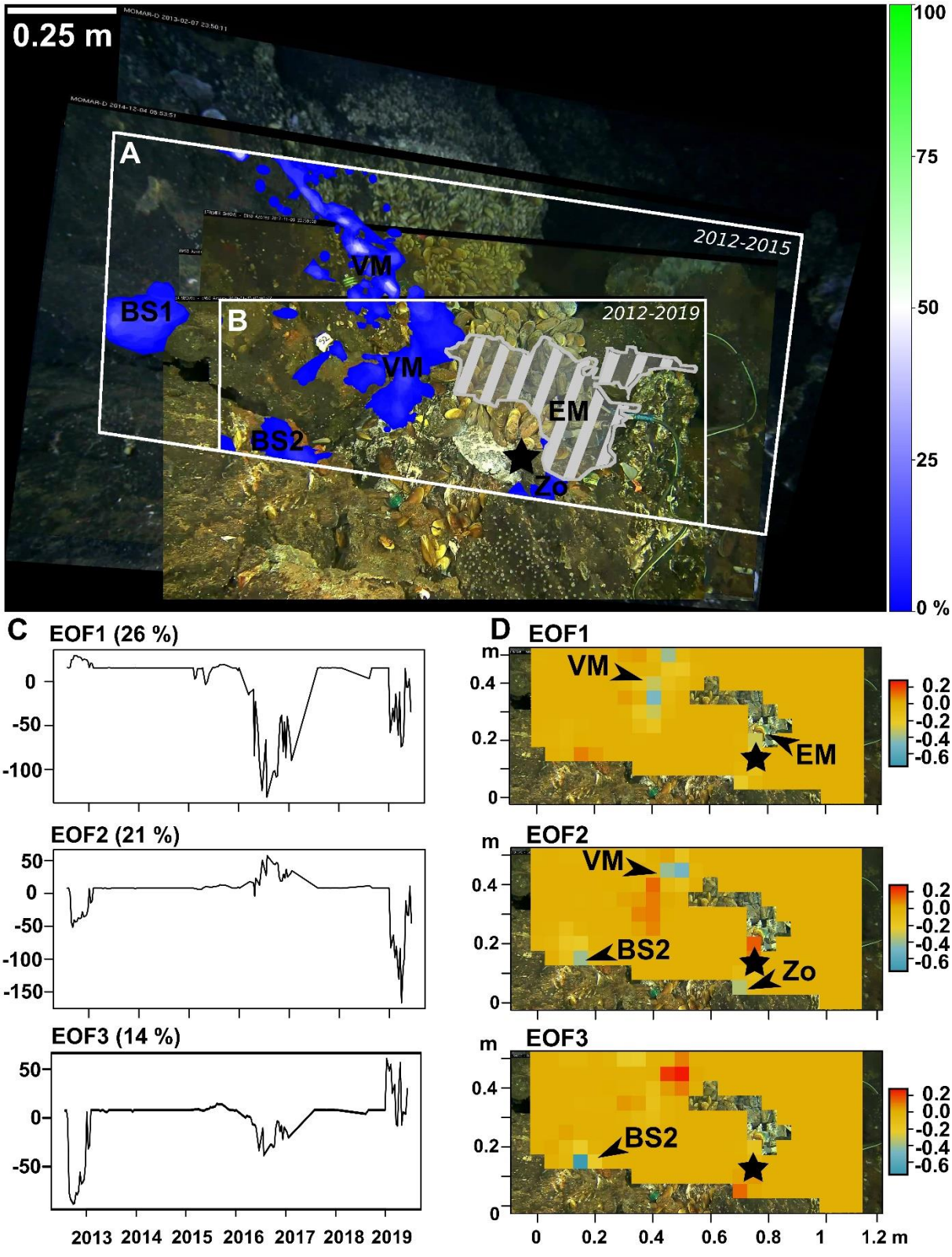

Figure II.5. (A-B) Maps of mean occurrence showing microbial mat cover distribution through time. The area occupied by the environmental module during the whole time series is hatched in grey. The colour gradient refers to the percentage of images displaying microbial mat cover at a given pixel (0% means full transparency): (A) for the large field of view (FoV) from 2012 to 2015 and (B) for the small FoV from 2012 to 2019. The white scale bar indicates an estimated length of 0.25 m. (C-D) Results of the empirical orthogonal function (EOF) analysis to identify areas with different temporal patterns of

variability. It was undertaken on a time x space matrix where space (i.e. 2012-2015 FoV) is divided in multiple cells of 5 x 5 cm. (C) Time series representing the coordinates of each observation date on the first 3 EOFs (variance explained = 61%). (D) Spatial projection of the factor loadings (FL) of each EOF. The grid cells are coloured according to the degree of correlation between the microbial mat cover of each grid cell and the given EOF time series. Red cells (positive values in Figure II.5D) indicate spatial patterns in years with positive coordinates (Figure II.5C), whereas blue cells (negative values) indicate other spatial patterns mainly observable in years with negative values. All metadata related to data acquisition and extraction are presented in Table II.1. VM: vicinity of the mussel assemblage, EM: environmental module, BS1-BS2: bare substratum, Zo: zoanthids, Black star: vent orifice.

Two patches also developed >1 m away to the left of the mussel assemblage (BS1-BS2 in Figure II.5A-B) and within the zoanthid assemblage at the bottom of the FoV (Zo in Figure II.5A-B). No mat was observed on the right side of the hydrothermal vent orifice (Figure II.5A- B). The first three EOFs accounted for 61% of the variance. FLs varied from -0.73 to 0.27, suggesting strong spatial structure in temporal variability. Results showed that changes in spatial patterns of mat cover occurred at a scale of 3 to 6 months (Figure II.5C). EOF1 explained 26% of the total variance and corresponded to the repeated development and decline of microbial mats in the vicinity of the mussel assemblage in 2016 and 2019 (FL < -0.4; VM in Figure II.5C-D). EOF2 accounted for 21% of the variance and corresponded to mats occurring at the same time in three distinct areas in 2012 and 2019 (FLs < -0.3): in the vicinity of the mussel assemblage (VM), on bare substratum on the left of the FoV (BS2), and within the zoanthid assemblage (Zo in Figure II.5D). EOF3 (14% of the variance) revealed the dynamics of a single patch located on the bare substratum that developed in 2012 and in 2016 (FL < -0.6; BS2 in Figure II.5D). EOF results for mat redundancy in the large 2012-2015 FoV highlight additional variations on the slab located on the left side of the FoV (BS1 in Figure II.5A; EOFs in Supplementary Figure II.8), away from mussel patches. The dynamics of these patches, i.e. lifetime of a patch, were similar to those in the small FoV, i.e. from 2 to 7 months (Supplementary Figure II.8). Dynamics observed in images are provided in Supplementary Video II.2.

II.3.2.3 Zoanthids

Manual annotations of zoanthids resulted in a minimum of 25.4 ind.dm^{-2} and a maximum of 69.3 ind.dm^{-2} compared with a minimum of 25.2 ind.dm^{-2} and a maximum of 51.7 ind.dm^{-2} for the automated algorithm (Figure II.3E; Supplementary Figure II.9). The manual and automated detection methods differed in terms of absolute density, but depicted the same pattern over time (Figure II.3E). The dispersion of the points differed among periods, with a maximum of 22.5% in November 2017 based on manual annotations.

II.3.2.4 S*egonzacia mesatlantica*

A total of 2600 crabs were counted from 2012 to 2019. The abundance of crabs reached a maximum of 7 individuals in one image, and 26.2% of the 3120 images revealed no individuals. Significant tidal periodicity was not detected in crab abundances. Infra-daily observations from 2012 to 2015 were subsampled at a 10-day time interval. The large 2012-2015 (n = 80 crabs) and small 2012-2019 (n = 326 crabs) FoVs were both analysed, but because 90% of the crabs present in the large FoV were already included in the small FoV, only results from the latter are presented (Supplementary Figure II.10A-B). 50.9% of the 326 crabs were detected on the mussel assemblage, 27.9% on the white material, 18.4% on the bare substratum, 2.5% on the environmental module, 0.3% in crevices, and none on microbial mats (Supplementary Figure II.11). Crab observations for both time series displayed significant differences in densities among substratum types (2012-2019; Friedman chi-squared = 279.53, df = 5, $p < 2.2e\text{-}16$). Post hoc tests revealed significantly higher occupancy in the mussel assemblage (Mean density ± SD = 0.14 ± 0.13 ind./dm²) and on the hydrothermal white material (0.15 ± 0.13 ind./dm²) than on microbial mats (0 ind./dm²), crevices (0.01 ± 0.1 ind./dm²), slab substratum (0.01 ± 0.02 ind./dm²) and the environmental module (0.02 ± 0.1 ind./dm²). Furthermore, we noticed that crabs, when located on the slab substratum, occupied areas close to the mussel assemblage (mean distance ± SD = 1.8 ± 2 cm, maximum distance of 8.6 cm; Supplementary Figure II.11A).

II.3.3 Biotic interactions

Avoidance behaviour of smaller mussel individuals were occasionally observed after the arrival of larger mussels in close vicinity (e.g. Supplementary Figure II.12A). Small mussels carried by larger ones were sighted in zoomed-in video sequences (e.g. Supplementary Figure II.12B). Over the whole set of video sequences, no feeding behaviour of crabs or fish were observed. Crabs occasionally attempted to open mussels or to catch approaching individuals of *M. fortunata* without success. Fish such as *Cataetyx laticeps* Koefoed, 1927 were observed swimming to stay in the FoV and *Gaidropsarus mauli* Biscoito & Saldanha, 2018 were often found on the bottom within crevices. *Synaphobranchus kaupii* Johnson, 1862 were occasionally observed visiting the crevices and the assemblages.

II.3.4 Environmental characterisation

II.3.4.1 Temporal variability of environmental conditions

Overall, dissolved iron concentrations ranged from 0.1 µmol/L in July 2017 to 49.5 µmol/L in November 2018 (Figure II.6A). Time series were characterised by discrete changes ranging from 0 to 10 µmol/L. The average temperatures were 6.8 ± 6°C and 9.6 ± 9.4°C as measured by the CHEMINI sampler and the optode probes, respectively. Values ranged from 4.4°C to 114°C (CHEMINI sampler) and 148°C (optode), these latter values being exceptional occurrences and probably most likely related to probe positioning (Figure II.6B-D). Temperatures exhibited a sharp increase during the 2018-2019 period when the highest value was measured (Figure II.6B-D). Overall, dissolved oxygen concentrations ranged from 0 to 327.7 µmol/L with an average of 172.1 ± 92.6 µmol/L. The 2012-2013 period showed a progressive decline in oxygen concentrations, but the 2014-2015 displayed a progressive increase, stabilising between 150 and 200 µmol/L (Figure II.6C). Oxygen concentrations displayed sharp monthly variability, except in 2016-2017 when they were more stable. Image observation suggested that the position of the TEMPO environmental module can change slightly during the time series. Hydrothermal deposits formed on the module during the 2018-2019 period (authors' pers. obs.).

The turbidity time series, measured at SeaMON East, 10 m from TEMPO, displayed occasional peaks and progressive increases starting around March-June (Figure II.6E). Bottom seawater temperature was stable throughout the entire time series (mean ± SD = 4.7 ± 0.1°C; Figure II.6F), exceeding 5°C in less than 1% of the measurements.

No significant periodicity was observed for iron concentrations, as shown by the Whittaker-Robinson periodogram outcomes (Figure II.6A). Most temperature time series displayed significant semi-diurnal and diurnal tidal periodicities (Figure II.6B-D-F). Significant tidal periodicities were observed in dissolved oxygen concentrations in 2016-2017 (Figure II.6C). No significant tidal periodicity was observed in turbidity (Figure II.6E). For the 7-day temperature time series measured every month by the iButton® sensors, 31.8% exhibited significant periodicities at periods of 12.5 h ± 1 h and 38.5% at periods of 25 h ± 1 h.

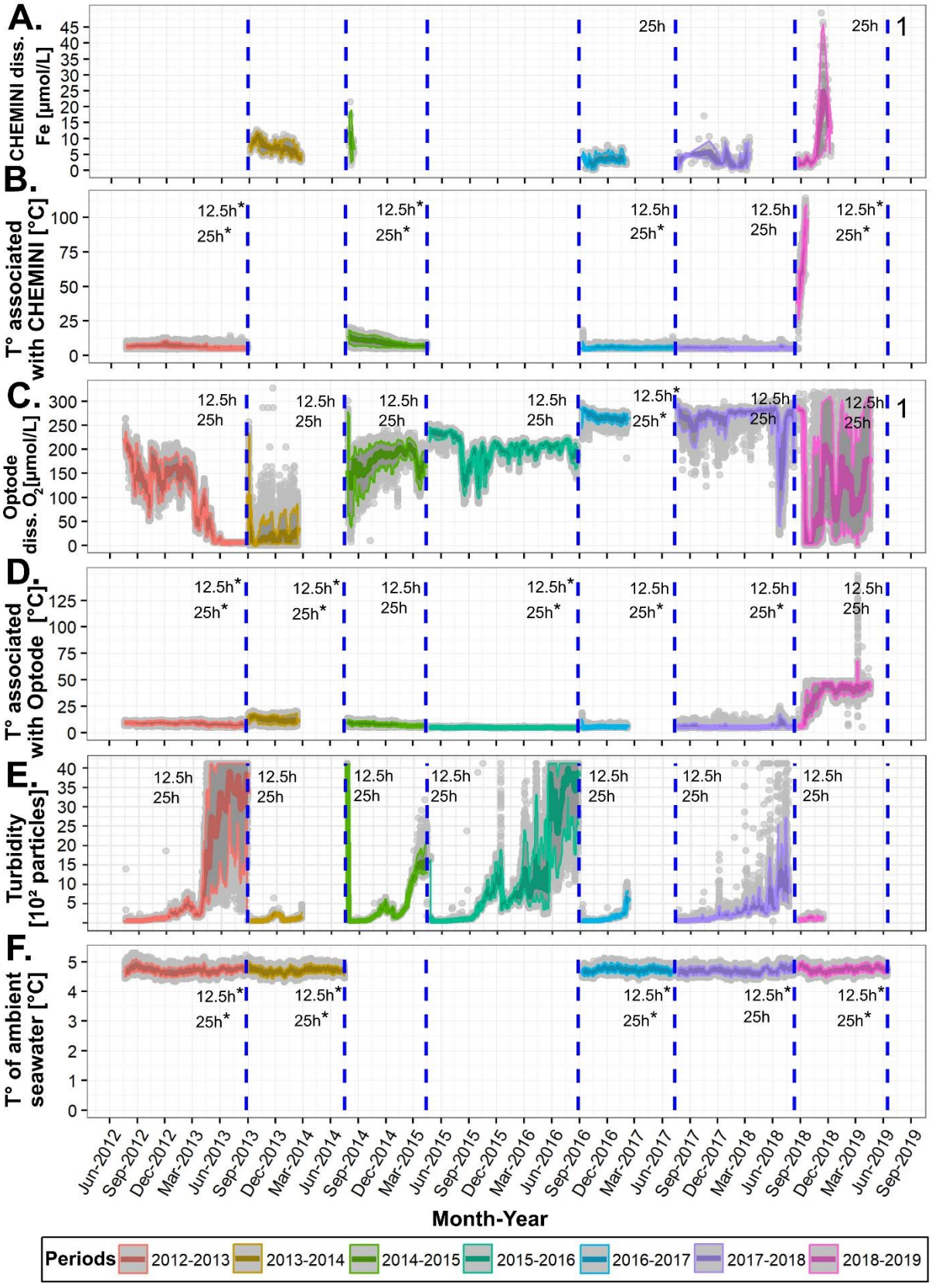

Figure II.6. (A-B-C-D) Environmental data recorded within the field of view (FoV) monitored by the TEMPO environmental module deployed at the base of the active Eiffel Tower edifice (Lucky Strike vent field, Mid-Atlantic Ridge). (A) Dissolved iron [Fe(II) + Fe(III)] concentrations [µmol/L] measured by a CHEMINI in situ analyser. (B) Temperature [°C] measured by a high-temperature probe positioned

next to CHEMINI. (C) Dissolved oxygen concentrations [µmol/L] measured by an Aanderaa optode probe. (D) Temperature [°C] measured by the probe associated with the optode. (E-F) Background environmental data measured outside the FoV. (E) Turbidity [10^2 particles counted] measured on the SeaMON East node 10 metres away from the TEMPO ecological module. (F) Temperature [°C] on the TEMPO ecological module. Grey areas depict the associated 5-95th percentiles. Grey circles represent values measured with the sensors. Dashed blue lines delimit periods of data acquisition, defined by the deployment and recovery of the sensors during the yearly MoMARSAT cruises. 12.5 h and 25 h indicate if a Whittaker-Robinson periodogram was generated to test for tidal periodicity. * indicates significant periodicity ($p<0.05$). (1) Note: the temperature associated with CHEMINI and optode probes reached over 100°C; therefore, the environmental module may have been dysfunctional for the 2018-2019 period.

II.3.4.2 Spatial variability of environmental conditions

Monthly temperatures measured by iButton® probes and averaged over one week showed that *B. azoricus* and microbial mats occupied areas in which mean temperatures were 6.8°C and 5.8°C, respectively, while crabs were observed in warmer habitats with a mean of 9.8°C (Table II.3). Moreover, *B. azoricus* and *S. mesatlantica* were present in more variable habitats in which temperatures can exceed 20°C (see maximum temperature, Table II.3). Larger mussels were found in warmer and more variable temperatures (Mean ± SD = 6.2 ± 1.5°C) than smaller mussels (5.0 ± 0.1°C). The sparse mussel assemblages occupied colder microhabitats less exposed to the hydrothermal outflow with lower concentrations of dissolved iron and total sulphide (Table II.3; Supplementary Figure II.13). Average temperature was 9.5°C with a maximum of 25.1°C on the white material (Table II.3), where white substratum accretion dynamics was observed (Figure II.7A). Temperatures measured away from that point were stable over the years, with the exception of a few points recorded in a small area 20-30 cm away that briefly exceeded 10.0°C in 2018-2019 (Figure II.7A; Supplementary Figure II.14).

Measurements with the submersible probes during yearly cruises led to similar results. The maximum temperature measured in the vent orifice with these probes reached 133.8°C, and all measurements in the surrounding microhabitats were below 10°C illustrating sharp, centimetre-scale spatial variability (Supplementary Figure II.13). Total sulphide concentrations and temperature were good indicators of fluid dilution and were used to discriminate habitats within the FoV according to a theoretical zonation of hydrothermal fluids along the mixing gradient (Table II.3). Standard deviations of the measured physico-chemical factors were on average higher and more variable closer to the vent orifice. Dissolved iron concentrations were higher in microbial mats and in sparse mussel patches than in dense mussel assemblage. The bare substratum was characterised by higher iron concentrations than the white material (Table II.3).

Table II.3. Environmental factors measured in the TEMPO ecological observation module (EMSO-Azores observatory) field of view: (A) Yearly submersible measurements (n = 116) of temperature for 1 minute (n = 87) and CHEMINI analysers (dissolved Fe(II) [n = 77] and total sulphide concentrations[n = 99]) from 2014 to 2019. (B) iButton® probe temperatures repositioned monthly by annotating their position in TEMPO images from 2014 to 2019. Average temperatures using continuous recordings were retrieved automatically using a temporal window of 1 week (± 0.5 °C) (n = 21,988). The maximum weekly average temperature is also given. Measurements were assigned to substratum and taxa based on the visual position of the submersible probes during dives (A) or considering a buffer zone with a radius of 5 cm around the iButton® probes (B). When iButton® temperature sensors were not linked to any particular substratum/taxon, temperature was assigned to the "no cover" class, i.e. the slab substratum. Classes (i.e. columns) are arranged according to the empirical distance of biological features (assemblage type or dominant taxon) and substrata to the vent orifice commonly observed at the hydrothermal edifice Eiffel Tower (Lucky Strike vent field; Cuvelier et al., 2009; Girard et al., 2020). Arrows indicate this theoretical gradient of the fluid dilution. No standard deviation refers to single point measurements.

		Farthest from the vent orifice Biological features	←	←	←	←	Hydrothermal vent orifice	→ Substratum	Farthest from the vent orifice
	Environmental factor	**Zoanthids**	**Microbial mat**	**Sparse *Bathymodiolus azoricus* assemblage**	**Dense *Bathymodiolus azoricus* assemblage**	***Segonzacia mesatlantica***	**Close vicinity to the vent orifice**	**White material**	**Slab substratum**
(A) Data collected during submersible dives	Mean temperature ± SD [°C]	5.1	*No data*	5.0 ± 0.1	6.2 ± 1.5	*No data*	39.1 ± 36.4	5.8 ± 0.4	4.9 ± 0.4
	Mean Fe concentration ± SD [µmol/L]	0.4	1.6	1.2 ± 2.9	1.1 ± 1.2	*No data*	9.0 ± 14.2	0.3 ± 0.5	1.3 ± 2.2
	Mean sulphur concentration ± SD [µmol/L]	7.4 ± 9.0	15.4	5.0 ± 7.9	19.0 ± 28.0	*No data*	107.2 ± 105.8	12.0 ± 13.9	10.9 ± 25.7
(B) Data collected via iButton® probes	Mean temperature ± SD [°C]	*No data*	5.8 ± 0.2	*(no distinction made in cover type)* 6.8 ± 3.2		9.8 ± 6.0	*No data*	9.5 ± 5.2	6.2 ± 1.6
	Maximum temperature [°C]	*No data*	6.0	25.1		23.8	*No data*	25.1	12.7

II.3.4.3 Environmental drivers of change

EOF analyses applied on gridded temperatures revealed two major temporal patterns that explained 99% of the total variance. FL values suggested a poor correlation between temperature and EOFs (FL < |0.2|, Figure II.7C). EOF1 was related to larger variations closest to the vent orifice, accounting for 85% of the variance with increased temperatures in 2015, 2018 and 2019 (FL ~ 0.2; Figure II.7B-C). EOF2 accounted for 14% of the variance and captured the opposite relationship between the warmest areas, strongly influenced by the hydrothermal outflow and an area on the left side of the FoV where temperatures fluctuate depending on the dilution gradient (FL ~ 0.15; Figure II.7C). The top left grid cell remained poorly affected by fluctuation of the hydrothermal fluid temperature (Figure II.7B-C).

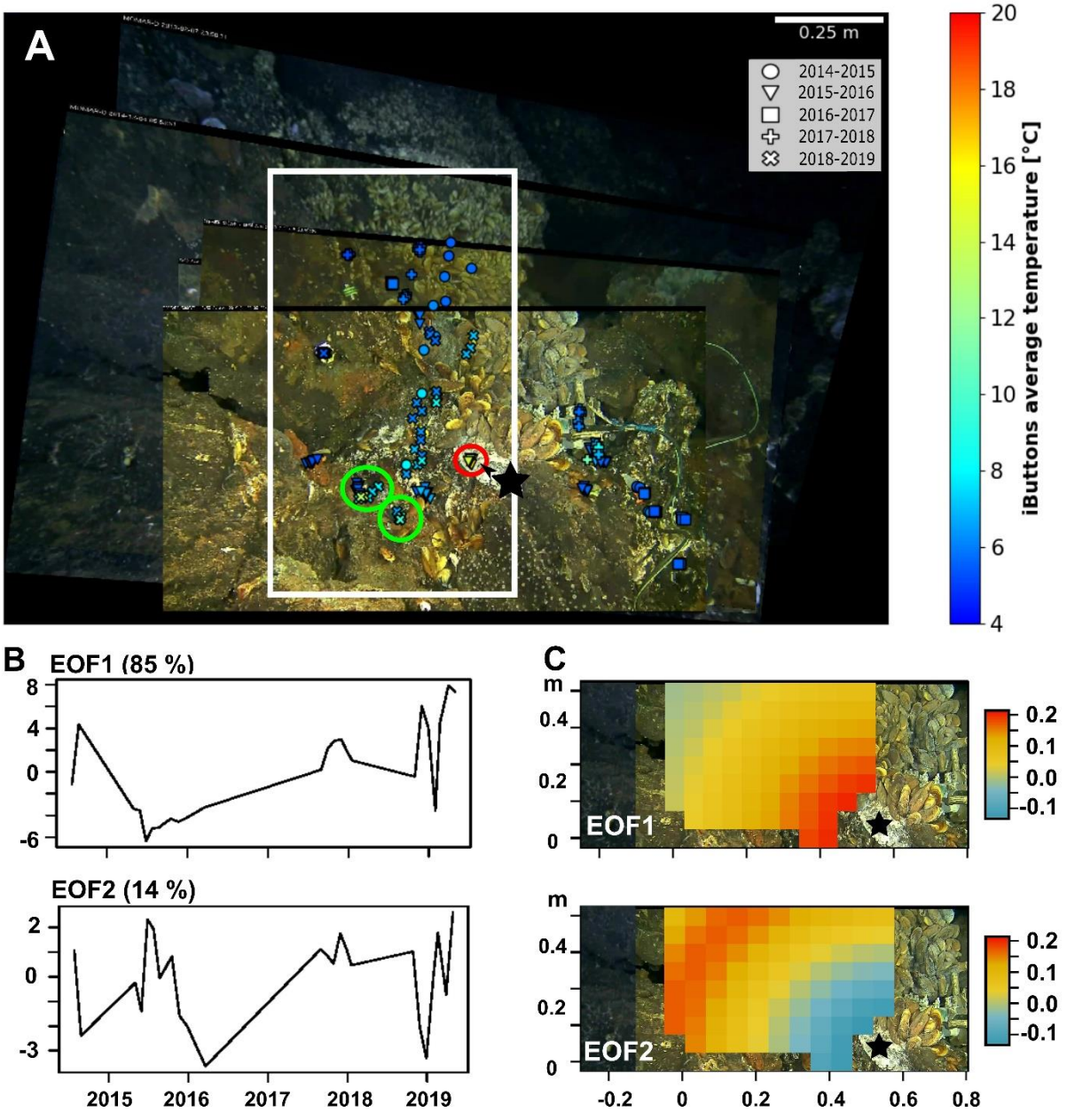

Figure II.7. Spatio-temporal analysis of the temperature recorded by the iButton® sensors averaged over a weekly interval every month. Black stars: vent orifice. (A) Spatial distribution of the measurements. Colour bar refers to temperature values [°C]. Red circle: the warmest temperatures recorded by temperature sensors. Linear regressions were based on the distance from that location using monthly temperatures. White box: only iButtons® from this side of the vent orifice were used to perform linear regressions. Green circle: locations of temperature anomalies (+ 2 to 5 °C). (B-C) Results of the Empirical Orthogonal Function (EOF) analysis undertaken on a time x space matrix where space (i.e. 2012-2019 FoV) is divided in multiple cells of 5 x 5 cm. (B) Time series of the first two EOFs representing the coordinates of each observation date along the first two EOFs (variance explained = 99%). (C) Spatial projection of the factor loadings (FL) of each EOF. The grid cells are coloured according to the degree of correlation between the local temperature time series of each grid cell and the given EOF time series (Figure II.7B). All metadata related to data acquisition and extraction are presented in Table II.1.

EOFs of gridded temperatures were poorly correlated with those of microbial mats ($p < 0.05$). Only temperature EOF1 and microbial mat EOF2 displayed a negative relationship (Pearson r = -0.46, t = -2.3629, $p = 0.028$) and corresponded to changes that occurred in 2012 and 2019. *B. azoricus* EOF1 was correlated with temperature EOF1 (Pearson r = 0.64, t = 3.3131, $p = 0.0044$) and EOF2 (Pearson r = -0.64, t = -3.2992, $p = 0.0045$). These correlations suggest a stronger link with temperature dynamics in the warmest areas. Finally, the three first EOFs of microbial mats showed significant correlations with those of *B. azoricus* for 7 EOF pairs out of 16 (Pearson r, $p < 0.05$, see details in Supplementary Table II.1). A closer look with zoomed-in videos showed that the appearance of microbial mats interlaced within the byssus threads (VM in Figure II.5D) coincided with the departure of mussels (LM in Figure II.4D).

II.4 Discussion

The EMSO-Azores observatory provides an unprecedented time series of biological and associated environmental data for a vent ecosystem. Imagery is non-destructive method, making it an ideal approach for the long-term study of vent communities (Tunnicliffe 1990; Sarrazin and Juniper 1998). The data analysed in this study constitutes the longest imagery time series of a vent faunal assemblage with high temporal resolution and is the first compilation of observatory-sourced biological data over a 7-year acquisition period. This novel approach, coupling spatial and temporal analyses, provides a baseline workflow, highly valuable for future observatory studies.

II.4.1 Limitations

Our study highlighted two main limitations that need to be kept in mind when interpreting the results. First, this study assessed a limited range of spatial scales. Although we can examine the underlying mechanisms of processes shaping ecological dynamics at the assemblage scale, our results cannot simply be extrapolated to larger scales (Levin 1992; Underwood et al. 2005; Gonzalez et al. 2020). Indeed, ecological processes are expected to change with increases in the spatial, temporal and organisational scales of the study from individuals to meta-communities, because larger scales may encompass a greater range of environmental conditions and biological features (Rosenberg and Freedman 1994; Zajac et al. 1998; Underwood et al. 2005). Seafloor observatory imagery data only provide information on the processes influencing faunal assemblages locally. However, they include a high-resolution time series of concomitant environmental fluctuations at the field scale (e.g. seismic activity, current variations, temperature) that could have impact at local scales. Therefore it is important to couple our observations with surveys at broader scales, also to incorporate a larger range of faunal assemblages and habitat heterogeneity. Nevertheless, despite the limited scale of our study (<1 m^2), our yearly presence at the study site (ET) made it possible to gain an integrated understanding of temporal variability at larger scales. At the other end of the spatial range, our image resolution also prevented the evaluation of the role of small-sized fauna (< 1 cm) in assemblage dynamics. The second major limitation involves the position of the recording modules and sensors. Consistency in spatial and temporal observations (i.e. FoV, sampling frequency) and temporal coverage of recordings are required to characterise the long-term evolution of faunal distribution, identify drivers of change and unveil the underlying mechanisms. Unfortunately, the yearly recovery of the TEMPO ecological observation module affected the position of the camera and sensors of the environmental module, which in turn affected the spatial overlap of images and *in situ* measurements along the time series. To solve part of this problem, the use of homography proved to be an efficient tool to retrieve a series of overlapping images, needed for quantitative temporal analyses. However, homography required discarding data from some non-overlapping portions of the image. Further development of the ecological observation module (e.g. pan-and-tilt module) should help optimise the overlapping surface area, as well as the zone under observation to ensure high zoom detail. The long-term detection of changes in fluid emissions at the assemblage scale was also difficult due to inadvertent small changes in the location of the chemical analyser between years. The surface being monitored undergoes a sharp dilution gradient of vent fluids, meaning that even a small centimetre-scale displacement of the sampler inlet can result in significant physico-chemical

changes. In addition, the occasional failure of the optode and CHEMINI analyser (e.g. after accumulation of white material on the inlet) added an element of uncertainty in the time series that could be solved in the future by taking more sampling replicates. Finally, mussel displacement also led to the constant reconfiguration of the iButtons® temperature grid. The use of a solid frame may be necessary to maintain the sensors in the same location.

II.4.2 Habitat and environmental dynamics

Different types of substrata and geological features were identified in our images. They include a bare substratum identified as the "slab". This mineral is common at LS and is composed of a hyaloclastite aggregation of basaltic glass, plagioclase crystals and sulphide grains hydrothermally cemented by amorphous silica and baryte (Langmuir et al. 1997; Humphris et al. 2002). A white material was also identified close to the fluid emission. The nature of this material (Figure II.2C) was difficult to assess from imagery only (Supplementary Video II.3). According to the literature and expert knowledge, it either corresponds to baryte or anhydrite deposits, forming at temperature higher than 60°C for the former (Jamieson et al. 2016a) and higher than 150°C for the later (Tivey 2007), or to thin microbial mats such as those produced by *Arcobacter* spp. (Taylor et al. 1999). Temperatures around the vent orifice reached 133.8°C in our study area.

Our time series confirmed the long-term stability of the diffuse flow habitat monitored by TEMPO (H1). On bare substratum, only minor changes were observed. They include the migration of a small group of large mussels aggregated around a patch of white material between July 2014 and June 2015. The departure of the mussels by the end of November 2015 coincided with the disappearance of the patch (Supplementary Figure II.15). Small variations in temperature (> 4°C) were also detected on the bare substratum in 2019. Aperiodic variability in temperature measurements could be due to a number of factors, including the relocation of small fluid orifices (Chevaldonné et al. 1991), the deviation of fluids by mussels (Johnson et al. 1994) or to the clogging of vent orifices as observed by (Sarrazin et al. 1997). Our observations showed that temperature changes could also arise from local physical rearrangements, such as the displacement of boulders or the formation of geological features that may contribute to diverting the flow of hydrothermal fluids. Several factors can trigger local changes in temperatures, making it difficult to determine possible causes. The diversity of spatial and temporal scales at which these changes can occur benefits from the use of multidisciplinary

observatories that provide an integrated network of physical, chemical, geological and biological data over a wide range of scales that inform on processes occurring at larger scales (e.g. seismic events or change in hydrothermal circulation). Finally, the significant tidal signal detected in temperatures measured over the bare substratum accounted for most of the environmental variability observed in the FoV throughout the time series. The role of tidal external forcing periodically modulating local environmental conditions along vent fluid orifices has often been reported (Chevaldonné et al. 1991; Johnson et al. 1994; Sarrazin et al. 2006, 2014; Cuvelier et al. 2014b; Lee et al. 2015; Lelièvre et al. 2017). Semi-diurnal and diurnal tides can modify exposure to fluids through changes in near-inertial bottom currents (Scheirer et al. 2006; Barreyre et al. 2014). Tides also temporarily modify the characteristics of vent emissions (e.g. velocity, subseafloor mixing) through variations in seafloor permeability and associated subsurface pressure gradients (Davis and Becker 1999; Pruis and Johnson 2004; Crone and Wilcock 2005).

Moreover, the most prominent changes to the physical habitat were restricted to the friable white material in the central diffuse-flow area. These changes include the formation of two small hydrothermal geological features, i.e. a 10-cm long spire and a 10-cm diameter flange. The growth of the small chimney corresponded with a temperature shift dropping from 30°C (April 2015) to 13°C (March 2016) that was recorded by one of our iButtons® located in the centre of the FoV. The formation of the flange coincided with a likely rearrangement of the plumbing vent system at the field scale in September 2015 as reported by Ballu et al. (2019). This event might have induced changes in physico-chemical conditions and explain the formation of this new feature. Moreover, the TEMPO environmental module, measured large variations in oxygen concentrations and monthly increases in dissolved iron concentrations in certain years, depending on the probe position near the vent orifice. As changes remained near the main outflow (~ 10-20 cm from the vent orifice), we conclude that there was no major relocation of the vent fluid orifice on a decadal scale within our FoV.

Outside the FoV, temperature data (probe located on the frame of the camera) also recorded the influence of tidal variations on bottom temperatures. Moreover, sporadic increases in turbidity measured 10 m away from the assemblage could result from periodic increases in plume exposure. Indeed, a recent study using the same data showed that tidal-modulated turbidity peaks can coincide with current reversion, causing currents to transport material away from the edifice (Lantéri et al. 2022). The observed increase of turbidity plateauing in June may also be due to an inflow of surface particles on the seafloor, originating from a phytoplankton bloom

known to occur in April-June (Khripounoff et al. 2008). Visual observations of increased marine snow at depths of 1700 m in early June at LS tend to support this hypothesis (authors' pers. obs.). However, because the sensor drifted considerably over time, we were not able to explore potential relationships further.

II.4.3 Dynamics in faunal distribution in relation to abiotic factors

The stability of the *B. azoricus* assemblage was characterised by the presence of a permanent cover with minor local variability, suggesting the apparent steady state of the population and confirming the hypothesis of little change over the long term (H2). This observed stability supports the observations made over a period of 2 years in the same area (Sarrazin et al. 2014) and 14 years at the scale of the entire edifice (ET, Cuvelier et al. 2011b). Our results however provide additional insights in our understanding of the functioning of ET (Cuvelier et al. 2011b). The apparently low mortality rate throughout 7 years indicates low population turnover, which offers additional support for the hypothesis that the ET habitat may have reached its carrying capacity before the start of this study (Cuvelier et al. 2011b). Similarly, mussel growth and recruitment led to only minor changes in mussel cover and had little impact on assemblage dynamics.

As shown for the environmental data, minor faunal changes were restricted to the assemblages located near the vent orifice. The most prominent decimetre-scale redistribution event corresponded to the overall displacement of a mussel assemblage from 2017-2019 and corresponding in time and space with the development of an active flange. In fact, the top of this hydrothermal feature was gradually colonised by large mussels, suggesting that mineralisation and induration may have possibly occurred throughout the directional accretion of the flange. A study at the Endeavour segment of Juan de Fuca Ridge (Sarrazin et al. 2002) proposed that, as the substratum matures (i.e. decrease in porosity), the habitat is less exposed to direct hydrothermal fluid exposure allowing ecological succession to proceed. Substratum maturation may also contribute to a decrease in its instability and friability, making surfaces more suitable for colonisation. In fact, large mussels appeared to have relocated in response to the opening of a new suitable habitat. Mussel migration is potentially the result of a trade-off between physiological tolerance to physico-chemical conditions and nutritional requirements (De Busserolles et al. 2009; Cuvelier et al. 2011b; also observed in Supplementary Figure II.15). Mussel habitat characteristics were in the range of those found previously in terms of

temperature and sulphide concentrations (Cuvelier et al. 2011a; Sarrazin et al. 2015; Husson et al. 2017). Large mussels colonised these areas of higher temperature, sulphide and iron concentrations and lower oxygen levels, but also of higher environmental variability. Our study also highlighted the large range of oxygen and iron concentrations that can be tidally modulated. Indeed *B. azoricus* has developed highly-responsive metabolic adaptations to cope with rapid fluctuations of environmental conditions inducing oxidative stress (Company et al. 2006; Demina and Galkin 2008; Bougerol et al. 2015), hypoxia and high-temperature exposure (Boutet et al. 2009). Despite *B. azoricus* robustness, alternating oxic/sulphidic conditions may be required for the adequate growth of vent mussels (Nedoncelle et al. 2015).

The displacement of individual mussels did not significantly affect the dynamics of the assemblage. Fleeting displacements over short distances have already been observed (Childress 1988; Johnson et al. 1994; Govenar et al. 2004), but their influence on distribution dynamics has never been assessed. Our results show that these 'mobile' mussels are capable of faster migration than those that are aggregated and bound by their byssus. The migration of these single individuals may be related to the search for suitable habitat due to competition for space or resources. Nevertheless, it remains unclear at what distance and on which time scales *B. azoricus* mussels are able to detect and travel to newly available or more suitable habitats. Directional patterns of displacement indicate the ability of individuals to orientate their migration towards vent orifices to reach optimal conditions, as hypothesised by other authors (Comtet and Desbruyères 1998; Colaço et al. 2006; Cuvelier et al. 2009; Sen et al. 2014).

Microbial mats occurred in habitats characterised by temperatures ranging from 4.7°C (background seawater) to a maximum of 10°C. Their growth in the vicinity of the zoanthid or mussel assemblages, and on the bare slab away from vent orifice suggests that they develop in conditions of low hydrothermal inputs as observed in other studies (Cuvelier et al. 2009, 2011a; Husson et al. 2017). Recurrent periods of appearance and disappearance of these mats over weeks to months were interrupted by periods of total absence, thus refuting the hypothesis of long-term stability (H3). This pattern was poorly correlated with measured temperature changes according to EOF analyses: the presence of infra-annual mat dynamics over a period of 7 years contrasts with the pluri-annual stability of hydrothermal conditions in the FoV. Therefore, other factors may play a role, including non-measured environmental variables or biotic interactions (see Section 4.4. on biotic interactions).

Zoanthid densities were roughly 25-70 ind./dm², which is within the range of those previously found in samples collected on ET (up to 30 ind./dm²; Sarrazin et al. 2015). Zoanthid density

showed little variation over several months, confirming the hypothesis of the high stability of these assemblages (H4). Overall, the distribution of these cnidarians remains poorly characterised at the LS vent field. At ET, they cover large portions of the edifice in areas away from vent orifices and in areas little exposed to currents carrying hydrothermal material (Girard et al. 2020a). However, their close association with chemosynthetic bacteria cannot be excluded without further investigation. For example, intracellular associations with sulphur-oxidising bacteria in hexacorallian species have been reported at hydrothermal vents (Goffredi et al. 2021), but have not been studied for the species at ET. The enhanced growth of non-vent sessile fauna in the vicinity of active vents has been reported in previous studies, suggesting that they benefit from allochthonous and chemosynthesis-derived food sources (Erickson et al. 2009, Sarrazin et al. 2006) or from the presence of prey such as copepods (Limén et al. 2008; De Busserolles et al. 2009). Understanding the link between peripheral zoanthid assemblages and hydrothermal activity warrants further investigation into their ecology. Overall, our results confirm the links between the spatio-temporal distribution of vent assemblages and local environmental conditions, including substratum properties (H5).

II.4.4 Role of biotic interactions

The role of biotic interactions in shaping the dynamics of the assemblages over time could be inferred from daily recording observations over 7 years. Surprisingly, mussel mortality (i.e. observation of empty shells) was rarely observed within the time period and no mass mortality event was recorded, suggesting a life expectancy of at least a decade for *B. azoricus* mussels of this assemblage. Previous studies showed only occasional predation by the crab *S. mesatlantica* as deduced from the presence of damaged mussels (Matabos et al. 2015) and from stomach content analyses (Colaço et al. 2002). These results are in accordance with stable isotope studies that indicate that *S. mesatlantica* crabs are more likely to be scavengers (De Busserolles et al. 2009; Portail et al. 2018). Predation by *Branchipolynoe seepensis* polynoids, found inside 70% of the mussels sampled at LS (Britayev et al. 2007; Bebianno et al. 2018), may be a potential stress factor for mussels, but there were only a few unidentified polynoids preying on mussel mantles in zoomed-in videos (Supplementary Video II.4). This low evidence for predation supports previous assumptions that, although partial predation exists on endosymbiotic species, it does not result in their death (Urcuyo et al. 2003; review in Govenar 2012). Finally, visiting

fishes with different types of activity regimes were occasionally sighted, but no clear interaction with resident vent species was observed.

The reduced occurrence of interacting behaviours and feeding activity suggest that predation may globally play a negligible role in shaping *B. azoricus* assemblages as suggested by other high-resolution studies at ET (Matabos et al. 2015). However, we cannot discount the role played by selective predation on mussel juveniles and recruits. In fact, a recent recolonisation study at a nearby edifice showed that the exclusion of predators leads to an increase in recruitment in mussel assemblages (Marticorena et al. 2021). In that study, crabs preferentially occupied the white material near the vent orifice and mussel assemblages. They may feed on recruits and juveniles that develop on mussel shells, on small mobile gastropods such as *Peltospira smaragdina* (authors' pers. obs.) and on microorganisms that potentially constitute the white patches. Microbial mats have indeed been suggested to be a potential food source for *S. mesatlantica* (Portail et al. 2018). These mats may also significantly contribute to the diet of several bacterivorous species, such as small mobile gastropods not visible on our images (Colaço et al. 2007; De Busserolles et al. 2009; Portail et al. 2018). Interestingly, the presence of microbial mats has been shown to be negatively correlated with the abundance of potential detritivores/grazers (Cuvelier et al. 2011a, 2017).

A few groups of small mussels (< 1 cm) were occasionally observed near the main mussel assemblage, possibly resulting from a recent recruitment event. In addition, large mussels with small individuals on their shells were observed in the permanent cover area, suggesting that this process contributes to the migration of small recruits and juveniles to areas of optimal environmental conditions (Van Dover et al. 1996). However, the resolution of our camera was insufficient to allow for the quantification of recruits on the substratum or mussel shells. Negative interactions, such as competition for space and resources, but also larviphagy and smothering, may contribute to the size segregation observed in hydrothermal mussel assemblages and may explain the rarity of smaller mussels in large mussel patches (Colaço et al. 1998; Lenihan et al. 2008). This type of negative interaction was corroborated by the arrival of a large mussel individual that caused the rapid departure of an entire patch of small mussels (i.e. < 5 mm), suggesting that larger mussels, with high mobility, may have a competitive advantage to access resources and occupy space. As observed in dense coastal mussel assemblages, these negative interactions may counterbalance the benefits of living in aggregation (Woodin 1974; Bertness and Grosholz 1985; Okamura 1986; Khaitov 2013).

Although imagery has the potential to assess the role of recruitment and growth, the observed decadal stability did not allow the description of these processes.

Positive interactions also occurred in the studied assemblages. EOF analyses suggested a strong correlation between mat and mussel dynamics that may be due to facilitation processes. The migration of *B. azoricus* individuals may help to clear suitable habitats for microbial mats. Their development may also be facilitated by the remaining byssus that create new, complex colonisation surfaces. Moreover, the lateral dispersion of the hydrothermal fluid by mussels, which extends the available redox conditions, may also contribute to locally enhance the growth of microbial communities (Johnson et al. 1994; Crépeau et al. 2011). Heterotrophic microorganisms found in these mats (Crépeau et al. 2011) may benefit from the particulate and dissolved organic material found in higher concentrations in the mussel assemblage (Sarradin et al. 1999; review in Govenar 2012). Although microbial mats do not appear to affect the fitness of mussels on which they grow (Martins et al. 2009), they may contribute to the environmental transmission of symbionts (Crépeau et al. 2011). Finally, the affinity of microbial mats for mussel assemblages support the role of these mussels as a foundation species (Rybakova and Galkin 2015).

II.4.5 Comparisons with intertidal mussel assemblages

In the present study, the major scales of variation detected were infra-annual, mainly related to tidal forcing, but also to a few aperiodic events linked to very localised changes in environmental conditions. This is comparable, albeit to a lesser extent, to what is observed in intertidal areas where tidal variability involves periodic variation in exposure to stressors and nutrients (Connell 1961; Suchanek 1978; Johnson et al. 1994; Nedoncelle et al. 2015). As a result both intertidal and vent species developed adaptation to cope with fluctuations of environmental conditions such as hypoxia (Intertidal: Newell 1973; McMahon 1988a – Hydrothermal: Hourdez and Lallier 2007; Hourdez and Jollivet 2020; Le Layec and Hourdez 2021). A review of the different environmental forcing acting on mussel assemblages at LS, but also in intertidal zones suggests a higher intensity of environmental stressors in the latter (e.g. wave action, air exposure; Table II.4). In intertidal zones, the main source of variability results from exchanges at the air/water interface and direct sun exposure, while in the deep sea, the temperature of bottom seawater is relatively buffered from any source of climate disturbance. This may be different at vents where tide-related shifts in currents may initiate changes in fluid

exposure for vent fauna (Nedoncelle et al. 2015; Lelièvre et al. 2017). For example, at diffuse-flow vents, tides may dictate most of the habitat variability in the short term with temperature variations limited to only a few degrees 10 to 30 centimetre away from the fluid exit (Sarrazin et al. 2014; Lee et al. 2015; Lelièvre et al. 2017). At high intertidal zones, tidal variability can be associated with large temperature gradients inducing mortality notably during extreme events caused by seasonality (Nakamura 1976; Dethier 1984). Predation also appears to have greater impact on intertidal mussels than those at vents (Table II.4), because multiple coastal species including crabs, whelks and seabirds are potential predators (Okamura 1986; Hilgerloh et al. 1997; Hunt and Scheibling 1998, 2001).

Moreover, extreme events such as storms can cause major mussel dislodgement and mortality events in the intertidal zone, creating large gaps in the assemblages (Sousa 1979; Paine and Levin 1981; Witman 1987; Dayton et al. 1989) or even in non-sheltered mussel population over kilometres (Nehls and Thiel 1993; Table II.4). Furthermore, centennial storms and earthquakes can severely alter the habitat by shaping the coastal geomorphology (Dayton et al. 1989; Castilla et al. 2010). Significant environmental variability at vents may result from aperiodic changes in subsurface hydrothermal circulation, structure collapses and from volcanic and tectonic events (Table II.4). If relocation of the fluid exit is relatively progressive and occurring over small scales, mobility is an ecological asset to relocate in suitable conditions (Govenar et al. 2004; Copley et al. 2007; Bates et al. 2010; Sen et al. 2014). However, in the case of larger-scale event, recolonisation by migration may be limited by specific mobility capabilities. Dramatic large-scale changes such as eruptions have been observed at vents, particularly at faster spreading ridges such as the East Pacific Rise or Juan de Fuca Ridge. These events, more common on fast spreading ridges, can eradicate the entire community back to the first colonisation stages (Tunnicliffe et al. 1997; Shank et al. 1998, 2003; Marcus et al. 2009). However, in this study, no such major event was observed during 7 years of investigation, neither at the local nor at the field scale. In fact, despite the limited spatial extent in our study, our repeated visits at LS indicate not only that the described stability was visually consistent over the entire studied edifice, but also, at the field scale, only a few sites have exhibited significant changes within the last 10 years.

Extreme events appear to be more frequent and intense in coastal areas compared with slow-spreading vent ecosystems where environmental variability is very low. Intertidal zones are particularly exposed during winter and summer, which are characterised by destructive storms, ice scouring or algal blooms (Table II.4). Regarding the MAR, volcanic events are extremely

rare (e.g. LS; Dziak et al. 2004; Ballu et al. 2019), although they may occur at a decadal frequency on faster-spreading ridges (review in Desbruyères 1998; Shank et al. 1998; review in Glover et al. 2010). This relative stability at slow-spreading ridges, questions the assumption that vent communities are exposed to extreme and highly variable conditions. It is obvious that vent ecosystem dynamics strongly contrast with that of the vast aperiodic and homogeneous surrounding deep sea, but our observations show that, at least at LS, mussel assemblages appear to experience relatively stable, clement and predictable conditions compared with their fast-spreading and coastal counterparts. That regime of infrequent and non-destructive disturbances can have important ecological implications. For example, under the "intermediate disturbance hypothesis" (Connell 1978), this regime may contribute to the lower diversity of the MAR vent fields previously attributed to higher isolation likelihood of slow-spreading system (review in Juniper and Tunnicliffe 1997; Van Dover and Trask 2000; Van Dover and Doerries 2005).

Table II.4. Abiotic and biotic conditions affecting the dynamics of mussel assemblages in the intertidal and hydrothermal environments. Not affected (-), affected (+; behavioural response, influence on few individuals only), strongly affected (++; > decimetre-scale influence in assemblages).

Source of influence	**Process involved**	**Effect**	
		Intertidal	**Hydrothermal**
Environmental			
Infra-daily			
Tides	Predictable changes Hydrodynamics & tidal variation	++ **Desiccation/Temperature stress**[1, 11, 22, 38, 43] **Physical disturbance (log/boulder drift, waves)**[2, 3, 18, 21, 28, 56]	+ **Changes in the distribution of the hydrothermal fluid carrying stressors and trophic resources** 23, 65, 66, 61, 70, 72
Infra-annual			
Substratum instability		Little investigated	++ **Structural collapse**[23, 36] **Activation/deactivation of fluid outflow**[36, 60, 67]
Season	Storms Disturbance on hydrodynamics	++ **Water velocity**[3, 13, 16, 18, 25, 26, 40]	+ **Bottom pressure, current velocity**[24, 30, 70]
	Climate extremes Disturbance linked to winter ice and high/low temperatures	++ **Physical dislodgement (e.g. ice scouring) and/or extreme environmental conditions** 11, 17, 18, 33, 34, 44, 52, 53	- Our data suggest high stability of the background deep-sea environment
	Life-history trait Spawning induction	+ *Mytilus edulis* spawns seasonally[7, 15, 31] *Mytilus californianus*: spawns continuously[12]	+ Seasonal spawning of all species of *Bathymodiolus*[42, 50, 51] except *B. thermophylus*[71]

Decadal and more			
Magmatic event	Eruption, earthquake	- *Not necessarily an intertidal feature. Few cases with mortality*[57]	++ *Fauna removal at medium to fast-spreading ridges*[59]
Long-term habitat change	Habitat suitability decline	++ **Sanding up**[58]	++ **Waning**[47, 62, 67, 68] **Landslide**[36]
Biotic			
Predation		++ **Interspecific**[3, 6, 9, 10, 11, 16, 27, 29, 32, 35, 39, 40]	-/+ **Interspecific**[45, 48, 49, 69, 63, 73] **Larviphagy**[54]
Competition for space/resources		++ **Interspecific**[1, 3, 4, 5, 9, 11] **Intraspecific**[19, 27]	++ **Interspecific**[36, 41, 55, 67]
Recolonisation		++ **Recruitment**[27, 64] **Passive/active displacement**[16, 27]	++ **Recruitment**[37,41] **Active displacement**[67, 69]

Connell 1. 1961, 2. 1985; 3. Dayton 1971; 4. Harger 1972; Paine 5. 1974, 6. 1976; 7. Wilson and Seed 1974; 8. Woodin 1974; 9. Menge and Sutherland 1976; 10. Menge 1978; Suchanek 11. 1978, 12. 1981; Sousa 13. 1979, 14. 1984; 15. Pieters et al. 1980; 16. Paine and Levin 1981; 17. Tsuchiya 1983; 18. Dethier 1984; 19. Bertness and Grosholz 1985; 20. Okamura 1986; 21. Denny 1987; 22. Mcmahon 1988b; 23. Tunnicliffe and Juniper 1990; 24. Cannon et al. 1991; 25. McGrorty and Goss-Custard 1993; 26. Nehls and Thiel 1993; Wootton 27. 1993, 28. 2001; 29. Petraitis 1995; 30. Cannon and Thomson 1996; 31. Gray et al. 1997; 32. Hilgerloh et al. 1997; 33. McCook and Chapman 1997; 34. Minchinton et al. 1997; 35. Nehls et al. 1997; 36. Sarrazin et al. 1997; 37. Comtet and Desbruyeres 1998; 38. Denny and Paine 1998; Hunt and Scheibling 39. 1998, 40. 2001; 41. Shank et al. 1998; 42. review in Tyler and Young 1999; 43. Denny and Wethey 2001; 44. Strasser et al. 2001; 45. Micheli et al. 2002; 46. Mullineaux et al. 2003; 47. Tsurumi and Tunnicliffe 2003; 48. Urcuyo et al. 2003; 49. Sancho et al. 2005; 50. Colaço et al. 2006; 51. Dixon et al. 2006; 52. Steenbergen et al. 2006; 53. Beukema and Dekker 2007; 54. Lenihan et al. 2008; 55. Lutz et al. 2008; 56. van De Koppel et al. 2008; 57. Castilla et al. 2010; 58. Dolch and Reise 2010; 59. review in Glover et al. 2010; Cuvelier et al. 60. 2011b, 61. 2014; 62. Fabri et al. 2011; 63. Govenar 2012; 64. Khaitov 2013; Nedoncelle et al. 65. 2013, 66. 2015; Sen et al. 67. 2014, 68. 2016; 69. Matabos et al. 2015; 70. Lelièvre et al. 2017; 71. review in Laming et al. 2018; 72. Mat et al. 2020; 73. Marticorena et al. 2021

II.5 Conclusion

Our results showed that faunal dynamics within the studied vent assemblage varied with changes in the local physico-chemical conditions at the decimetre scale. Moreover, as hypothesised in other studies (Sarrazin et al. 1997, 2002), substratum properties (e.g. maturation stage in terms of friability, porosity, mineralogy) can constrain the distribution of species, especially in more variable habitats such as the immediate vicinity of vent orifices. Imagery data, although limited to a few visible taxa, allowed us to characterise and confirm a few biotic processes or interactions. We confirmed the role of *B. azoricus* as a foundation species, providing a habitat to a variety of associated species, transporting smaller individuals and

facilitating the installation of microbial mats through habitat modifications. Larger mussels can migrate in response to environmental changes, as previously suggested by several authors. The role of this mobility in the local dynamics of vent assemblages must be considered, although it had no significant effect on the studied assemblage. Other observations, such as the displacement of individual mussels, needs further attention. The negligible role of predation on mature mussel individuals was supported by the absence of significant mortality over the study period. However, this process may be more important during the first colonisation stages: a single observation of a competitive relationship between large and small mussels lends support to this assumption. To conclude, the observations made in the present study were insufficient to support our hypothesis (H6) on the significant influence of biological interactions on assemblage dynamics. Further investigations on the role of these interactions on the fate of hydrothermal assemblages are required. Manipulative experiments on the seafloor, such as predator exclusion or recruitment studies may hold the key to obtaining some answers. Overall, this unprecedented 7-year daily imagery time-series reveals a high stability in vent assemblage in terms of fluid discharge, species distribution and the absence of major growth or recruitment. These results questions the assumption that, at least along the slow-spreading centres of the MAR, vent communities are highly dynamic and exposed to extreme and highly variable conditions.

Data availability statement

Raw data used in this paper are available on the EMSO-Azores platform: https://www.emso-fr.org/EMSO-Azores. Additionally, their individual references were provided in the section "Materials and methods". Processed data are stored in the SEANOE database: i) homography-transformed images (https://doi.org/10.17882/87389) and ii) image annotations (https://doi.org/10.17882/84672).

Authors' contribution

JS and MM conceived this study. JS, PMS and AL participated in the development of the TEMPO ecological & environmental modules and the EMSO-Azores observatory. LVA, MM and JD performed image analyses. AL processed sulphide and iron concentrations data acquired with the CHEMINI chemical analysers. ABA and LVA carried out statistical analyses. LVA, MM and JS interpreted the data and drafted the manuscript. All co-authors reviewed the manuscript.

Declaration of Competing Interest

The authors declare that they have no known competing financial interests or personal relationships that could have appeared to influence the work reported in this paper.

Acknowledgments

We warmly thank the crews of the R/Vs Pourquoi pas?, L'Atalante and Thalassa and pilots of the HOV Nautile and ROV Victor6000 submersibles who have participated in the MoMARSAT cruises since 2010 (https://d oi.org/10.18142/130). We acknowledge P.-M. Sarradin and M. Cannat for co-leading and managing the MoMARSAT cruises and the EMSO- Azores observatory. We are grateful to the engineers and technicians from the RDT and LEP research labs at the IFREMER REM department for the development and on-board maintenance of the TEMPO ecolog- ical module and the SeaMON East node, the development and mainte- nance of in situ chemical analysers, and support with instrumentation at sea. The EMSO-Azores observatory has been set up for over a decade; we gratefully thank anyone who has contributed to this research. We acknowledge the work of interns V. Courant, E. Jaulin, L. Le Goffic and C. Raffault who helped for image annotation. We are grateful to three anonymous reviewers who improved considerably the quality of this article. This manuscript was professionally edited by C. Engel-Gautier. This work and LVA's PhD thesis were supported by the European Union's Horizon 2020 research and innovation project iAtlantic under Grant Agreement No. 818123. This output reflects only the authors' view and the European Union cannot be held responsible for any use that may be made of the information contained therein. We also acknowledge financial support from the EU project EMSO (http://www.emso-eu. org/) and the French observatory EMSO-Azores funded by IFREMER and CNRS. The authors declare that the research was conducted in the absence of any commercial or financial relationships that could be construed as a potential conflict of interest. The authors declare that the research was conducted in the absence of any commercial or financial relationships that could be construed as a potential conflict of interest.

Appendix A. Supplementary material

Supplementary data to this article can be found online at https://doi. org/10.1016/j.pocean.2022.102791.

II.6 Supplementary Material

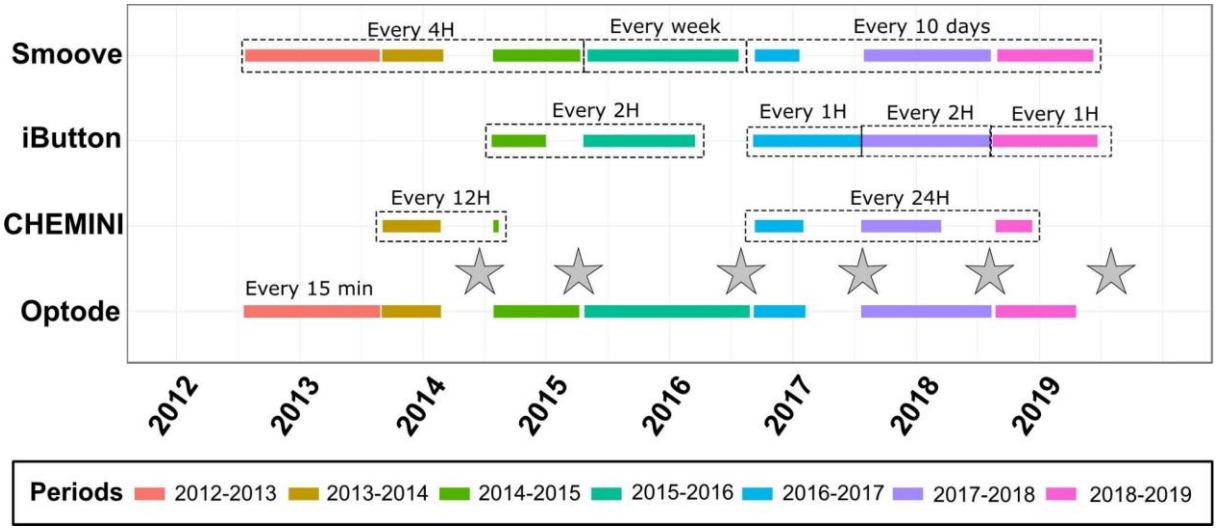

Supplementary Figure II.1. Temporal coverage of the data acquired by the EMSO-Azores observatory to study the long-term evolution of a diffuse-flow habitat located at the base of Eiffel Tower, a sulphide edifice of the Lucky Strike vent field (Mid-Atlantic Ridge). The camera system (Smoove) mounted onto the ecological module TEMPO records video sequences with a zoomed-out focus. iButton® temperatures were deployed in the field of view starting from 2014. The environmental module is composed of a CHEMINI analyser measuring *in situ* dissolved iron concentration (Fe(II) + Fe(III)) and of an Optode probe measuring oxygen concentrations. Both sensors are associated with a temperature probe. Grey stars represent measurements with the submersible during yearly cruises using CHEMINI chemical analyser for dissolved iron and total sulphide concentrations and a temperature probe.

Supplementary Figure II.2. Snapshot of a video sequence acquired on 08/11/2015 by the ecological observation module TEMPO connected to the EMSO-Azores observatory and located at the base of the active edifice Eiffel Tower (Lucky Strike vent field, Mid-Atlantic Ridge). The image shows a thin spire (around 25 cm high) that grew a few centimetres in front of the *B. azoricus* mussel assemblage.

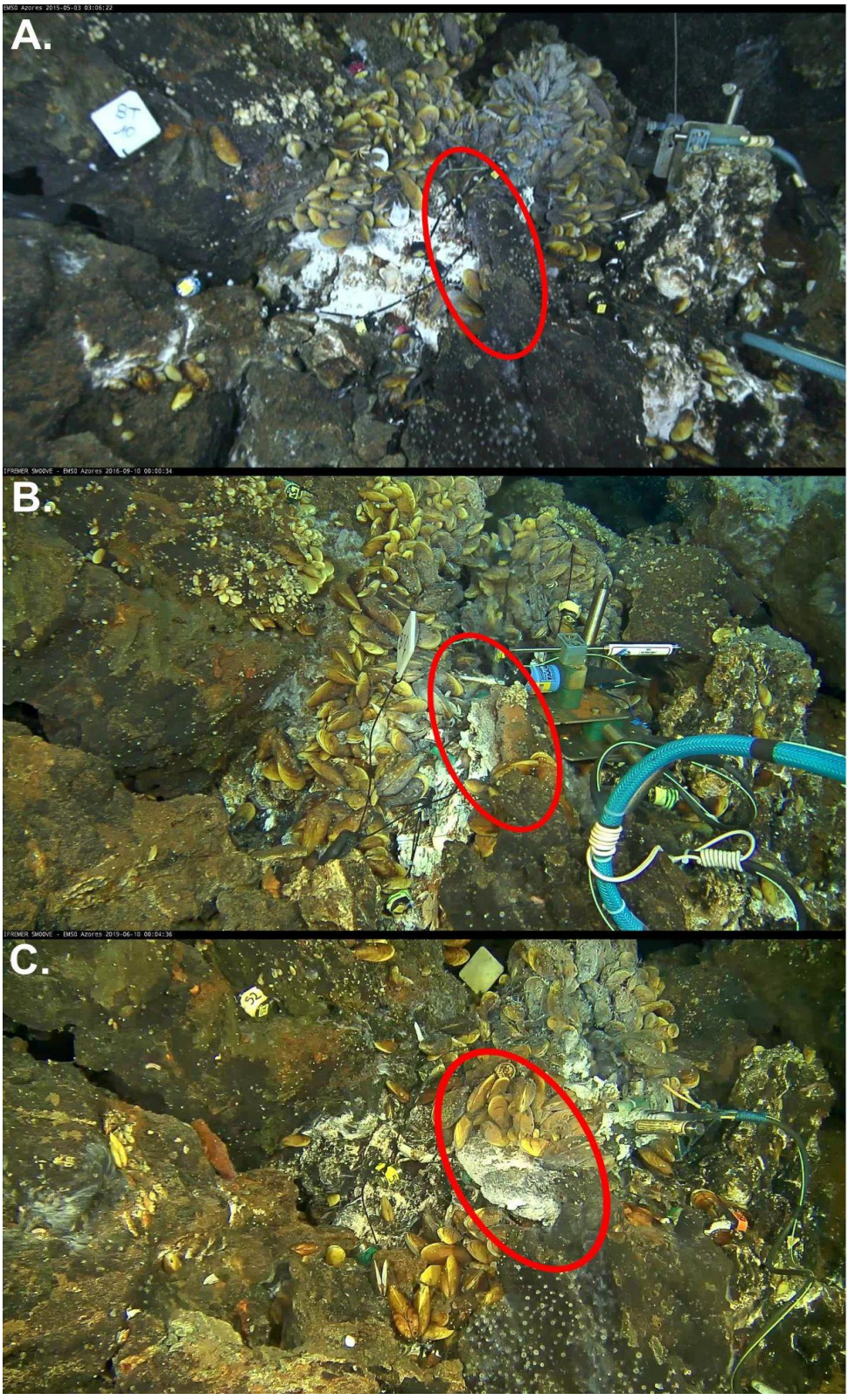

Supplementary Figure II.3. Growth of a 10-cm flange which started to develop in July 2016: (A) 03/05/2015, (B) 10/09/2016, (C) 10/06/2019. *B. azoricus* colonised this new feature in June 2019, resulting in a global displacement of the assemblage to the right. Snapshots were from video sequences acquired by the ecological observation module TEMPO connected to the EMSO-Azores observatory and located at the base of the active edifice Eiffel Tower (Lucky Strike vent field, Mid-Atlantic Ridge).

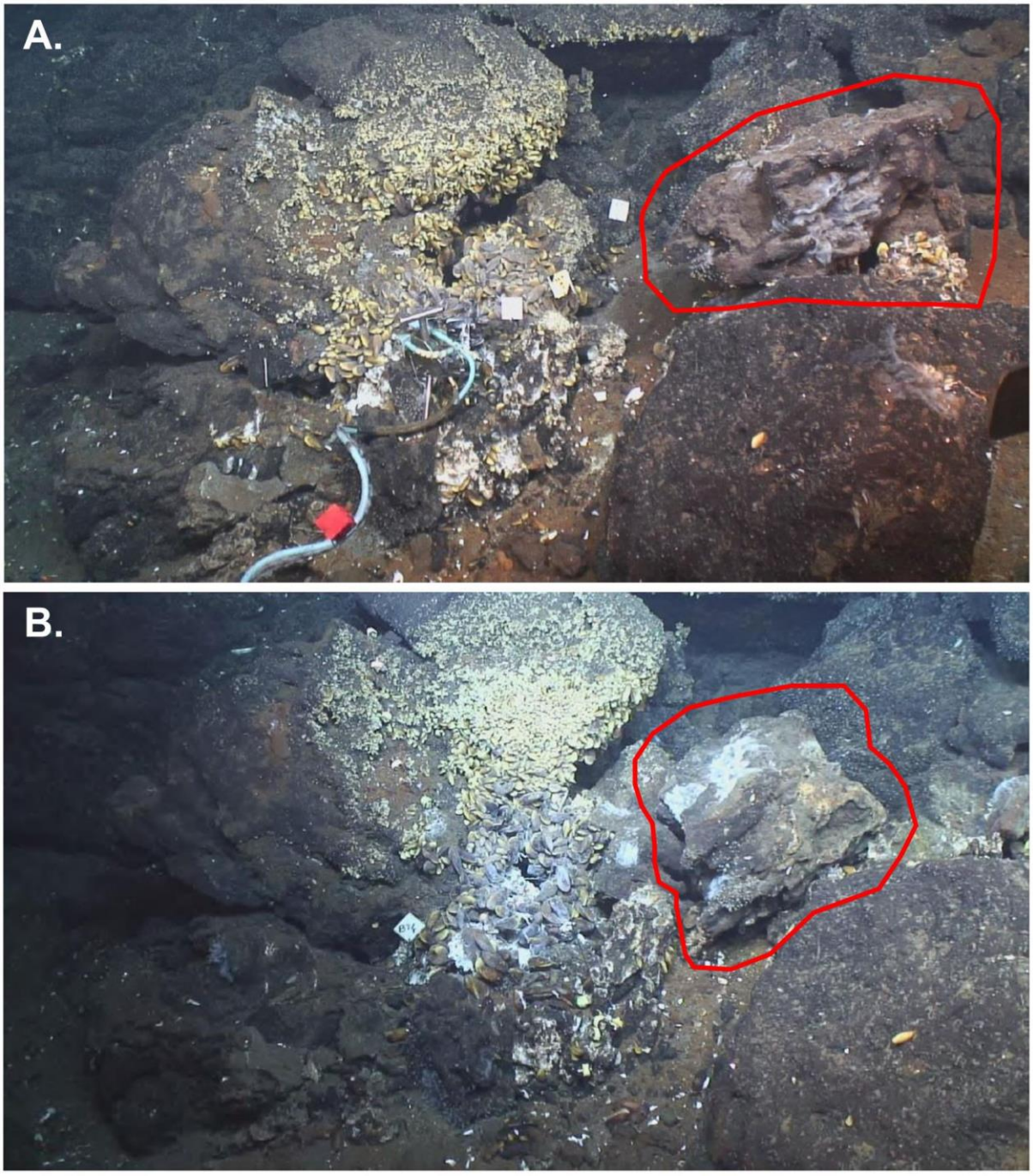

Supplementary Figure II.4. A boulder with a diameter larger than 0.5 m slid towards the permanent *B. azoricus* mussel assemblage. Its geometry and spatial position suggest that it may have detached from the upper hydrothermal edifice Eiffel Tower. Pictures were taken with the ROV *Victor6000* camera in (A) April 2015 and (B) January 2017.

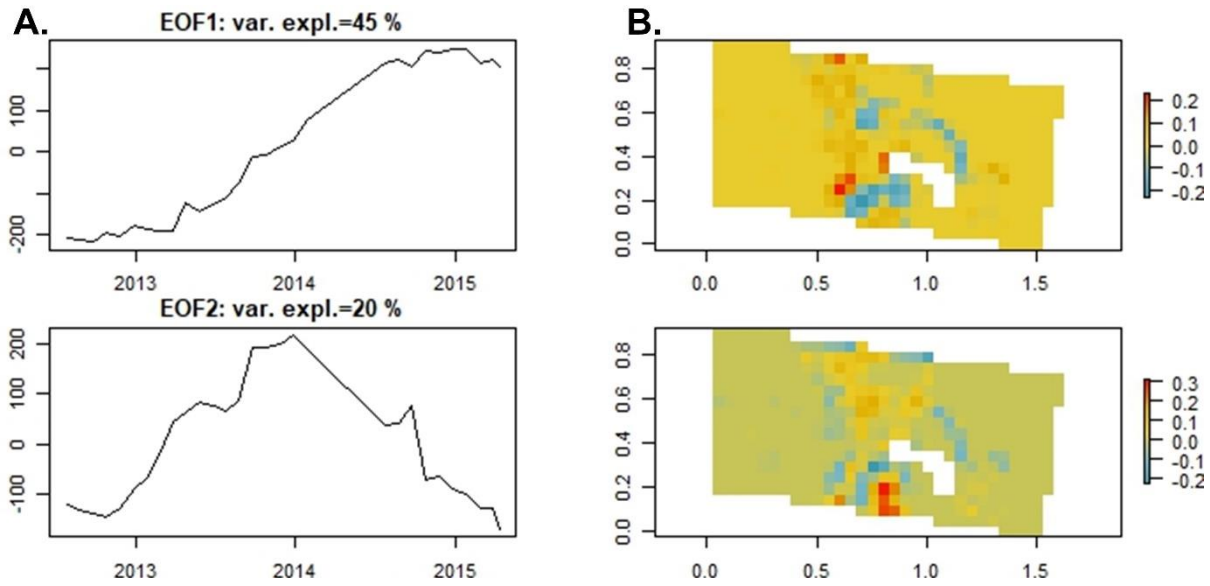

Supplementary Figure II.5. Spatio-temporal analyses of the *Bathymodiolus azoricus* mussel cover variability using Empirical Orthogonal Functions (EOF) to identify areas with different temporal patterns of variability. 29 images from 27/07/2012 to 12/04/2015 were considered for the Field of View (FoV) 2012-2015. The results of the EOF analysis undertaken with a mesh grid of 5 cm present (A) the time series of the first two EOFs (var. explained = 65%) and (B) the factor loadings for each cell of the grid with a colour bar. Images were recorded by the ecological observation module TEMPO connected to the EMSO-Azores observatory and located at the base of the active edifice Eiffel Tower (Lucky Strike vent field, Mid-Atlantic Ridge).

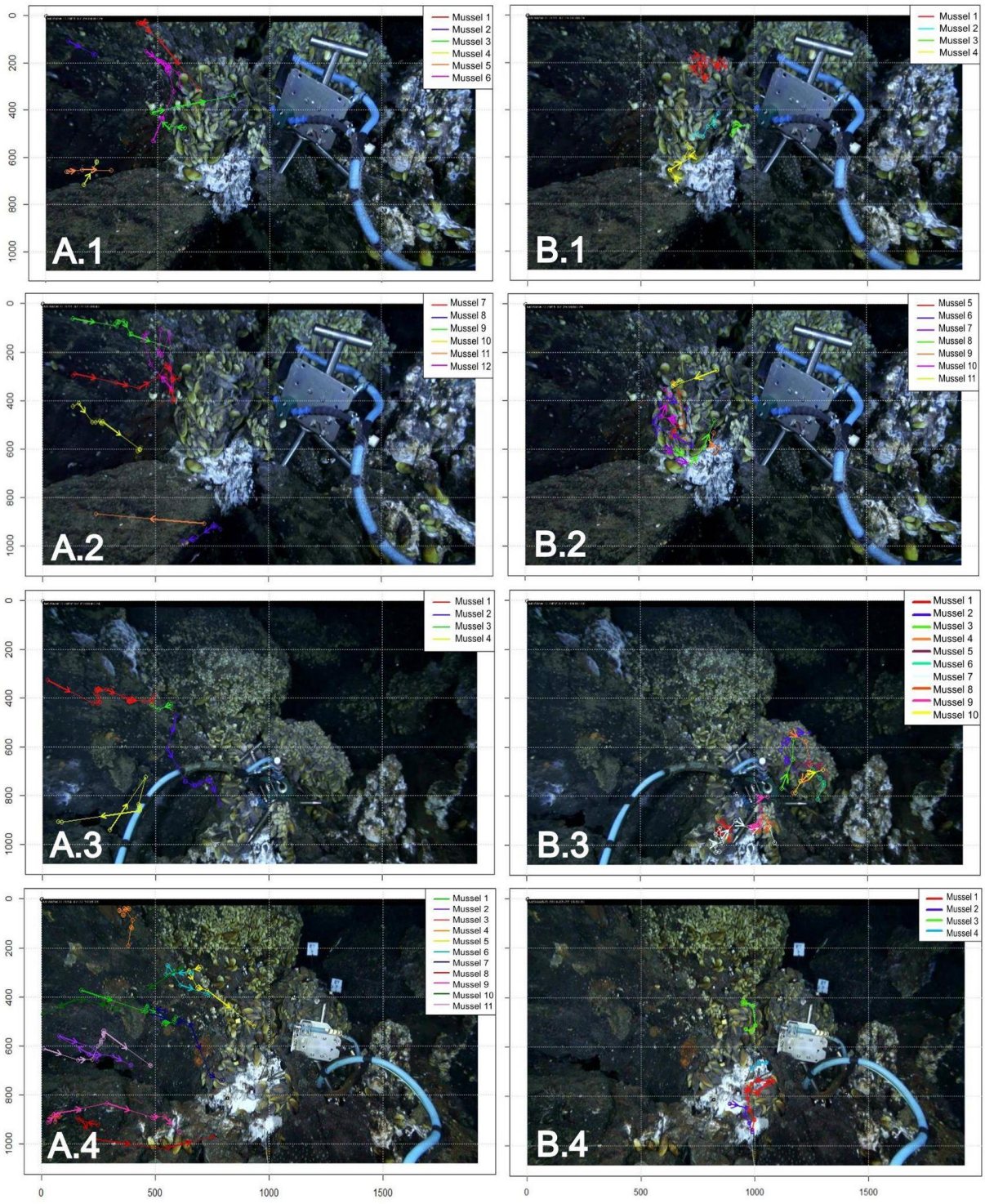

Supplementary Figure II.6. Tracks of *B. azoricus* mussel individuals. Two types of displacement were annotated (A) over the bare substratum at the left side of the wall and (B) within the central mussel assemblage for periods (1) and (2) 2012-2013, (3) 2012-2013 and (4) 2014-2015. Units of axes are in pixels with the following scale factors: 2011-2012, 1.43 px/mm; 2012-2013, 1.25 px/mm; 2014-2015, 1.3 px/mm. Images were recorded by the ecological observation module TEMPO connected to the EMSO-Azores observatory and located at the base of the active edifice Eiffel Tower (Lucky Strike vent field, Mid-Atlantic Ridge, -1695 m).

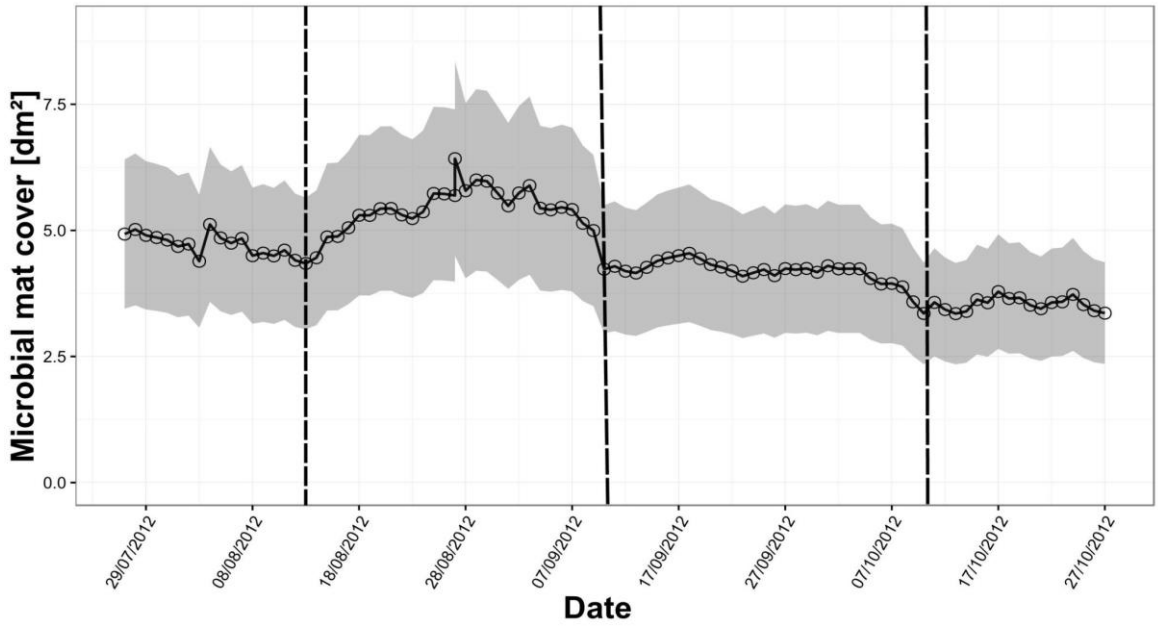

Supplementary Figure II.7. Cover [dm²] of the microbial mats annotated with a 1-day time step over 3 months from the 27/12/2012 to the 27/10/2012 using images acquired by the TEMPO ecological observation module deployed at the base of the active Eiffel Tower edifice (Lucky Strike vent field, Mid-Atlantic Ridge). Grey interval refers to annotation error assessed to reach ± 30% of the total cover. Dashed lines delimited periods of around a month harbouring a similar microbial mat coverage.

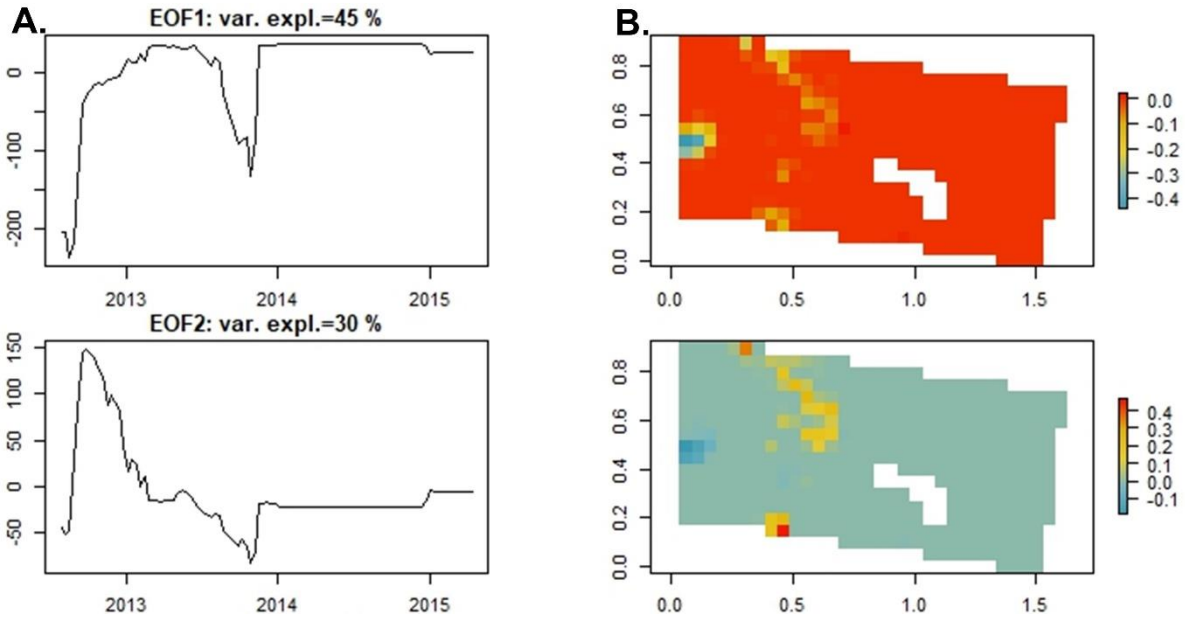

Supplementary Figure II.8. Spatio-temporal analyses of the microbial mat cover variability using Empirical Orthogonal Functions (EOF) to identify areas with different temporal patterns of variability. 185 images (27/07/2012 to 12/04/2015) were considered for the Field of View (FoV) 2012-2015. The results of the EOF analysis undertaken with a mesh grid of 5 cm present (A) the time series of the first two EOFs (var. explained = 75%) and (B) the factor loadings for each cell of the grid with a colour bar. Images were recorded by the ecological observation module TEMPO connected to the EMSO-Azores observatory and located at the base of the active edifice Eiffel Tower (Lucky Strike vent field, Mid-Atlantic Ridge).

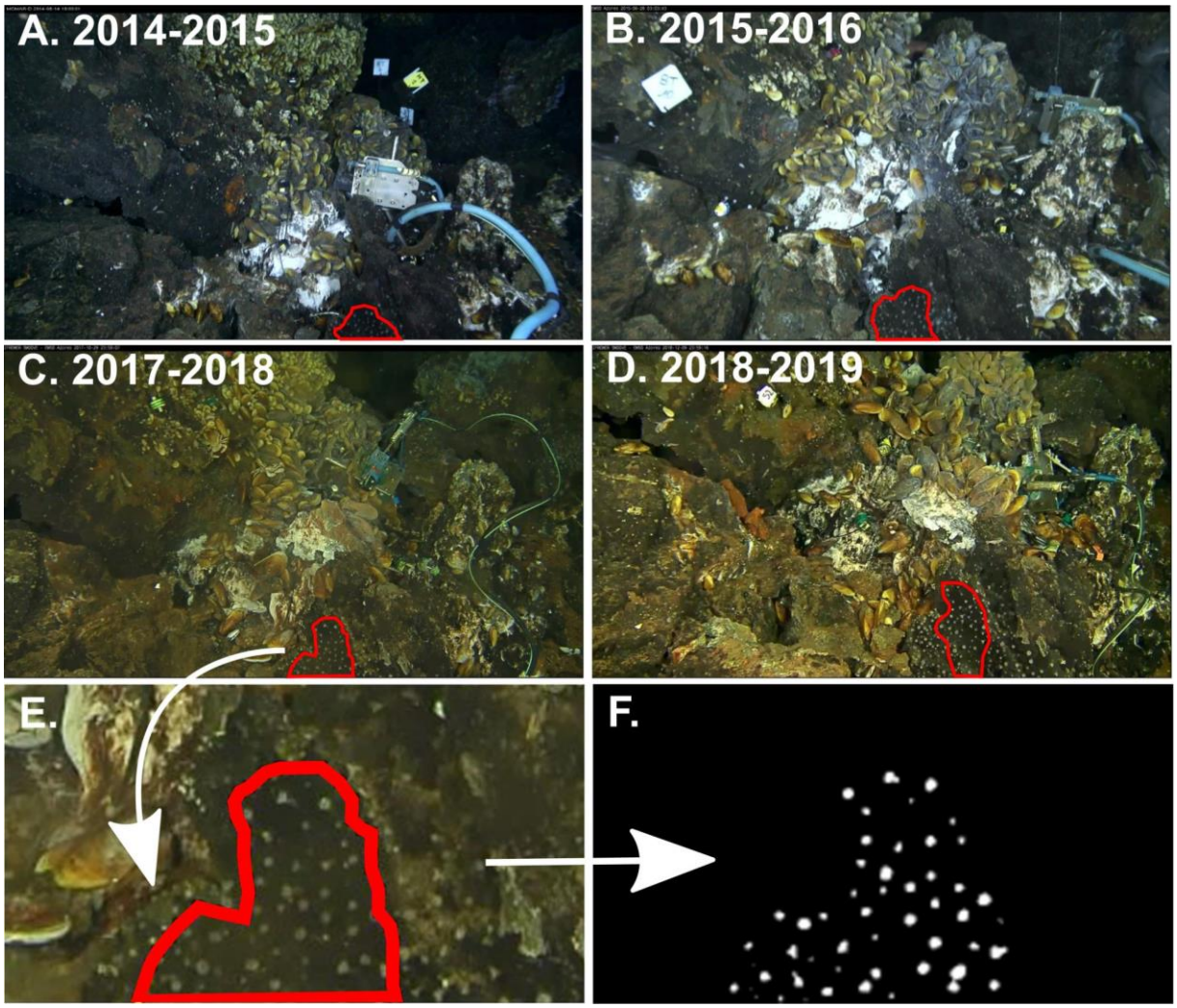

Supplementary Figure II.9. Locations of the zoanthid assemblages for (A) 2014-2015, (B) 2015-2016, (C) 2017-2018, (D) 2018-2019. Each coloured picture displays the raw screenshot of the FoV recorded by the TEMPO ecological module. For each of the regions of interest (ROIs) delimited by a red line (bottom of the image), individuals of zoanthid were isolated using an image segmentation routine. (E) Closer view of a zoanthid assemblage with the ROI delimited in red. (F) Isolation of zoanthid individuals using an automated algorithm based on image segmentation. Images were recorded by the ecological observation module TEMPO connected to the EMSO-Azores observatory and located at the base of the active edifice Eiffel Tower (Lucky Strike vent field, Mid-Atlantic Ridge).

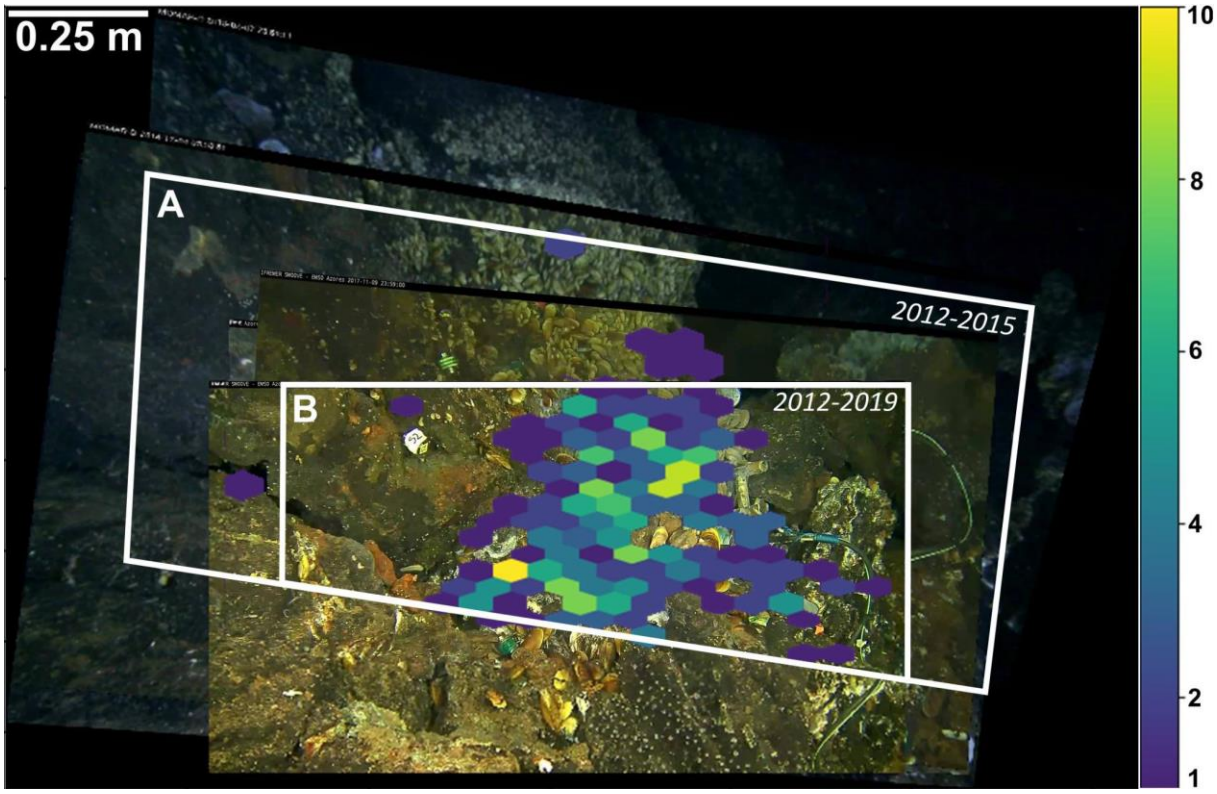

Supplementary Figure II.10. Spatial distribution of occurrences of the crab *Segonzacia mesatlantica* in the FoV of the TEMPO observation module deployed at the base of the Eiffel Tower edifice (Lucky Strike, Mid-Atlantic Ridge). The colour bar refers to the number of crab observations summed over the whole time series: (A) 80 individuals for 2012-2015 (112 images, every 10 days) and (B) 326 individuals for 2012-2019 (202 images, every 7-10 days). Absence of observation is presented as transparent.

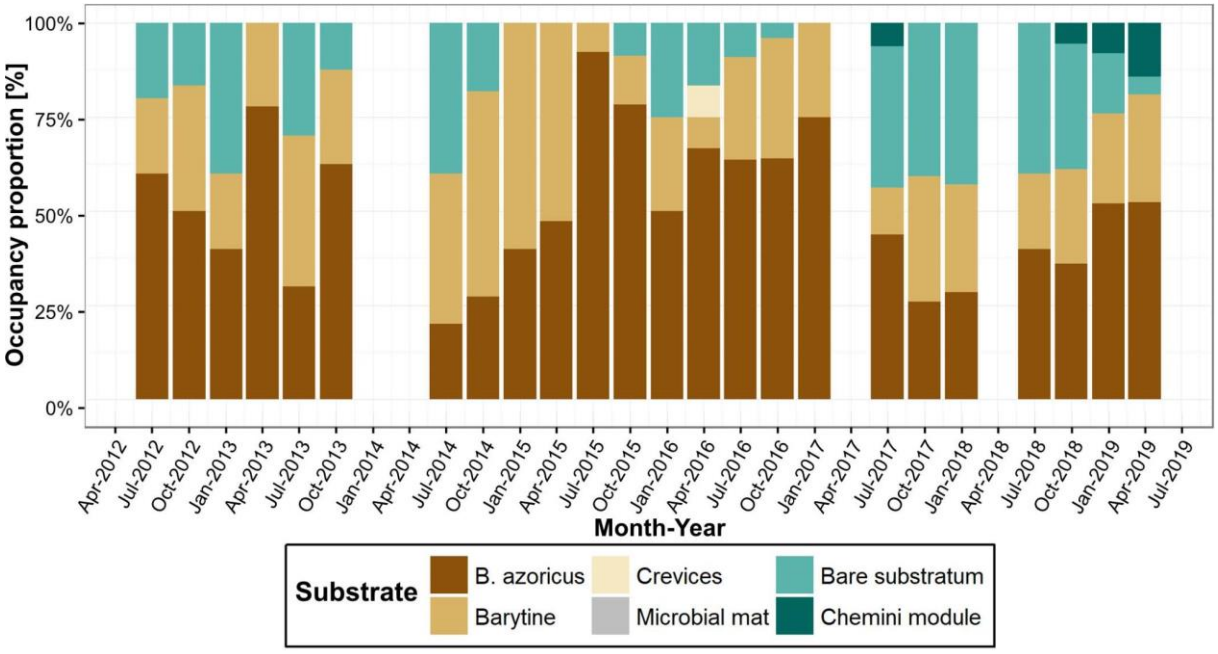

Supplementary Figure II.11. Proportion of crabs' occupancy per abiotic and biotic substrata for the small 2012-2019 FoV with observation acquired at a frequency of 7 to 10 days and aggregated over a period of 3 months.

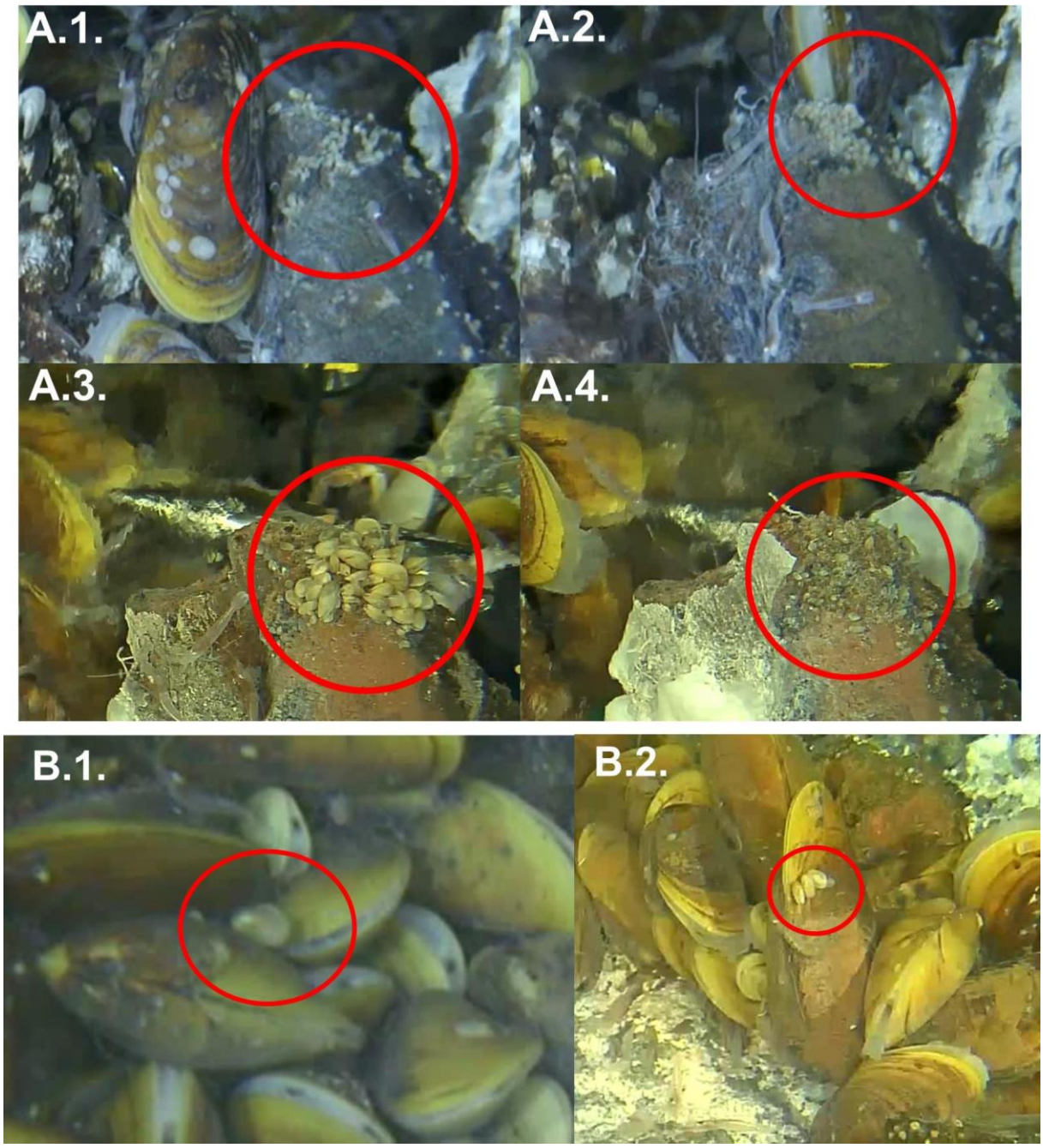

Supplementary Figure II.12. Snapshots extracted from zoom-in video sequences acquired by the ecological module TEMPO connected to the EMSO-Azores observatory and located at the base of the active edifice Eiffel Tower (Lucky Strike vent field, Mid-Atlantic Ridge). (A) These images show few observations made on a small mussel patch. (A.1) A large individual settled in the vicinity of the small mussels patch (09/09/2015). (A.2) Small mussels started aggregating after a few days (23/09/2015). (A.3) The development of small individuals was noticeable (18/09/2016). (A.4) The small mussel patch disappeared for unknown reasons (05/10/2016). (B) These images illustrate two observations of larger *B. azoricus* mussels carrying one or more smaller individuals: (B.1) 28/11/2015 and (B.2) 29/03/2019. Although these observations were rare, they suggest that movement of larger individuals could contribute to the transfer of small individuals to the main mussel assemblage located closer to the fluid exit.

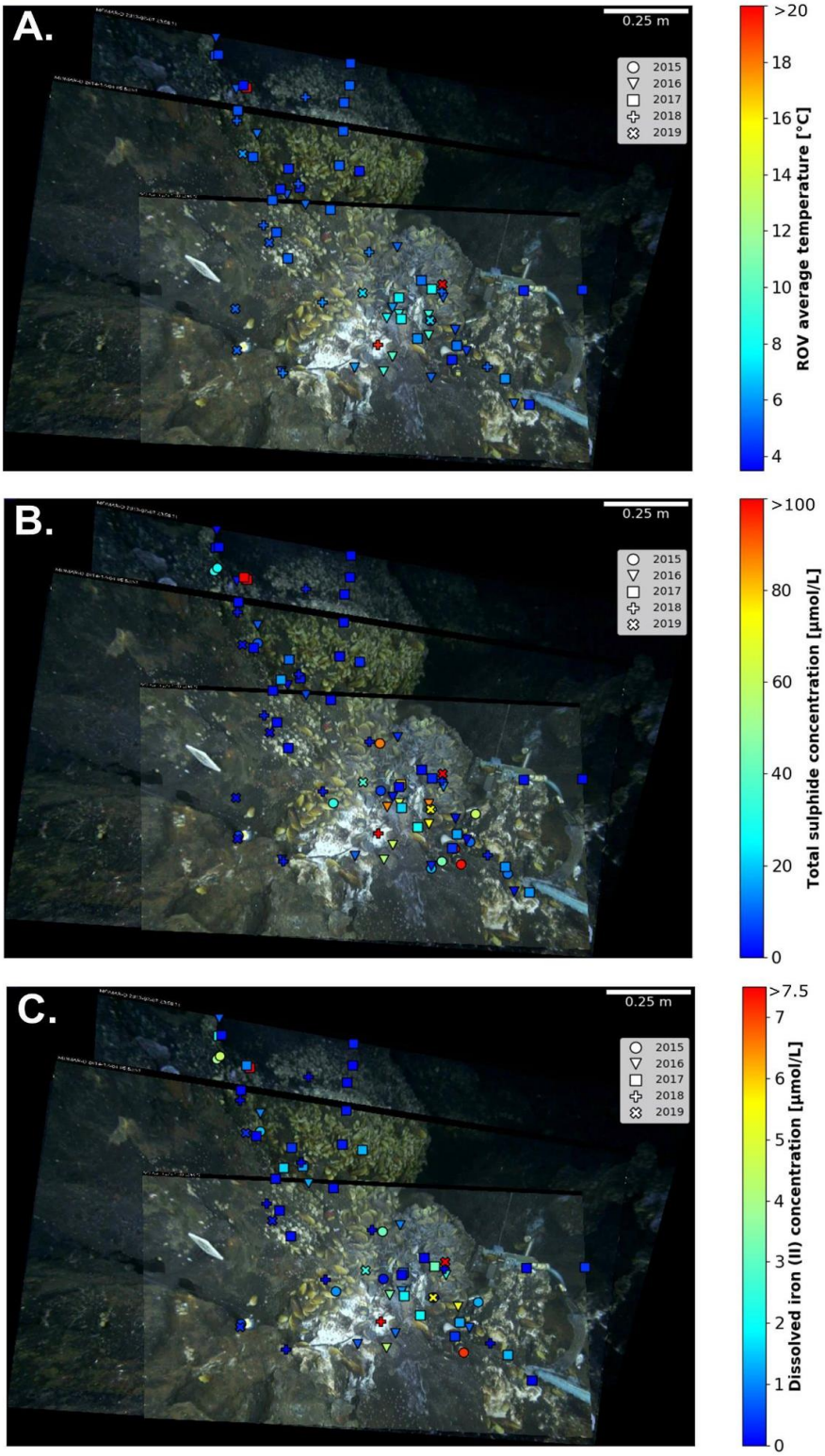

Supplementary Figure II.13. Measurements made in the whole field of view with submersibles during the Momarsat maintenance cruises between 2015 and 2019. (A) Temperatures averaged over a minute of measurement [°C], (B) Total sulphide ($\Sigma S = H_2S + HS^- + S^{2-}$) concentrations [µmol/L], (C) Dissolved iron [Fe (II)] concentrations [µmol/L]. Colour bar refers to values of temperature and concentrations. Symbols refer to the year of acquisition. Images were recorded by the ecological observation module TEMPO connected to the EMSO-Azores observatory and located at the base of the active edifice Eiffel Tower (Lucky Strike vent field, Mid-Atlantic Ridge).

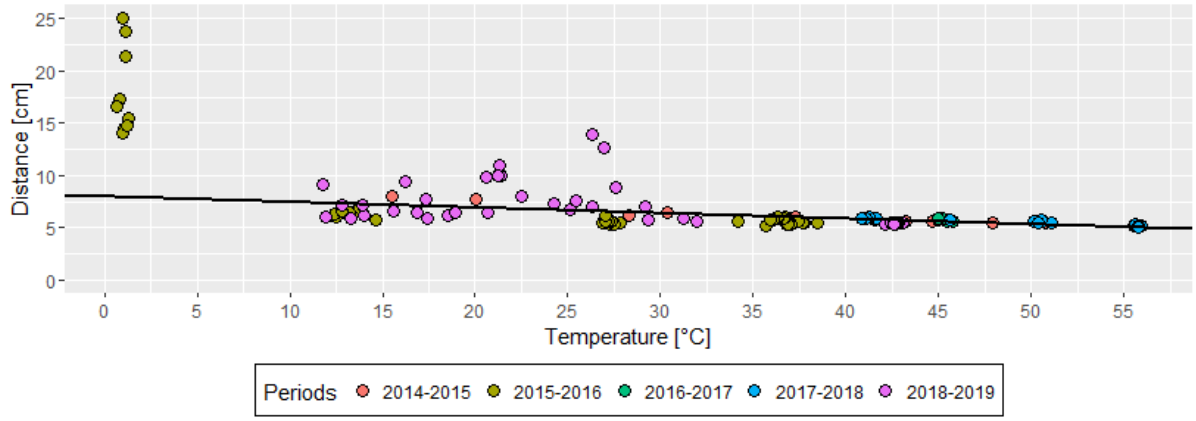

Supplementary Figure II.14. Plots of the temperature recorded by the temperature sensors according to the distance from the location of the warmest temperature measurements throughout the whole time series. Colours refer to different periods of recordings. The red circles identify the warmest temperature measurements as a starting point from which linear regressions were achieved every month to extrapolate the temperature in the FoV. The green circles highlight zones of warmer temperatures suggesting some change in the hydrothermal fluid distribution throughout the time series.

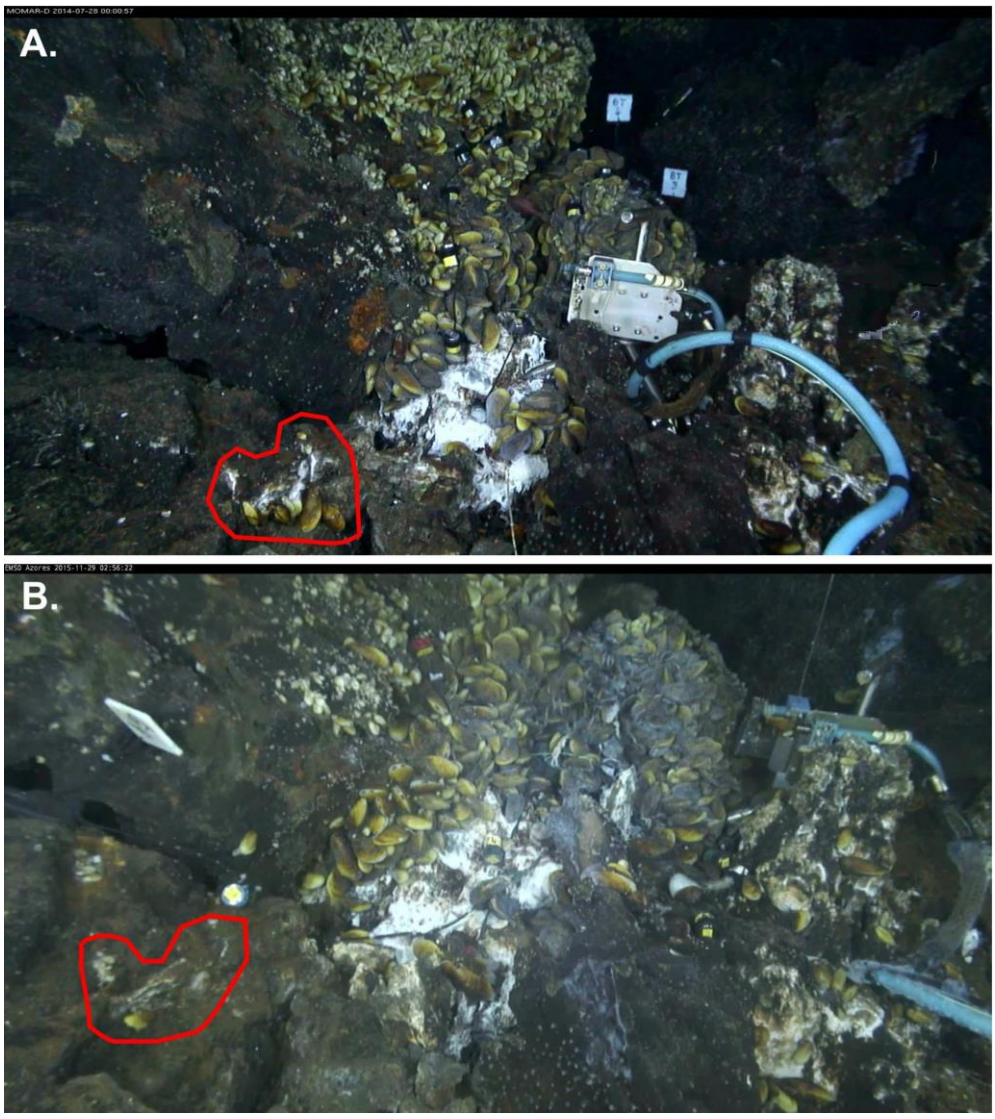

Supplementary Figure II.15. Snapshots extracted from video sequences acquired by the ecological observation module TEMPO connected to the EMSO-Azores observatory and located at the base of the active edifice Eiffel Tower (Lucky Strike vent field, Mid-Atlantic Ridge). (A) White deposit reflecting possible hydrothermal influence ~ 6-dm² area; 28th July 2014. A small patch of < 10 individuals of *B. azoricus* mussels were aggregated around it. (B) Mussels abandoned the area within a month which coincided with a decrease in the white cover (29th November 2015).

Supplementary Video II.1. Temporal evolution of the *Bathymodiolus azoricus* mussel assemblage. Pictures were overlaid onto each other using homography techniques. Snapshots were extracted from video sequences acquired by the ecological observation module TEMPO connected to the EMSO-Azores observatory and located at the base of the active edifice Eiffel Tower (Lucky Strike vent field, Mid-Atlantic Ridge). https://ars.els-cdn.com/content/image/1-s2.0-S0079661122000520-mmc3.gif

Supplementary Video II.2. Temporal evolution of the microbial mats. Pictures were overlaid onto each other using homography techniques. Snapshots were extracted from video sequences acquired by the ecological observation module TEMPO connected to the EMSO-Azores observatory and located at the base of the active edifice Eiffel Tower (Lucky Strike vent field, Mid-Atlantic Ridge). https://ars.els-cdn.com/content/image/1-s2.0-S0079661122000520-mmc4.gif

Supplementary Video II.3. Daily evolution of the white hydrothermal deposits. It remains unclear if they are organic or inorganic. This video also captures the development of a small flange from 08/09/2016 to 28/01/2017. Snapshots were extracted from video sequences acquired by the ecological observation module TEMPO connected to the EMSO-Azores observatory and located at the base of the active edifice Eiffel Tower (Lucky Strike vent field, Mid-Atlantic Ridge). https://ars.els-cdn.com/content/image/1-s2.0-S0079661122000520-mmc5.mp4

Supplementary Video II.4. Video sequence illustrating partial predation in the form of rapid biting of a polynoid worm on two *Bathymodiolus azoricus* mussels (lower left of the video sequence). Mussels subsequently closed their valves after the worm extruded its mouth. This is possibly the only predation activity that *B. azoricus* mussels undergo. This "zoom-in" video sequence was acquired the 12/10/2016 by the ecological observation module TEMPO connected to the EMSO-Azores observatory and located at the base of the active edifice Eiffel Tower (Lucky Strike vent field, Mid-Atlantic Ridge). https://ars.els-cdn.com/content/image/1-s2.0-S0079661122000520-mmc6.mp4

Supplementary Table II.1. Pearson r, p-value and t of correlation bewteen all pairs of the 4 first EOFs computed on *B. azoricus* cover, microbial mat cover and the dilution model over space and time with iButtons ® temperature.

	Pearson r				**p-value**				**t**			
	EOF1	EOF2	EOF3	EOF4	EOF1	EOF2	EOF3	EOF4	EOF1	EOF2	EOF3	EOF4
MM/B. azoricus (df = 43)												
EOF1	-0.155	0.15	-0.325	0.4393	0.3092	0.3226	0.02943	0.002534	-1.0292	1.007	-2.2528	3.2068
EOF2	-0.322	0.431	0.575	-0.065	0.03119	0.003095	3.69E-05	0.6737	-2.2276	3.1349	4.60E+00	-0.42401
EOF3	-0.227	-0.48	0.309	-0.272	0.1342	0.0008371	0.03894	0.07063	-1.5266	-3.5922	0.03894	2.13
EOF4	-0.121	0.174	-0.036	-0.139	0.4299	0.2533	0.812	0.361	-1.8538	-0.79694	-0.23938	-0.92335
Dilution/B. azoricus (df = 16)												
EOF1	0.6379	-0.6363	-0.2201	0.3066	0.004397	0.004527	0.3801	0.216	3.3131	-3.2992	-0.90266	1.2883
EOF2	0.1429	-0.1153	0.1772	0.1866	0.5717	0.6488	4.82E-01	0.4585	0.57738	-0.46419	7.20E-01	0.75969
EOF3	0.2121	-0.2876	-0.125	0.1642	0.3982	0.2472	0.6213	0.5149	0.8681	-1.2012	-0.5038	0.66601
EOF4	0.2227	-0.1111	0.3113	0.1447	0.3744	0.6608	0.2086	0.5667	0.91372	-0.44716	1.3102	0.58494
Dilution/MM (df = 21)												
EOF1	-0.2756	-0.4583	0.3501	0.0528	0.2031	0.02786	0.1015	0.8109	-1.3136	-2.3629	1.7125	0.24236
EOF2	0.1963	-0.0474	-0.0941	-0.3454	0.3693	0.8298	6.70E-01	0.1065	0.91743	-0.21767	-4.33E-01	-1.6866
EOF3	0.1465	0.2319	0.1176	0.3739	0.5048	0.2871	0.5929	0.07885	0.67857	1.0922	0.54289	1.8473
EOF4	-0.2594	-0.0636	0.03359	0.1863	0.232	0.7729	0.8791	0.3948	-1.2307	-0.29227	0.15399	0.8688

II.7 Synthèse des résultats

Identifier les échelles et les moteurs de la variabilité écologique est essentiel à une compréhension complète du fonctionnement des écosystèmes. Au niveau des sources hydrothermales des grands fonds, la dynamique infra-annuelle reste mal décrite. Cette étude avait pour objectif de caractériser les facteurs qui déterminent la dynamique des assemblages de faune dominés par les moules *Bathymodiolus azoricus*. Nous avons analysé une série chronologique de 7 ans d'images et de données environnementales recueillies à une profondeur de 1695 m à la base de l'édifice actif Tour Eiffel au niveau du champ hydrothermal Lucky Strike (dorsale médio-atlantique). La fréquence d'acquisition s'est effectuée à des pas de temps variant de l'infra journalier au mensuel, ce qui a permis d'identifier les processus agissant à plusieurs échelles temporelles. En utilisant les images acquises par le module écologique TEMPO, connecté à l'observatoire EMSO-Açores, nous avons évalué l'influence des changements des conditions environnementales sur la dynamique des assemblages de faune (moules, zoanthaires), des tapis microbiens et de la faune mobile (crabes) à proximité d'une source de fluide diffus.

Nos résultats montrent que les conditions de l'habitat étaient généralement stables au cours de la période de 7 ans, avec une variabilité temporelle principalement liée à la périodicité des marées ainsi qu'à quelques anomalies locales de température, probablement en lien avec la turbulence, mesurées par des sondes déployées dans le champ de vue. Les moules et les zoanthaires ont montré une stabilité spatio-temporelle remarquable, cohérente avec la stabilité de l'habitat. Les changements localisés liés à l'exposition au fluide hydrothermal diffus et à l'instabilité du substrat ont gouverné les mouvements des moules de grandes tailles observées à l'échelle interannuelle. Ces observations ont permis de montrer l'importance de la mobilité des moules dans leur réponse à ces changements. De manière contrastée, les tapis microbiens ont présenté des changements infra-annuels caractérisés par une croissance et un déclin apériodiques mais répétitifs. Leurs modes de développement n'ont pas pu être entièrement associés aux conditions environnementales mesurées, ni aux observations faites par imagerie. D'autres facteurs non-mesurables avec l'imagerie, y compris des interactions biotiques, pourraient être impliqués, incluant une consommation par les organismes brouteurs. En général, peu d'interactions biotiques ont été observées au cours des 7 ans de l'étude. La population de crabes *Segonzacia mesatlantica* occupait préférentiellement l'habitat des moules, mais aucune prédation n'a été observée. Les observations vidéo suggèrent que la compétition pour l'espace est le processus biotique majeur régissant la distribution des moules en fonction de l'habitat.

Les échelles de variation et les facteurs déterminant la variabilité environnementale ont été comparés à ceux régissant la variabilité des écosystèmes intertidaux. Sur la ride médio-atlantique, les assemblages de moules semblent connaître des conditions environnementales relativement stables, régulières, périodiques et modérées par rapport à leurs homologues côtiers. Les conditions infra-annuelles clémentes combinées à l'absence d'impact d'événements magmatique ou éruptif majeurs remettent en question notre perception sur la dynamique de l'environnement hydrothermal qui a souvent été considéré comme extrême et imprévisible suite aux expériences étudiant la recolonisation post-éruption (Tunnicliffe et al. 1997; Shank et al. 1998; Marcus et al. 2009).

Cependant, notre étude ne s'est focalisée que sur un assemblage hydrothermal localisé à la base de l'édifice de Tour Eiffel. L'absence de réplicas nécessite donc de vérifier les observations faites grâce à un suivi temporel à une échelle plus large (i.e. édifice). Cette approche permettra de considérer une plus grande diversité d'habitats. Le chapitre suivant présente donc une étude à l'échelle de l'édifice ayant pour but d'évaluer la dynamique temporelle de l'environnement et des communautés sur des échelles spatiales plus représentatives de l'hétérogénéité de l'habitat hydrothermal. L'utilisation de reconstructions photogrammétriques de l'édifice Tour Eiffel en 3D a permis un suivi spatio-temporel quantitatif plus précis que les méthodes classiques se basant sur des mosaïques d'images en deux dimensions (Cuvelier et al. 2011b; Sen et al. 2014; Du Preez and Fisher 2018). L'utilisation de mosaïques 2D ne permet pas de considérer le caractère tridimensionnel du substrat et donc de quantifier les changements à petite échelle sur des structures complexes. Dans le chapitre III, nous considérons les changements dans la distribution des différents assemblages en lien avec l'évolution de l'activité hydrothermale et les changements topographiques sur une période de 5 ans. L'imagerie sous-marine est une technique efficace pour élucider la dynamique spatio-temporelle des assemblages benthiques en eaux profondes et identifier les facteurs qui en sont responsables. Cependant, le manque de résolution des images 2D a longtemps empêché la caractérisation des processus à de fines échelles (~ cm à dm). L'étude du chapitre III utilise des annotations 3D réalisées sur une série pluriannuelle de reconstructions photogrammétriques afin d'acquérir un modèle de compréhension à une échelle fine de la dynamique de l'environnement et de la faune à l'échelle de l'édifice Tour Eiffel (champ hydrothermal Lucky Strike, dorsale médio-atlantique).

Chapter III

Pluri-annual monitoring of hydrothermal vent assemblages at the scale of the edifice

Monitoring ecological dynamics on complex hydrothermal structures: a novel photogrammetry approach reveals scales of faunal assemblage variability

Van Audenhaege Loïc[1]*, Sarrazin Jozée[1], Legendre Pierre[2], Perrois Garance[1], Cannat Mathilde[3], Matabos Marjolaine[1]

[1] *Univ Brest, CNRS, Ifremer, UMR6197 BEEP, F-29280 Plouzané, France*

[2] *Département de sciences biologiques, Université de Montréal, Montréal, Québec, Canada*

[3] *Université Paris Cité, UMR 7154, CNRS et Institut de Physique du Globe de Paris, France*

*__Corresponding author__: loic.van.audenhaege@ifremer.fr

Keywords: vent ecology, monitoring, photogrammetry, assemblage dynamics, regime of change, stability, succession

To be submitted to *Limnology & Oceanography*

Abstract

Imaging the seabed is an efficient technique to unravel spatio-temporal dynamics of deep-sea benthic assemblages. However, the lack of resolution of 2D images has long prevented the characterisation of the fine-scale processes (~ cm to dm) acting on the observed faunal variability. Hereby, we make use of 3D annotations performed on a pioneer pluri-annual time series of photogrammetric reconstructions to acquire a fine-scale model of comprehension of the dynamics of the environment and of the vent fauna at the Eiffel Tower sulphide edifice (Lucky Strike vent field, MAR). Over 5 years of monitoring, microbial mats underwent a general decline emphasising their lack of pluri-annual stability, possibly due to magmatic events previously detected over the vent field. The mussel cover was highly stable, hence extending the known stability of that climax population to 25 years. Environmental variability predominantly consisted in the decimetre displacement of the vent activity resulting from the opening or closure of vent exits or due to the progressive accretion of sulphide material on spire outcrops and flanges. Vent mussels predominantly underwent infra-metre variability in the immediate vicinity of vent exits. That variability was corroborated with the migration of mussels, repositioning in response to the fine-scale variability of the vent activity suggesting a regime change of low intensity. Successional patterns showed consistent small changes resulting in a dynamic equilibrium of the ecological system.

III.1 Introduction

For the past decades, there has been a growing interest in seafloor massive sulphide deposits (SMS) that build up over time as a result of particle deposition from the hydrothermal plume (Sánchez-Mora et al. 2022). As SMS exploitation could become profitable in the near future, impacts to the marine environment should be taken into account (Hoagland et al. 2010; Boschen et al. 2013). Understanding the natural dynamics of vent ecosystems is of utmost importance to assess community resilience and hence design management plans that mitigate the environmental impacts of deep-sea mining activities on these ecosystems (Van Dover 2014). The acquisition of ecological knowledge to explain and predict the behaviour of ecological systems requires the identification of the patterns and sources of variability observed in natural communities. This can be achieved by characterising changes in the spatial distribution of biological communities over time and linking the observed variability with the driving forces acting on multiple spatial and temporal scales (Sousa 1984a).

Hydrothermal vents are characterised by the emission of heated fluids at the seafloor in areas of intense tectonic and volcanic activities. Venting can occur in the form of black or white focused smokers or diffuse outflows characterised by different temperatures and concentrations of reduced minerals. The composition and strength of venting are strongly influenced by the nature of the rocks in the subseafloor, the geodynamical context of the region as well as the journey of seawater within the oceanic crust. This seawater is modified by chemical reactions and phase separation induced by magmatism as well as by the pathway of percolation and advection that influences mixing processes (Douville et al. 2002; Barreyre et al. 2014; Chavagnac et al. 2018). Vent ecosystems support lush and endemic communities that are characterised by low species diversity and exceptionally high biomass of species that are able to thrive despite the harshness of environmental conditions (Tunnicliffe 1991). Vent communities rely on chemoautotrophic microorganisms that harness energy from the oxidation of chemical compounds (H_2S, CH_4, Fe and H_2) contained in the fluids, a process called chemosynthesis (Jannasch 1985). The vent habitat is highly heterogeneous offering a variety of small-scale niches created by the vent dilution gradient (Podowski et al. 2009; Lee et al. 2015). Species distribution is mainly driven by their physiological tolerance and nutritional needs (Fustec et al. 1987; Henry et al. 2008; Moore et al. 2009; Podowski et al. 2009).

In addition to this spatial heterogeneity, the temporal dynamics interplays and contributes to the observed variability in ecosystems (Sousa 1984a). Temporal monitoring allows the building of successional models which are useful to predict the fate of faunal assemblages over time

(Odum 1969; Zajac et al. 1998; Mullineaux et al. 2009). At vents, the temporal dynamics, natural regime of disturbance and recovery potential can be monitored by considering a reference time after a disturbance event that sets communities back to an early stage of colonisation. For instance, volcanic events represent great opportunities to study faunal dynamics over broad scales after activation/deactivation of hydrothermal activity or lava eruption (Tunnicliffe et al. 1997; Shank et al. 1998, 2003; Marcus et al. 2009; Gollner et al. 2020; Mullineaux et al. 2020). A few authors observed the rapid recovery through different successional stages (Lutz et al. 1994, 2001). However, the observations of such destructive events remain limited to fast-spreading ridges. In the absence of large-scale resetting of faunal communities at slow-spreading ridges, the pluri-annual variability over large scales has been monitored under a continuous regime of venting (review in Glover et al. 2010). For the past decade, those study settings underlined the small spatial and pluri-annual temporal scales at which faunal assemblage dynamics occur on sulphide edifices (Copley et al. 2007; Gebruk et al. 2010; Cuvelier et al. 2011b; Sen et al. 2014; Du Preez and Fisher 2018; Zhou et al. 2018). By using optical imagery, such investigations enabled the detection of subtle redistribution of the fauna easily observable with photographs and proposition of successional models (Sarrazin et al. 1997; Cuvelier et al. 2011b; Sen et al. 2014). Imaging techniques are not destructive and thus ideal to monitor dynamics of vent fauna over large scales (Sarrazin et al. 1997; Juniper et al. 1998; Cuvelier et al. 2011b, 2012).

The first studies on the spatial distribution of the vent fauna were conducted using 2D high-resolution mapping (Fustec et al. 1987; Hessler et al. 1988; Sarrazin et al. 1997; Marsh et al. 2013; Du Preez and Fisher 2018). However, in the case of structures with complex topography, the detection of small-scale changes through the analysis of 2D images can be highly biased by the 3D perspective (e.g. Cuvelier et al. 2011b). The resulting decrease in the accuracy of scaled annotations, the precision of space-time continuity among observations and the detection of subtle changes, warrant the use of 3D representations. Structure-from-motion photogrammetry (SfM; Moulon et al. 2017) is an optical imaging technique that allows to build centimetre-resolution 3D mesh models of terrain using 2D images acquired with a standard camera mounted on an underwater vehicle (Kwasnitschka et al. 2013; review in Huvenne et al. 2018). As colour images can be projected over the 3D mesh, SfM is an ideal approach to perform high-resolution mapping of deep-sea benthic habitats and species distribution, measure quantitative biometrics and compute topographical or distance-based environmental descriptors (Robert et al. 2017, 2020; Gerdes et al. 2019a; Price et al. 2019; Girard et al. 2020a; Lim et al. 2020;

Mitchell and Harris 2020; Fabri et al. 2022). The use of photogrammetry surveys over time has been successful in monitoring centimetre-scale topographical changes in terrestrial and marine environments (Cucchiaro et al. 2018; Fugazza et al. 2018; D'Urban Jackson et al. 2020) such as forests (Honkavaara et al. 2013) or coral reef structures (Rossi et al. 2020). Furthermore, high-resolution imaging methods could help unravel subtle 3D processes of sulphide edifice building (Delaney et al. 2016) as an alternative to usual mineralogical investigations (Butler et al. 1998). However, despite their high resolution, deep-sea photogrammetry surveys have never been employed to investigate temporal dynamics over spatial scales greater than at the individual scale (Bennecke et al. 2016).

Since the discovery of the Lucky Strike hydrothermal vent field (LS) in 1992 (Langmuir et al. 1993), numerous studies at the Eiffel Tower sulphide edifice provided considerable knowledge on the fauna and vent ecology (Sarradin et al. 1999; Cuvelier et al. 2009, 2011a; Sarrazin et al. 2015; besides others). The temporal dynamics of Eiffel Tower vent communities was studied over various temporal scales, hence providing a robust knowledge on the drivers of vent faunal change over a wide range of temporal scales. Previous work captured the effect of infra-daily tidal modulation on vent mussels *Bathymodiolus azoricus* in addition to the effect of biological interactions (Matabos et al. 2015; Mat et al. 2020) and high stability of a mussel assemblage was highlighted over a small study area (Sarrazin et al. 2014; Cuvelier et al. 2017; Van Audenhaege et al. 2022). Repeated visits imaged a 14-year also suggested a certain stability of assemblages at the scale of the edifice over time (Cuvelier et al. 2011b) but the use of 2D imagery on such a complex structure limited the ability to quantify assemblage coverage and the ability to detect small changes.

This study aims at assessing and quantifying the temporal dynamics of the fauna and its environment on the Eiffel Tower sulphide structure, as well as bring new insight in the successional ecology of Lucky Strike vent assemblages. Based on previous studies (Cuvelier et al. 2011b; Girard et al. 2020a; Van Audenhaege et al. 2022), we expect a high stability in the distribution of faunal assemblages over time with small changes restrained to local venting discharges This work pioneers the use of time series high-resolution 3D models to retrieve accurate quantitative measurements and evaluate the fine-scale dynamics of hydrothermal ecosystems.

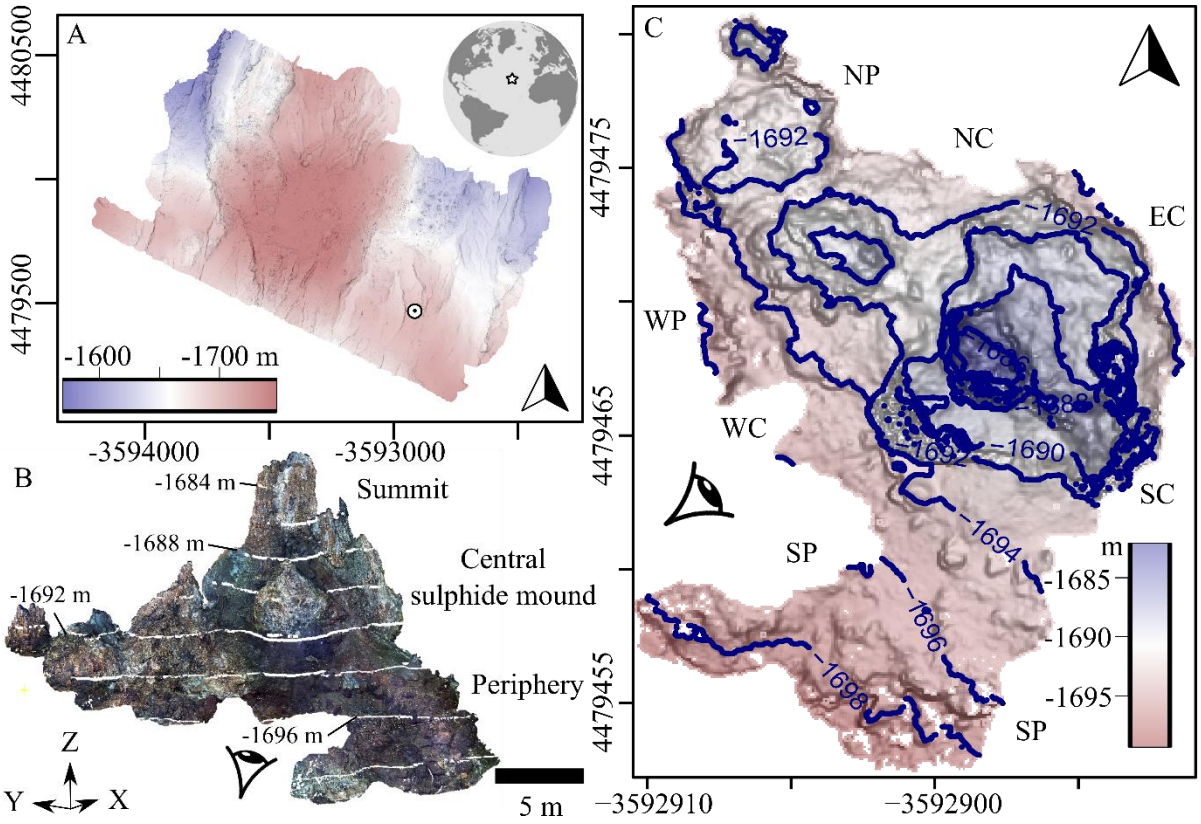

Figure III.1. (A) Bathymetric map of the Lucky Strike (LS) vent hydrothermal vent field (Ondréas et al. 2009). The star designates the location of LS in the upper-right inset of the Atlantic Ocean. The bathymetry is represented with a blue to red colour gradient. The circle locates the Eiffel Tower hydrothermal edifice at LS. (B) 3D textured model of Eiffel Tower in 2015. The regions of the summit, central sulphide mound and periphery are indicated. The orientation of the XYZ axes are provided by the arrows. Isobaths are delineated in white The eye indicates a common landmark with panel C. (C) Downward-looking bathymetric map of the 3D model of Eiffel Tower in 2015 with blue 2-m bathymetric isolines and a blue-to-red gradient. Large black & white arrows indicate the North. The "sides" are indicated with capital letters: e.g. NC = North Central (sulphide mound), NP = North periphery. All coordinates are plotted in metres (EPSG: 3857).

III.2 Material and methods

III.2.1 Study site

Lucky Strike (LS) is a basalt-hosted hydrothermal vent field located south of the Azores Islands of the Mid-Atlantic Ridge (MAR; Figure III.1A; Langmuir et al. 1993; Humphris et al. 2002). A deep-sea observatory (EMSO-Azores) has been deployed for over a decade on this field (Matabos et al. 2022). Since then, yearly maintenance cruises have provided the opportunity to gather additional time series data over a variety of disciplines providing new insights in geophysics (Crawford et al. 2013; Barreyre et al. 2014), geochemistry (Chavagnac et al. 2018), microbiology (Rommevaux et al. 2019; François et al. 2021) and ecology (Alfaro Lucas et al.

2020; Sarrazin et al. 2020, 2022; Marticorena et al. 2021). LS hosts Eiffel Tower, a mature hydrothermal edifice which comprises a central ~ 11 m-high sulphide tower harbouring focused venting activity surrounded by a mix of sulphide deposits and sulphide-indurated slab displaying numerous cracks and flanges (Wheeler et al. in prep.; Figure III.1B). The topography is complex with 5-m large bulbous topography distributed at the base of the main tower and inactive sulphide constructions located in the NW periphery (Figure III.1B-C). The fauna is characterised by patchy assemblages of vent endemic invertebrates occupying distinct habitats along the vent fluid dilution gradient (Cuvelier et al. 2009; Sarrazin et al. 2015; Husson et al. 2017). The vent shrimp *Mirocaris fortunata* occupies habitats more exposed to the vent fluids, close to anhydrite precipitation and sulphide deposits (Cuvelier et al. 2009; Sarrazin et al. 2015; Girard et al. 2020a). Assemblages of the symbiotic mussel *Bathymodiolus azoricus* are distributed further away from the vent exit, decreasing in size and density along the fluid dilution gradient (Cuvelier et al. 2009, 2011a). These mussels dominate the biomass of Eiffel Tower by ~ 90% and provide shelter to a variety of smaller associated species (Sarrazin et al. 2015, 2020; Husson et al. 2017). Those assemblages can be covered by white filamentous microbial mat dominated by sulphur-oxidising *Beggiatoa* Gammaproteobacteria which benefit from distal exposure to black smokers mediated by bottom current and edifice topography (Crépeau et al. 2011; Girard et al. 2020a). The crab *Segonzacia mesatlantica* resides in large mussel assemblages, likely preying on bactivorous preys or scavenging on dead material (Colaço et al. 2007; De Busserolles et al. 2009; Matabos et al. 2015). Dense aggregations of small unidentified zoanthids, arboramminid foraminifera, hydroids and empty mussel shells are observed in the coldest habitats (Desbruyeres et al. 2006; Husson et al. 2017; Girard et al. 2020a).

III.2.2 Building the dataset

The dataset aimed to investigate dynamics over two temporal windows with i) cm-resolution 3D reconstructions of Eiffel Tower (2015, 2018 and 2020) to which we aggregated ii) lower-resolution 2D photomosaics captured from various orientation from 1994 to 2008 (1994, 1998, 2001, 2002, 2005, 2006 & 2008; Cuvelier et al. 2011b). Data acquisition for the period 1994-2008 has been extensively detailed in Cuvelier et al. (2011b). Data for 3D reconstruction were acquired during the Momarsat 2015, 2018 and 2020 cruises (Cannat and Sarradin 2010). During the MoMARSAT cruises, video sequences were acquired by carrying out transects along the

Eiffel Tower edifice with a forward-looking camera mounted on the ROV *Victor6000* in April 2015 (duration = 4h20, definition = HD; Sarradin and Cannat 2015), August 2018 (5h14, HD; Cannat 2018) and September 2020 (3h17, 4K; Sarradin and Legrand 2020). The purpose of these video transects was to image the entire edifice from the summit to the base, by maintaining the ROV, as much as possible, at a constant pace and distance from the edifice to ensure transect overlap (i.e. at least 70% of image area). Images were extracted from video sequences every 3 seconds and colour corrected in *MATISSE* (v.1.4.0; Ifremer; Arnaubec et al. 2015). Those images were used to reconstruct 3 different textured meshes of Eiffel Tower for each year of survey (hereafter referred to as ET 2015, ET 2018 and ET 2020), using structure-from-motion (SfM) techniques embedded in *MATISSE*. The 3D reconstructions were georeferenced based on the ROV navigation to provide i) metric measurements of surface and ii) spatial alignment (i.e. registration) among 3D reconstructions. The ROV navigation consisted in a combination of the output of an ultra-short baseline system (USBL), a Doppler velocity logger (DVL) and a photonic inertial navigation system (PHINS). However, offsets larger than a metre were still observed between the 3D models, possibly due to variable quality of ROV navigation between dives and focal distortion in areas blurred by hydrothermal emission. As we were not able to clearly identify the causes of offset, we defined a post-processing methodology to improve registration down to an acceptable threshold, using ET 2015 as the reference (max. 20 cm). Although ET 2018 and 2020 cover a larger surface than ET 2015, only the area delimited by the latter was investigated (total area = 452 m²; Figure III.1C). ET 2018 and 2020 were divided in portions based on their cardinal orientation and position (i.e. either on the main tower or in the periphery) corresponding to the "sides" defined by Girard et al. in ET 2015 (2020; Figure III.2). Rotations, scaling and translations were applied sequentially in order to improve the registration of key topographic features: 1) manually and 2) using the ICP fine registration tool (CloudCompare v.2.11; Zhang 1994; Cucchiaro et al. 2018). If an offset of > 20 cm was still detected with the cloud-to-cloud distance tool of Cloud Compare (C2C), we repeated that operation on sub-portions of the sides. Furthermore, since "sides" defined by Girard et al. (2020; i.e. portions of 3D models) corresponded to the same area defined as "sides" in Cuvelier et al. (2011b; i.e. 2D photomosaic of forward-looking images), that division simultaneously allowed to assemble a 25-yrs image set. Photomosaics with less than 50% of overlap were not included in analyses (EC 1998, NP 2002 and 2005, SP, 2002 and 2006, WC 2002 and WP 2002; see Figure III.1C for acronym definition).

III.2.3 Annotation of the 3D models

In order to assess the variability observed at Eiffel Tower, the position of 3 types of observation was annotated: i) the substratum and biological assemblage cover, ii) the vent outflows and iii) the structural changes observed in Eiffel Tower.

The biological assemblage and type of substratum to annotate from 2015 to 2020 were defined based on categories provided by existing catalogues developed at Eiffel Tower (Cuvelier et al. 2011b; Girard et al. 2020a; see details of methodology in Suppl. Mat. 1). Two independent levels of annotation were performed: for "static" assemblages and substrata and for "mobile" species. Substratum and sessile benthic assemblages, possibly covered by microbial mats, were first annotated with polygons. Substratum categories were interpreted from their colour varying from black material (recent sulphide-bearing deposits), white material (anhydrite $CaSO_4$ and barytine $BaSO_4$ deposits possibly mixed with *Arcobacter* microbial communities; Taylor et al. 1999), or brownish bare substratum optionally covered by microbial mats (oxidised sulphide-bearing material, hereafter "bare substratum"). Biological assemblages included the symbiotic mussel *Bathymodiolus azoricus* from small (mean length ± SD: 1.15 ± 0.63 cm), medium (3.27 ± 1.49 cm), to large individuals (5.96 ± 1.44 cm), zoanthids and empty shells that could all be possibly covered by microbial mats (see in Girard et al. 2020a for catalogue and sizes). Still for "static" assemblages, erected white morphotypes that we could not differentiate between cladorhizid microcarnivorous sponge (e.g. *Asbestopluma* sp.) and arboramminid foraminifer *Luffammina atlantica* were annotated (Desbruyeres et al. 2006). Undetermined cover was annotated. For annotations of "static" cover, each polygon was labelled by the time series of the cover it contained each year (e.g. see Supplementary Method 1), such that ET was decomposed in a number of polygons which position and number was stable over time. Assuming structural stability of Eiffel Tower, this allowed to reduce annotation time and mitigate any bias induced by differences in agreement between annotators and progressive self-learning (Schoening et al. 2016). Annotation stopped when only stable bare substratum remained unannotated. The annotation of "mobile" organisms accounted for the cover of highly mobile organisms such as *Mirocaris fortunata* shrimps annotated with polygons and individuals of *Segonzacia mesatlantica* crabs and *Phymorynchus* sp. snails both annotated using point.

Using exclusively the ROV video sequences, we classified vent fluid outflows based on plume geometry, intensity and colour. They were relocated over the 3D models and labelled as points for focused vent, if the fluid was released from a discrete vent orifice, as points for diffusion

zones, if only shimmering water was observed, and as lines in the case of flanges. Focused vents were sub-categorised based on the colour of the venting fluid as i) “black smoker” or ii) “white smoker”.

Structural changes were annotated with polygons after detection of a net modification in the mesh surface between 3D models. The process involved was specified from two main criteria: i) if some material was lost or built up and ii) if the change involved material either exposed to venting at least recently (black or white material) or that remained inactive (brown bare substratum). Those changes were documented with screenshots of video sequences (Supplementary Figure III.1 to Supplementary Figure III.5).

All 3D annotations were performed on the 3D mesh following interpretation of textures, colour and disposition by loading simultaneously the ET 2015, 2018 and 2020 as layers in the software *3DMetrics* (v.0.6.0; Laranjeira et al. 2020). All annotations were systematically confirmed with ROV video sequences. Polygon/point/line labelling, XYZ coordinates of the vertices and 3D surface/length computed by *3DMetrics* were extracted in *.json* files.

Polygon cover from 1994-2008 consisted in the same categories annotated from 2015 and 2020 and were performed by Cuvelier et al. on photomosaics of the sides of Eiffel Tower (2011b). Polygon annotations were saved in *.psd* files that were transformed to *.png* images. As pixels of the *.png* images were given a RGB signature based on their assigned categories, the number of pixels exhibiting each category-specific RGB code was summed in Python (v. 3.7.4).

III.2.4 Estimation of registration uncertainty

Alignment (i.e. registration) errors among 3D models were assessed with three measurements of distances in order to validate the post-processing registration. Firstly, we created 30 ground points equispaced by 4 m and randomly distributed over ET 2015. They were visually matched from ET 2015 to their homologue points in ET 2018 and 2020 in 3DMetrics from which we calculated the Euclidean distance between all possible pairs (Cucchiaro et al. 2018). Registration uncertainty was also assessed using the C2C and the M3C2 tools of CloudCompare based on point clouds acquired from 3D models (density = 1 point/mm; Lague et al. 2013; James et al. 2017). Results are presented as mean ± SD of point distances as a measure of registration accuracy and precision (Cucchiaro et al. 2018).

III.2.5 Data analyses

As polygons are not a standardised unit of sampling, they were aggregated following three spatial scales: edifice, sides and 1.7-m² tiles. From 2015 to 2020, dynamics was firstly investigated at the edifice scale to retrieve the general patterns of temporal change by summing the cover for each category. In addition, the total cover of polygon that changed or did not change by categories and among time steps was used as a proxy for assessing the spatial variability of cover. Furthermore, the total cover that changed from one annotation category to another was used to investigate directional changes among categories aiming to compute a succession model based on quantitative data.

In order to investigate quantitative spatial changes from 2015 to 2020, we pooled polygons in 200 tiles which size corresponded to the area of the largest polygon annotated over all models (i.e. $\mu \pm SD$: 1.79 ± 0.35 m²). This operation allowed to standardise sampling units for further statistical analyses. To this end, polygons containing undetermined cover and stable bare substratum were discarded. Analyses on microbial mat dynamics were made independently as they can occur with the rest of "static" assemblages and substrata, by covering them. As the pooling operation was coded to take into account the spatial proximity among polygons, tiles always formed continuous areas over space. To locate tiles over Eiffel Tower, their XYZ centroid was computed as the surface weighted-mean of each tile's polygon centroid (i.e. itself being the mean of its vertices' coordinates). Annotations of "mobile" organisms (i.e. shrimp cover and abundance of crabs and snails) were assigned to tiles based on their proximity to the tile's polygons. This provided a community matrix containing squared-meter cover data (i.e. tiles x categories) for each time step in 2015, 2018 and 2020 that could be easily handled for further analyses. Firstly, the total surface of all polygons of "static" cover that changed within a tile was computed and mapped over the edifice. Secondly, the net change of cover for each category was computed by tile, by subtracting the surface occupied in t_i from that of t_{i+1}. These were mapped in space for each category of cover separately. However, by computing a net change at the scale of a tile, those maps only represented a fraction of the total variability occurring within polygons. To provide an idea of that uncertainty, we computed the fraction of the total variability of polygons rendered in maps, and averaged it for all 3 combinations of time steps (2015-2018, 2018-2020 and 2015-2020).

The annotation protocol was detailed in Supplementary Material III.1. Any faunal or structural change was confirmed by visual observations made in the temporal series of the 3D models are provided in Supplementary Material III.2.

In order to assess patterns of variability in tile composition, a principal component analysis (PCA) was applied on a full community matrix of "static" assemblages and substrata, containing 600 rows after combining the 3 community matrices for 2015, 2018, 2020. Each row (i.e. combination of tile and year) was divided by the total surface of the tile and squared-rooted to correspond to a Hellinger transformation. As the observations displayed a clear arch known to represent a gradient from low to high vent exposure in the dataset, we fitted a quadratic regression over the first two principal component axes to model that gradient. Regression parameters were tested for significance ($\alpha = 0.05$). Each tile got assigned a position based on the nearest point of that regression (interpolation iteration = 0.001) that represented the position along the gradient from 0 (= coldest) to 100% (= warmest). Microbial mats and mobile species were also repositioned on that gradient. Furthermore, we computed the net change of position along the gradient from 2015 to 2020.

Trajectory analyses were computed to test for pattern of variability for "static" cover categories (Legendre and De Cáceres 2013; De Cáceres et al. 2019; Legendre 2019). They were plotted over the edifice for detection of any spatial trend (Sturbois et al. 2021). Further multivariate analyses were conducted in order to identify any drivers of cover change, based on the distance from 5 types of features being i) topographic changes and ii) the four types of hydrothermal outflows (i.e. black and white smokers, flanges, diffuse zone). Exposure to those features was modelled considering two types of spatial influence: local or distal. To account for local influence, the number of vent exits/topographical changes located within the tile were counted (i.e. being the closest tile centroid from the feature). If the feature was not within a given tile, the inverse distance from that tile centroid was computed to account for the distal influence. Local and distal were summed for each variable independently. We computed a redundancy analysis (RDA) and multivariate regression tree (MRT) on square-rooted relative cover of tiles with those environmental variables scaled between 0 and 1 (De'ath 2002; Borcard et al. 2018). Further information on the methodology and R code is detailed in Supplementary Material III.3.

The evolution over 25 years was restricted to the whole population of mussels (i.e. all sizes) and microbial mats. However, as covers were in pixels (1994-2008) and in squared metres (2015-2018), they were standardised by dividing with the total surface annotated for each side in order to obtain a proportional cover. For photomosaics (1994-2008), the total surface

represented the total number of pixels annotated. For portions of 3D models (2015-2020), it represented the total surface contained in the 3D mesh. A univariate regression tree (URT) was applied to detect breakpoints in the time series (De'ath 2002).

III.3 Results

III.3.1 Registration accuracy

The distance among pairs of 3D models rarely exceeded 0.15 m following ground points (mean ± SD = 0.06 ± 0.05 m, 95% = 0.14 m), C2C (0.03 ± 0.04 m, 95% = 0.11 m) and M3C2 distances (0.05 ± 0.10 m, 95% = 0.16 m).

III.3.2 Habitat changes

Table III.1. Characteristics of the topographical changes observed over 5 years of monitoring at the Eiffel Tower hydrothermal edifice (total area = 452 m²). The net change is either positive (+; material accumulation) or negative (-; material loss) and involves (recently) active and inactive substrata. The surface that underwent change was computed with *3DMetrics* and the process and features involved were visually interpreted (see Supplementary Figure III.1-Supplementary Figure III.2-Supplementary Figure III.3-5). The number of observations (n) is indicated in parentheses.

Net change	**Hydrothermal activity**	**Total surface that underwent a change [m²] Number of features in parentheses**		**Process inferred from observations**
		2015-2018	2018-2020	
+	Active	0.36 (11) 3.95 (31) 1.57 (19)	0.39 (9) 3.41 (26) 0.68 (11)	Vertical accretion of spires Lateral/downward accretion of 3D outcrops Forward & downward accretion of linear features (flanges & screed-like)
	Inactive	1.38 (19)	0 (0)	Debris building up at the base of the edifice as scree or chimneys fragment
	Total	*7.26*	*4.48*	
−	Active	0.86 (21) 0.08 (1)	0.37 (10) 0.08 (2)	Chimney collapse Outcrop detachment
	Inactive	2.01 (18)	0 (0)	Boulder detachment or scree displacement
	Total	*2.95*	*0.45*	
All	*Total*	*10.21*	*4.93*	

Changes in topography – The highest rate of topographic change occurred between 2015 and 2018 and involved a total area of 10.21 m² accounting for 2.26% of the surface of ET 2015

(Table III.1). Areas undergoing a build-up of material were always twice as large as those of material loss.

Between 2015 and 2020, 64% of the areas displaying a net positive change were related to hydrothermal activity, being the directional growth of active geological features such as 3D outcrops, or flanges features overhanging or blanketing the seabed (Table III.1; Supplementary Figure III.1-Supplementary Figure III.2-Supplementary Figure III.3). For flanges, we were able to determine an average rate of displacement reaching up to 10.6 cm.yr^{-1}. Voluminous changes at the base of large bulbous outcrops were related to the accretion of material in areas from which shimmering water was emitted (categorised as "flanges"; e.g. Supplementary Figure III.4). Except for vertical spires, active features rarely collapsed (Table III.1). Often located on top or sides of bulbous outcrops (Supplementary Figure III.3-Supplementary Figure III.4), spires made of black friable sulphide underwent repetitive growth and collapse. Changes of recently active substratum occurred in a few localities and persisted over time from 2015 to 2018 and from 2018 to 2020 (Supplementary Figure III.5). The largest change of inactive substratum was related to the fall of a large boulder from a vertical face (0.84 m²; Supplementary Figure III.6). Changes over inactive substratum occurred predominantly in 2018 and were largely restricted to the western periphery of the edifice (Supplementary Figure III.5).

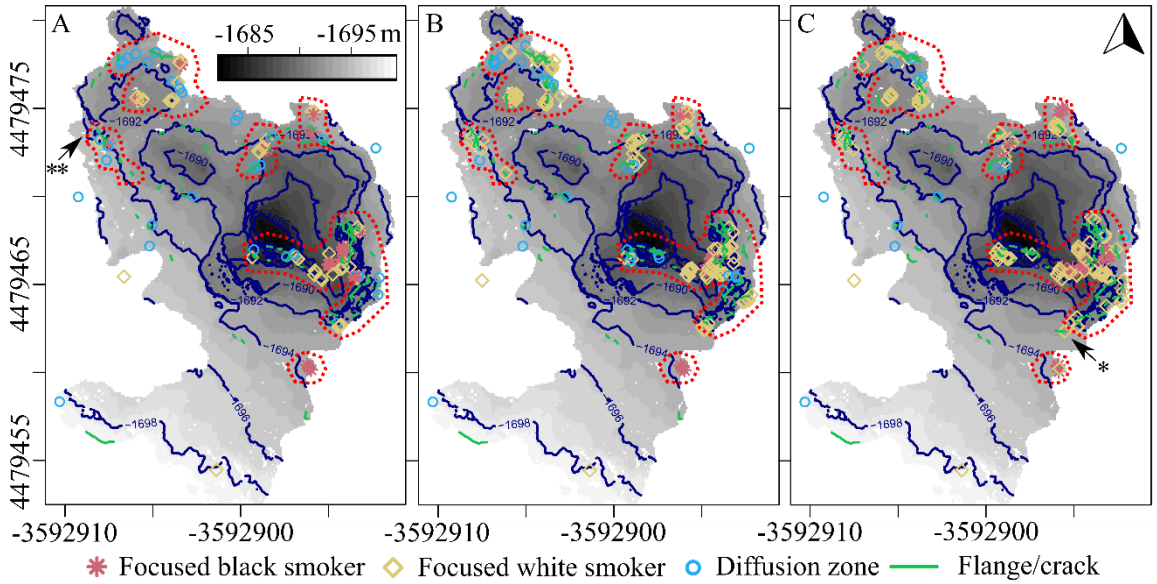

Figure III.2. Bathymetric maps positioning and describing the variability of venting features over the Eiffel Tower edifice in (A) 2015, (B) 2018 and (C) 2020. Red dotted polygons delimit hydrothermal areas harbouring a continuous spatial aggregation of venting features identified based on ROV video sequences. A black star indicates the position of hydrothermal precipitate emerging from the soft sediment observed in Supplementary Figure III.4. The double star indicates the position of the fall of the large boulder (Supplementary Figure III.6). Bathymetry is provided by the 2015 3D model, with 2-

m isolines and a black to grey colour gradient. Coordinates are provided in the metric Mercator CRS (EPSG = 3857). The arrow indicates north.

Changes in the distribution of venting features – Changes in the position of venting features occurred at small scales (cm to dm; Figure III.2), especially for hydrothermal chimneys and directional accretion of material (Table III.1; Supplementary Figure III.1-Supplementary Figure III.2-Supplementary Figure III.3). As they occurred within small venting clusters, there was no significant displacement of activity when considering larger clusters of activity harbouring locally dense aggregations of hydrothermal outflows (Figure III.2). Those clusters of activity consisted in a mix of diffusion zones, white and black smokers often interspaced with flanges and screed-like features. The largest cluster of activity was located in the south-east of Eiffel Tower (Figure III.2). In its vicinity, we observed the activation of a vent outflow with hydrothermal anhydrite clearly emerging from a soft sediment talus (Supplementary Figure III.7). Counted black smokers were variable from 2015 (n = 31), 2018 (17) and to 2020 (39). Overall, the number of white smokers doubled from 2015 (50) to stabilise in 2018 (112) and 2020 (119).The amount of flanges slightly increased from 70, 87 and 89 in 2020. Diffusion zones were stable from 2015 to 2018 (33 to 37) and dropped in 2020 (17).

III.3.3 Faunal and substratum spatio-temporal dynamics

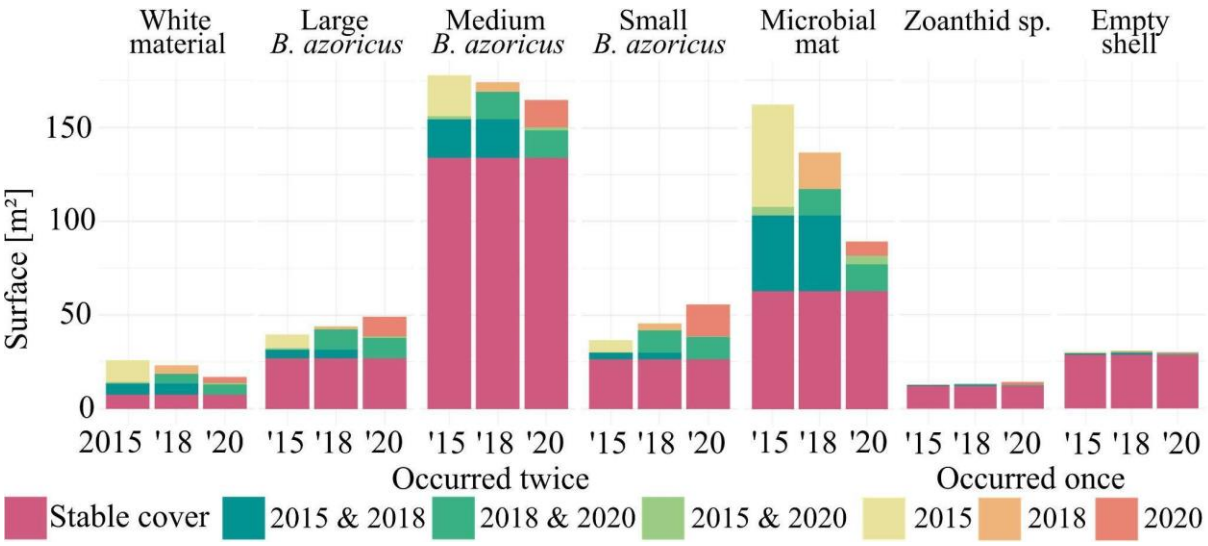

Figure III.3. Barplots of the total cover [m²] of assemblages and substrata for each year of monitoring (2015, 2018 and 2020). The colours correspond to the portion of the total cover that underwent a change: i) red being the cover of polygons that never changed, ii) dark to light green being the polygons that were occupied twice by a given assemblage and iii) yellow to orange being the surface of polygons that were only occupied once. Due to the low surface occupied by erected morphospecies and black amorphous sulphide (≤ 2 m²), they were not presented therein.

On average, the total area covered by all mussel assemblages reached 262.84 ± 7.50 m², representing 58.15% of the total surface of the edifice (Figure III.3). While the more abundant medium-mussel assemblage slightly decreased from 2015 to 2020 (−13.29 m²), the surface occupied by large and small-mussel assemblages increased gradually by 2020 of + 9.36 and + 18.8 m² respectively. Despite little change in total cover for each category over time, a substantial amount of polygons of large (45.05%), medium (32.33%) and small (52.29%) mussel assemblages underwent a modification from 2015 to 2018 or from 2018 to 2020. For all mussel sizes, modification of polygon occupancy was gradual since the occupancy was rarely exclusive to 2018 (< 3%; Figure III.3). Microbial mat cover varied the most with a 44.92% decline in five years (−72.84 m²). From the surface covered by microbial mats annotated initially in 2015, 38.75% never disappeared in 2020 and accounted for 70.36 % of the microbial mats present that year (Figure III.3). Zoanthid assemblages remained highly stable over time and persisted over an area of 12.01 m² until 2020 (83.17% of their total cover). Empty shell deposits remained highly stable over space and time (Figure III.3). Erected sessile morphotypes remained rare, but stable (Mean ± SD = 1.88 ± 0.22 m²; not represented in Figure III.3). The white hydrothermal material covered 22.06 ± 4.49 m² and only 33.60% persisted spatially over 5 years (Figure III.3). The black "amorphous" material was usually restricted to the immediate vicinity of focused emissions, representing up to 2 m² with only 10.07% that persisted over 5 years in the same polygon (not represented in Figure III.3).

Successional patterns were highly conservative over time (Figure III.4). Between 2015-2018 and 2018-2020, succession among biological assemblages occurred on an average surface of 28.75 m², representing 6.36% of the total area investigated. The majority of those transitions involved medium *B. azoricus* assemblages (90%). Succession between large and small mussels was extremely rare (< 0.5 m²). Transition between biological assemblages and substrata involved ~ 31.09 m². Approximately 63.01% of that surface transitioned between bare substratum and mussel assemblages while 32.00% transitioned between white material and mussels. An average of 9.41 m² only involved change in substratum with a large part (78.63%) of it being between white material from/to bare substratum. Finally, temporal changes involving areas covered by black substratum, zoanthids or empty mussel shells were not frequent (Figure III.4).

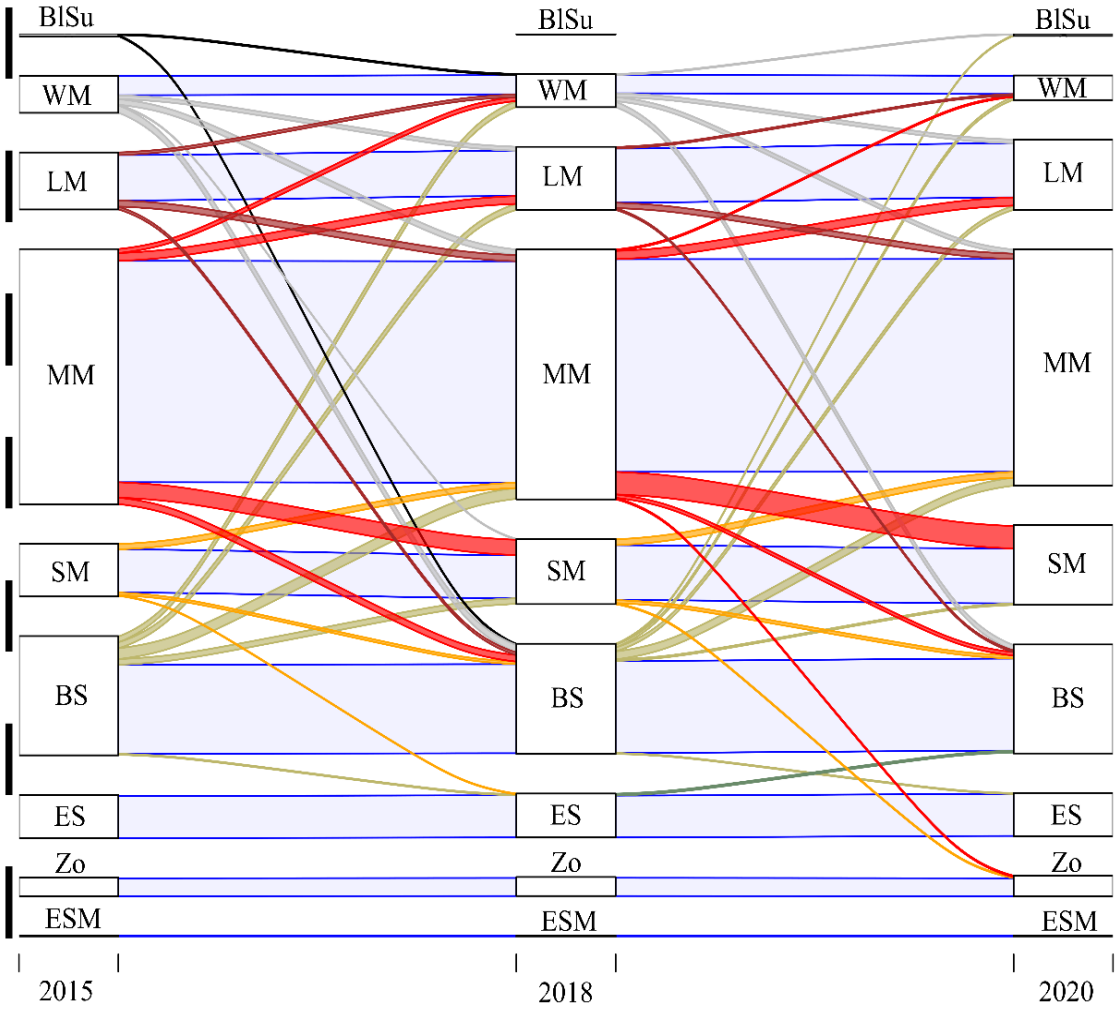

Figure III.4. Sankey diagram describing patterns of assemblage succession for all polygons annotated on 3D reconstructions of Eiffel Tower in 2015, 2018 and 2020 (i.e. the stages). White rectangles (i.e. the nodes) correspond to assemblage cover at given stages. Coloured segments (i.e. the flows) describe the successions occurring from a given node at stage $_{(t)}$ to others at stage $_{(t+1)}$. When no change was observed, the flow is coloured in light blue. The vertical black bars scales the size of the nodes and flows at 50 m². Only flows ≥ 0.5 m² were represented. The full diagram was drawn in Supplementary Figure III.8. BlSu = black amorphous sulphide, WM = white material, LM = large mussels, MM = medium mussels, SM = small mussels, BS = bare substratum, ES = Empty shell, Zo = zoanthid sp., ESM = erected sessile morphotype.

Change of polygon of "static" cover from 2015 to 2020 accounted for 24.23% of the edifice (114.35 m²). A large share of that change occurred in the venting cluster located in the south-east central sulphide mound (47.24%; Figure III.5). The remaining variability strongly coincided with the position of hydrothermal venting clusters spread around the Eiffel Tower edifice (Figure III.5).

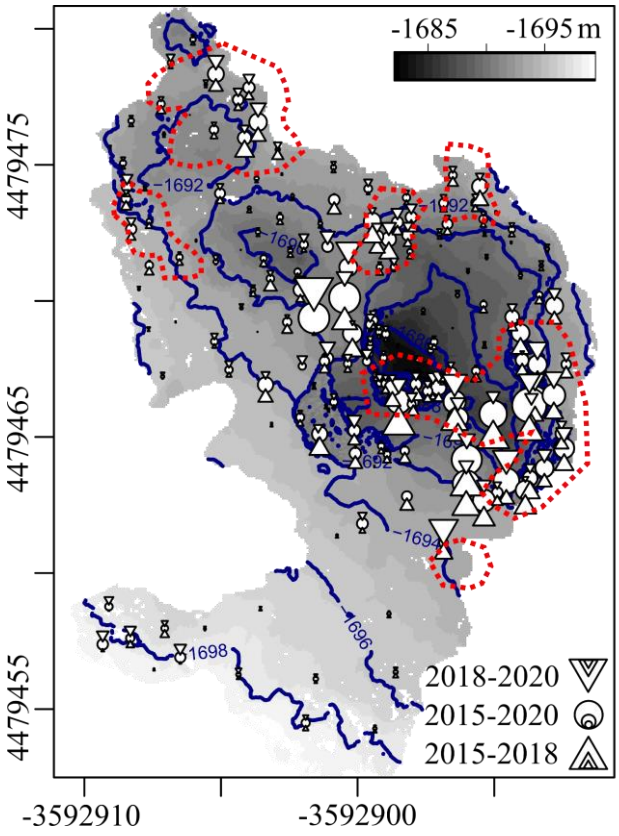

Figure III.5. Total area of polygons displaying cover variability within a tile. Microbial mats were not included in the calculation. The circles represent the total change from 2015 to 2020. Upward/downward triangles represent changes from 2015-2018/2018-2020 respectively. Symbols nested with different sizes in the legend represent changes of 0.5, 1 and 2 m². Red dotted polygons delimit hydrothermal areas harbouring a continuous spatial aggregation of venting features identified based on ROV video sequences (see Figure III.2). Bathymetry is provided by the 2015 3D model, with 2-m isolines and a black to grey colour gradient. Coordinates are provided in the metric Mercator CRS (EPSG = 3857).

For mussel assemblages, the computation of assemblage net change by tile rendered from 68 to 83% of the total polygon variability of each mussel assemblage (Figure III.6A-B-C). In other words, this means that less than 32% of change was overlooked by computing net change of assemblage cover change by tiles. Large *B. azoricus* distributed in a few delimited patches on the edges and top of the edifice (Figure III.6A). They were highly stable except for the SE assemblage that underwent an increase of + 5.64 m² starting from the left in 2018 and progressing to the right in 2020 over a continuous area (Figure III.6A; Supplementary Figure III.9). This change accounted for 60.26% of the net increase of large mussel assemblages from 2015 to 2020 over the edifice (Figure III.3).

Medium mussels were widely distributed over the whole edifice as well as in the southern periphery (Figure III.6B). Overall, medium-mussel assemblages were stable through space and time as changes remained constrained to isolated groups of polygons in the central and south-east part of the edifice.

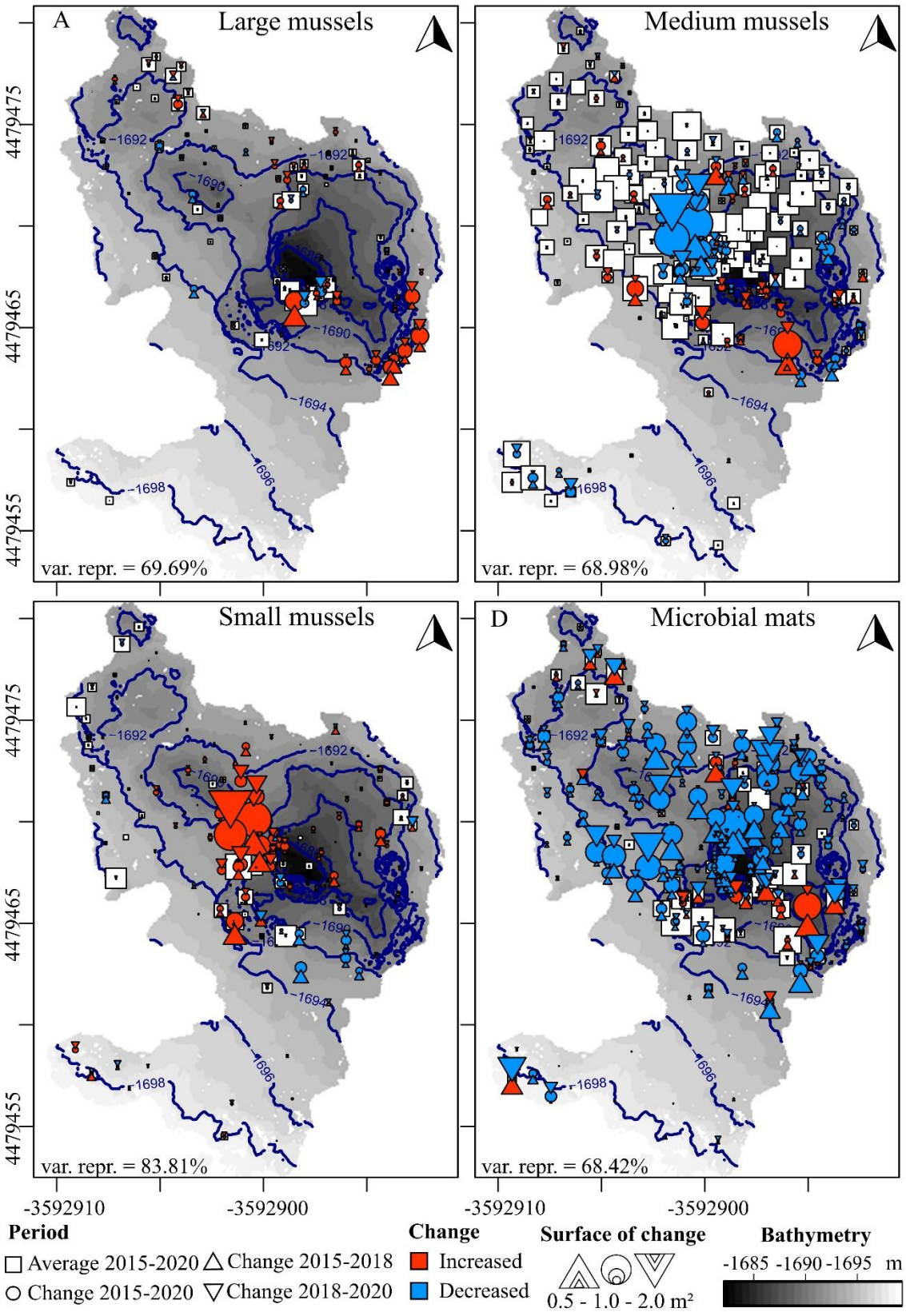

Figure III.6. Net change in biological assemblages and within tiles of (A) large mussels, (B) medium mussels, (C) small mussels and (D) microbial mats. A square represents the average assemblage cover over the three observation years in a given tile. The circles represent the total change from 2015 to 2020. Upward/downward triangles represent changes from 2015-2018/2018-2020 respectively. The size of nest symbols represents the size of the changing surface (0.5-1-2 m²). If it increased/decreased, they are

plotted in red/blue. Squares were plotted under the circles in order to underline in a given tile the presence of communities that were stable (i.e. the white square is visible) or that were completely gone in 2020 (i.e. the white square is not visible anymore since fully overlaid by a blue circle). "var. expl." refers to the fraction of variability rendered by those maps compared to the total surface of polygons that changed. Cartography of total polygon variability is provided in Figure III.5. Bathymetry is provided by the 2015 3D model, with 2-m isolines and a black to grey colour gradient. Arrows in the upper-right corner of each map indicate north. Coordinates are provided in the metric Mercator CRS (EPSG = 3857).

The largest change was a decrease in the centre, near the summit (-10.97 m² in Figure III.6B; Supplementary Figure III.10) that represented 82.54% of the net decrease of the medium-mussel assemblage from 2015 to 2020 (Figure III.3). In the South-East, a local increase in medium mussel cover coincided with a large mussel cover increase and the emergence of a circular white hydrothermal material from soft sediment the recent opening of hydrothermal outflow there (Figure III.6A-B; Supplementary Figure III.7 & Supplementary Figure III.11).
Small mussel assemblages were patchily distributed on the edifice except for the central part of the structure near the northwest side of the summit where they covered a large area (Figure III.6C). The largest change occurred in that area with a continuous cover increase from 2015 to 2020 (+11.43 m²; Figure III.6C), which represented 60.83% of the net increase observed over the whole edifice from 2015 to 2020 (Figure III.3). It coincided with the largest decrease in medium-mussel assemblage (Figure III.6B; Supplementary Figure III.10)

Microbial mats formed an extensive cover in 2015 over a large continuous area (162.16 m²; Figure III.6D). The cover continuously declined from 2015 to 2020 especially in the West and North of the central mound and in the summit of the edifice (−72.85 m²). Increase was rarely observed and the remaining mats formed a patch in the South in 2020 (Figure III.6D). The distribution of other assemblages (*M. fortunata*) and substrata (white material/black sulphide/empty shells) is provided in Supplementary Figure III.12. Their distribution was sporadic and changing over time. Empty shells deposited in a continuous area of the southern periphery and showed no sign of change (Supplementary Figure III.12). *Phymorynchus* occurred in a single area, occupying the bare substratum a few decimetres away from mussel assemblages (pers. obs.).

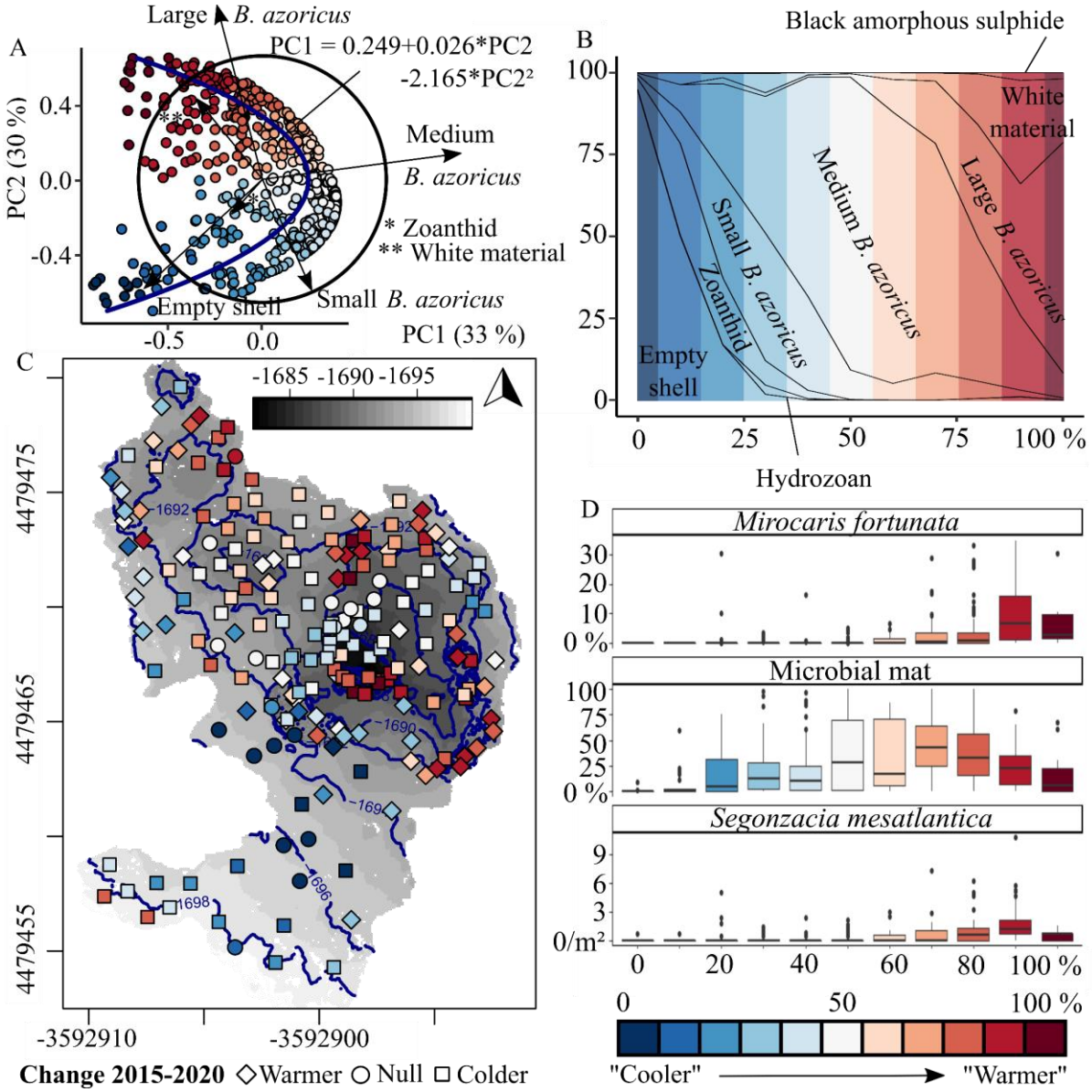

Figure III.7. Investigation of ecological dynamics along the tile composition gradient retrieved from a principal component analysis (PCA). That gradient is displayed in all panels with a blue to red colour scale referring to "colder" to "warmer" habitat categories along a tile composition gradient expressed as a percentage over the interpolated points of the regression (resolution = 0.1%). (A) The first two principal components (PC) (63% of variance explained) showing an "arc-like" gradient of tile composition in assemblages and substrata. The circle of correlation is plotted. Arrows display the most contributing categories. The blue parabola is the fitted quadratic regression performed on the PC1-2 space. Each tile got assigned a position in 2015, 2018 and 2020 along that regression. (B) Average composition of tiles along the tile composition gradient, with assemblages used in the PCA (Figure III.6A). (C) Mapping of the average 2015-2020 tile composition represented as circles/squares/diamonds if the change was null or tended to colder/warmer assemblages respectively. The map is plotted in a downward-looking view of the Eiffel Tower topography of 2015. The topography is shown with a black and white colour scale provided by the 2015 3D model. Bathymetric isolines in dark blue every 2 m. Coordinates are provided in the metric Mercator CRS (EPSG = 3857). (D) Boxplots of the distribution of biological categories along the tile composition gradient. Those categories were not included in the PCA (Figure III.6A). Covers of *Mirocaris fortunata* and microbial mats are expressed relatively to the tile cover. *Segonzacia mesatlantica* crabs are expressed in densities [ind.m^{-2}].

The cartography of average position underlined the presence of "warmer" assemblages on the northern and eastern edges and on the summit of the edifice (Figure III.7C). The position of "warm" tile communities coincided with clusters of hydrothermal activity delineated in Figure III.2. A large share of tiles with cool-to-intermediate composition can be found extending from west to east over the main edifice. Most of them became colder between 2015 and 2020. Tiles of the southern periphery were predominantly represented by colder assemblages compared to that of the main summit (Figure III.7C). A few tiles underwent strong compositional change in 2 to 3 years. Those tiles corresponded to particular events of change underlined in Figure III.6. Of all tiles, 32% got "warmer" and located mostly in a few areas with warm assemblages. Tiles that got "colder" from 2015 to 2020 accounted for 58% and represented a large continuous area of the sulphide mound and periphery (Figure III.7C). Although not included in multivariate analyses, tile cover proportion of *M. fortunata* and densities of *S. mesatlantica* increased in relation to "warmer" assemblages (Figure III.7D). Microbial cover occupied a variety of habitats along the assemblage gradient, but seemed to favour "intermediate" assemblages (Figure III.7).

As the results of multivariate analyses were redundant in the case of the MRT and trajectory analysis or mostly described spatial patterns of distribution and not temporal changes for RDAs, we provided these analyses in Supplementary Material III.3. The methodology could be reused for further 3D monitoring.

25 year time series – Mussel total cover ranged from ~ 45 to 55% despite high variability across edifice sides (Figure III.8A). The URT depicted a breakpoint between 2008 and 2015. Microbial mat cover was much more variable, ranging from ~ 15 to 45% in average over 25 years (Figure III.8B). However, standard deviations were less variable than for mussel cover depicting lower spatial heterogeneity of cover among sides (Figure III.8). The URT identified breakpoints between 1998 and 2001 and between 2015 and 2018. After 2001 the cover tended to stabilise following an average increase of ~ 30% until 2015 after which it dramatically declined (Figure III.8).

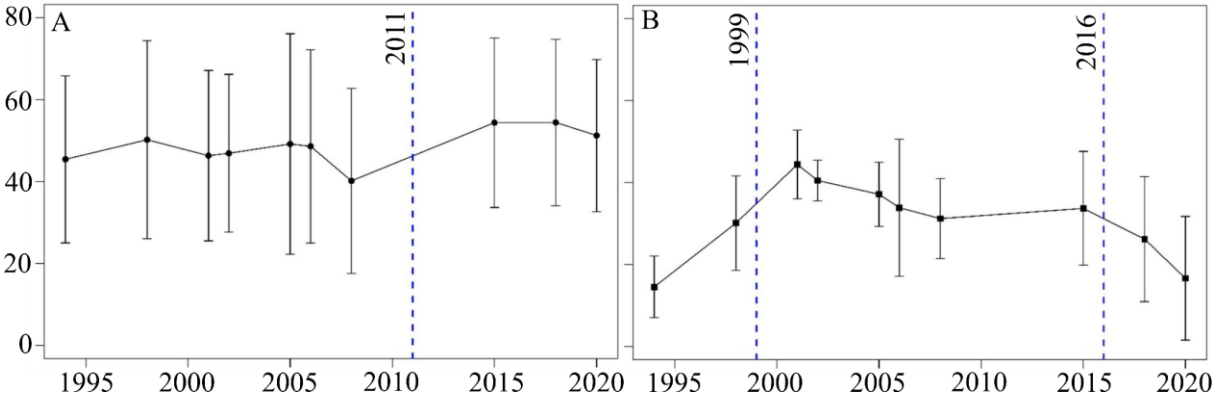

Figure III.8. Mean relative cover [%] of Eiffel Tower assemblages for (A) mussels (sum of small, medium and large mussels) and (B) microbial mat cover. Points represent the average assemblage cover computed between edifice sides for each time step from 1994 to 2020. Whiskers are the associated standard deviations of assemblage cover among sides. The blue dashed lines represent breaking points detected by the univariate regression tree (URT) analysis.

III.4 Discussion

Using a temporal series of 3D models, this study described the variability of assemblage cover in space and time, from the whole edifice to the tile scale, and over a complex sulphide edifice in the deep sea. To our knowledge, this study is the first to apply 3D quantitative techniques to resolve the fine-scale dynamics of hydrothermal vent communities. As a result, it sets a methodological and analytical baseline workflow to unravel processes at scales rarely approached in the past.

III.4.1 Limitations

We obtained a maximum of 15 cm error in spatial resolution, demonstrating the usefulness of the high resolution provided by 3D models. Although higher compared to terrestrial studies that used unmanned aerial vehicles (UAVs; e.g. M3C2 distance: max. 0.08 ± 0.08 m in Cucchiaro et al. 2018), this result is a real achievement in a deep-sea context where the acquisition of imagery is constrained by a number of technological challenges. Indeed, drifts in ROV navigation accuracy and precision among dives and years can contribute to increase registration errors (Boittiaux et al. in prep.). With ongoing technological improvements in navigation systems, this approach will become more accurate over the coming years, although we noticed that areas exposed to venting can locally affect the reconstruction resolution.

Uneven image acquisition could also alter the accuracy of temporal monitoring, because of i) uneven distances of the ROV from the edifice across years, ii) differences of image sharpness due to changing turbidity, or iii) change in camera resolution from HD to 4K (between 2018

and 2020). This led to heterogeneous resolution of 3D meshes over models and among years which may ultimately alter the accuracy of centimetre-scale measurement of surfaces. Although the footprint of the image is larger, the identification of small features in video sequences or 3D models is ultimately biased (Schoening et al. 2016; Thornton et al. 2016). In our case, this makes uncertain the detection of shimmering outflows and of the small fauna (e.g. *M. fortunata*, *Peltospira smaragdina*). The use of pre-programmed tracks may be the only way to overcome uneven sampling. It remains to be implemented for deep-sea 3D features (e.g. for UAVs: Fugazza et al. 2018).

Finally, changes detected between the year 2008 and 2015 may also correspond to the methodological switch of method from 2D images to 3D reconstructions. Further work is needed to homogenise both time series.

III.4.2 Edifice habitat dynamics

Topographic changes occurred mostly in areas restricted to the close vicinity of hydrothermal outflows because of the precipitation of minerals. Rapid formation of friable chimneys and spires, their collapse and incorporation into the structure were proposed to be one of the processes through which sulphide edifices grow out and upward (Butler et al. 1998). However, as those were highly difficult to track in space and time, the evaluation of this process was limited to sporadic observation of debris accumulating at the base of Eiffel Tower that may contribute to build the sulphide talus (Hannington et al. 1995). However, visual inspection did not suggest a change in soft sediment piles at the base of Eiffel Tower, built up by the deposition of hydrothermal particles (Butler et al. 1998); thus infra-decadal time scale would not be long enough to detect change in the talus thickness. Instead, we hypothesise that the outward growth of the edifice occurs mostly through directional accretion of hydrothermal features such as flanges and outcrops. As the accretion proceeds, the apparent switch from white material to consolidated and oxidised material was observed similarly to other temporal monitoring using images (Cuvelier et al. 2011b; Du Preez and Fisher 2018). As the collapse of oxidised material was only sporadic, it suggests that the bare substratum may sustainably persist over years. Over the longer term, those features may slowly contribute to the building of the edifice. In particular, the large bulbous outcrops that exhibit dense concentration of focussed and diffuse outflows may contribute significantly to the large-scale development of Eiffel Tower (this study; Cuvelier et al. 2011b). Nevertheless, our temporal monitoring is no more than a drop in the

development history of Eiffel Tower knowing that the oldest trace of hydrothermal activity have been dated back to ~ 650 years ago (Sánchez-Mora et al. 2022).

Venting clustered in a few areas of several square metres containing flanges, diffusion zones and focused emissions and were located on the edges of the summit of Eiffel Tower: southeast, north and northwest. The spatio-temporal stability of venting clusters suggests the absence of major redistribution events of venting activity. Considering the change in tile assemblage composition, with assemblages evolving towards colder composition, we confirmed a subtle but generalised trend of cooling over the edifice except in the east side of Eiffel Tower. This trend is supported by the decline of microbial mats in similar areas. One explanation may reside in the decrease in diffuse outflows over the edifice between 1996 and 2009 that led to hypothesise the activity in the Eiffel Tower area to be declining (Barreyre et al. 2012). Although confirmation over a longer time window is needed, this suggests that change in assemblages may be used as indicators of changes in the overall vent activity of an area.

Considering finer scales, repositioning of vent exits remained predominantly constrained within clusters. These changes could be due to topographic modification by progressive mineral precipitation, feature collapse or even to subsurface clogging by mineral precipitates (Humphris et al. 1995; Tivey 1995). Hereby, we predominantly observed the directional relocation of vent outflow, following accretion and oxidation of the hydrothermal material.

III.4.3 Faunal assemblage dynamics

Mussel dynamics - Overall mussel coverage (~ 263 m²) was remarkably stable over time, consistent with the lack of dramatic changes in the hydrothermal habitat and topography. This corroborates the high stability observed from 1994 to 2008 by Cuvelier et al. (2011b). These authors described the mussel assemblages of Eiffel Tower as being “well established” with modifications only occurring at fine scales. The absence of global change suggests that these mussels have had the time to reach a balanced population and final stage of succession defined as a ‘climax’ state (Connell 1978; Cuvelier et al. 2011b). The overall lack of change demonstrates an apparent ‘steady state’ of the mussel population over 25 years of monitoring. In the absence of dramatic event of disturbance (e.g. magmatic/tectonic disruption), the abundant mussel population has thrived there at least for three decades since the first scientific visit at Lucky Strike in 1992.

Local changes in assemblage composition along with the consistency of successional patterns over time further supports the ‘dynamic equilibrium’ of the population and highlight the high

capacity of mussels to relocate and migrate over the structure. Hence, considering assemblages as a whole (i.e. total cover) at the edifice scale would hide processes acting at smaller scales and that are responsible for most of the variability observed in this study (e.g. patch dynamics approach; Paine and Levin 1981; Levin 1992). Indeed, mussel assemblages still displayed a high spatial variability over 5 years at the polygon scale (Figure III.3). For instance, ~ 45% of the surface occupied by large mussels in 2020 did not correspond to that observed in 2015. By performing analyses of cover distribution at smaller scales, we disentagled two scales of variability. We first detected two distinct areas of ~ 5 to 12 m² undergoing a peculiar mussel cover shift, accounting for the main trends in mussel cover at the edifice scale (Figure III.6). However, those shifts poorly explained the total amount of variability occurring at the polygon scale. Since the remaining variability predominantly occurred within tiles, we confirm the hypothesis of Cuvelier et al. (2011b) that the natural regime of modification concentrates at infra-metre scales. The lack of clear pattern of change in tiles may have contributed to the difficulty to extract a temporal trend for multivariate analyses (RDA). In the absence of significant habitat modification, other studies under a regime of continuous venting have shown the importance of the small-scale vent repositioning as they inevitably remain the main drivers of assemblage modifications (Hessler et al. 1988; Sarrazin et al. 1997; Copley et al. 2007; Gebruk et al. 2010; Sen et al. 2014; Du Preez and Fisher 2018; Zhou et al. 2018). In our study, most of the variability in assemblage cover within polygons remained indeed predominantly restricted to areas exposed to venting activity (Figure III.5). This confirms that the closer to the vent exit(s), the more dynamic the habitat and the spatial distribution of assemblages will be, as already suggested following an 8-year monthly monitoring at a single diffuse outflow of Eiffel Tower (Van Audenhaege et al. 2022). The high stability of smaller mussel assemblages located outside venting activity may be related to the stable background environment influenced by the cold deep-sea waters buffering the influence of venting as dilution occurs (Van Audenhaege et al. 2022). Bottom currents may also provide a steady trophic supply by redistributing hydrothermal vent plume and suspended particles all over the edifice (Martins et al. 2008; Girard et al. 2020a).

Observations made in this study allowed us to refine the qualitative successional model that Cuvelier et al. (2011b) identified (Figure III.9). Firstly, we confirm a sequential and linear pattern of succession strongly coinciding with the known spatial zonation of the fauna along the vent fluid dilution gradient (Cuvelier et al. 2011a; Husson et al. 2017). That directional and sequential order of successions suggests the lack of a chronic disturbance regime resetting

communities in a more random pattern (Horn 1976) compared to what was observed at other vents in the Pacific (Sarrazin et al. 1997; Marcus et al. 2009).

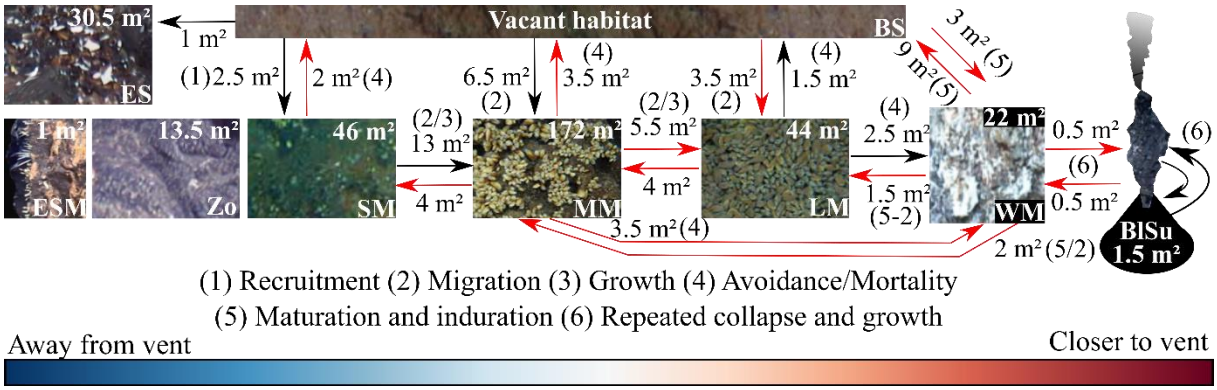

Figure III.9. Schematic summary of the successional model refined from Cuvelier et al. (2011b). Arrows represent cover fluxes [m²] among assemblages ordered by their position along the vent fluid dilution gradient (see Figure III.7). Red arrows highlight transfers overlooked in Cuvelier et al. (2011b). Because of different dynamics, microbial mat cover and vent shrimps were not included in this scheme. The number in m² represents the average area that underwent a given transition from 2015 to 2018 and from 2018 to 2020. The number in parentheses next to each arrow informs on the most likely mechanism at stake based on observations. If multiple mechanisms are possible, '/' is specified. Assemblages/substrata: BlSu = black amorphous sulphide sometimes displaying a soft-sediment talus, WM = white material, LM = large mussels, MM = medium mussels, SM = small mussels, BS = bare substratum, ES = Empty shell, Zo = zoanthid sp., ESM = erected sessile morphotype.

Cuvelier et al. (2011b) described directional processes from smaller to larger assemblages through migration or growth. However, our results suggest that, within two years, a given patch can also transition back to a colder assemblage emphasising and supporting the 'dynamic equilibrium' hypothesis (Figure III.9). As mortality or migration displaces the initial assemblage, it can be replaced through the settlement of smaller individuals. This suggests the importance to consider the whole population as a dynamically balanced system that can buffer local variability by rapidly filling in the space left empty at small scales, but also at ~ 10 m² scales as shown by the transition from medium to small mussels in the central part of the edifice from 2015 to 2020.

Only a few successional models included the importance of substratum maturation at the early stages of the succession model (Sarrazin et al. 1997, 2002; Cuvelier et al. 2011b; Du Preez and Fisher 2018; Marticorena et al. 2021). Hereby, we demonstrated the importance of induration (i.e. white material visually becoming bare substratum through oxidation; Figure III.9) to provide a consolidated substratum for mussel colonisation. As accretion proceeds, the vent outflow and microhabitat are also translated over a few decimetres (Van Audenhaege et al. 2022). Large mussels would benefit from the new hard substratum to adapt their position to

optimal vent fluid exposure through migration of large individuals (~ 0.1-0.3 m.day^{-1}) or, more slowly, of byssus-bounded mussel aggregations (~ 0.1-0.2 m.yr^{-1}; Van Audenhaege et al. 2022). Such rates of displacement are comparable to those of hydrothermal material accretion. Therefore, it seems reasonable to assume that mobility is a fundamental functional trait ensuring mussels to cope with fine-scale changes of the hydrothermal habitat. Mobility of mussels is well known for shallower species (Bovbjerg 1957; Okamura 1986). At vent edifices, it may be particularly important to sustain a pole position in a habitat that may constantly change at small scales. Sen et al. (2014) hypothesised that mobile vent gastropods would be able to orientate their displacement towards adequate vent exposure, as hypothesised more recently for *B. azoricus* (Van Audenhaege et al. 2022). As predation on medium to large mussels of Eiffel Tower can be fairly excluded (Matabos et al. 2015; Portail et al. 2018; Van Audenhaege et al. 2022), competition for space and access to resources may be the main processes accounting for the steady assemblages of large mussels of Eiffel Tower (Van Audenhaege et al. 2022)). Taking advantage of those gradual small-scale changes should therefore help mussels to rapidly gain access to resources and avoid intraspecific competition (e.g. smothering, pressure from dense aggregations). As hypothesised by several authors, mobility may be involved in maintaining a pattern of spatial segregation usually observed at vents (Comtet and Desbruyères 1998; Cuvelier et al. 2009; Sen et al. 2014).

Cuvelier et al. (2011b) observed no successional link between medium and large mussels leading to divide assemblages into two distinct communities with no apparent connection. Instead, our results suggest that as large mussels displace, they leave room for the settlement of widespread medium mussels or even recruits, as local competition decreases (Lenihan et al. 2008). Furthermore, the displacement of vent fluid could trigger the development of medium mussels through a shift of their flexible symbiont community (Won et al. 2003; Duperron et al. 2006). In contrast the growth of small mussel assemblage may be limited by their suspension-feeding mode (De Busserolles et al. 2009; Duperron 2010). If exposure conditions are met, mussels could reach a sufficient size quickly enough to avoid being outcompeted by smothering of larger migrants (Nedoncelle et al. 2015; Van Audenhaege et al. 2022). Some authors have shown the rapid growth and multi-decadal longevity of vent Pacific mussels (Rhoads et al. 1981; Nedoncelle et al. 2013). As for other vent species, fast growth was hypothesised as an adaptation to the instability and ephemerality of the vent environment at fast-spreading ridges (Lutz et al. 1994; Shank et al. 1998; Nedoncelle et al. 2013). Similar growth rates and high longevity (~ 18 yrs) were observed in *Bathymodiolus brevior* despite a suggested decadal

stability of the vent environment in intermediately-spreading back-arc basin (Schöne and Giere 2005; Du Preez and Fisher 2018). Growth rate and longevity of *B. azoricus* remains to be assessed, but recent monitoring suggested slow growth (Marticorena et al. 2021; Van Audenhaege et al. 2022). However, in the case of wider areas (~ 5 m²) colonised by large mussels after the opening of a new habitat, we were not able to discriminate from the contribution of recruitment or rapid growth. Infra-annual monitoring of such areas would be ideal to gain knowledge on mechanisms of larger-scale colonisation under natural conditions (Van Audenhaege et al. 2022).

Our data were based on the presence of cover, but not on their absence. As observed by Cuvelier et al. (2011b), mussels never colonized the white material. The intense outflow and substratum instability could explain their difficulty to maintain their positions (Van Audenhaege et al. 2022). The disappearance of mussel patches, concomitant to directional accretion, support the hypothesis that this process may displace or kill mussels (Figure III.9; Cuvelier et al. 2011b). Other areas covered by black soft sediments were also depleted of mussels. Several processes can account for this observation. The substratum may be unsuitable for mussel settlement because they cannot anchor on soft sediments, the continuous deposition of hydrothermal particles may smother mussels or the repeated collapse of large sulphide spires can contribute to mussel removal (Figure III.9).

The regime of a disturbance can be defined by its areal extent, magnitude, frequency, predictability and turnover rate (Sousa 1984a). These characteristics have great implications on community composition as they contribute to habitat heterogeneity and influence species survival. Furthermore, over evolutionary time scales, the regime of disturbance is a factor of selection to which species adapt to maintain their populations through time and has thus a strong influence on the resilience of communities (Levin 1992). Overall, since mussel total population was extremely stable over the Eiffel Tower edifice, we can infer that *B. azoricus* mussels are well adapted to the small-scale regime of hydrothermal changes which contributes to maintaining their population at the carrying capacity of the edifice (e.g. Hessler et al. 1988). Eiffel Tower is a mature edifice compared to others nearby (e.g. White Castle). Its high stability as well as extensive and vertical topography allows the settlement of vent mussels over 58.18% the area of the edifice. As mussels are foundation species, a stable community over such a large area may be important for supplying recruits for the rest of the Lucky Strike vent field hence possibly explaining the high share of taxa of Eiffel Tower with other edifices (Sarrazin et al. 2020). Finally, our results raise the question of the capacity of *B. azoricus* to withstand larger-

scale disturbances, such as those induced by volcanic eruptions or SMS mining. This is in line with previous studies that inferred a low resilience of vent communities at slow-spreading ridges (Sen et al. 2014; Van Dover 2014; Du Preez and Fisher 2018).

Other faunal assemblages – *M. fortunata* shrimp distribution was restricted to areas harbouring medium to large mussels and active hydrothermal substrata. It remained relatively stable over the edifice which is consistent with the relatively stable venting pattern. However, local change in shrimp cover was still detectable as they are able to quickly reposition following small-scale variability of hydrothermal activity (Copley et al. 2007). The distribution of *S. mesatlantica* crabs matched that of shrimps and they were almost absent from small-mussel assemblages as observed with infra-daily images (Matabos et al. 2015; Van Audenhaege et al. 2022), suggesting their affinity for the vent environment. Zoanthid assemblages distributed in the southern periphery over flat to smooth-slope areas remained highly stable over time. Being located in cold habitats (max. 5 °C), their stability may be explained by the highly stable conditions of the ambient seawater while their high densities assume a trophic reliance on vent productivity (Husson et al. 2017; Girard et al. 2020a). Although much less represented, erected sessile morphospecies (i.e. foraminifers or microcarnivorous cladorhizids) occurred sporadically on inactive features, such as at extinct chimneys located in the west of Eiffel Tower. They colonised exclusively vertical structures suggesting they may benefit from entrainment of particles and prey by enhanced currents (Erickson et al. 2009). *Phymorynchus* buccinid gastropods formed only a single < 10 ind. aggregation that remained a few decimetres near mussels over time.

Microbial mats – The distribution of microbial mats confirmed their association with small and medium mussels in cold to intermediate temperature niches (i.e. 4.9 to 6.2 °C; Cuvelier et al. 2011a; Sarrazin et al. 2015). Microbial mat distribution is hypothesised to coincide with the redistribution of the plumes of main smokers by bottom currents (Girard et al. 2020a). However, that driver alone cannot explain the lack of steadiness of microbial mat distribution that showed transient conditions between 2015 and 2020. That decline contrasts with the general stability of hydrothermal assemblages and stable distribution of venting areas, similarly to what was observed over 7 years at centimetre and infra-annual scales in the periphery (Van Audenhaege et al. 2022). We hypothesised that other factors explain the lack of persistence of mats over years such as the biological impact from grazers that may regulate microbial cover (Micheli et al. 2002; Cuvelier et al. 2011a). While mussels exhibited very heterogeneous covers between edifice sides, the distribution of microbial mats was more consistent across sides from 1994 to

2020. Although it remains difficult to speculate on the causes of microbial mat instability, this suggests that microbial mat dynamics would be more predictable considering factors at larger scales. A dike intrusion detected in 2001 coincided with an increase of mat cover over LS and Eiffel Tower (Dziak et al. 2004; Cuvelier et al. 2011b). Similarly, unusual events of seismic activity occurred in 2015 and 2016 (Ballu et al. 2019; Bohidar et al. 2022). Those possibly created temporary conditions for microbial mats to subsist over a few months before they declined, as also observed immediately with increase of microbial productivity after eruptive events (Juniper et al. 1995; Shank et al. 1998).

Our results emphasise that the predominant scales of variability in faunal distribution and venting activity at Eiffel Tower is restrained to decimetres scales and that large shifts are rare, even inexistent, over multi-decadal time periods. The breakpoint identified over 25 years in substrate and assemblage coverage, along with the decline of microbial mats starting in 2015, suggested a possible impact of the unusual seismic activities registered in 2015 and 2016. However, this event was not accompanied by major shifts in Eiffel Tower habitats and communities distribution indicating that this events might have only increased hydrothermal activity variability locally. In this study, we observed strong similarities in scales and patterns of environmental and faunal variability in the vicinity of the vent exit when comparing to a high-resolution long-term monitoring at the scale of the assemblage (Van Audenhaege et al. 2022). Indeed, our results and observations showed that the mechanisms and processes observed at smaller scales with infra-daily images could also apply at the scale of the edifice. This supports the interest of using small-scale biological observatory modules connected to pluri-disciplinary deep-sea observatories to identify the infra-annual and long-term processes shaping community dynamics at vents (Sarrazin et al. 2007).

III.5 Supplementary Material

III.5.1 Supplementary Figures

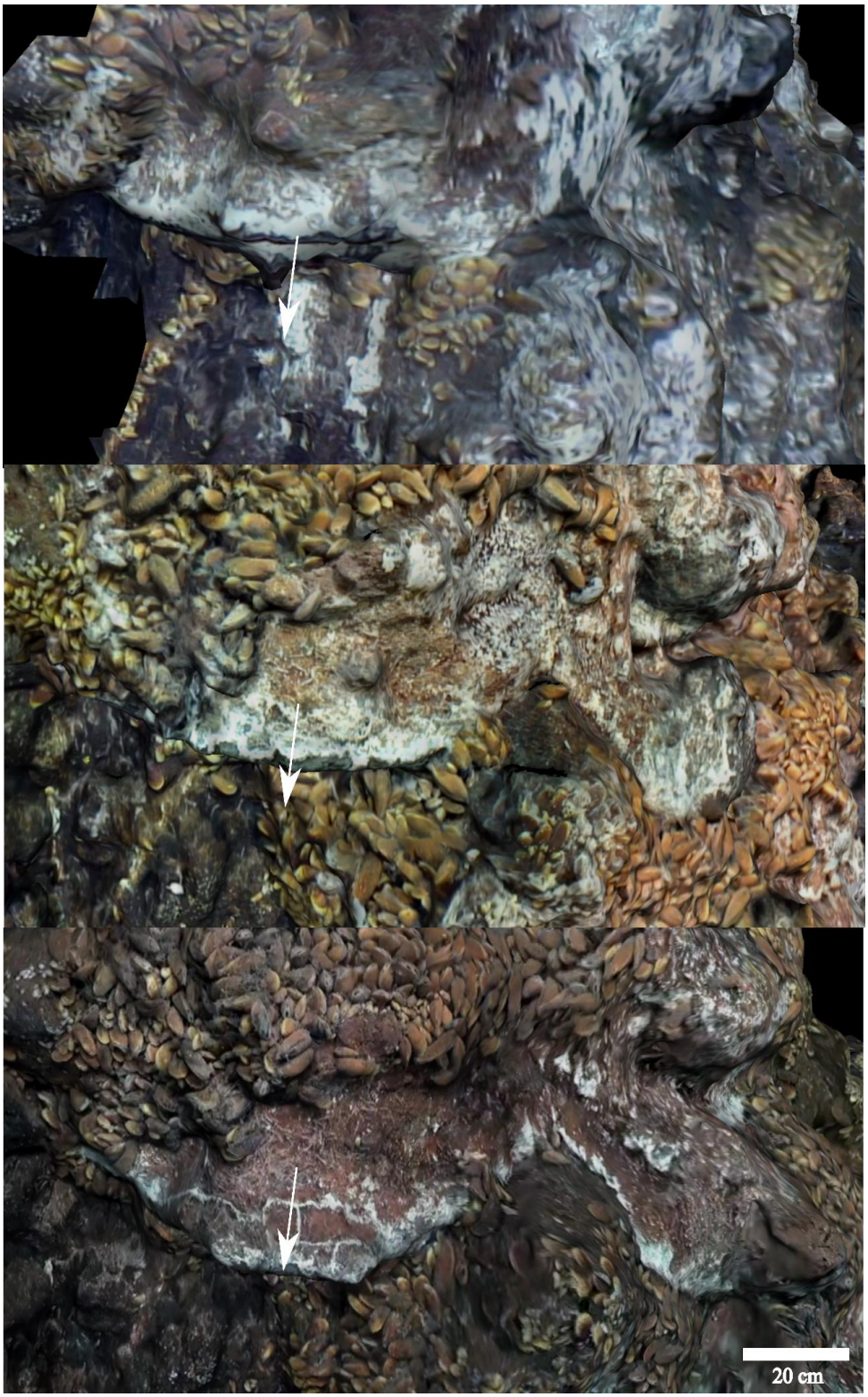

Supplementary Figure III.1. Directional forward growth of a flange measured by the 20-cm white arrows drawn over the 3D models from 2015, 2018 to 2020 (top to bottom). The white bar represents 20 cm. Note the mineralisation of that flange over time, switching from black to white to brown to reddish. That event occurred in the North Side of ET.

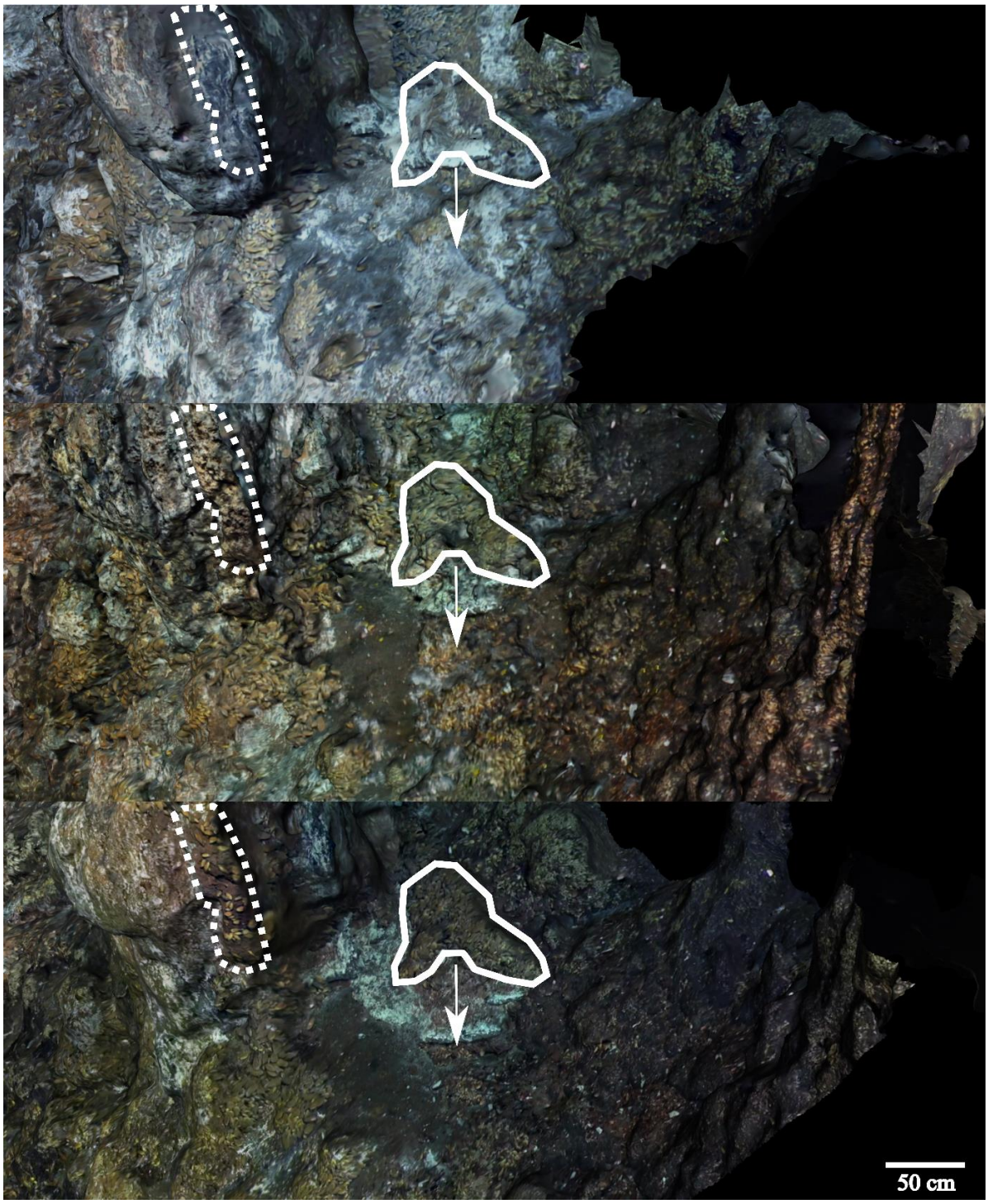

Supplementary Figure III.2. Directional downward "run-off" of the front of a "screed-like" hydrothermal precipitation onto the original substratum. That displacement is measured by the 53-cm white arrows drawn over the 3D models from 2015, 2018 to 2020 (top to bottom). The white bar represents 50 cm. Note that the mineralisation of the substratum may have occurred over time, as mussels colonised the area inside the full-contour white polygon and as the white material switched to a red-brownish colour. The dash-contour polygon illustrates the 1. mineralisation from 2015 to 2018 (white to brownish) and 2. colonisation of a few mussel individuals of medium size.

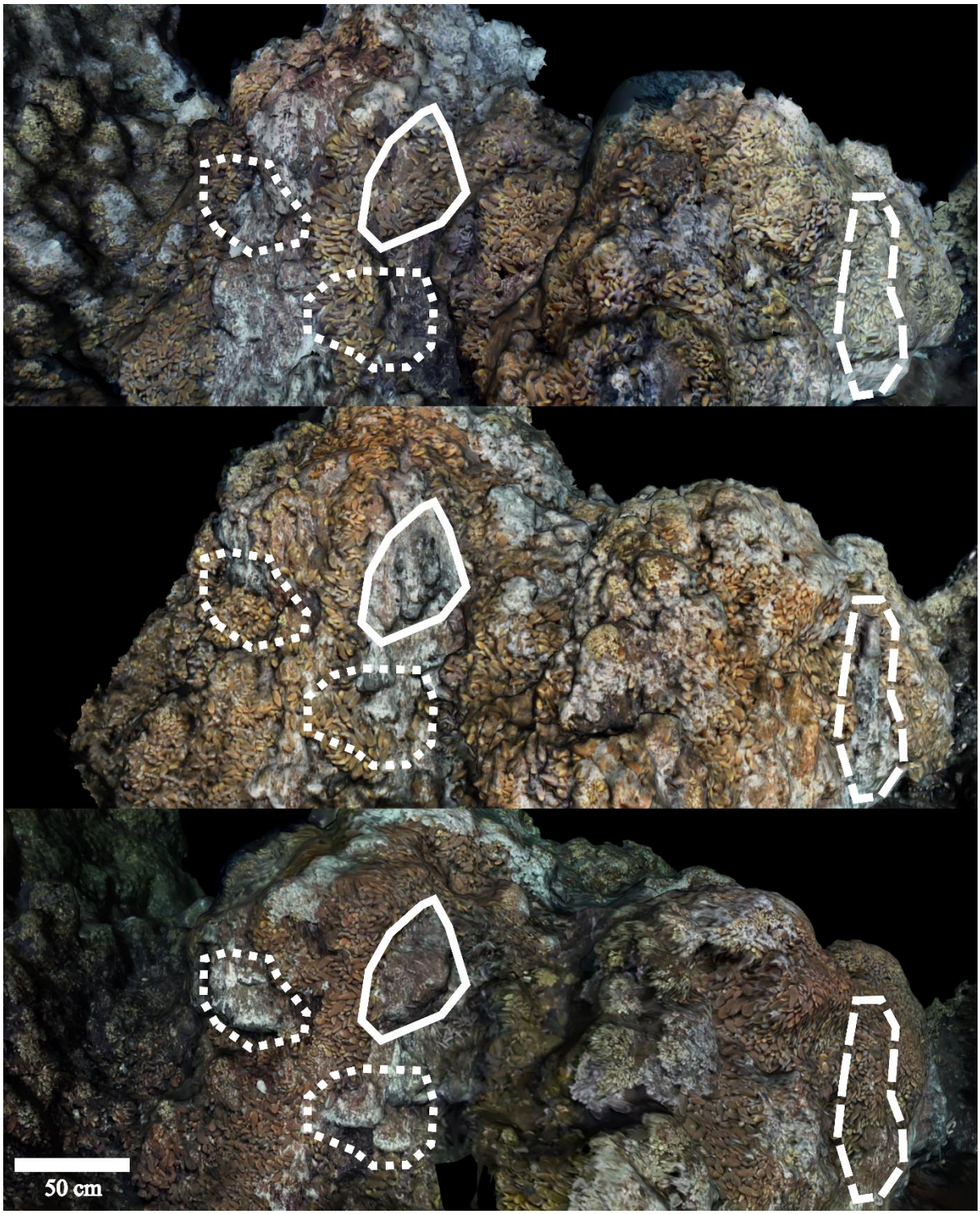

Supplementary Figure III.3. Multidirectional build-up of an active outcrop delimited by full-contoured polygons over the 3D models from 2015, 2018 to 2020 (top to bottom). The white bar represents 50 cm. Note that within that polygon, large mussels in 2015 were removed after the possible reactivation of an active area that built up to form an outcrop in 2018. That area underwent mineralisation and started to be colonised by mussels in 2020. The long-dash contoured delimits another outcrop/chimney that grew between 2015 and 2018 and subsequently removed mussels that recolonised the feature in 2020. The short-dash contoured polygons illustrate other areas exhibiting local variability in the field of view, with growth of flange and outcrops and resulting in the colonisation or removal of mussels.

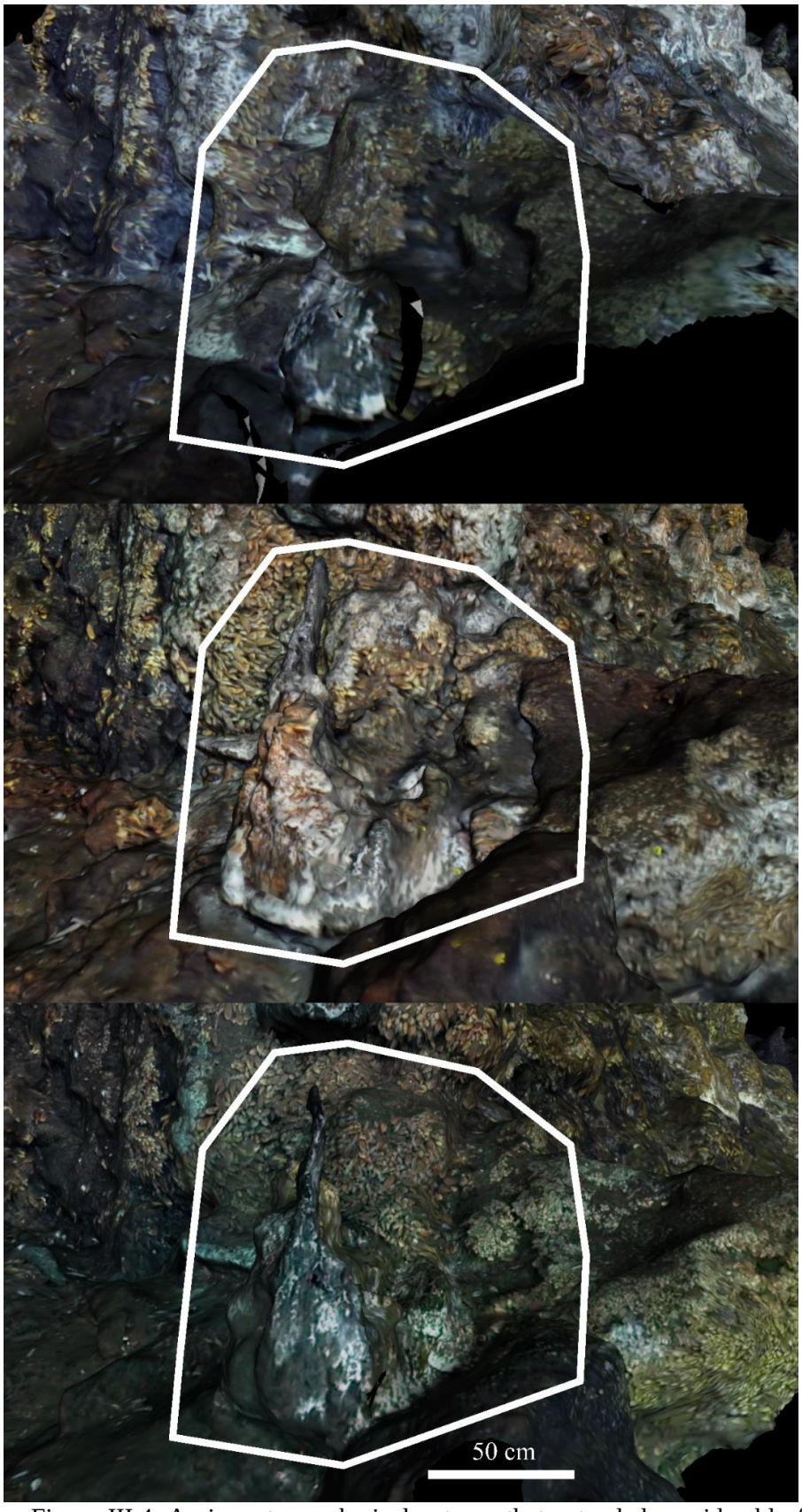

Supplementary Figure III.4. An immature spherical outcrop that extended considerably from 2015 to 2018. It displays a black smoker on top releasing vent fluid from the main conduit, while more diluted fluid is forced to exit from underneath the outcrop.

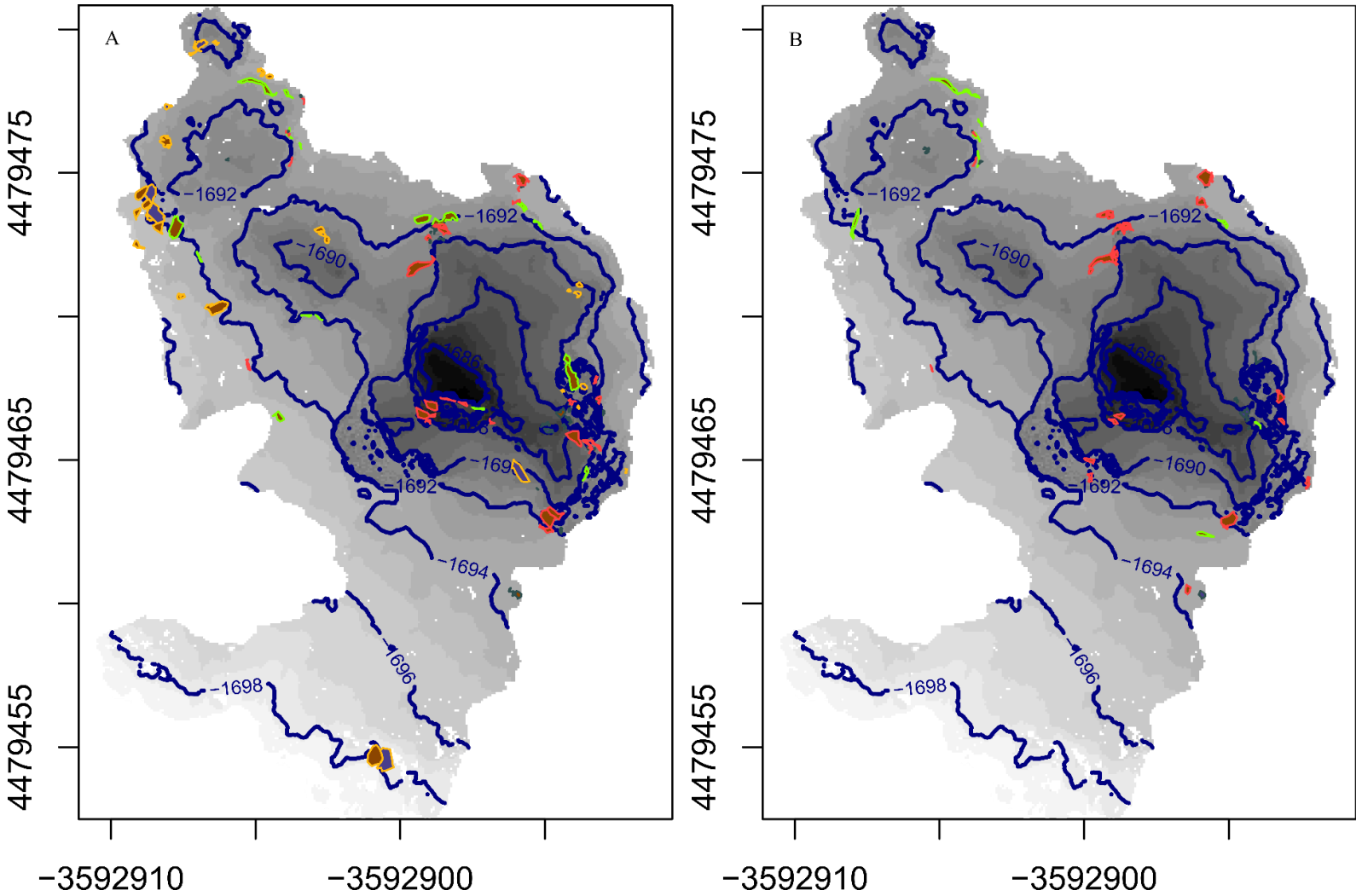

Supplementary Figure III.5. Topographic change observed from the top of the Eiffel Tower edifice in successive 3D models in 2015-2018 (left) and in 2018-2020 (right). Colours of the contour of polygons refer to the type of topographic features that underwent a change: orange: inactive substrata, green: active flanges or cracks, red: active outcrops and black: active chimney and spires. The filling colour refers if a gain or loss was observed: brown: gain and purple: loss.

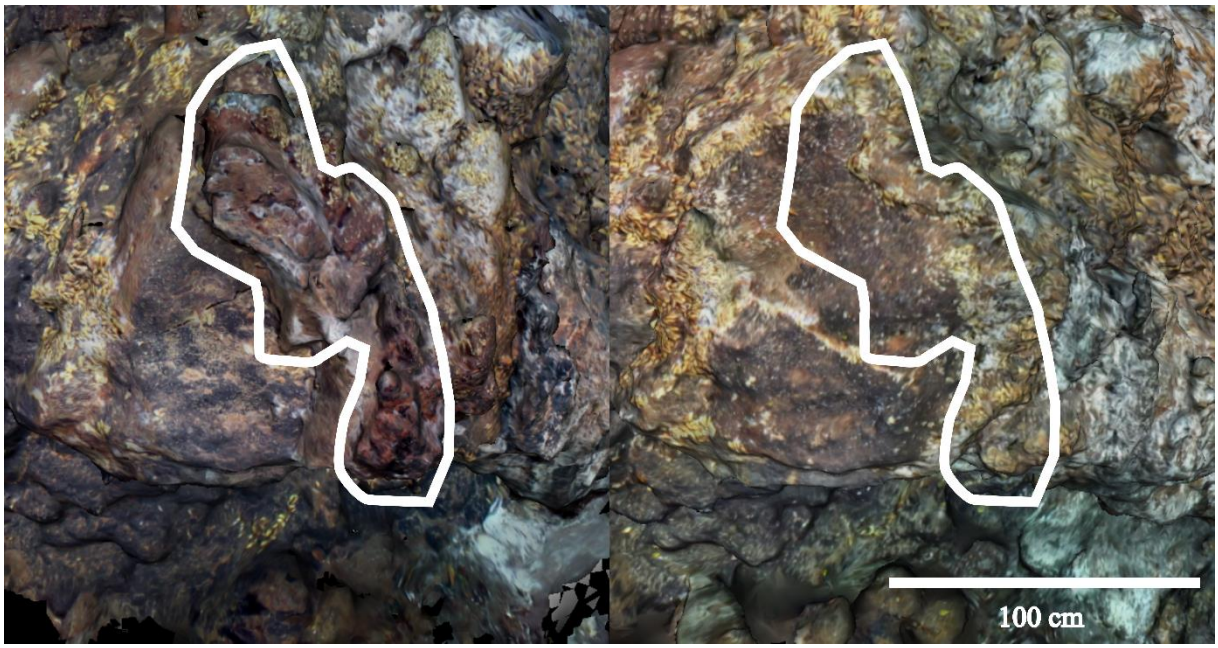

Supplementary Figure III.6. Detachment of a large portion of an inactive section in the western periphery of ET drawn with full-contour polygon from 2015 (left) to 2018 (right). Note the increase of size of the active outcrop in 3 years on the right of that detachment.

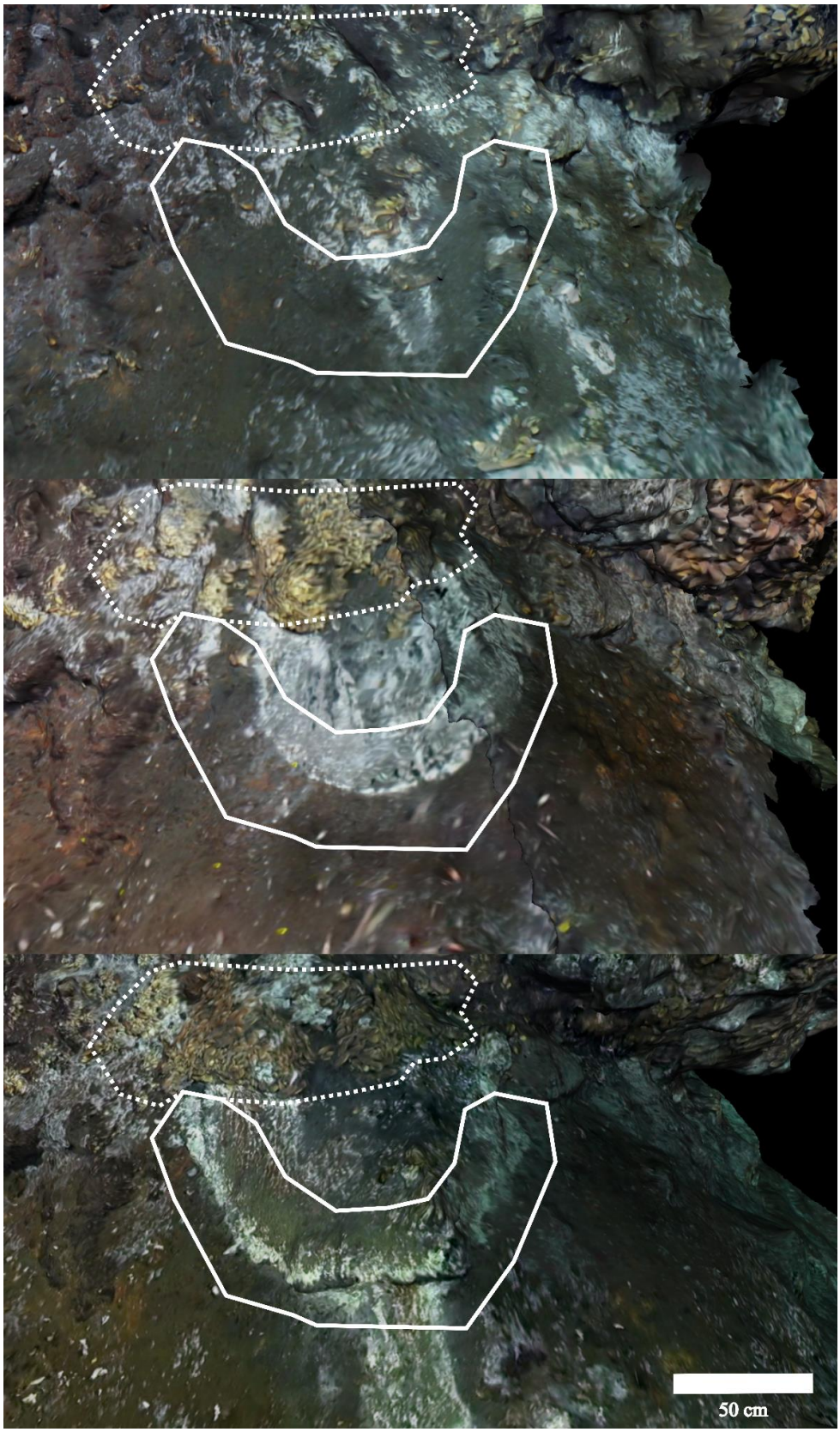

Supplementary Figure III.7. Emergence and directional displacement of a circular feature within black soft sediment from 2015 to 2020 (full-contour white polygon). Note the resulting colonisation of a mix of medium and large mussels on top as delimited by the dashed-contour polygon. The field of view is located right beneath Supplementary Figure III.11.

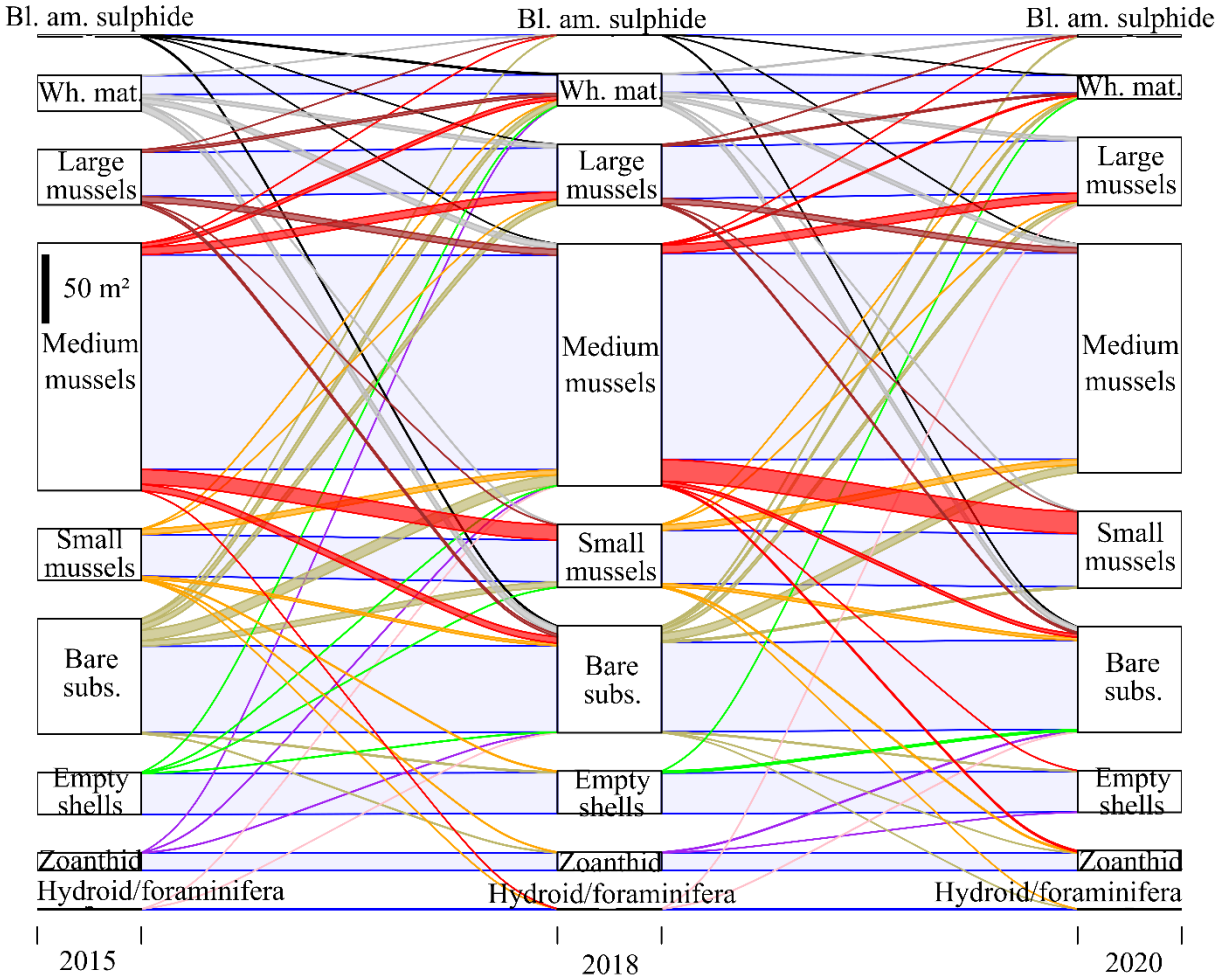

Supplementary Figure III.8. Full Sankey diagram describing patterns of assemblage succession for all polygons annotated on 3D reconstructions of ET in time steps of 2015, 2018 and 2020 (i.e. the stages). White rectangles (i.e. the nodes) correspond to assemblage cover at given stages. Coloured segments (i.e. the flows) describe the successions occurring from nodes from stage $_{(t)}$ to stage $_{(t+1)}$. When no change was observed, the flow is coloured in light blue. The vertical black bar scales the height of nodes and the width of flows. Only flows of 0.5 m² were drawn.

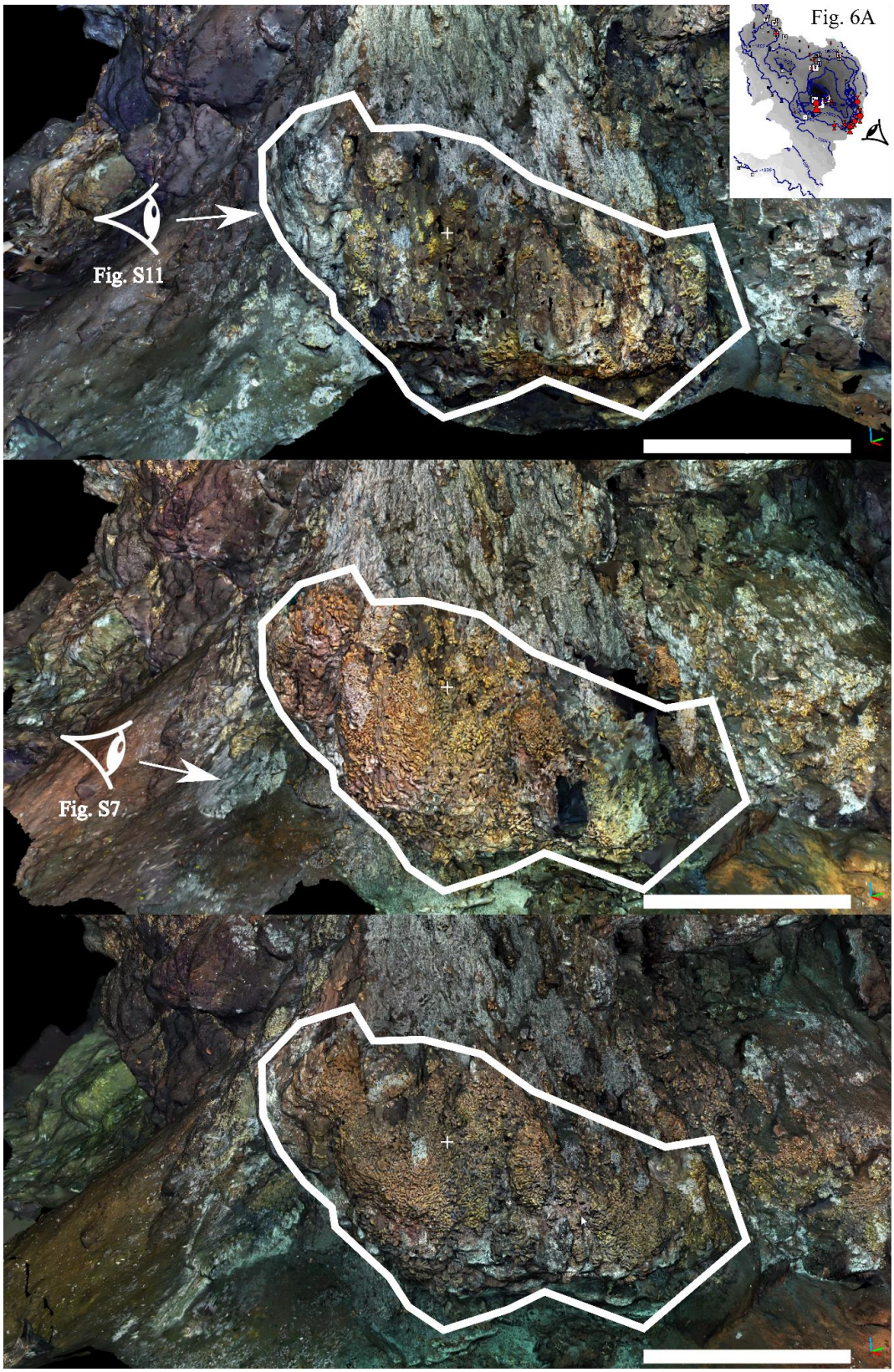

Supplementary Figure III.9. Event of colonization by large mussel *B. azoricus* delimited by white polygons drawn over screenshot of the 3D models from 2015, 2018 to 2020 (top to bottom). The white eyes position the fields of view of Supplementary Figure III.7 & Supplementary Figure III.11. White bars represent 2 m. The top right panel maps the balance of large *B. azoricus* assemblages at Eiffel Tower viewed from the top (see Figure III.6A). The black eye corresponds to the position of the camera when taking the screenshot in 3D models.

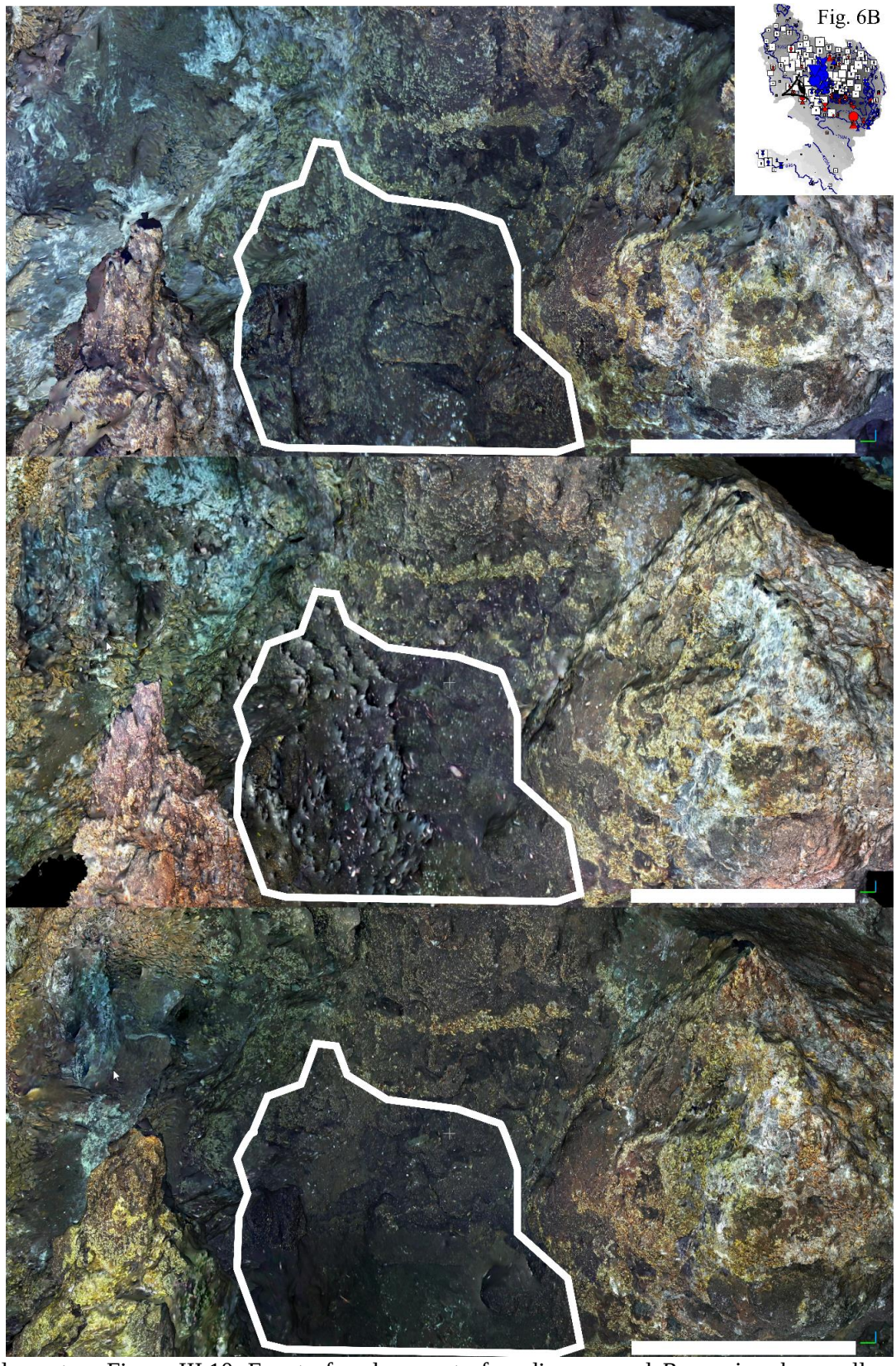

Supplementary Figure III.10. Event of replacement of medium mussel *B. azoricus* by small mussels delimited by white polygons drawn over screenshot of the 3D models from 2015, 2018 to 2020 (top to bottom). White bars represent 2 m. The top right panel maps the balance of *B. azoricus* assemblage at Eiffel Tower viewed from the top (see Figure III.6B; see also Supplementary Figure III.9). The black eye corresponds to the position of the camera when taking the screenshot in 3D models. Note the centimetre grey artefacts in the polygon of the model of 2018.

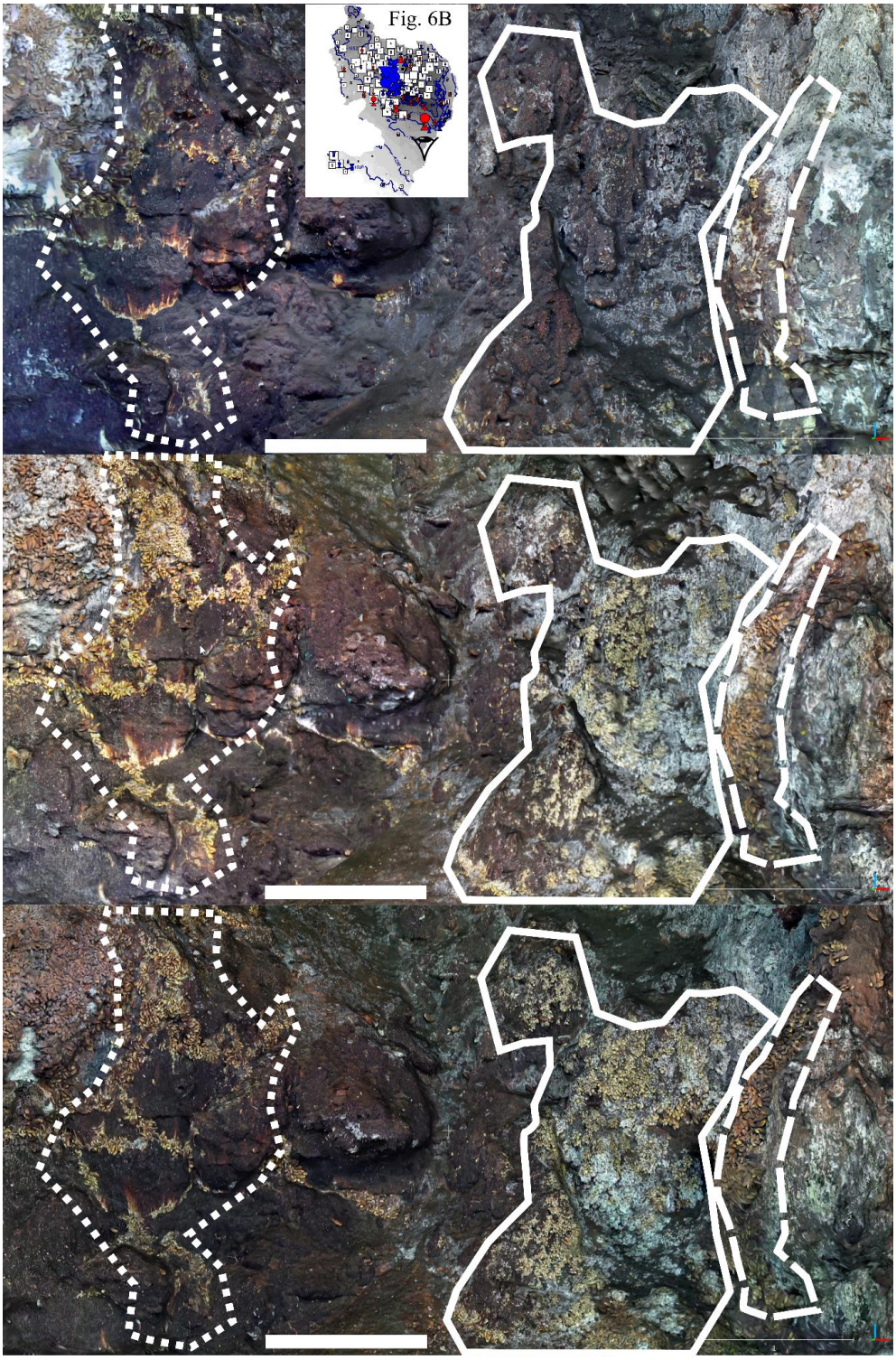

Supplementary Figure III.11. Event of colonisation of medium mussel *B. azoricus* delimited by white polygons drawn over screenshot of the 3D models from 2015, 2018 to 2020 (top to bottom). The field of view is located right above Supplementary Figure III.7. White bars represent 1 m. The black eye corresponds to the position of the camera when taking the screenshot in 3D models. The short-dash contour delimits a network of medium mussels that settled and grew. The long-dash contoured polygons illustrate large mussels that colonised the area as shown in Supplementary Figure III.9.

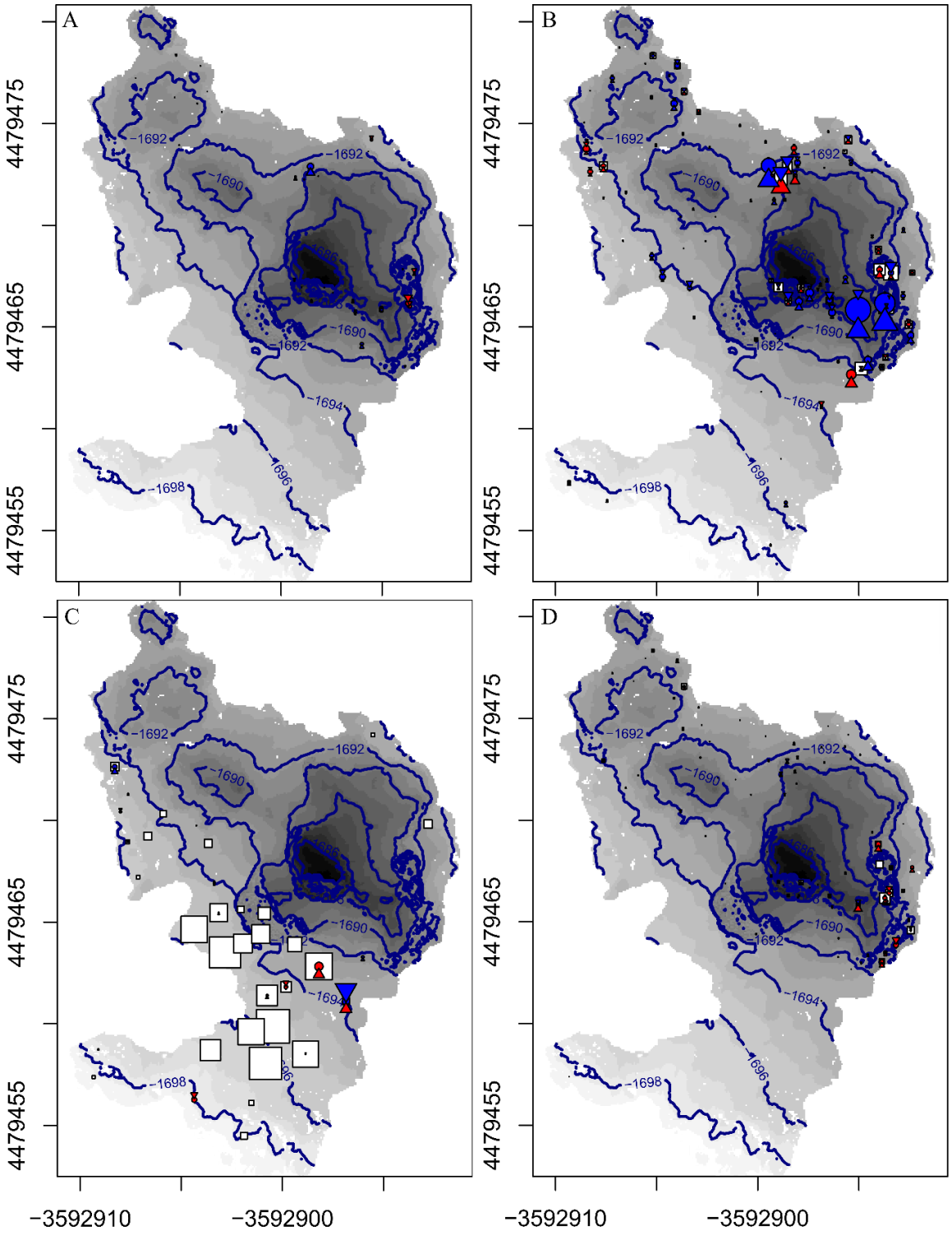

Supplementary Figure III.12. Balance of assemblages and substrata for (A) black sulphide, (B) white material, (C) empty shells and (D) shrimps *M. fortunata*. A square represents the average assemblage cover in a given tile. The circles represent the total balance from 2015 to 2020. Upward/downward triangles represent changes from 2015-2018/2018-2020 respectively. The size of symbols represents the surface that changed. If it increased/decreased, they are plotted in red/blue. Squares were plotted under the circles in order to underline tile communities that were stable (i.e. the white square is visible) or that were completely gone in 2020 (i.e. the white square is not visible anymore since fully overlaid by a blue circle). The surface exhibiting variability in those maps is informed as a percentage of the total surface of polygons that switched to another cover. Bathymetry is provided with 2-m isolines and a black to grey colour gradient. Arrows indicate north.

III.5.2 Supplementary Material III.1

Supplementary Method 1 provides a detailed protocol of the protocol of annotationv on *3DMetrics* of a time series of 3D models rebuilt by photogrammetry with *MATISSE* (Ifremer, Arnaubec et al. 2015; Laranjeira et al. 2020; https://github.com/IfremerUnderwater).

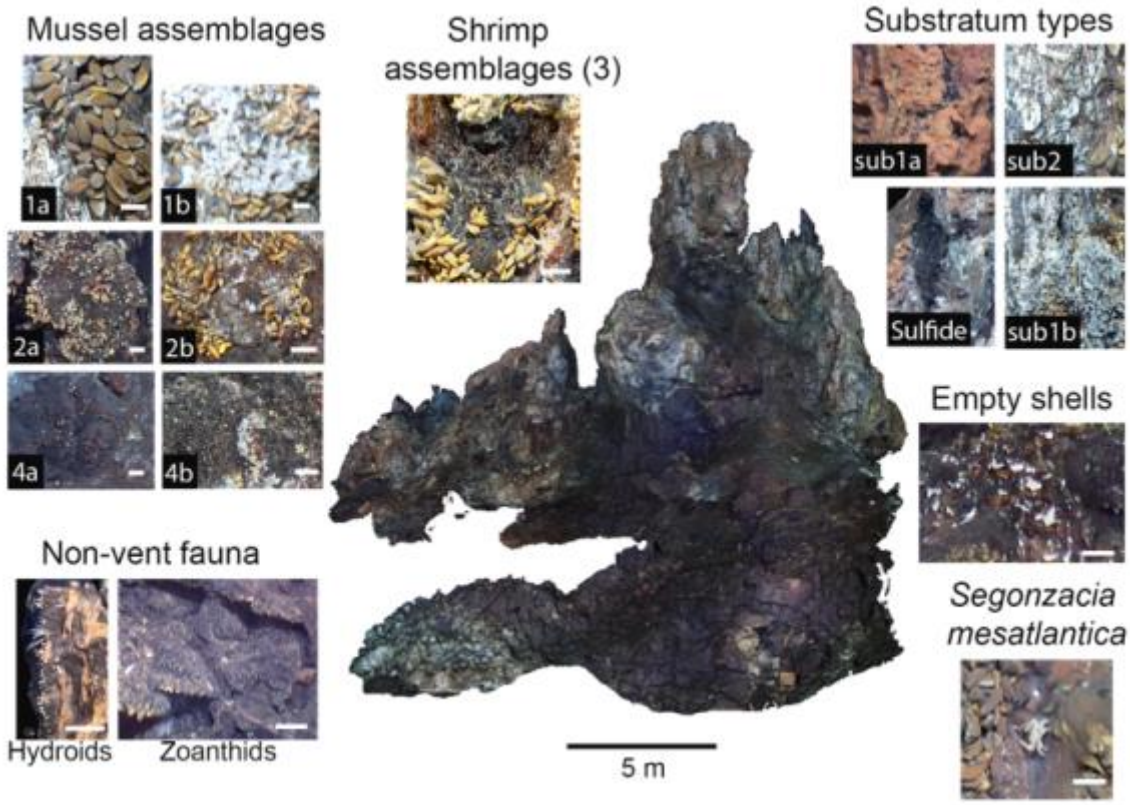

Supplementary Figure III.13. Different categories annotated over the 3D reconstructions of Eiffel Tower. "Static" cover of substrata and assemblage was annotated with polygons and a specific code. Categories were substrata: black material ('Sulfide'), white material ('sub2') and bare substratum ('sub1'), and biological assemblages: mussel assemblages of different size: large ('1'), medium ('2') and small ('3'; see Girard et al. [2020a] for length intervals); empty shells, erected sessile morphospecies ('hydroids') or zoanthids. Those substrata and assemblages could be covered by microbial mats, so we added the suffix ('a') if microbial mat cover was absent or ('b') if the assemblage/substratum was covered by microbial mats. "Mobile" assemblages were alvinocaridid shrimps ('3') or *Segonzacia mesatlantica* crabs annotated with points. Figure from Girard et al. (2020a).

Annotating each survey time step independently is time consuming and the monitoring could be biased by annotation variability induced by differences in agreement between annotators and progressive self-learning (Schoening et al. 2016). To ensure an accurate quantification of changes over time, we reused and modified annotations made on ET 2015 by Girard et al. (2020) rather than reiterating the full annotation process for ET 2018 and 2020. Annotations corresponded to polygons delimiting a "static" single substratum/assemblage type covered or not by microbial mats (i.e. hereafter "polygon cover"). First, we simultaneously loaded the three

registered 3D models (i.e. after spatial alignment of the georeferenced models) and the annotations made on ET 2015 as layers using *3DMetrics*. For each polygon, we checked that the polygon cover did not change over the three 3D models. *3DMetrics* comes with the option to modify the attribute table of the annotations usually stored in a single *.json* file. The sequence of polygon covers from 2015, 2018 to 2020 was recorded manually by labelling the given polygon with a specific methodology. For example, if a polygon captured a stable large mussel assemblage (1) with no microbial mat (a) from 2015 to 2020, it was annotated "1a.1a.1a". If a polygon captured a stable large mussel assemblage (1) with no microbial mat (a) from 2015 to 2018 and then switched to medium mussels (2) covered by microbial mats (b) in 2020, it was annotated "1a.1a.2b" in *3DMetrics*. Only if a change was observed within the polygon, the latter was split according to the new spatial arrangement of cover. Annotation was stopped as soon as only bare substratum remained unannotated. This method of annotation can be easily imported in R with the package "jsonlite". As cover time steps are separated with a ".", we can easily separate the cover of each polygon with the function *strsplit*.

Annotation of mobile fauna was reiterated for each 3D reconstruction by watching the videos that were used for photogrammetry reconstructions as the latter tended to filter out such small individuals that can move rapidly. Annotations were similar to that of "static" assemblages except that if no shrimp was observed in 2015, and for instance, observed repeatedly in the area in 2018 and 2020, it was annotated ".s.s". The absence of shrimp in 2015 is informed with the absence of any symbol before the first ".".

Annotation of hydrothermal outflow was annotated with the following code with points for focused outflow ('bs'), diffusion zone ('dz') and with lines for flanges ('f'). If the focused outflow was not a black smoker, "not black" was added in the comment field of the attribute table.

Annotation of structural change was annotated with a specific protocol. If it involved black material that built up from 2015 to 2018 lasting also in 2020, it was annotated with "-.s.s". If it collapsed in 2020, it would be annotated "-.s.-". Hence, "-" signifies the absence of the feature. The comment section was fed with the observations that were made through time. For instance, for a chimney following the sequence "-.s.s", we commented: "2015: growth 2018: chimney 2020: chimney". If a chimney eventually collapsed following the sequence "-.s.s", we commented: "2015: growth 2018: chimney 2020: chimney".

III.5.3 Supplementary Material III.2

Pictures of change of topography, vent habitat or assemblages are catalogued via this link: https://drive.google.com/drive/folders/1OUo6WtwFJCUEq9vRDbu_qgbgrBijz5kx?usp=sharing.

III.5.4 Supplementary Material III.3

III.5.4.1 Dataset overview

The analyses presented here are computed with temporal sequences of cover retrieved from polygons annotated on 3D reconstructions of the Eiffel Tower hydrothermal edifice (Lucky Strike) in 2015, 2018 and 2020. Polygons were already aggregated in tile.

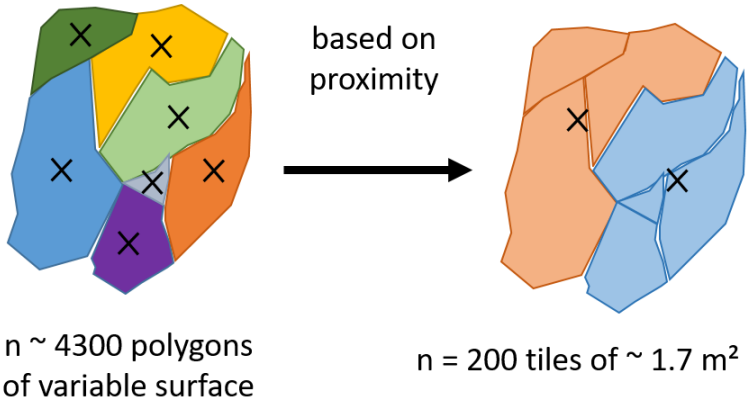

Supplementary Figure III.14 Scheme illustrating the proximity-based aggregation of 4300 polygons in 200 tiles. The example shows 7 polygons aggregated in two tiles of approximately similar surfaces and forming two continuous regions.

Annotation was achieved using polygons. Annotations were using the following labels: Sessile fauna/substratum cover: 1, 2, 4 = mussel *B. azoricus* assemblage (depending on density and size of mussels), Sub1 = bare substratum (either consolidated brownish sulphur, unconsolidated hydrothermal particles or fine sediment; this will be removed for further analyses), a = white hydrothermal deposit, s = black amorphous sulphur minerals constituting the vent surface pipe, z = zoanthid sp., h = *Cladorhiza* sp., cv = empty mussel shell on bare substratum. Microbial mat covering the top of the assemblages and substrata annotated with presence or absence (b or a respectively, and added after the cover label, e.g. 1b = large mussels covered by microbial mats). If it was not possible to determine the annotation: i = undetermined. Occupancy of "mobile" species covering the top of the assemblages and substrata were labelled as 3 = shrimps *Mirocaris fortunata*, g = gastropod *Peltospira smaragdina*. Two environmental proxies were calculated based on the distance from i) topographic changes and ii) the four types of hydrothermal outflows (i.e. black and white smokers, flanges, diffuse zone). The first proxy

counted the number of hydrothermal features occurring within the spatial extent of a tile by finding the nearest polygon. Then, for each tile, we summed the inverse distance of the tile centroid to each outflow that was located within that tile. The inverse distance comes with the benefit that it minimises the influence of distant features.

Data were extracted from *3DMretrics* by a routine reading the .JSON file in R (package '*jsonlite*'). Factors can be listed as followed and will be used to investigate spatio-temporal dynamics of the response variable (i.e. assemblages and substrata): year (2015, 2018, 2020) (and as a result, year transition), spatial position x-y-z (provided by a polygon annotation), spatial cover (m2), Side of the edifice (N, S, W, E) and position on the sulphide mount or at the base of the edifice (Side or periphery; NS = North Side), position x-y-z of hydrothermal activity ("main" focused black smoker, "secondary" focused translucent smoker, diffusion area as point features and flanges as line features) and topographic changes annotated as polygon.

Data are loaded in a matrix configured for multivariate analyses (i.e. observations in rows, variables in columns). We load the output of pre-processing scripts (not presented here) and discard the bare substratum and the unidentified cover. Firstly, we examine the surface of each tile based on the sum of the surface of polygons shared among 2015, 2018 & 2020.

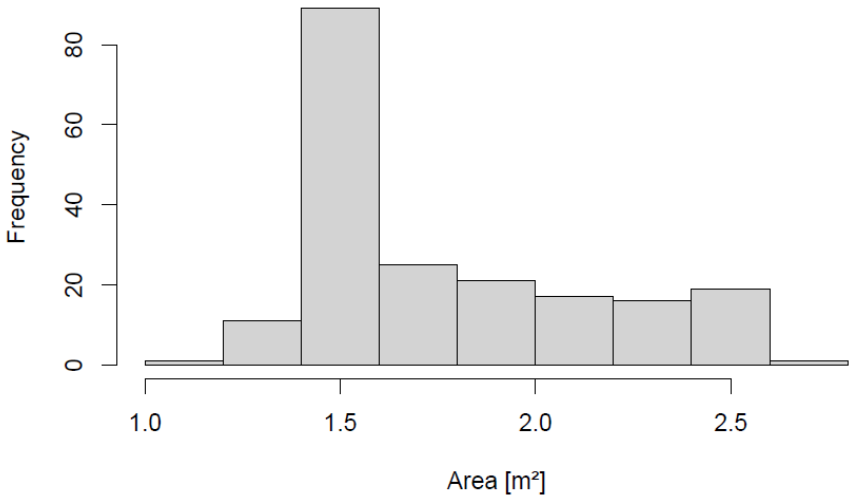

Supplementary Figure III.15. Histograms of areas aggregated for analyses by tiles of polygons.

The lack of normal distribution shows the difficulty to link polygons to tiles because of a trade-off between surface and spatial proximity.

In each community matrix, data are organised as follow: 1. each row corresponds to a tile to which is assigned two IDs (i.e. among and within side), the sum of all polygons assigned to that

tile, XYZ coordinates [m] of the tile centroid (i.e. mean of polygons' centroid weighted by their specific area) and the side. We display that information for the year 2015.

```
head(Matrix_RDA_group_2015[,1:7],10)
```

```
##    Original_ID ID_tot     Area Centroid_x Centroid_y Centroid_z Side
## 1          260      1 1.983091   14.00839  -9.669603  11.564273   SS
## 2          257      2 1.799056   13.45408  -8.645261  11.254791   ES
## 3          254      3 1.931393   14.21711  -9.652415  10.361668   SS
## 4          249      4 1.565404   13.92157  -8.293676   9.816375   ES
## 5          247      5 1.754464   14.34365  -9.351373   9.201676   ES
## 6          243      6 1.579983   13.81203  -9.786435   8.293649   SS
```

We now display the assemblage/substratum cover for the community matrix. Each tile (i.e. row) contains the sum of the area [m²] of the polygons annotated for a given assemblage/substratum cover. We decide to divide the surface of each assemblage by the total surface of each tile to get relative abundances.

```
Matrix_RDA_group_2015[,8:20] = Matrix_RDA_group_2015[,8:20]/Matrix_RDA_group_2015$Area
Matrix_RDA_group_2018[,8:20] = Matrix_RDA_group_2018[,8:20]/Matrix_RDA_group_2018$Area
Matrix_RDA_group_2020[,8:20] = Matrix_RDA_group_2020[,8:20]/Matrix_RDA_group_2020$Area
head(Matrix_RDA_group_2015[,8:20],10)
```

```
##    Large B. azoricus Medium B. azoricus Small B. azoricus
## 1         0.62784992          0.32455845        0.02801790
## 2         0.04803632          0.63404183        0.27305581
## 3         0.57379727          0.05802035        0.00000000
## 4         0.00000000          0.90909750        0.09090250
## 5         0.57154545          0.25070580        0.00000000
## 6         0.52378556          0.00000000        0.00000000
## 7         0.00000000          0.86843126        0.13156874
## 8         0.00000000          0.82819410        0.17180590
## 9         0.12713548          0.73445941        0.02618499
## 10        0.31732690          0.39826262        0.25230251
##    white hydrothermal deposit Empty shell Hydrozoan sp. Amorphous sulphur
## 1                  0.00000000           0             0                 0
## 2                  0.00000000           0             0                 0
## 3                  0.03633720           0             0                 0
## 4                  0.00000000           0             0                 0
## 5                  0.06488362           0             0                 0
## 6                  0.37820810           0             0                 0
## 7                  0.00000000           0             0                 0
## 8                  0.00000000           0             0                 0
## 9                  0.00000000           0             0                 0
## 10                 0.00000000           0             0                 0
##    Zoanthid sp. Microbial mat S. mesatlantica Phymorhynchus sp. M. fortunata
## 1             0     0.7730584       0.0000000                 0   0.00000000
## 2             0     0.2750248       0.0000000                 0   0.00000000
## 3             0     0.2902998       0.8042291                 0   0.00000000
## 4             0     0.6192059       0.0000000                 0   0.00000000
## 5             0     0.6483385       0.6497420                 0   0.00000000
## 6             0     0.0000000       0.4005854                 0   0.02822113
## 7             0     0.2086696       0.0000000                 0   0.00000000
## 8             0     0.1308291       0.0000000                 0   0.00000000
## 9             0     0.7608667       0.5473211                 0   0.00000000
## 10            0     0.7836366       0.6733563                 0   0.00000000
##    P. smaragdina
## 1              0
## 2              0
## 3              0
## 4              0
```

We now display the values for the 10 proxies stored in the environmental matrix of 2015. Again, each row contains the data for a tile. It contains the cumulative inverse 3D distance computed over the edifice from each smoker, diffusion zone, flange and topographic change. Furthermore, it contains the number of features that were found within a tile for each of those environmental variables.

```
head(Matrix_RDA_group_2015[,21:30],10)
```

```
##    Main smoker Secondary smoker Diffusion zone    Flange Topographic change
## 1     4.668703         6.861264       3.221347  7.109135           18.73524
## 2     4.498794         6.812066       3.372187  7.124585           19.12071
## 3     5.719286         8.534949       3.790170 10.827556           21.30316
## 4     5.454148         8.197698       4.023879  8.818034           21.79968
## 5     6.722933        11.076439       4.737846  8.924891           24.31052
## 6     6.512776         8.310382       3.280202  6.982936           26.25118
## 7     4.140712         6.419308       3.339107  8.951264           18.60859
## 8     4.887020         7.400806       4.048363 10.167555           21.67400
## 9     6.010065         9.038661       4.597240 12.385299           23.99502
## 10    4.281003         7.062636       3.705686 11.322022           20.37453
##    Main_Smoker_within Secondary_smoker_within Diffusion_zone_within
## 1                   0                       0                     0
## 2                   0                       0                     0
## 3                   0                       0                     0
## 4                   0                       0                     0
## 5                   0                       0                     0
## 6                   0                       4                     3
## 7                   0                       0                     0
## 8                   0                       0                     0
## 9                   0                       0                     0
## 10                  0                       0                     0
##    Flange_within Topographic_change_within
## 1              4                0.00000000
## 2              4                0.00000000
## 3              1                0.00000000
## 4              5                0.00000000
## 5              2                0.00000000
## 6              6                0.04377759
## 7              0                0.00000000
## 8              2                0.00000000
## 9              0                0.00000000
## 10             0                0.00000000
```

III.5.4.2 Environmental dynamics and drivers of change

A first PCA was computed to assess differences in the spatial distribution of tiles' assemblage distribution over the edifice. Then, a redundancy analysis (RDA) using the set of ten environmental variables was employed to identify the drivers of change considering i) each Hellinger-transformed community and environmental matrix for each time step independently and ii) considering Hellinger-transformed assemblage cover net change and the net change in environmental proxies (i.e. by subtracting the proxy value in 2015 to the value reached in 2020).

Prior to analyses, the environmental matrices were systematically scaled between 0 and 1. RDA axes and environmental proxies were tested for significance (permutations = 9999; Borcard et al. 2018). Based on the adjusted of that RDA, a forward selection was performed to reduce the amount of variables used to compute a second RDA (function forward.sel.R of package adespatial, p = 0.01, permutations = 9999).

A trajectory analysis was performed to monitor intensity and directionality of tile composition change (De Cáceres et al., 2019). First, a PCoA was performed on the Hellinger-transformed community composition data, i.e. the square-root of the relative proportion of each category within a tile, obtained by dividing the category surfaces with the tile. Trajectory metrics (i.e. net change and length of segments) were then computed on the axes of that PCoA (De Cáceres et al., 2019; package 'ecotraj' v. 0.0.3). The net change of the trajectory is the length among tile observations from t_i to t_{i+2}, hence 2015 to 2020. The length of each segment is the trajectory length among observations from t_i to t_{i+1} (i.e. 2015-2018 and 2018-2020). If the net change was respectively smaller or larger than the length of the first segment (i.e. 2015-2018), an exclusive criterion being "recovering" or "departing" was assigned to each tile (Sturbois et al. 2021). Those metrics were represented in a 2D cartography following Sturbois et al. (2021).

Alternatively, we computed a multivariate regression tree to partition tiles based on Hellinger-transformed assemblage net changes, constrained by environmental drivers (MRT; De'ath 2002; function mvpart. R of package mvpart). Splits were selected in order to maximise the among-group sum of squares. The number of groups was chosen to minimise the cross-validation error (CV error ranging between 0 and 1).

Details of analyses are provided below.
Firstly, we compute a PCA with community matrix of the year 2015. Data are then square rooted (i.e. Hellinger transformation).

```
plot_i = plot_i+1
cov_2015 = Matrix_RDA_group_2015[,8:15]
env_2015 = Matrix_RDA_group_2015[,21:30]
env_2015=apply(env_2015, MARGIN = 2, FUN = function(X) (X - min(X))/diff(range(X))) # We sc
cov_hel_2015 = sqrt(cov_2015) #we square to perform a hellinger transformation on assemblag
cov_hel_pca_2015 = rda(cov_hel_2015)
```

```
#screeplot(cov_hel_pca, bstick=TRUE)
proportion_explained_2015 = sum(summary(cov_hel_pca_2015, display=NULL)[["cont"]][["importance"]][2,1:2
cleanplot.pca(cov_hel_pca_2015, label.sites = F,plot_sites_col = T, col_factor = side_majority)
#mtext(paste0("Proportion of variance explained ", round(proportion_explained_2015), " %"), side=3)
legend("bottomright", legend = levels(as.factor(side_majority)), pch = 20, cex = 0.8, col = as.factor(l
mtext(paste0("Var. explained: PC1 = ", as.character(round(summary(cov_hel_pca_2015, display=NULL)[["con
```

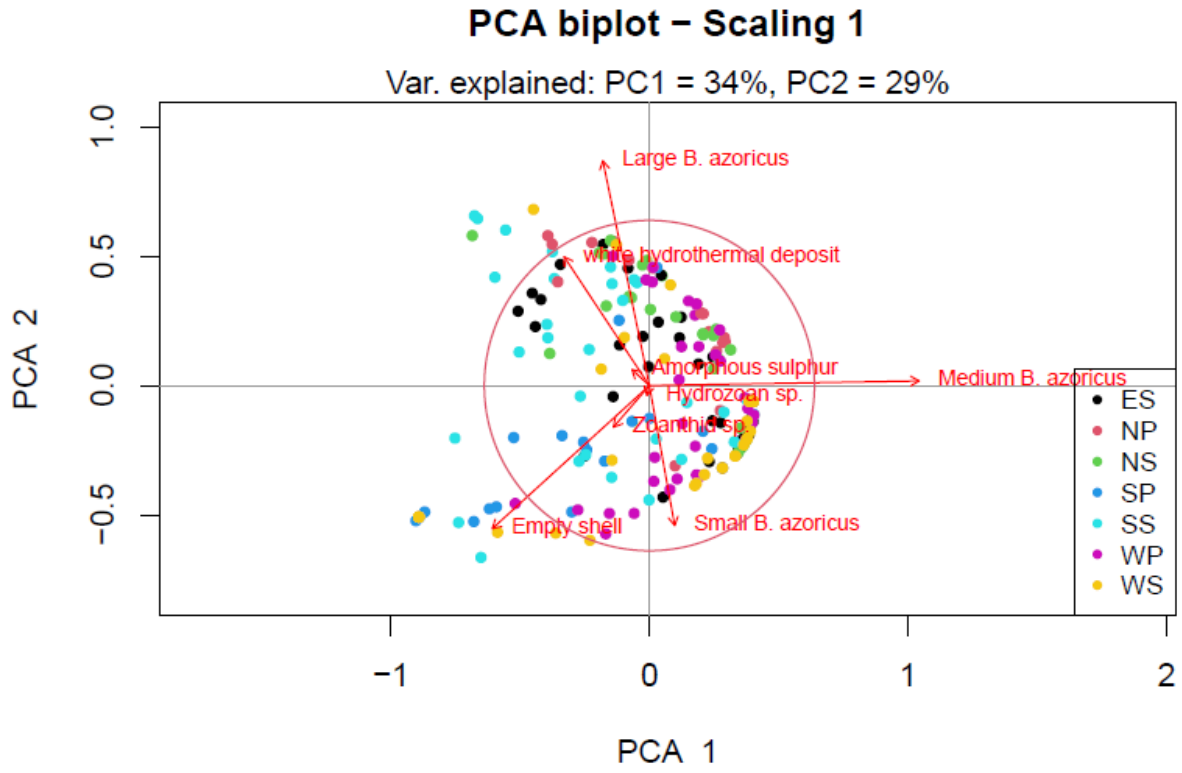

Supplementary Figure III.16. Biplot of the first two axes of the PCA. Points refer to each observation. The colour refers to the side of the edifice. Arrows refer to the influence of each assemblage on the data distribution in the PC space.

The PCA exhibits a clear arc gradient from white material, size-decreasing *B. azoricus* assemblages to empty shells (Supplementary Figure III.16). Clearly, we can see that sides do not have the same distribution in the PCA space.

We now compute a RDA with environmental factors with the year 2015 and test the significance of the axes. Additionally, we test for environmental variables that may significantly correlate with the significant axes.

```
plot_i = plot_i+1
env_2015=as.data.frame(env_2015)
cov_hel_rda_2015 = rda(cov_hel_2015~., data=env_2015)
triplot.rda(cov_hel_rda_2015, ax1=1, ax2=2, label.sites = F, plot_sites_col = T, col_factor = side_maj
```

```
## ------------------------------------------------------------------------
## Site constraints (lc) selected. To obtain site scores that are weighted
## sums of species scores (default in vegan), argument site.sc must be set
## to wa.
## ------------------------------------------------------------------------
##
##
## No factor, hence levels cannot be plotted with symbols;
## 'plot.centr' is set to FALSE
```

```
legend("bottomright", legend = levels(as.factor(side_majority)), pch = 20, cex = 0.8, col = as.factor(
mtext(paste0("Proportion of variance explained: Constrained by RDA axes", round(sum(summary(cov_hel_rd
```

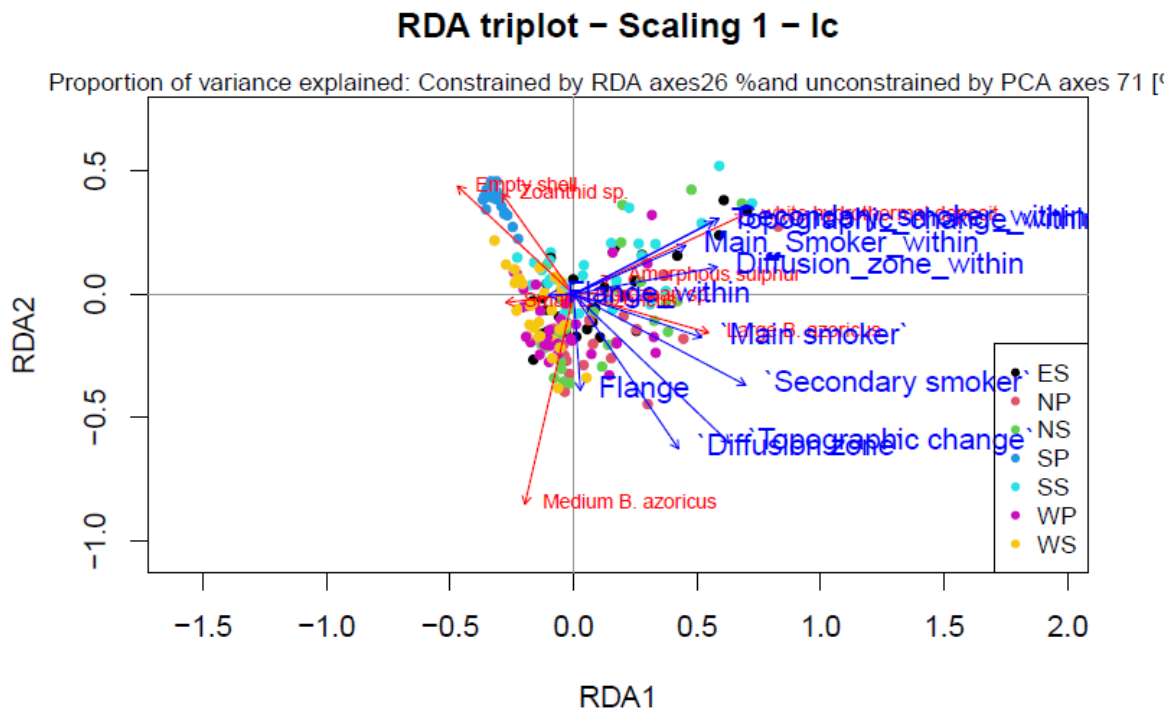

Supplementary Figure III.17. Triplot of the first two axes of the RDA. Points refer to each observation. The colour refers to the side of the edifice. Arrows refer to the influence of each assemblage (red) and the correlation with environmental variables (blue).

We now test to identify what axes are significant after which we test what environmental variable significantly influences each of the significant axes.

```
(axes <- anova(cov_hel_rda_2015, by = "axis"))
```

```
## Permutation test for rda under reduced model

## Forward tests for axes
## Permutation: free
## Number of permutations: 999
##
## Model: rda(formula = cov_hel_2015 ~ `Main smoker` + `Secondary smoker` + `Diffusion zone` + Flange +
##           Df Variance       F Pr(>F)
## RDA1       1 0.053712 38.2231  0.001 ***
## RDA2       1 0.044445 31.6288  0.001 ***
## RDA3       1 0.006405  4.5580  0.313
## RDA4       1 0.002946  2.0964  0.940
## RDA5       1 0.001450  1.0320  0.998
## RDA6       1 0.000317  0.2252  1.000
## RDA7       1 0.000236  0.1683  1.000
## RDA8       1 0.000009  0.0064  1.000
## Residual 191 0.268395
## ---
## Signif. codes:  0 '***' 0.001 '**' 0.01 '*' 0.05 '.' 0.1 ' ' 1
```

```
nb.ax <-
    length(which(axes[ , ncol(axes)] <=  0.05))
rda.axes <-
  scores(cov_hel_rda_2015,
         choices = c(1:nb.ax),
         display = "lc",
         scaling = 1)
summary(lm(rda.axes~., data = env_2015))
```

```
## Response RDA1 :
##
## Call:
## lm(formula = RDA1 ~ `Main smoker` + `Secondary smoker` + `Diffusion zone` +
##     Flange + `Topographic change` + Main_Smoker_within + Secondary_smoker_within +
##     Diffusion_zone_within + Flange_within + Topographic_change_within,
##     data = env_2015)
##
## Residuals:
##        Min         1Q     Median         3Q        Max
## -1.030e-15 -8.250e-18  1.037e-17  2.479e-17  2.306e-16
##
## Coefficients:
##                             Estimate Std. Error    t value Pr(>|t|)
## (Intercept)               -1.197e-01  2.020e-17 -5.923e+15   <2e-16 ***
## `Main smoker`             -1.152e-01  1.052e-16 -1.095e+15   <2e-16 ***
## `Secondary smoker`         3.375e-01  8.746e-17  3.859e+15   <2e-16 ***
## `Diffusion zone`           1.696e-03  8.834e-17  1.920e+13   <2e-16 ***
## Flange                    -1.203e-02  3.057e-17 -3.935e+14   <2e-16 ***
## `Topographic change`      -2.070e-02  9.666e-17 -2.142e+14   <2e-16 ***
## Main_Smoker_within         6.415e-02  5.983e-17  1.072e+15   <2e-16 ***
## Secondary_smoker_within    1.049e-01  6.405e-17  1.638e+15   <2e-16 ***
## Diffusion_zone_within      1.155e-01  3.821e-17  3.023e+15   <2e-16 ***
## Flange_within             -3.344e-02  3.983e-17 -8.395e+14   <2e-16 ***
## Topographic_change_within  1.183e-01  3.932e-17  3.010e+15   <2e-16 ***
## ---
## Signif. codes:  0 '***' 0.001 '**' 0.01 '*' 0.05 '.' 0.1 ' ' 1
```

```
##
## Residual standard error: 9.053e-17 on 189 degrees of freedom
## Multiple R-squared:      1,  Adjusted R-squared:      1
## F-statistic: 1.504e+31 on 10 and 189 DF,  p-value: < 2.2e-16
##
##
## Response RDA2 :
##
## Call:
## lm(formula = RDA2 ~ `Main smoker` + `Secondary smoker` + `Diffusion zone` +
##     Flange + `Topographic change` + Main_Smoker_within + Secondary_smoker_within +
##     Diffusion_zone_within + Flange_within + Topographic_change_within,
##     data = env_2015)
##
## Residuals:
##        Min         1Q     Median         3Q        Max
## -8.349e-16 -1.042e-17  7.370e-18  1.866e-17  3.111e-16
##
## Coefficients:
##                             Estimate Std. Error    t value Pr(>|t|)
## (Intercept)                1.627e-01  2.010e-17  8.094e+15   <2e-16 ***
## `Main smoker`             -3.237e-02  1.047e-16 -3.092e+14   <2e-16 ***
## `Secondary smoker`         1.663e-01  8.703e-17  1.911e+15   <2e-16 ***
## `Diffusion zone`          -9.739e-02  8.790e-17 -1.108e+15   <2e-16 ***
## Flange                    -6.995e-02  3.041e-17 -2.300e+15   <2e-16 ***
## `Topographic change`      -3.198e-01  9.618e-17 -3.325e+15   <2e-16 ***
## Main_Smoker_within         3.949e-02  5.954e-17  6.633e+14   <2e-16 ***
## Secondary_smoker_within    1.070e-01  6.373e-17  1.679e+15   <2e-16 ***
## Diffusion_zone_within      4.054e-02  3.802e-17  1.066e+15   <2e-16 ***
## Flange_within              1.807e-02  3.963e-17  4.559e+14   <2e-16 ***
## Topographic_change_within  1.214e-01  3.913e-17  3.102e+15   <2e-16 ***
## ---
## Signif. codes:  0 '***' 0.001 '**' 0.01 '*' 0.05 '.' 0.1 ' ' 1
##
## Residual standard error: 9.008e-17 on 189 degrees of freedom
## Multiple R-squared:      1,  Adjusted R-squared:      1
## F-statistic: 1.257e+31 on 10 and 189 DF,  p-value: < 2.2e-16
```

Only the first two axes are significant. All variables significantly contribute to explain the axes. We clearly see the importance of hydrothermal vent features as well as topographic change for SS, ES, WP and NS based on the RDA triplot (Supplementary Figure III.17). They explain predominantly the distribution of large mussels, black sulphide and white material. This means those assemblages are located close to hydrothermal activity, at least closer to zoanthid and small to medium mussel assemblages that are not correlated with hydrothermal activity. This shows that they locate further away than the hydrothermal activity and suggests that their presence may be filtered by vent fluid exposure.

We now start the temporal analysis. First we perform a RDA for 2015 and 2020 separately.

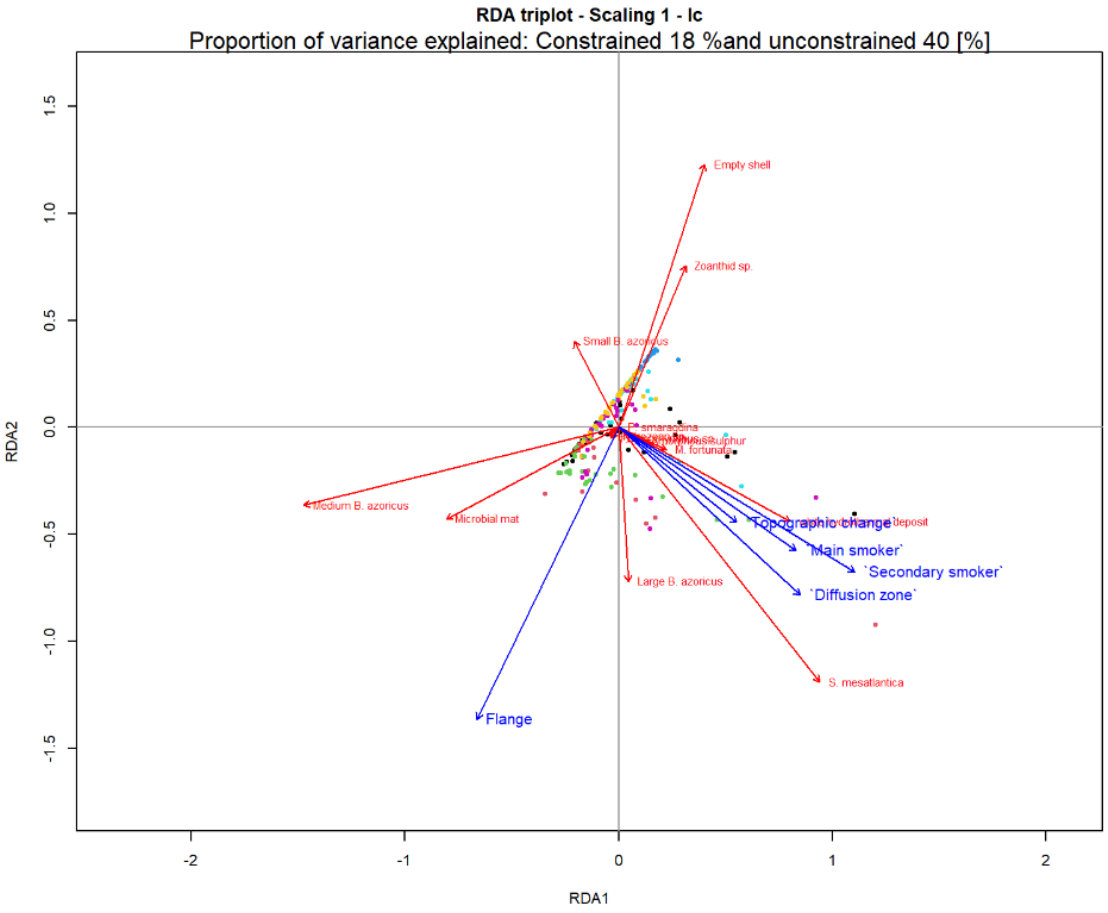
RDA triplot - Scaling 1 - lc
Proportion of variance explained: Constrained 18 %and unconstrained 40 [%]
Empty shell
Zoanthid sp.
Small B. azoricus
Medium B. azoricus
Microbial mat
Large B. azoricus
Topographic change
Main smoker`
`Secondary smoker`
`Diffusion zone`
S. mesatlantica
Flange
RDA1
RDA2

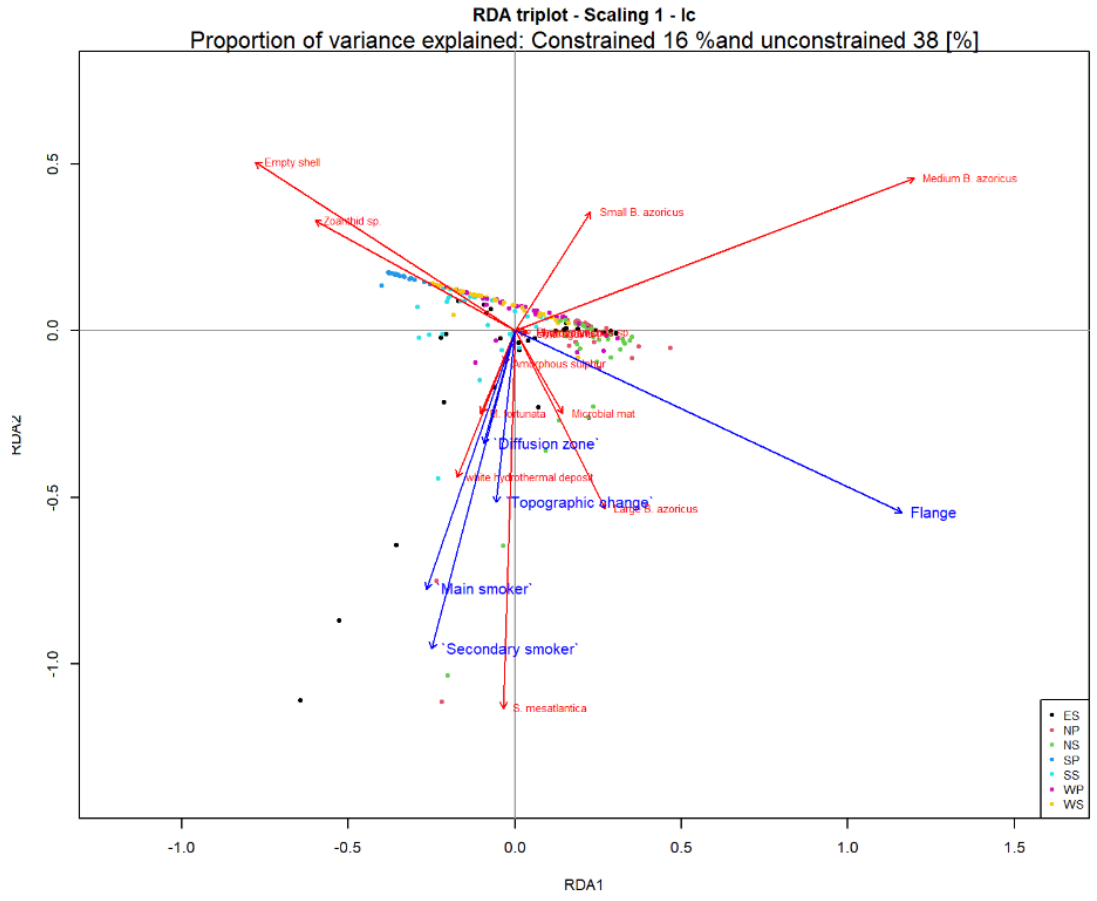
RDA triplot - Scaling 1 - lc
Proportion of variance explained: Constrained 16 %and unconstrained 38 [%]
Empty shell
Zoanthid sp.
Small B. azoricus
Medium B. azoricus
Microbial mat
`Diffusion zone`
Topographic change
Large B. azoricus
Flange
Main smoker`
`Secondary smoker`
S. mesatlantica
ES
NP
NS
SP
SS
WP
WS
RDA1
RDA2

Supplementary Figure III.18. Triplots of the first two axes of the RDA (up to bottom: 2015, 2020). Points refer to each observation. The colour refers to the side of the edifice. Arrows refer to the influence of each assemblage (red) and the correlation with environmental variables (blue).

Patterns remain the same from 2015 to 2020, although each RDA is oriented differently. As the orientation is meaningless for RDA, we conclude that the structure of the spatial distribution is stable enough so that no pattern of differences among years emerges from the data (Supplementary Figure III.18). Changes may be constrained to specific tiles and local areas. Still, we observe a pattern of change for microbial mat cover. It appears to coincide in tiles with medium mussels in 2015, but, in 2020, the correlation gets considerably lower and poorly explained by the two axes. This lower importance of microbial mats in the RDA of 2020 suggests microbial mats declined over the edifice. As a result, we exclude them from the next analyses as their dynamics may be different than for the dynamics of the mussels (see Chapter II). We now consider using a trajectory analysis in order to assess for changes in space and time together. To do so, we bind by rows each community matrices of 2015-2018-2020.

```
cov_aggregated = rbind(cov_2015,cov_2018,cov_2020)
cov_hel_aggregated = sqrt(cov_aggregated)
options(warn=-1)
library(Kendall)
library(ecotraj)
```

```
## Le chargement a nécessité le package : Rcpp
```

```
#plot(pcoa(dist(cov_hel_aggregated, method="euclidean"))$vectors[,1:2])
trajectoryPCoA(dist(cov_hel_aggregated, method="euclidean"), axes=c(1,2), sites=c(rep(seq(1,200),3)), l
```

```
#trajectoryPCoA(dist(cov_hel_aggregated, method="euclidean"), axes=c(3,4), sites=c(rep(seq(1,200),3)),
```

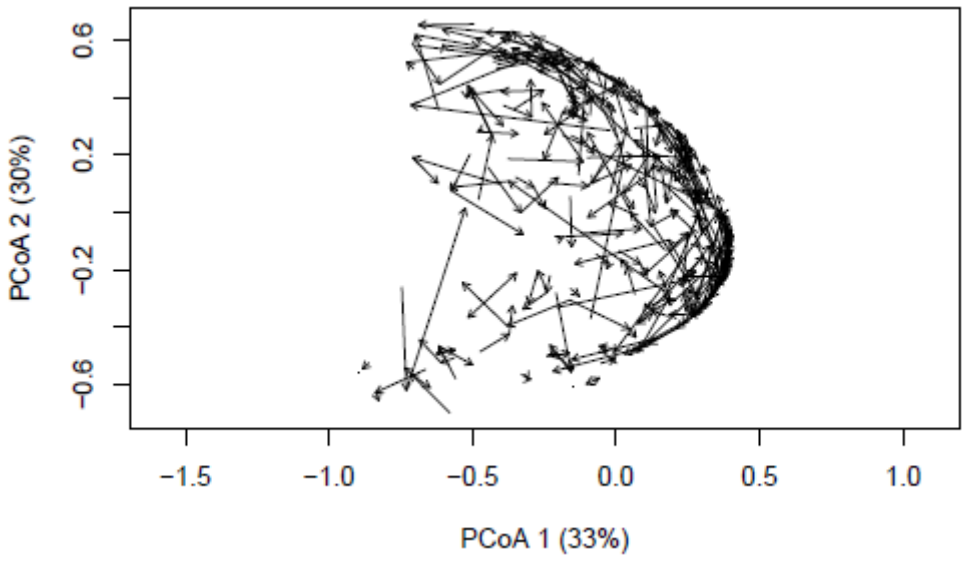

Supplementary Figure III.19. Trajectory of tile assemblages represented on the first two axes of the PCo space. Consecutive arrows describe the change from 2015 to 2018 and from 2018 to 2020.

Observations over time seem to distribute as previously observed in the PCA. However, some of those observation appear considerably to change as suggested by large arrows "short-cutting" the arc formed by the observations (Supplementary Figure III.19). However, other observations seem to change with a lower intensity as they move along that arc. We assess for each tile if its trajectory is "departing" or "recovering" from its initial position (Sturbois et al. 2021). For instance, "recovering" tiles will be identified by detecting the tiles undergoing a shorter change (i.e. trajectory length) from 2015 to 2018 than from 2015 to 2020. We reproject this indicator for with XY coordinates to analyse the spatial pattern of change.

```
D = dist(cov_hel_aggregated, method="euclidean")
nc = trajectoryDistances(D, sites=c(rep(seq(1,200),3)))
segment = segmentDistances(D, sites=c(rep(seq(1,200),3)))
lengths = trajectoryLengths(D, sites=c(rep(seq(1,200),3)))
angles=trajectoryAngles(D, sites=c(rep(seq(1,200),3)), stats=F)
dir=trajectoryDirectionality(D, sites=c(rep(seq(1,200),3)))

T1_2 = lengths$S1
T2_3 = lengths$S2
indices_to_extract=cbind(seq(from=1, to=400,by=2),seq(from=2, to=400,by=2))
T1_3 = segment$Dinifin[indices_to_extract]

#symbols(x=Centroids$Centroid_x, y=Centroids$Centroid_y, circles=T1_3,
#       ann=F, bg="grey", fg="black", inches =FALSE)
#symbols(x=Centroids$Centroid_x, y=Centroids$Centroid_y+T1_3, squares=T1_2,
#       ann=F, bg="grey", fg="black", inches =FALSE, add=T)
#symbols(x=Centroids$Centroid_x, y=Centroids$Centroid_y-T1_3, squares=T2_3,
#       ann=F, bg="grey", fg="black", inches =FALSE, add=T)

#Recover?
recover = (T1_2>T1_3)*1
ti_pch = rep(NA, length(recover))
ti_pch[which(recover==1)]=25
ti_pch[which(recover==0)]=24
recover[which(recover==1)]="black"
recover[which(recover==0)]="grey"



#recover[which(angles$`S1-S2`<=90)]="black"
#recover[which(angles$`S1-S2`>90)]="grey"
#recover[which(is.na(angles$`S1-S2`))]=NA

plot(x=Centroids$Centroid_x, y=Centroids$Centroid_y, pch=1, cex=T1_3*3,col="blue", lwd=2, xlab="X [m]"
points(x=Centroids$Centroid_x, y=Centroids$Centroid_y-0.5, pch=24, cex=T1_2*3, bg=recover)
points(x=Centroids$Centroid_x, y=Centroids$Centroid_y+0.5, pch=ti_pch, cex=T2_3*3, bg=recover)
#legend("topright", , inset=c(-0.25, 0),
legend("bottomright", legend=c("Trajectory","Recovering", "Departing", "Period","2015-2020", "2015-201
```

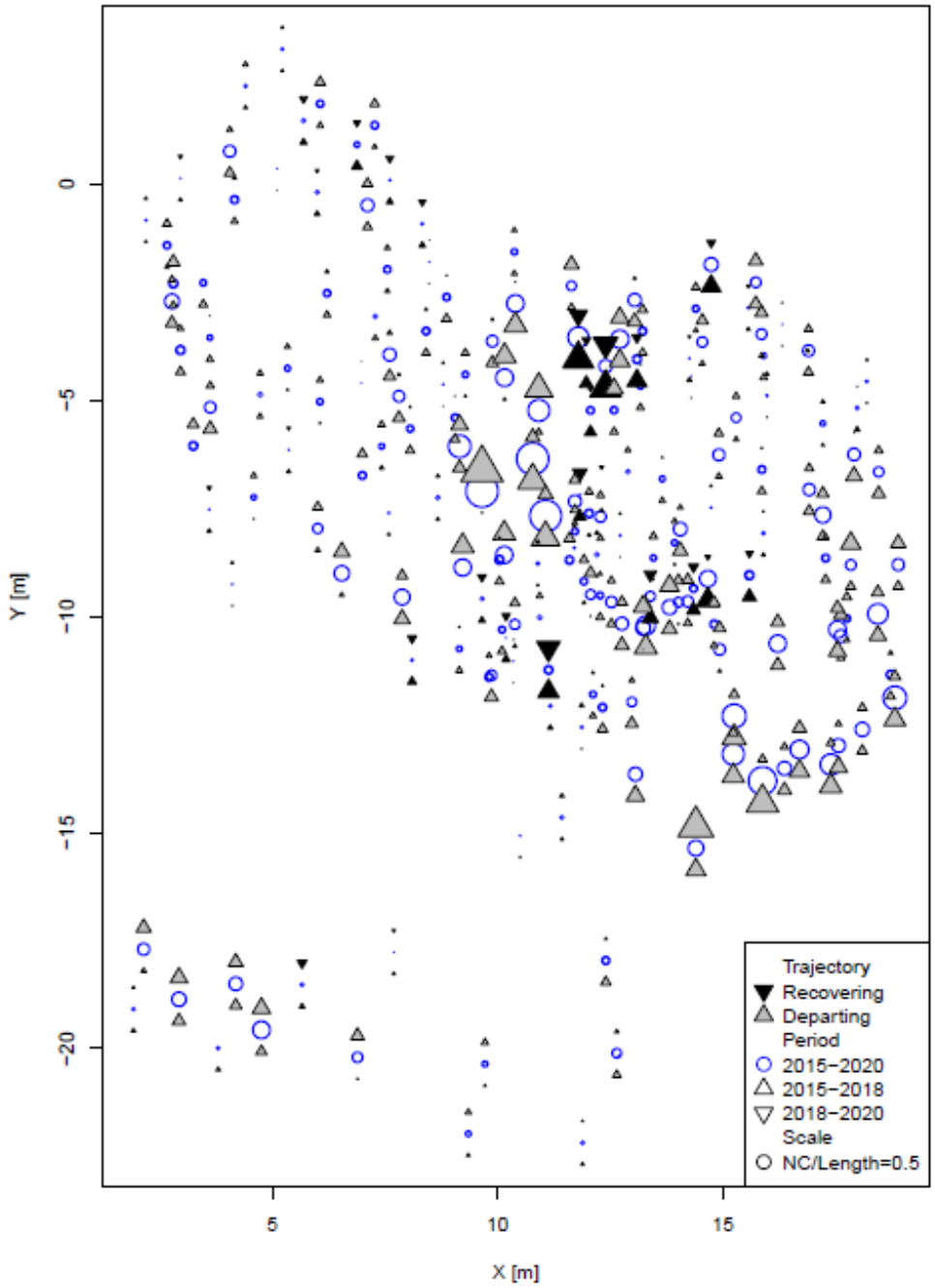

Supplementary Figure III.20. Reprojection of tile trajectory length patterns in space. The circle depicts the total trajectory length from 2015 to 2020, while triangles refer to trajectory length from 2015 to 2018. The triangle can be either black (recovering) or grey (departing). Size of symbols are relative to the scale provided in the low-bottom inset.

It seems that we detect an event of change in the South-East as assemblages are “departing” there (Supplementary Figure III.19). Additionally, we detect an increase in the centre of Eiffel Tower (Supplementary Figure III.19). Because of changes appear to be local, we decide to change our strategy and compute the net change of cover between the year 2015 and year 2020. With that new matrix, we perform a multivariate regression tree that will help us to identify any of the environmental drivers potentially responsible for that change.

```
env_2015_2020=env_2015_2020[,c(1,2,3,4,6,7,8,9,10)]
res.part = mvpart(data.matrix(cov_2020-cov_2015) ~ ., data=env_2015_2020, size=2, xv="pick", xvmult=10

## X-Val rep : 1  2  3  4  5  6  7  8  9  10  11  12  13  14  15  16  17  18  19  20  21  22  23  24
## Minimum tree sizes
## tabmins
##  1  2  9 11 12
## 72 24  1  2  1
```

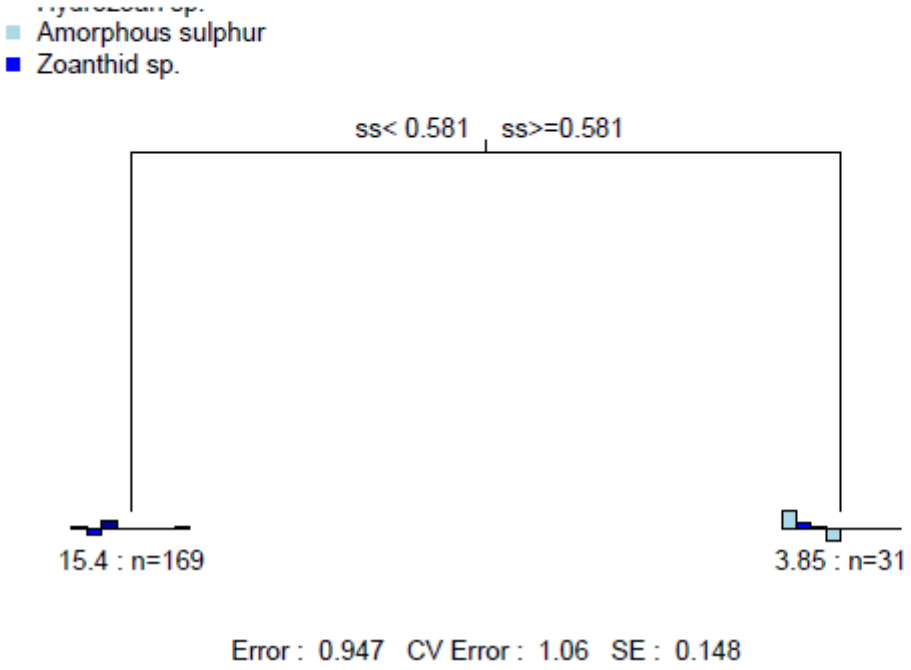

Supplementary Figure III.21. MRT analysis splitting the dataset the first node. Above the node, the environmental the variable responsible for that change is displayed. Histograms refer to the average net change displayed in the order of biological/substratum categories stored in the community matrix.

The MRT is split at the first node between a group of 31 and 169 tiles. The group of 31 tiles seems to be explained by an increase of large mussel assemblage and a decrease of white hydrothermal substratum (see the blue bars being the average of the cover change for a given assemblage/substratum; Supplementary Figure III.21). This suggests a colonisation from large mussels in this area following an increase of distal exposure to secondary smokers (i.e. see ss >=0.581 above the split; Supplementary Figure III.21). Therefore we extract those tiles to plot them with the XY coordinate system of Eiffel Tower in order to confirm if the changes we detected with the MRT were similar to those observed with the trajectory analysis.

```
#res.part = mvpart(data.matrix(cov_hel_2015) ~ ., data=env_2015, size=8, xv="min", xvmult=100)

MRT.24F.3gr = res.part$where
# [1] 2 2 2 2 5 5 5 5 5 4 4 4 4

# Save the classification in 3 groups, to be drawn on top of the PCA ordination (next step)
MRT.24F.3gr  = data.frame(MRT.24F.3gr)
```

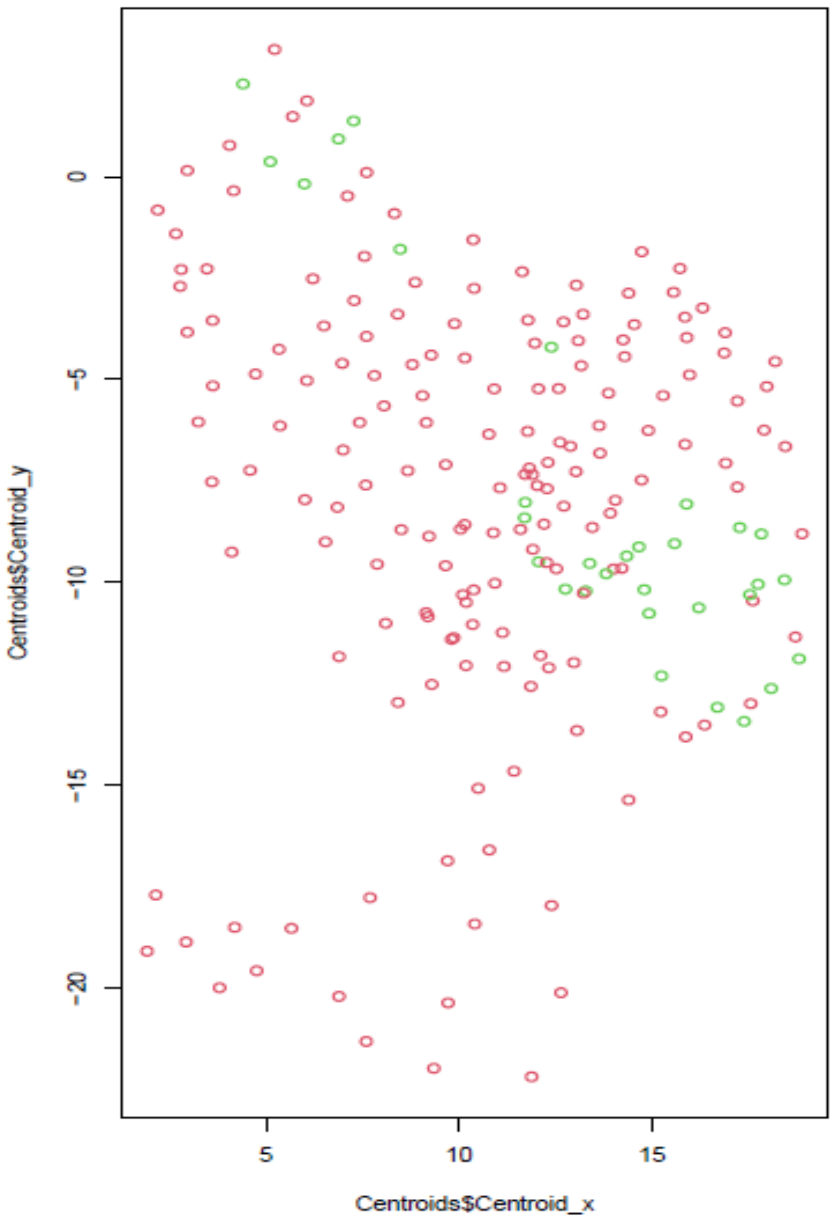

Supplementary Figure III.22. Spatial reprojection of the tiles that were separated by the MRT. Red reports tiles split in the left (n = 169) and green shows tiles contained in the right split (n = 31) as shown in Supplementary Figure III.21.

We detect a change predominantly located in the South-East. This is redundant with what we observed in the cartography of the trajectory analysis. However, we were not able to explain the change in small mussel assemblage in the central area. Those analyses and visualisation methods were useful as they helped used to dissect the regime of change from the overall pattern being stable except for microbial mats to the local patterns for vent mussels. Furthermore, it helped us to define the results that were relevant to show in the manuscript. For instance, we created maps of cover following the results provided by those multivariate analyses (Figure III.6).

III.6 Synthèse des résultats

Cette étude pionnière a utilisé des annotations 3D réalisées sur une série pluriannuelle de reconstructions photogrammétriques. Elle nous a permis de comprendre la variabilité à échelle fine de l'environnement et la dynamique de la faune à l'échelle de l'édifice Tour Eiffel (champ hydrothermal Lucky Strike, dorsale médio-atlantique). Nos résultats confirment les résultats et les hypothèses proposées par Cuvelier et al. (2011b). Au cours des 5 années de suivi, les tapis microbiens ont subi un déclin général soulignant l'influence probable de facteurs agissant à des échelles temporelles plus grandes que celle de l'étude. Les événements magmatiques précédemment détectés sur le champ hydrothermal grâce à l'observatoire EMSO-Açores semblent corréler avec les points de rupture observés (2001: Dziak et al. 2004; 2005: Ballu et al. 2019). A l'inverse, la couverture de moules est restée très stable, étendant ainsi la stabilité connue de cette population climax à une période de 25 ans. Le déplacement petite échelle (dm) de l'activité hydrothermale est resté concentré dans des zones étendues d'émission à l'ouest de l'édifice. Cette variabilité résulte de l'ouverture ou de la fermeture des sorties de fluide, de l'accrétion progressive de matériaux sulfurés au niveau d'affleurements et de surplombs ou d'effondrements de cheminées. Cela suggère un régime de modifications et de perturbations spatialement localisées et de faible intensité s'étalant sur plusieurs années. La variabilité des assemblages de moules *Bathymodiolus azoricus* s'est principalement traduite par des modifications à l'échelle infra-métrique dans le voisinage immédiat des sorties de fluide. Cette étude a montré que ces moules sont capables de modifier leur position en réponse aux changements locaux, suggérant l'importance de la mobilité comme trait fonctionnel pour évaluer leur adaptation à l'environnement. Les transitions entre assemblages montrent que ces changements sont relativement constants entre les pas de temps, maintenant ainsi un équilibre dynamique du système écologique. Nous proposons ainsi un nouveau modèle de succession complétant celui de Cuvelier et al. (2011b).

Ces résultats corroborent ceux de l'étude du chapitre II avec une variabilité infra-métrique localisée dans le voisinage de l'activité hydrothermale. L'invariance d'échelle confirme que, dans le cas de Tour Eiffel, les processus révélés par l'étude à haute fréquence grâce au module d'observation TEMPO informent sur ceux agissant à l'échelle de l'édifice et permet de valider l'utilisation du module écologique pour le suivi des communautés associées à Tour Eiffel.

L'édifice Tour Eiffel procure ainsi un environnement relativement stable pour les populations locales sur le long terme. A l'échelle du champ, d'autres facteurs peuvent influencer la structure

des communautés incluant la circulation hydrothermale générale, la composition des fluides, le substrat et/ou l'export de particules d'origine chimiosynthétique vers la périphérie (Arquit 1990; Boschen et al. 2016; Gerdes et al. 2019b). En effet, à l'échelle du champ, les sites varient dans leur configuration et la chimie de leur fluide (Barreyre et al. 2012; Chavagnac et al. 2018). Pour ces raisons, ils ont été regroupés en quatre domaines chimiques distincts (Chavagnac et al. 2018), mais l'impact sur la faune est encore mal connu. Afin de déterminer les facteurs contrôlant la dynamique des communautés benthiques à l'échelle du champ, nous avons réalisé des mosaïques 2D de plusieurs sites du champ Lucky Strike grâce à la caméra verticale du ROV Victor 6000 à partir de transects horizontaux effectués à 3 m du fond. Cependant, en raison de la limite du temps disponible en mer, il n'a pas été possible de réaliser un suivi de ces boîtes dans le temps. L'analyse de ces images permet néanmoins de fournir une première description de la faune périphérique des sites hydrothermaux actifs ainsi que de déterminer les facteurs environnementaux responsables de la répartition spatiale des habitats et des communautés sur le champ Lucky Strike en focalisant sur l'hétérogénéité de l'habitat, les variables de terrain et la proximité aux sources de fluide.

Chapter IV

Spatial distribution of hydrothermal and peripheral assemblages at the scale of the vent field

Spatial distribution of hydrothermal and peripheral assemblages at the Lucky Strike hydrothermal vent field

Van Audenhaege Loïc[1]*, Matabos Marjolaine[1], Ramière Annah[1], Marcillat Marin[1], Soto Vega Pedro Juan[1], Marticorena Julien[4], Colaço Ana[5], Cannat Mathilde[3], Sarradin Pierre-Marie[1], Sarrazin Jozée[1]

[1] *Univ Brest, CNRS, Ifremer, UMR6197 BEEP, F-29280 Plouzané, France*

[2] *Département de sciences biologiques, Université de Montréal, Montréal, Québec, Canada*

[3] *Equipe de Géosciences Marines, Université de Paris, Institut de Physique du Globe de Paris, UMR CNRS, Paris, France*

*__Corresponding author__: loic.van.audenhaege@ifremer.fr/loic.vanaudenhaege@gmail.com

Keywords: seabed images, hydrothermal vent, periphery, faunal distribution, mapping, environmental drivers, deep-sea

To be submitted in 2023

Abstract

The continuous improvement of underwater platforms and optical technologies have provided access to images of the deep seabed enabling the mapping of habitats and large epibenthic organisms. Despite extensive survey efforts, the distribution of vent and non-vent species have been rarely resolved over vent field scales. In order to assess the sphere of influence of hydrothermal activity, we annotated the environment as well as biological and microbial assemblages at and around four active vent edifices of the Lucky Strike vent field. Parallel transects of seabed images were done, covering a total surface of ~ 23340 m². We then developed an innovative workflow that consisted in geo-referencing each image imprint to produce a map of the vent and non-vent fauna and environmental factors related to bathymetry, vent activity and substratum types. Using multivariate analyses, we assessed the drivers of the observed spatial distribution patterns. Edifices in the South-East harboured large mussel assemblages associated with zoanthid assemblages. The low cover of mussels and the absence of zoanthids at the south-central edifices suggest the importance of mature edifices to host extensive cover of vent assemblages such as in the South-East. In addition to "white material" associated with vent activity, we observed the wide distribution of orange deposits, testifying of another source of primary productivity endorsed by iron-oxidising mats. Their large cover over the vent field suggests their geochemical significance but no ecological link with the vent fauna was observed. A few morphospecies dominated the non-vent communities. In the close proximity of sites or fluid exits areas, the distribution of sessile morphospecies was driven by particular affinity or avoidance to active venting. In the periphery, the occurrence of an adequate substratum for attachment or suspension feeding drove organisms' spatial distribution. Our study highlighted the potential of seabed image acquisition to better apprehend the different mechanisms responsible for the hydrothermal influence over large spatial scales. As a result, it opens new research perspectives to characterise the trophic influence of the vent habitat on epibenthic megafauna for which a targeted sampling can now be designed.

IV.1 Introduction

Identifying and characterising the factors driving the distribution of biological communities is a major goal in ecology, and especially for management for which baseline information are needed (Levin 1992). Hydrothermal vent fields can harbour sulphide massive deposits (SMS) that are of interest to the mining companies (Boschen et al. 2013). Mining activities if they occur could generate direct (e.g. habitat destruction) and indirect impacts (e.g. sediment plume, noise, light) that could severely damage surrounding benthic and pelagic communities (Van Dover 2014; Levin et al. 2016b). This economic context motivates the need to investigate the spatial structure of benthic communities in the close vicinity of active and inactive vent sites as well as their peripheries (Levin et al. 2016a; Van Dover 2019).

Numerous studies have demonstrated the importance of the vent dilution gradient to create a myriad of chemical habitats that organisms occupy based on their trophic need and tolerance to vent exposure (Sarrazin et al. 1999; Levesque et al. 2003, 2006; Bergquist et al. 2007; Moore et al. 2009). These mosaics of habitats result in a spatial zonation of the vent fauna, described from seabed imagery at several vent fields in the Pacific, Indian, Antarctic and Southern oceans (Cuvelier et al., 2009; Fisher et al., 1994; Gerdes et al., 2019; Hessler et al., 1985; Marsh et al., 2012; Sarrazin et al., 1997; Zhou et al., 2018). Typically, endemic vent species live nearby the emissions of vent fluids in a "central vent zone", often represented by an active sulphide structure or by fissures on the seafloor (Arquit 1990; Podowski et al. 2009; Kim and Hammerstrom 2012). As the distance to the vent fluid increases, conditions tend to become similar to the surrounding deep-sea ecosystem, allowing the colonization of an outer fauna, composed of less tolerant species, up to tens of metre in the periphery of active areas (Copley et al. 1999; Marcus and Tunnicliffe 2002; Podowski et al. 2009; Fabri et al. 2011; Kim and Hammerstrom 2012). These peripheral organisms can form dense assemblages of suspension-feeding and microcarnivorous organisms contrasting with the low biomass found in the background communities (Hessler et al. 1988; Arquit 1990; Sen et al. 2014). Stable isotope investigations revealed trophic flux to the peripheral fauna linked to chemosynthetic primary productivity export, possibly through enhanced advective currents (Galkin 1997; Erickson et al. 2009). Moreover, non-vent predators making incursion to feed on vent species also contribute to the export of organic matter (Van Dover 1986; Tunnicliffe and Jensen 1987; Colaço et al. 1998). The contribution of chemosynthesis-derived material to the diet of non-vent fauna declines with distance in favour of photosynthesis-derived material (Alfaro-Lucas et al. 2020; Roohi et al. 2022). Rare extensive effort of image acquisition suggested the

influence of vents on faunal spatial distribution over hundreds of metres (Arquit 1990; Gerdes et al. 2019b). As the distance from venting increased, the authors documented a density peak of non-vent species in the "distal vent zone" before the community progressively switched to the regular regional deep-sea community, in the "non-vent zone" (Arquit 1990; Gerdes et al. 2019b). In the Manus Basin, differences in peripheral community composition seems higher within sites than among sites (Collins et al. 2012). Not only the distance from the vent, but the nature of the substratum also influences habitat suitability for colonisation of sessile organisms (Arquit 1990; Sen et al. 2016; Gerdes et al. 2019b; Soto and Kim 2022). Inactive vent areas also provide habitat to communities that are different from those found at active vents (Van Dover 2011, 2019; Collins et al. 2012; Gerdes et al. 2019b; Neufeld et al. 2022). Those habitats may provide local food supply through the oxidation of vent deposits and the accumulation of bacterial biomass (Juniper and Sarrazin 1995; Erickson et al. 2009; Kato et al. 2010). However, extensive mapping of non-vent fauna has mostly taken place in the Pacific, and much less is known about community composition and distribution at the Mid-Atlantic Ridge. Therefore, there is an urgent need to document peripheral communities as well as map their detailed distribution to improve our knowledge on the large-scale processes involved in shaping the "sphere of influence" of vents (Levin et al. 2016a).

This lack of knowledge is also true for well-known vent field such as Lucky Strike (LS) on the MAR. LS is a basalt-hosted vent field harbouring a central fossil lava lake in the central area surrounded by three volcanic cones (Langmuir et al. 1997; Ondréas et al. 2009). At LS, chemical characteristics of vent outflows can strongly vary among sites and would belong to five chemistry domains (Pester et al. 2012; Chavagnac et al. 2018b). Moreover, photomosaic cartography has revealed different settings of venting depending on the types of substratum and the presence of faults (Barreyre et al. 2012). Despite knowledge on the habitat, recurrent visits allowing the acquisition of significant ecological knowledge since LS discovery and the deployment of the deep-sea EMSO-Azores observatory in 2010, peripheral communities remain poorly studied (e.g. Cuvelier et al. 2009; Husson et al. 2017). The only study to date looking at peripheral communities involved a metabarcoding approach on a very small limited area (Cowart et al. 2020). Results highlighted strong differentiation between active, inactive and peripheral habitats based on metazoan community composition.

The recent development of underwater remote sensing tools have provided non-invasive ways to characterise the natural variability of deep-sea communities over large and continuous spatial scales. Although only a visible fraction of the fauna can be imaged (Cuvelier et al. 2012), the

underwater imaging technology typically picture organisms larger than a centimetre (Durden et al. 2016). Over the last decade, the computation of accurate cartography has also benefited from the improvement in the accuracy of underwater navigation (Steinke and Buckham 2005). Using a high-resolution camera deployed on an underwater vehicle, this study aims to document the peripheral fauna of LS and unravel the spatial distribution of peripheral assemblages in order to investigate the sphere of influence of hydrothermal vents. High-resolution mapping from seafloor imagery will be combined to the extensive dataset gathered through the EMSO-Azores observatory to (1) map and identify the peripheral fauna, (2) evaluate the presence of distinct distributional patterns along the vent dilution gradient from the active sites to their peripheries, (3) evaluate what factors are driving the spatial distribution of various taxa and (4) determine if those patterns are recurrent or vary among active vent sites on the LS vent field.

IV.2 Material and methods

IV.2.1 Building the dataset

Seabed images were collected during the MoMARSAT 2018 cruise on the research vessel *L'Atalante* using the Remotely Operated Vehicle (ROV) *Victor6000* (Cannat 2018). The ROV was equipped with a downward-looking HD OTUS camera capturing one .JPG image (4000 x 6000 pixels) per 3 seconds. Parallel transects of the ROV were predefined to image the seabed over rectangular areas of a few thousands of m², hereafter called "transect box". Transects were spaced ~ 1.8 m apart each other to ensure 70% overlap for photogrammetry reconstruction. The ROV was flown at a constant speed (~ 0.2 $m.s^{-1}$) and altitude (~ 4 m) using the cruise control capability of *Victor6000* (Simeoni et al. 2007). Repositioning of the ROV was recorded with an ultra-short baseline system (USBL), a Doppler velocity logger (DVL) and corrected with photonic inertial navigation system (PHINS). Transect boxes were performed at two different regions of LS in the south-centre and south-east of the vent field (Figure IV.1). Each transect box covered areas in the vicinity of the following edifices: i) Eiffel Tower (ET), ii) Montségur (MS), iii) White Castle (WC) and iv) Sapins (SA; Figure IV.1). The site Sapins includes the edifices Sapins, White Castle, South Crystal, Crystal and Pico.

As part of the EMSO-Azores observatory, three bottom-tilt current meters were deployed around Eiffel Tower from September 2016 to August 2018 and one near Sapins from July 2017 to August 2018 (TCM-3, Lowell Instruments LLC, North Falmouth, MA, USA; Figure IV.1).

The current metres use a magnetometer and an accelerometer to log the direction and speed of the current every second.

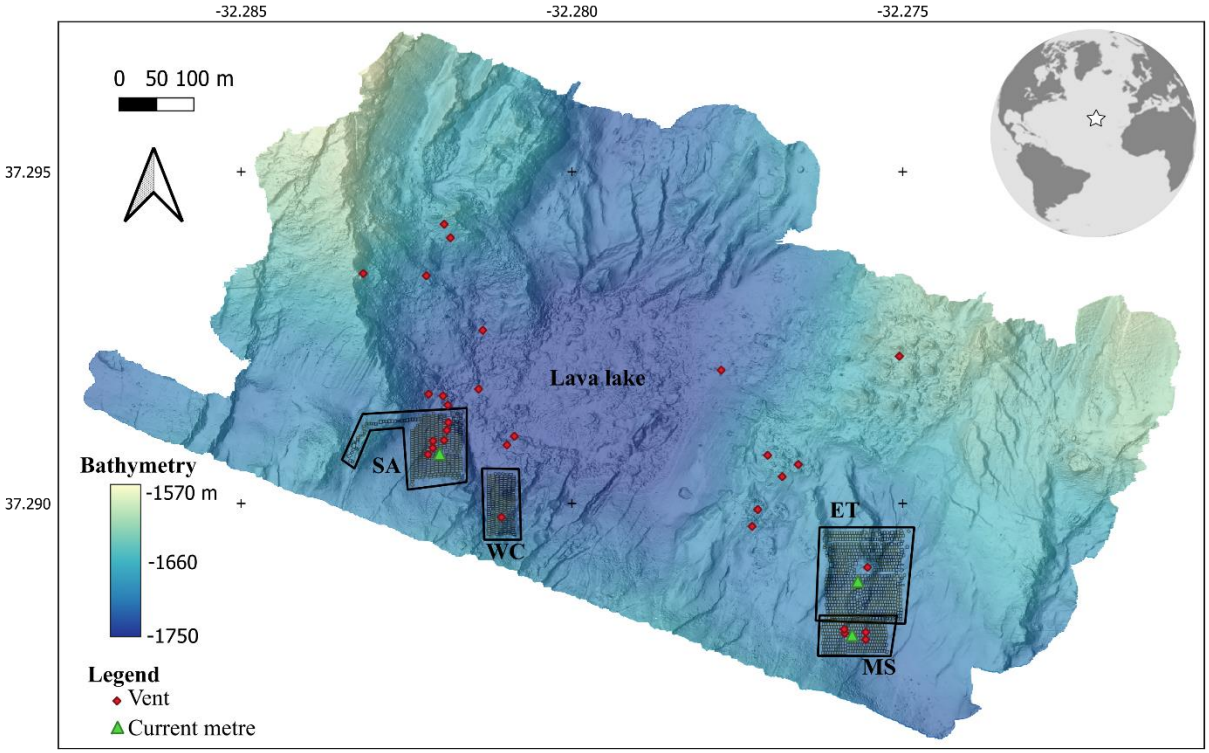

Figure IV.1. Bathymetric map of the Lucky Strike hydrothermal vent field (LS). The symbols indicate active vents known at LS (red point) and the position of the current metres (green triangle). The location of the sites is shown with polygons for (left to right) Sapins (SA), White Castle (WC), Eiffel Tower (ET) and Montségur (MS). Within the sites, the imprint of seabed images displayed are delimited with smaller black polygons. Note the slight overlap between MS and ET. The upper right inset locates LS in the Atlantic Ocean. Coordinate grid is provided in WGS84.

First blurred and obscured images were removed from the dataset. The software Matisse3D was used to perform image pre-processing (v.1.4.0; Ifremer; Arnaubec et al. 2015; https://github.com/IfremerUnderwater). The *MATISSE* pre-processing tool was used to perform colour correction on disjoint mosaics (blue colour attenuation and illumination, contrast and saturation homogenisation). A subset of *.jpg* images (n = 1626) was selected in order to obtain a set of still images with no overlapping imprint to form 2D mosaics to be annotated, hereafter called "disjoint mosaics". The imprint of *.jpg* images was projected in a coordinate reference system (CRS) and additionally saved as *.geotiff* files, knowing the altitude and attitude (i.e. pitch, roll) of the ROV as well as the extrinsic (i.e. position) and intrinsic (i.e. optical) parameters of the OTUS camera (Rigaud 2007).

The *.jpg* images making the disjoint mosaics were uploaded on the Biigle software for manual annotations (Langenkämper et al. 2017). Different levels of annotation were considered. Firstly,

substratum characteristics of the seafloor were annotated at the image level using image labels. Images were classified based on seabed lithology, either basalt, sulphur, slab or volcanoclastic sediment and by geomorphology with the non-exclusive presence of fractures, scree rubbles and brecciated pillow lava. Note that substrata of SA were annotated using different deep-learning models of convolutional neural networks calibrated on ET, MS and WC (Soto Vega et al. in prep.). Venting was recorded as flanges if a linear white deposit was observed or as focussed black or translucent smokers if a plume was observed within the images. Anthropogenic, biological and microbial features were systematically delimited with polygons within the image, also helping the development of machine-learning algorithms. Anthropogenic material consisted of various scientific modules of the EMSO-Azores observatory as well as by marine litter including glass, iron, plastic and unknown material. Biological annotations contained vent and peripheral organisms identified at the higher taxonomical level possible and called morphospecies when the taxonomy was unknown. As vent communities usually form spatially continuous aggregations of individuals, they are hereafter called "assemblages" (e.g. *Bathymodiolus azoricus* mussels, zoanthid sp. or white and orange material possibly formed by microbial mats). Those were annotated as polygons. If an assemblage of metazoans contained less than five organisms, no annotation was made to avoid a time-consuming annotation. All other morphospecies were annotated individually, hereafter called "individual organisms". The annotation catalogue will be available at DOI: 10.17882/92955.

Labels and annotations were withdrawn from Biigle as .csv files. They were georeferenced in *.shp* files in the software *Chubacapp* (https://github.com/marinmarcillat/CHUBACAPP; Marcillat et al. in prep.), by tracing back the homography matrix between the *.jpg* image and its georeferenced homologous *.tiff* image using feature matching (Marcillat et al. in prep.). As *Chubacapp* computes an area in m² for each polygon and image stored in *.shp* files, faunal abundance, assemblage and substratum covers were retrieved and divided by the total area of the image to acquire relative metrics (i.e. faunal densities, relative assemblage and substratum covers). Taking advantage of image geo-referencing, we used the high-resolution (~ 50 cm) bathymetry and backscatter rasters acquired over the entire LS vent field (Ondréas et al., 2009). Bathymetry was transformed to slope, terrain position index (TPI), aspect and proxies for terrain complexity (i.e. terrain rugosity index (TRI) and roughness; 'raster' package v.3.5.21; neighbours = 8). Aspect was transformed to eastness and northness (Wilson et al. 2007). We extracted the average backscatter and bathymetry derivatives with a buffer provided by a sphere with a diameter equivalent to the largest edge of the *.tiff* image imprint.

Once the dataset was fully processed, a procedure to clean and standardise annotation was established. First, defining lithology type from a single image without a larger-scale geological context of the area could lead to overestimate the heterogeneity of the habitat because of annotation unconsistency. To mitigate this bias, all images were considered for substratum cleaning in the context of surrounding images. If one or two consecutive image(s) were isolated within a group in terms of lithology annotation, the label was replaced by the ones of the surroundings images. This allowed to ensure spatial consistency of the seafloor annotation despite a possible underestimation of the substratum diversity. Second, because images had various spatial imprints, and to enable multivariate analyses (i.e. mitigate the amounts of 0 in the multivariate matrices – see chapter III), we established a methodology to "standardise" the dataset (Benoist et al. 2019). Images were pooled in tiles at two different spatial scales: i) by sites and ii) by image tiles. Image tiles were based on i) their spatial proximity and ii) cumulated image areas per tile ($n = 184$; $\mu \pm sd = 126.83 \pm 15.08$ m²). Furthermore, the number of images within a tile should be at least more than four times bigger than the "cleaning unit" which was set to 2 (see above). They should allow to keep a sufficient amount of "samples' (i.e. tiles) for statistical analyses. This threshold was set to 30 tiles. A tile size should be equivalent to the size of the smallest active hydrothermal edifice delimited by hand (i.e. ~ 126 m² for WC). While labels, annotation areas and abundances were simply assigned to tiles with a sum, backscatter and bathymetric derivatives were summed and weighted by the specific area of the image.

IV.2.2 Analyses

Cartography of environmental and faunal annotations was based on *.shp* files. To avoid a time-consuming splitting of annotations in QGIS, *.shp* files were firstly converted in *.gpkg* files in QGIS to facilitate their import in R ('sf' package, v.1.0.9; Pebesma 2018). This allowed to split the matrices according to the annotation level in order to produce one *.gpkg* layer for each level and plot them separately on QGIS. Tiles were used as replicated observation for statistical and multivariate analyses to examine community composition and possible driving factors.

To evaluate sampling, sample-based species accumulation curves (*Mao Tau estimator*) were computed to estimate morphospecies richness as a function of the number of tiles of each site ('vegan' package v. 2.6.2; Oksanen et al., 2007). To construct intervals of confidence, the function finds the unconditional variance without sample replacement ($\alpha = 0.05$; Colwell et al.

2012). Furthermore, K-dominance curves were plotted by sites in order to assess the influence of dominant species in communities by sites (Warwick et al. 2008). K-dominance curve ranks morphospecies by decreasing abundance computed for each site separately. It iteratively plots their contribution to the total abundance of the site as a cumulative percentage dominance.

Analyses were divided between surfaces of faunal and microbial assemblages and densities of individual organisms. Differences in the presence of all morphospecies among sites were assessed with a Venn diagram. For organisms only, they were tested using a Bray-Curtis dissimilarity matrix computed on tile densities with i) ANOSIM and ii) PERMANOVA (Clarke 1993; Anderson 2001). Both analyses involve a test with permutations ($n = 9999$; $p \leq 0.05$; 'vegan' package v. 2.6.2; Oksanen et al., 2007). ANOSIM provides a measure (R) for the dissimilarity/similarity (1/0) among sites. It tests if the similarity among sites is greater than the similarity within sites. PERMANOVA computes a non-parametric test similar to an ANOVA. A SIMPER analysis was computed to identify the morphospecies that contributed the most to differences among sites with 9999 permutations (Clarke 1993).

In order to better disentangle the effect of predominant factors on benthic communities, we computed a redundancy analysis (RDA; Legendre and Legendre, 2012). A Hellinger transformation was applied: the matrix of assemblages and organisms arranged in tiles was divided by the total area of the tile to acquire relative surfaces and densities respectively and was twice square-rooted. This allows to preserve the Hellinger distance which is appropriate in analyses based on Euclidean distances such as RDA as it is less sensitive to double-zeros (Legendre and Borcard 2018). The environmental matrix arranged in tiles contained lithology, geomorphology, count of outflows and area covered by anthropogenic wastes. Furthermore, we added the presence of assemblages as they comprised ecosystem-engineer species and mats of microbial primary producers. To account for lack of matching units, we scaled each variable between 0 and 1. A forward selection was applied to eliminate extraneous variables based on the R^2 of the first RDA ($\alpha = 0.10$; permutations = 999; 'adespatial' package, v. 0.3.7). A second RDA was then performed and RDA axes and environmental proxies were tested for significance (permutations = 999; Borcard et al. 2018). Spearman correlations were computed among substratum characterstics and tile faunal composition to further evaluate relationships. For morphospecies of individual organisms with abundance ≥ 5, only significant correlations were retained ($p \leq 0.05$). All analyses were computed in R (v.4.2.1; R Core Team).

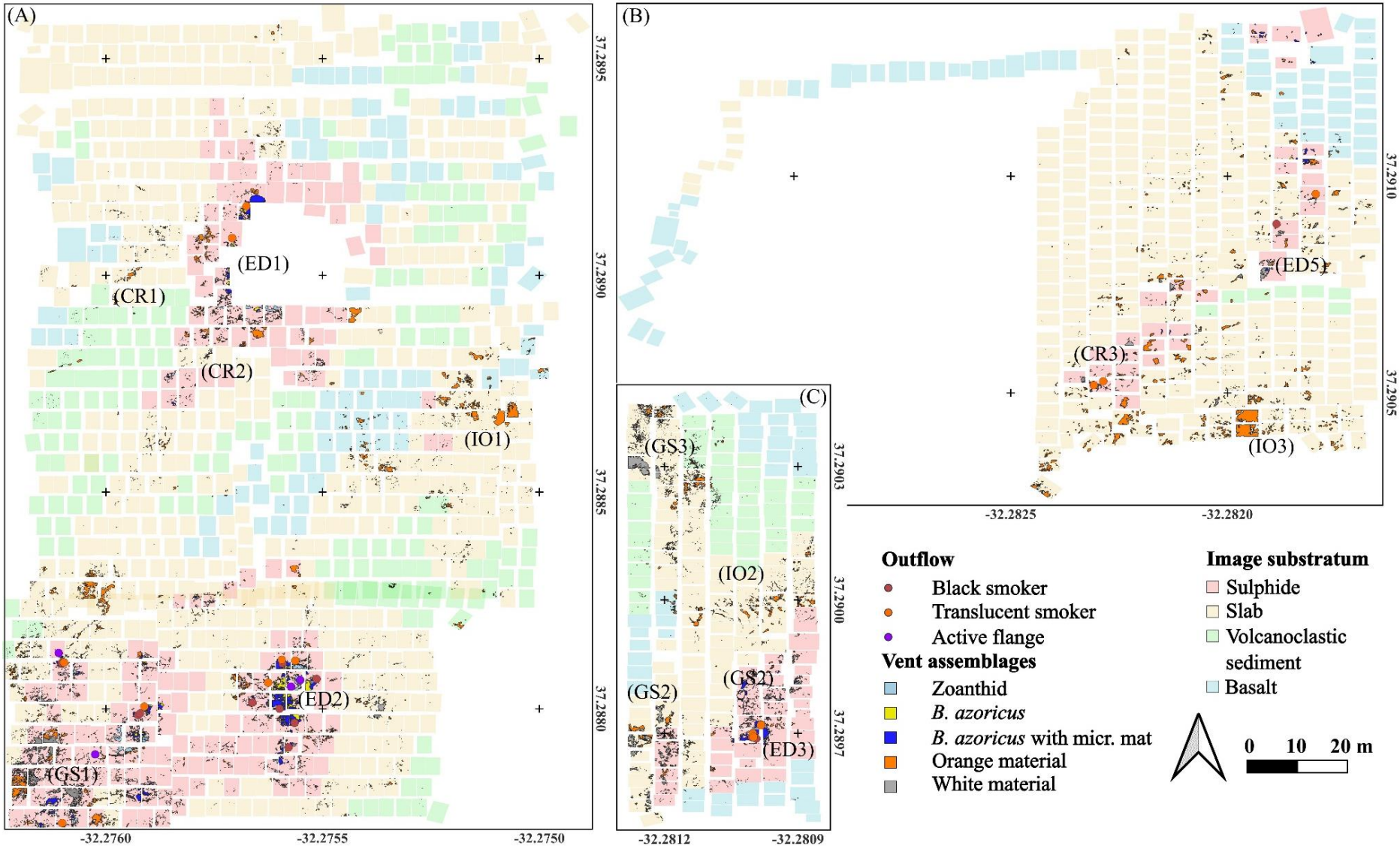
(A)
(ED1)
(CR1)
(CR2)
(IO1)
(ED2)
(GS1)
37.2895
37.2890
37.2885
37.2880
-32.2760
-32.2755
-32.2750
(B)
(ED5)
(CR3)
(IO3)
37.2910
37.2905
-32.2825
-32.2820
(C)
(GS3)
(IO2)
(GS2)
(GS2)
(ED3)
37.2903
37.2900
37.2897
-32.2812
-32.2809
Outflow
Black smoker
Translucent smoker
Active flange
Vent assemblages
Zoanthid
B. azoricus
B. azoricus with micr. mat
Orange material
White material
Image substratum
Sulphide
Slab
Volcanoclastic sediment
Basalt
0 10 20 m

Figure IV.2. Maps of distribution of hydrothermal features and substrata for the sites in the south-east (A) including Eiffel Tower (ET) in the north and Montségur (MS) in the south, and in the south centre including (B) Sapins (SA) and (C) White Castle (WC). Image substrata are plot with a colour code associated with the imprint of each image annotated. Outflows and flanges are located with colour-specific points. To ease presentation of the results, the presence of different types of hydrothermal settings is presented with a character code: ED = Main edifice, GS = Grey sandy areas, CR = Cracks in the periphery of the main edifice and IO = isolated orange material. Vent assemblages are shown with polygons of different colours. The coordinate grid is expressed in WGS84. Note the gap in Figure IV.2A showing the location of the Eiffel Tower edifice, a structure ~ 11 m high that was not possible to image with a forward-looking configuration on the ROV.

IV.3 Results

IV.3.1 Environment

Substrata were predominated by slab, reaching 55% overall, while basalt, volcanoclastic sediment and sulphide represented between 13 to 17% (Table IV.1). Sulphide made up a higher proportion of lithology at Montségur than at other sites and basalt never occurred there (Table IV.1; Figure IV.2). Volcanoclastic sediment lithology rarely occurred at Sapins, where slab was more predominant than at all sites. Basalt was correlated with the presence of brecciated pillow lava (Spearman r = +0.81) and scree rubbles (+0.40) and high topographic complexity (TRI: +0.37). While basalt (−0.39) and volcanoclastic sediment (−0.58) displayed negative correlation with fractured seabed, the latter was associated with slab (+0.30) and sulphide (+0.43). Black smokers, translucent outflows and flanges were observed at all sites. They were mainly found over the sulphide edifices, emitting from sulphide material (Figure IV.2; Spearman r = +0.47 with flanges, +0.39 with translucent smoker and +0.35 with black smokers).

Table IV.1. Relative proportions of lithological features identified in seabed images for Eiffel Tower (ET), Montségur (MS), White Castle (WC), Sapins (SA) and all sites combined.

	Sulphide [%]	Slab [%]	Volcanoclastic sediment [%]	Basalt [%]
ET	10.84	53.06	21.70	14.40
MS	41.00	47.97	11.03	0.00
WC	18.36	42.38	19.91	19.35
SA	9.42	71.87	1.70	17.01
All sites	16.83	55.41	14.65	13.11

Regime of current remained of low velocity (< 2 cm/s) for all sites (~ 62%, ~ 76%, ~ 58% of all measurements made at ET, MS and WC respectively). Current metres revealed the presence of a predominant current oriented southward and, to a lesser extent, northward at both ET and

MS (Figure IV.3). In the West of LS, currents were predominantly oriented east to east-northeast.

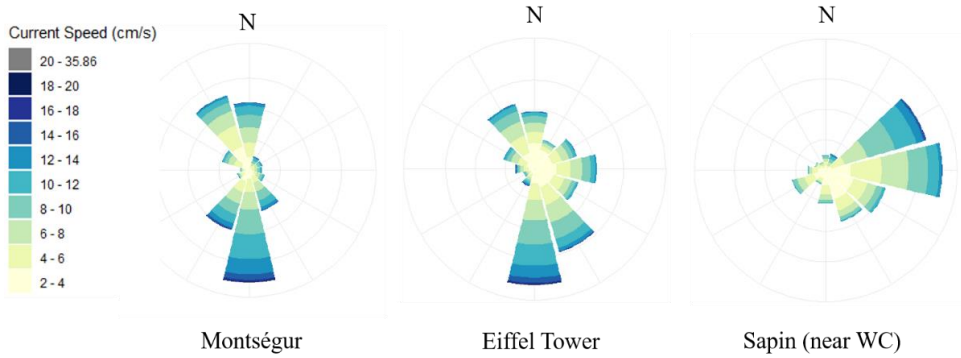

Figure IV.3. Rose diagrams of current orientation monitored from September 2016 to August 2018 at Montségur and Eiffel Tower and from July 2017 to August 2018 at Sapin. Current speeds (cm/s) are displayed with a gradient colour. Current speeds of < 2 cm/s or > 35.86 cm/s are not represented. "N" indicates the North azimuth. Position of the current metres is shown in Figure IV.1.

IV.3.2 Distribution of assemblages

The total area covered by mussel assemblages was 98.59 m², representing 0.42% of the seabed imaged (Table IV.2). The mussel cover at MS accounted for 65.48 % of the total mussel cover across all sites. In general, mussels were more often covered by microbial mats in the western sites WC and SA (98.76% and 87.04% respectively) than for the eastern sites (ET: 23.48%, MS: 34.76%; Table IV.2). Zoanthid assemblages were absent from the western SA and WC sites (Table IV.2). White material potentially representing sulphide oxidation totalised 21.56 m². Orange material potentially representing iron oxidation covered a larger area 337.96 m² which represented 1.45% of the surface imaged.

Table IV.2. List of morphospecies and vent assemblages annotated in seabed images of the Lucky Strike vent field. Abundance of non-vent morphospecies and cover of assemblages (m²) by site: ET = Eiffel Tower, MS = Montségur, WC = White Castle, SA = Sapins. The total surface area (m²) considered and the number of images and tiles analysed per site are included at the end. Cells containing information on vent assemblages are shaded in grey.

Phylum (abundance)	**Class/Sub-class**	**Order**	**Family**	**Morphospecies**	**ET**	**MS**	**WC**	**SA**	**Total**
Annelida	Polychaeta	Phyllodocida	Polynoidae			1			1
Arthropoda	Crustacea	Decapoda	Alvinocarididae	*Mirocaris fortunata* or *Rimicaris chacei*	6	4	4	6	20
				Red demersal shrimp	807	243	150	513	1713
			Bythograeidae	*Segonzacia mesatlantica*	29	55	33	4	121
			Inachidae	*Chaceon* like	8	0	0	0	8
			Muninidae	gen. sp.	1	0	0	0	1
	Pycnogonida	Pantopoda			15	2	1	2	20
Chordata	Holocephali	Chimaeriformes	Chimaeridae	*Hydrolagus pallidus*	2	0	0	0	2
	Chondrichthyes			gen. sp.	1	0	1	1	3
	Actinopteri	Ophidiiformes	Bythitidae	*Cataetyx laticeps*	35	13	8	6	62
		Gadiformes	Macrouridae	*Nezumia sclerorynchus*	0	0	1	0	1
				gen. sp.	6	0	2	1	9
			Lotidae	*Gaidropsarus mauli*	0	1	1	0	2
		Notacanthiformes	Notacanthidae	*Polycanthonotus rissoanus*	9	0	3	2	14
		Anguilliformes	Synaphobranchidae	*Synaphobranchus kaupii*	1	0	2	0	3
Mollusca	Gastropoda	Neogastropoda	Raphitomidae	*Phymorynchus* sp.1	0	1	0	0	1
			Buccinidae	gen sp.	0	2	0	0	2
Echinodermata	Echinoidea			gen sp.	2	0	7	3	12
	Holothuroidea			gen. sp.	0	1	0	1	2
	Ophiuroidea			gen. sp.	4	2	0	1	7
Cnidaria	Ceriantharia				4	4	1	9	17
	Hexacorallia	Actiniaria	Actiniidae	Orange anemone	8	6	3	3	20
		Antipatharia			1	0	0	4	5
		Scleractinia	Caryophylliidae	*Solenosmilia variabilis*	2	0	0	0	2
	Octocorallia	Alcyonacea	Plexauridae?	Named “Gorgonacea” hereafter	0	0	0	37	37
		Pennatulacea	Pseudumbellulidae?		0	0	0	1	1
Porifera	Desmopongiae	Poecilosclerida	Cladorhizidae	Stick	2617	843	555	1184	5199
				Arborescent	189	0	11	148	348
		Hexactinellida		Blue vase sponge	90	21	23	142	276
				Brown to yellow vase sponge	7	3	4	35	49
Foraminifera	Monothalamea	Astrorhizida	Arboramminidae	*Luffamina atlantica*	129	239	36	430	834
Category/phylum (area in m²)	**Class/Sub-class**	**Order**	**Family**	**Morphospecies**	**ET**	**MS**	**WC**	**SA**	**Total**
Mollusca	Mytilida	Bivalvia	Mytilidae	*Bathymodiolus azoricus*	3.70	22.44	0.15	0.81	27.07
				B. azoricus covered with *white mats*	12.06	42.12	11.90	5.44	71.52
Cnidaria	Hexacorallia	Zoantharia		gen. sp.	1.04	3.02	0	0	4.05
Hydrothermal material			White material	Anhydrite, grey sand or white microbial mat of thiotroph bacteria	3.96	9.68	6.61	1.32	21.56
			Orange material	Orange deposit/iron-oxydiser microbial mat	96.61	70.29	52.70	118.37	337.96
Total area [m²]					10437.58	4155.85	3002.89	5739.78	23336.1
# of images					730	290	220	386	1626
# of tiles					83	33	25	43	184

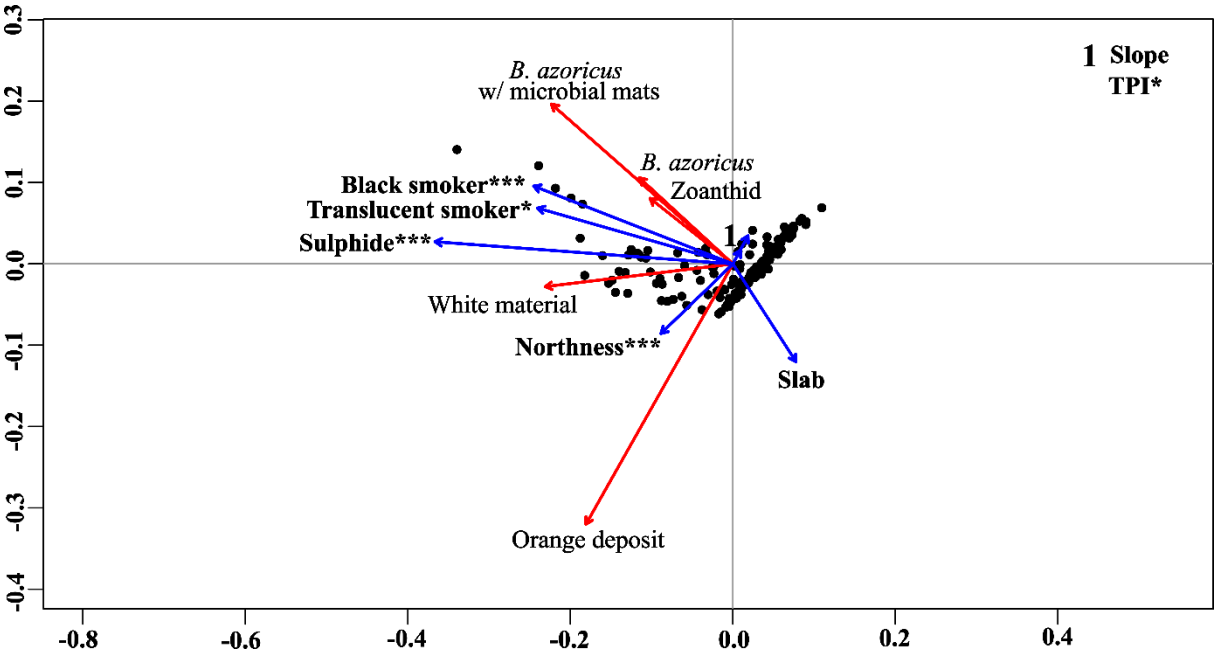

Figure IV.4. RDA triplot of tile composition of vent faunal and microbial assemblages in relation to environmental proxies. The first two axes were significant ($p < 0.01$; var. axis 1 = 32.51%, var. axis 2 = 6.68%). Observations are represented with black dots. Red arrows represent correlation with morphospecies. Blue arrows indicate correlation with environmental variables (in bold) with proxies for hydrothermal activity (abundance of vent exits and cover of vent assemblages), topography, substratum properties and litter. That environmental subset of variables was defined with a forward selection. Significance of those variables was assessed with a permutational test (*** = $p \leq 0.001$, ** = $p \leq 0.01$, * = $p \leq 0.05$). The number 1 refers to variables that were not discernible in the centre of the triplot. Those variables are listed in the upper-right corner.

The first two axes of the RDA were significant and explained respectively 32.51% and 6.68% of the variance (Figure IV.4). After forward selection, sulphide, slab, black smokers, northness and TPI were significant. The RDA indicated the association of white material with sulphide substratum and of *B. azoricus* assemblages and zoanthids with vent outflows. (Figure IV.4). Orange material formed a separate entity in the RDA explained by northness (Figure IV.4). All assemblages and deposits were positively correlated with the presence of sulphide and predominantly coincided with the presence of hydrothermal outflow (Table IV.3), usually occurring over sulphide edifices. Mussels colonised the active zones while zoanthids remained on the smooth slope of the edifice (Figure IV.2). Nevertheless, we observed sporadic mussel and zoanthid assemblages in cracks at the edifice periphery and near grey sandy deposits (CR in Figure IV.2). Orange material distributed widely over all sites (Figure IV.2). Although poorly, they were significantly correlated with hydrothermal outflows, and developed in the periphery of actively venting areas such as in cracks (CR in Figure IV.2; Table IV.3). However, we also observed their presence in the periphery of large grey sandy areas (GS in Figure IV.2)

and in aggregations at isolated areas without hydrothermal outflow, probably resulting in the low correlation coefficient observed (IO in Figure IV.2).

In general, hydrothermal assemblages rarely occurred over basaltic or volcanoclastic sediment where no hydrothermal activity was observed (Table IV.3). Furthermore, there was no correlation with iron litter (Table IV.3), although few observations demonstrated the presence of orange material around these features.

Table IV.3. Spearman correlations of hydrothermal assemblages with substrata, vent outflows and all categories of iron litter. Only significant correlation coefficients were presented ($p > 0.05$). NS: not significant.

	Sulphide	Slab	Basalt	Volcanoclastic sed.	Black	Shimmer	Flange	Iron
White material	0.68	NS	-0.31	-0.33	0.33	0.34	0.47	-0.07
B. azoricus w/ mats	0.80	-0.31	-0.21	-0.33	0.37	0.44	0.49	-0.01
B. azoricus	0.73	-0.28	-0.24	-0.34	0.39	0.47	0.51	-0.02
Zoanthid	0.56	-0.18	-0.25	-0.22	0.37	0.34	0.42	NS
Orange material	0.39	NS	-0.34	-0.26	0.16	0.16	0.24	NS

IV.3.3 Distribution of individual organisms

In total, 32 morphospecies were annotated. They belonged to the phyla Annelida, Chordata, Mollusca, Echinodermata, Cnidaria, Porifera and Foraminifera (Table IV.2). Four to 5 dominant morphospecies considerably contributed to the overall abundance observed at each site (Table IV.2). They were represented by stick cladorhizids (n = 5199), red demersal shrimps (n = 1713), arboramminid foraminifera (n = 834), hexactinellid blue and brown vase sponges (n = 325) and arborescent sponges (n = 348) the latest being absent from MS. Arthropoda were also characterised with high abundances of *Segonzacia mesatlantica* crabs (n = 121) and a few large abyssal pycnogonids (n = 20). Chordata were dominated by Actinopteri fishes dominated by *Cataetyx laticeps* (n = 62) and, to a lesser extent, gadiform specimens (n = 12) and *Polycanthonotus rissoanus* (n = 14). Echinoderm morphospecies were dominated by echinoids (n = 12). Cnidarians harboured few morphotypes with more than 10 individuals such as cerianthids (n = 17), actiinids (n = 20) and gorgonians only in SA (n = 37). Sites shared 50% of morphospecies (Figure IV.5). Only a few morphospecies were exclusive to a given site, with a maximum of four for ET. ET hosted the largest share of morphospecies (Figure IV.5) possibly because it benefited from a more extensive seabed characterisation effort (Figure IV.6A).

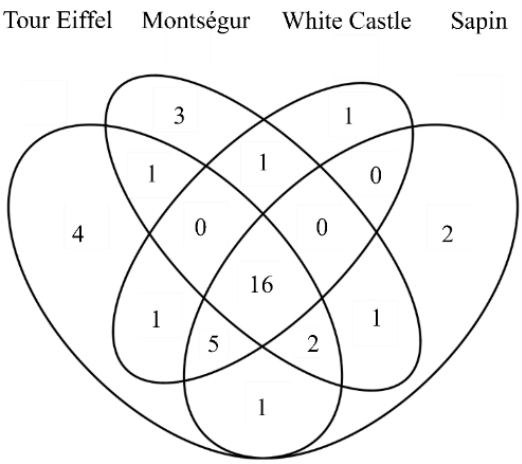

Figure IV.5. Venn diagram of the different morphospecies, faunal and microbial assemblages (n = 32) found in the vicinity of the Eiffel Tower, Montségur, White Castle and Sapins sites.

The accumulation curves described similar behaviours among sites suggesting similar richness among them (Figure IV.6A). MS harboured a slightly lower richness than at other sites of a few morphospecies. In general, the asymptote was not reached at any sites although it started to plateau at ET. However, the combined accumulation curve for all sites suggested the presence of site-exclusive species as the curve never plateaued, behaving linearly when the sampling totalised ~ 60 tiles. A similar observation was made with rarefaction curves. K-dominance species curves demonstrated the high predominance of four to five morphospecies at all sites, contributing to ~ 95% of the whole abundance identified (Figure IV.6B).

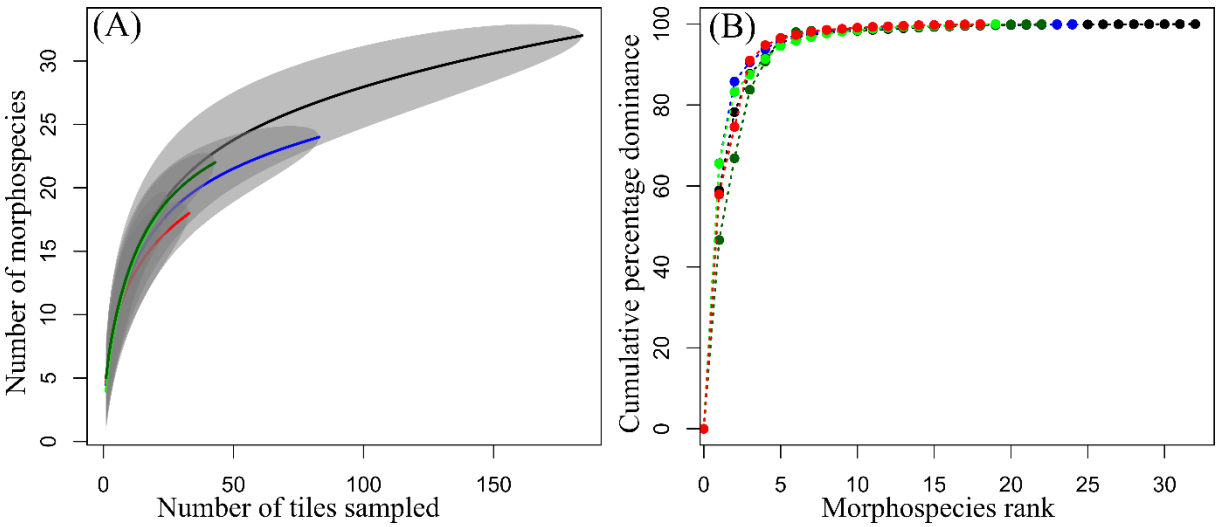

Figure IV.6. (A) Accumulation curves for each hydrothermal vent site along tile sampling. Grey areas describe confidence interval of 95%. (B) K-dominance species curve for each hydrothermal vent site. Vent assemblage and microbial mats were not included. Black = all sites combined, blue = ET, red = MS, light green = WC, dark green = SA.

ANOSIM on the abundance of non-vent fauna exclusively, revealed that sites were significantly different in terms of species despite weak R similarities among site communities ($R = 0.055$; $p = 0.028$). PERMANOVA computed among all sites was significant ($R^2 = 0.044$; $p = 0.002$). With the exception of the pairs WC-ET and WC-MS ($R^2 = 0.014$-0.020; $p > 0.166$), PERMANOVA tests among pairs of sites were all significant ($R^2 = 0.020$-0.062; $p < 0.05$). The SIMPER analysis revealed differences in densities of the dominant morphospecies among sites. Stick cladorhizids contributed to explain that difference for at least 50% of the paired sites. Red demersal shrimp and foraminifera contributed together to explain an additional 27 to 30% of the variance among pairs.

RDA triplots revealed two significant axes explaining respectively 14.98% and 9.14% of the variance (Figure IV.7). The total variance explained by the model of the RDA reached 23.66% indicating that the considered abiotic variables only partially explained the observed patterns in megafaunal community distribution. The first two axes of the RDA divided assemblages in three main groups associated with hydrothermal activity, basalt or slab. The first axis was associated with arboraminnid foraminifera that seemed to occupy areas harbouring fractures and sulphide substratum in the vicinity of mussel assemblages harbouring *S. mesatlantica* and alvinocaridid shrimps (Figure IV.7; Figure IV.8). Hexactinnelid sponges and arborescent cladorhizid and, with less importance, red demersal shrimps were found over basalt (Figure IV.7). Stick cladorhizid occupied both sulphide basaltic substrata. Correlations confirmed the positive influence of sulphides on the abundance of arboramminid foraminifera (Spearman r = +0.54). Hexactinnelid vase sponges & red shrimps were poorly associated with sulphide (−0.34 & −0.30). Red demersal shrimps were not significantly correlated with basalt, hence describing their wide distribution (Figure IV.8). Correlations confirmed the importance of basalt for hexactinnelid sponges (+0.27), arborescent cladorhizids (+0.48). Stick cladorhizids did not have a strong particular affinity for any substratum and were found on basalt (+0.30), fractured seafloor (+0.24) and sulphide (+0.32; Figure IV.8). Volcanoclastic sediment was avoided by stick cladorhizids (−0.31), foraminifers (−0.27) and arborescent cladorhizids (−0.16). The slab tended to be avoided by stick cladorhizids (−0.21) and vent species (*S. mesatlantica*: −0.25; alvinocaridid shrimps: −0.26). Vase hexactinellid and red shrimp distributed over slab (+0.22 and +0.29 respectively). We finally noticed the importance of terrain complexity (i.e. TRI) in favouring the presence of gorgonians in the East of SA (+0.20; Figure IV.8) as well as arborescent (+0.29) and stick cladorhizids (+0.19). In contrast, terrain complexity (TRI) did not favour the presence of pycnogonids possibly because of low climbing capability (−0.20). No

organism was positively correlated with orange material despite that stick cladorhizids and red demersal shrimps could be found in their close vicinity (Figure IV.8). See Supplementary material

Supplementary Table IV.1 for the full results computed with the Spearman's correlation coefficient.

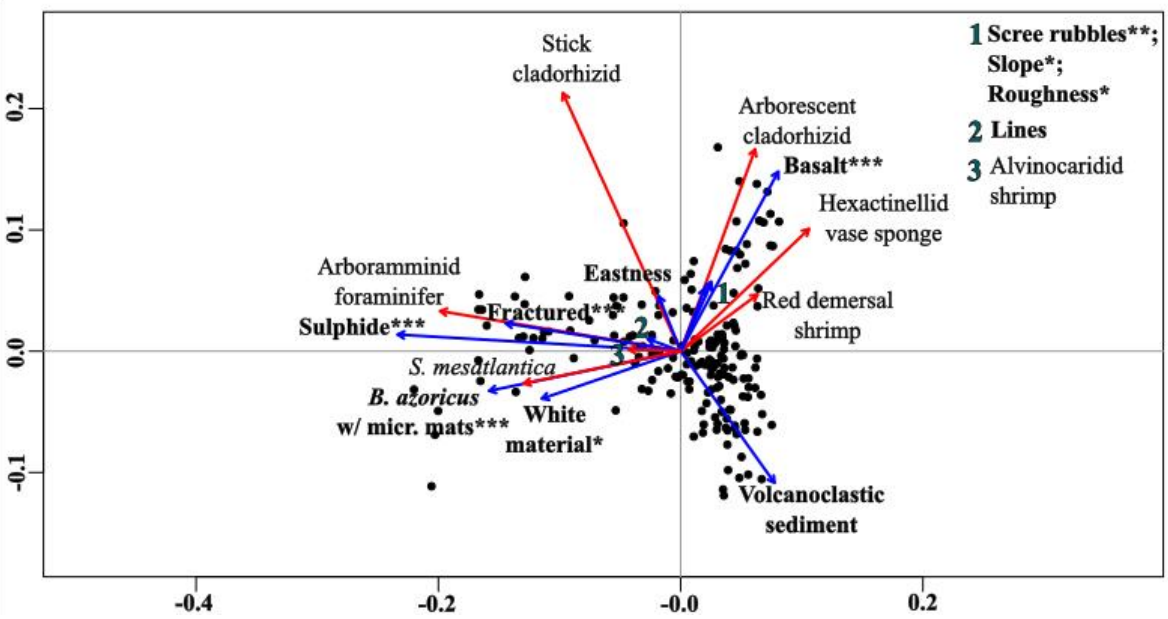

Figure IV.7. RDA triplot of tile composition of non-vent morphospecies in relation to environmental proxies. The first two axes were significant ($p < 0.01$; var. axis 1 = 14.96%, var. axis 2 = 8.70%; adj. $R^2 = 0.26$). Observations are represented with black dots. Red arrows represent correlation with morphospecies. Blue arrows indicate correlation with environmental variables (in bold) with proxies for hydrothermal activity (abundance of vent exits and cover of vent assemblages), topography, substratum properties and litter. That subset of environmental variables was defined with a forward selection. Significance of those variables was assessed with a permutational test (*** = $p \leq 0.001$, ** = $p \leq 0.01$, * = $p \leq 0.05$). The numbers 1, 2 & 3 refer to variables that were not discernible in the centre of the triplot. Those variables are listed in the upper-right corner.

IV.4 Discussion

Using high-resolution images of the seabed, this study provided detailed information on the composition of vent and non-vent megafaunal communities, their spatial distribution patterns, and associated drivers. In general, patterns of zonation from the vent to the non-vent fauna was highly consistent throughout vent sites (see Figure IV.9). We identified few environmental variables as drivers of the observed patterns within and among vent sites but a large amount of the variance remained unexplained.

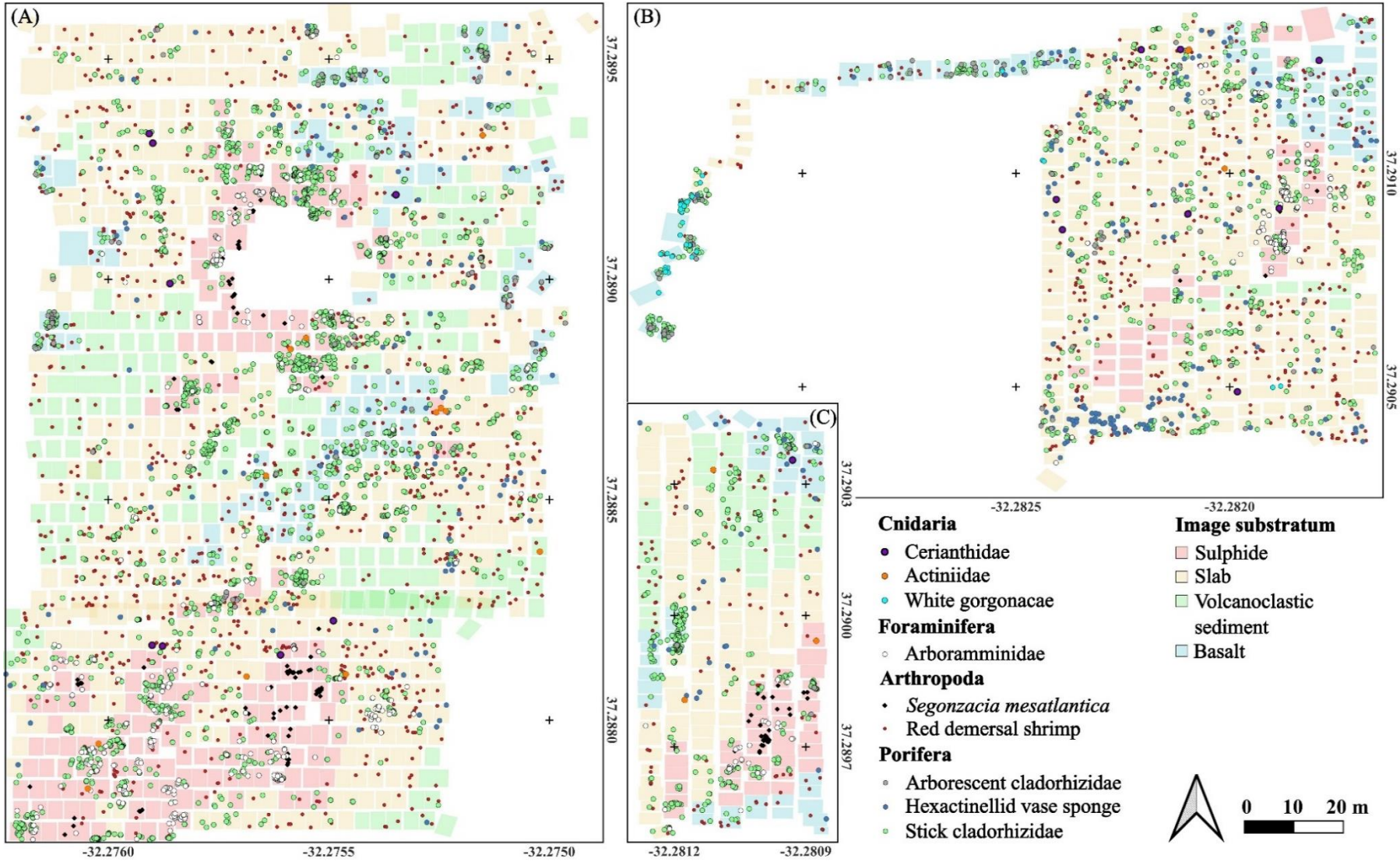

Figure IV.8. Maps of distribution of dominant organisms as point over sites in the south-east sites (A) Eiffel Tower (ET) in the north and Montségur (MS) in the south, and in the south centre sites (B) Sapins (SA) and (C) White Castle (WC). Image substrata are plot with a colour code associated with the imprint of each image annotated. Coordinates are in WGS84.

IV.4.1 Limitations

This study was strongly limited by the resolution at which the fauna was imaged. This limited the identification of small fauna especially in images with higher altitude of the ROV (from 3 to 5 m) or in areas harbouring steep terrain such as faults. Furthermore, it was impossible to identify individuals at the species level because of image quality but also of a limited knowledge of the fauna related to a low sampling effort. Hence, although considered as morphotypes, we can thus not rule out that these groups actually consist in different species potentially differentially distributed. The patterns observed should thus be considered with caution until all morphotypes are sampled and identified in the lab. By overlooking small-size fauna and because of the lack of species identification, we expect species richness to be overlooked. Furthermore, mobile species remain capable to move from one picture to another (e.g. red demersal shrimp). Over- or underestimation may depend on the mobility capability and on the behaviour of each species. In fact, illumination from an underwater vehicle could strongly affect the panel of species observed because of attraction, repulsion or neutral response (Raymond and Widder 2007).

The ROV navigation still contains an error of repositioning ranging from 1 to 3 metres (pers. obs.). As the selection of non-overlapping images could have been biased by the repositioning uncertainty, we acknowledge that duplicated annotations could result in overestimating abundance, especially for dominant species that are statistically more likely to be duplicated. One solution would be to reproject annotations over 3D models of the seabed using ray-tracing algorithms as parallel transects were originally designed for photogrammetry reconstruction (see routine in *Chubacapp*). In fact, those algorithms were highly promising to reposition annotation with an error < 5 cm (Marcillat et al. in prep.). In parallel, the extraction of topographic indicators would be more accurate and more representative of the microtopography than the bathymetry acquired by multibeam echosounder mounted on a ROV (Ondréas et al. 2009).

IV.4.2 Active vent assemblages

Active faunal assemblages displayed variability in terms of structure. Some species are well known to occupy mussel assemblages (e.g. *S. mesatlantica*, ophiuroids; Husson et al. 2017; Sarrazin et al. 2020). Within sites, *B. azoricus* predominated over hydrothermal edifices, despite

a few observations at other venting settings (e.g. within cracks in edifice periphery or next to grey sandy outflows). The presence of *B. azoricus* at all sites suggests it may not be sensitive to differences in fluid composition among the south-central and eastern sites (Chavagnac et al. 2018). However, mussel cover strongly varied between sites. WC and SA harboured very limited surface of mussel cover compared to MS. Compared to the eastern ET and MS sites, the south-centre sites may harbour a higher number of immature edifices. These latter are classically described as chimney-like structures of short height harbouring a few black smokers (Hannington et al. 1995). As it matures, a sulphide mound builds up and outflows are redirected in the periphery (Hannington et al. 1995). Such mature and complex edifices are more likely to provide larges surfaces exposed to the vent fluid through diffusing and fluid dispersion (Girard et al. 2020a), and then enhance the availability of suitable habitat for the mussels to develop. Conversely, biological colonisation at immature edifices with a few focused outflows may simply be conditioned by the low surface that is appropriately exposed. This suggests the importance of considering the complexity of vent edifice as a keystone structure of the vent fauna population. In addition, the cover imaged at ET was not representative as we were not able to fly the ROV over the complex topography of the edifice there. Forward-looking images quantified ~ 270 m² of mussel cover at ET (Chapter III). Although downward-looking images have overlooked that population, that extensive surface may still account for a significant portion of the population of mussel compared to the ~ 100 m² of mussel cover imaged in this study. This high population proportion suggests considering the ET habitat as an important structural factor for the *B. azoricus* population over the scale of the vent field (e.g. source for larvae supply). The distributional patterns of several species (e.g. stick cladorhizids, arboraminnid foraminifera) coincided with the presence of *B. azoricus* and white material that is indicative of a sulphur-oxidation conditions (Taylor et al. 1999; Crépeau et al. 2011). A higher proportional cover of sulphur-oxidising microbial mats on mussels was found at WC and SA harbouring focused outflows. This supports the fundamental role of that type of venting on microbial mat distribution (Girard et al. 2020a).

Chavagnac et al. (2018) detected differences in the composition of the end-member vent signatures between ET or MS and WC or SA (e.g. lower chlorinity and concentrations of Mn, Na, Ca, K at ET and MS). In addition to differences in edifice sizes, differences in vent fluid composition may create different chemical habitat conditions among sites, possibly explaining the absence of zoanthids at WC and SA. However, the local hydrography which is dominated by North-South currents may still limit exchange of larvae from the east to the west

(Khripounoff et al. 2008). Testing the presence of zoanthids at the Isabel edifice located in the vicinity of ET and belonging to the vent site of WC may provide further insights. However, there remains a knowledge gap regarding the dispersal capability and vent tolerance of zoanthids in addition to a proper identification of this morphospecies also observed in the Tiancheng vent field (South-West Indian Ridge; Zhou et al. 2018). Our large-scale mapping revealed they form dense assemblages in proximity to the vent habitat (< 10 m; Figure IV.2; Chapters II & III). This supports the idea that they benefit from chemosynthetic-derived material which will require further trophic ecology investigation. For instance, the lack of extensive *B. azoricus* assemblages close to which they usually cluster at ET and MS could explain their absence at SA and WC, because they possibly benefit from the proximal export of macrofaunal preys (e.g. copepods; Plum et al. 2017).

IV.4.3 Non-vent assemblages

Non-vent communities were highly similar among sites of study. A few dominant morphotypes explained these differences. Spearman's r correlation coefficient computed on tiles of neighbour images revealed different patterns of spatial distribution and relationship.

Non-vent morphotypes tended to avoid the sulphide substratum located in the vicinity of hydrothermal discharge. Local exposure to hydrothermal release may filter out the non-vent megafauna because of the lack of adaptation to withstand vent fluid toxicity hence creating a spatial zonation gradient as observed at other vent fields (Marsh et al. 2012; Sen et al. 2013; Gerdes et al. 2019b). For instance, as the densities of hexactinellid sponges and red demersal shrimps decreased on sulphide substratum, we can fairly infer that they remain excluded in certain conditions of vent exposure. Still, we noticed the presence of a few non-vent species that aggregated near vent activity (Figure IV.9). The high abundance of *Luffamina atlantica* foraminifers in the direct vicinity of the vent fluid reveals the importance of the vent habitat for the ecology of that species, as also observed on inactive substrata (Desbruyeres et al. 2006). Stick cladorhizids aggregated massively over and around edifices hence revealing their tolerance for vent fluid exposure. The positive correlation between actiniids with sulphide substratum and black smokers revealed the importance of the vent habitat for that morphospecies occurring in the periphery. At TAG, Snake Pit or Ashadze, anemones can aggregate in dense assemblages in colder habitats in the periphery of active venting areas (Lopez-Gonzalez et al. 2003; Fabri et al. 2011). They probably feed opportunistically on mobile

megafauna (e.g. shrimps; Fabri et al. 2011), although symbiotic relationships cannot be excluded (Goffredi et al. 2021). At vents, microcarnivorous species benefit from the vent primary productivity that may be exported (Erickson et al. 2009). A few authors suggested the importance of advective currents created by hydrothermal discharge and that may contribute to convey food particles (Lonsdale 1977; Galkin 1997; Levin et al. 2016a). High food supply of zooplankton from vents was suggested to enhance the growth rate of cladorhizids, observed in the Pacific (Sen et al. 2016). Still, stick cladorhizids were observed over a wide array of habitats suggesting they are not specialists. Cladorhizid sponges are well known to occur at vents in the Pacific (Sen et al. 2016). Their microcarnivorous feeding mode and low size may be an adaptation to survive in food-poor habitat (Vacelet & Boury-Esnault 1995; Vacelet 2007). Their morphology and feeding mechanism also suggest they are found in low-flow regime habitats (Vacelet and Duport 2004; Schönberg 2021).

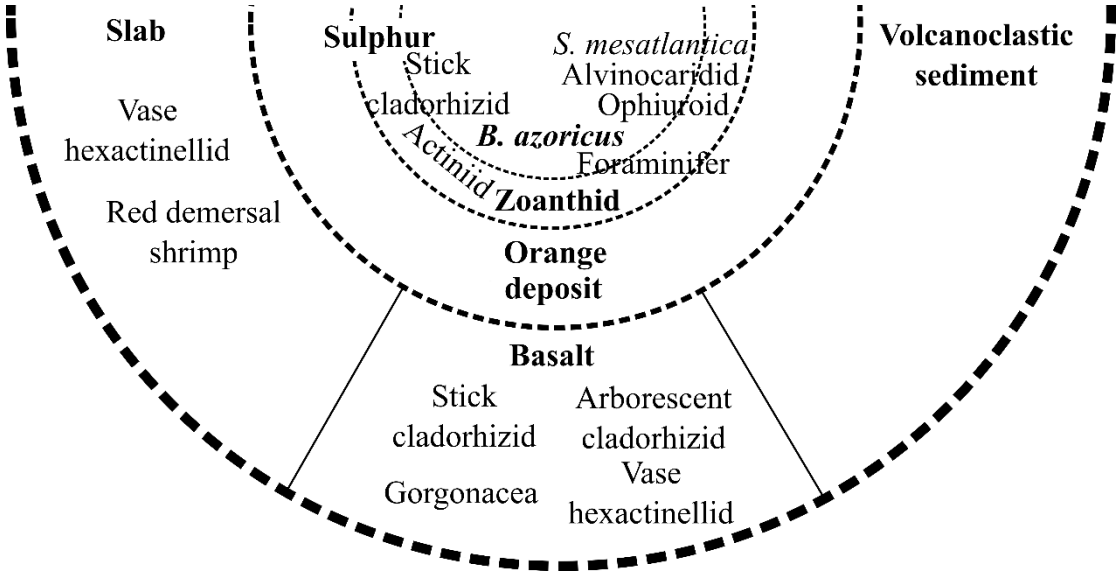

Figure IV.9. Schematic distribution of vent and non-vent morphotaxa in relation to their distance from the vent exit being the centre of the semi-circle, and to the biogenic assemblage and substratum delineated in bold and compartmented with dashed lines. A morphospecies mentioned within one substratum compartment relays a significant positive Spearman's correlation coefficient with that substratum. Morphospecies can overlap over different compartments.

In the periphery, the scattered distribution of the vent shrimps suggest no particular substratum affinity. In the Pacific, caridean shrimps are known to benefit from vent activity by occupying both soft and hard substrata (Boschen et al. 2015, 2016; Gerdes et al. 2019b). Stick cladorhizids and hexactinellid sponges were found on slab all over the sites. For instance, they were observed colonising decimetre-high offset between individual slabs. Volcanoclastic sediment was usually depleted of sessile species, probably because of the difficulty to anchor on soft substratum. Furthermore, the presence of basalt appeared to strongly contribute to the

distribution of stick and arborescent cladorhizids, hexactinellids and especially gorgonians. Studies at Juan de Fuca Ridge also demonstrated the importance of basalt for rossellid sponges (Neufeld et al. 2022). Firstly, the hard substratum provides a sustainable anchorage. Secondly, the presence of scree rubbles, pillows of lava enhancing topographic complexity may locally accelerate currents and facilitate food resuspension. A few studies at the MAR revealed the importance of photosynthetic supply to meio- and macrofauna at distances > 100 m from vents (Alfaro-Lucas et al. 2020; Roohi et al. 2022). Alfaro-Lucas (Alfaro-Lucas et al. 2020) even suggested food limitation to act as an environmental filter on those assemblages at LS. This may explain the importance of basalt in non-venting areas. Its topographic complexity will contribute to food particle resuspension and buffer the possible food limitation in those areas. However, we cannot exclude that those assemblages can be supplied by chemosynthetic-derived material, even if partially. For instance, microbes usually associated with chemosynthetic environments were detected on individuals located ~ 20 m away from venting: *Cladorhiza* sponges from the East Scotia Ridge and *Spinularia* sponges from the Juan de Fuca Ridge (Georgieva et al. 2020).

Still, we observed the presence of a few rarer sessile and ichthyofaunal morphotaxa that explained the overall lack of richness plateau provided by our seabed image sampling (Figure IV.6A). As those rare species remained sporadic (e.g. *Hydrolagus pallidus*; anthipatharian) and since they are capable of high mobility (*Cataetyx laticeps*) we were unable to analyse confidently their spatial distribution. As no interaction with the vent fauna has been observed over 7 years (Chapter II), the use of baited remote underwater camera (BRUV) could inform on the trophic ecology of the ichthyofaunal at LS (Farnsworth et al. 2007).

Our study also revealed the distribution of an iron-oxidising habitat as observed with the presence of orange material extending in the vicinity of venting areas or even in areas with no observable outflow. At LS, this orange material can result from iron-oxide precipitation within microbial mats (Henri et al. 2015), as also observed at other vent sites (Loihi seamount; Emerson et al. 2007). Those microbial mats grow in low-temperature venting or inactive chimneys (Emerson 2007; Li et al. 2012; Henri et al. 2013). Their wide distribution and large cover suggests this metabolic pathway of primary productivity at vents to be of geochemical significance (Juniper and Sarrazin 1995). However, we did not observe any significant link with the megafauna although a few non-vent morphospecies partially coincided with orange material (e.g. stick cladorhizids). This suggests that iron-oxide material may not provide a habitat favouring the development of those sessile communities. Similarly, Juniper and Sarrazin (1995)

suggested the difficulty for bacterivores to access the microbial biomass encapsulated within a matrix of mineral precipitates. Although this needs to be confirmed, this statement supports the exclusivity of thiotrophic productivity in supplying the whole vent and non-vent community. Finally, the lack of significant relationship with iron waste (i.e. predominantly ballasts) currently suggests only a local geochemical impact of that litter material.

IV.4.4 Sphere of hydrothermal influence

The sessile community can be qualitatively delimited between two main communities exhibiting spatial zonation (Figure IV.9). In our study, we observed the transition from vent communities on sulphide substratum to the peripheral assemblages that either inhabit the slab or the basaltic areas. Slab and basaltic communities do share similar morphotaxa such as stick cladorhizae, actiniids and hexactinellids, but higher abundance of other poriferans and, anecdotally, of gorgonaceans at SA, were found in basaltic assemblages (Figure IV.9). One can first ask if that community is specific, or at least reliant, to the hydrothermal habitat and thus differ from the background deep-sea community located in an areas with no hydrothermal influence (Collins et al. 2012). Unfortunately, we have no information on that background reference community. However, comparing our results to other investigations showed that those communities were distinct from the biological facies usually found at the Azores Islands (Tempera et al. 2012). In addition, assemblage composition and associated spatial zonation over a hundred metres are consistent to peripheral community structure observed at vents of the south-west Pacific (e.g. dominance of cladorhizids; Sen et al. 2016; assemblage II in Gerdes et al. 2019). Such comparison indicates the dependence to chemosynthesis-derived material of a portion of the peripheral communities. As distances increase, we hypothesise that the reliance to photosynthesis-derived material starts predominating (Alfaro-Lucas et al. 2020; Roohi et al. 2022). Stable isotope investigations should confirm if that gradient also occurs at for non-vent megafaunal communities (e.g. Erickson et al. 2009).

Despite the provision of hard substratum, the degree of influence of the hydrothermal environment was not demonstrated *strictu senso* for most morphospecies as they widely distributed over the study extent. Typically, exposure to vent primary chemosynthetic productivity can be considered as a function of the distance from a vent exit. Over hundreds of metre, the hydrothermal influence on corals and sponges will likely predominate because of observation of density peaks followed by density decline at Juan de Fuca Ridge and East Pacific Rise (Arquit 1990; Neufeld et al. 2022). This demonstrates that the sphere of hydrothermal

influence is a process that may also occur over a kilometre scale allowing the gradual transition to a background community (Arquit 1990). However, our effort of sampling rarely imaged the seabed over distances exceeding a hundred metres such as at ET, thus limiting our insights to a restricted portion of habitat conditions and assemblages in the periphery. Despite rare occurrence of anemones, zoanthids within the first fifty metres from the vent exit, cold-water corals, holothurians were only sporadically observed compared to other studies in the Pacific (Arquit 1990; Milligan and Tunnicliffe 1994; Gerdes et al. 2019b; Neufeld et al. 2022). Crinoids were absent although observed in the Pacific (Milligan and Tunnicliffe 1994; Neufeld et al. 2022). For cold-water corals, gorgonaceans still made an apparition in photographs located ~ 150 m away from vent exits of SA. That distance is of typical order of magnitude of the spatial range at which coral communities start predominating in benthic communities at vent fields of the Pacific (Gerdes et al. 2019b; Neufeld et al. 2022). As a result, one must take caution that the small extent of the study may not have sampled the full representative community of LS. Finally, as observed for ET, the extent of sampling can greatly affect the richness as a result of greater sampling effort. compared to the number of morphotaxa we observed in our study case (32), larger study extents usually resulted in higher richness (Boschen et al. 2015: 186; Gerdes et al. 2019: 63; Neufeld et al. 2022: 101). As the extent of the study increases, more habitats are considered within an investigation (Underwood et al. 2005). For example, our study did not include inactive substratum because it was absent from transects. Despite extinction, inactive substrata can host a significant amount of bacterial biomass that could feed non-vent communities (Kato et al. 2010) and were suggested to host a specific endemic community base on metabarcoding approach (Cowart et al. 2020). Inactive sulphide edifices are often associated with coral communities (Boschen et al. 2016; Neufeld et al. 2022). Further surveys at LS should therefore extends imaging effort over inactive areas such as at the Bairo Alto edifice. The use of autonomous underwater vehicle could help to extend our knowledge at larger scales to capture a larger heterogeneity of habitats (Thornton et al. 2016, 2021).

IV.5 Supplementary material

Supplementary Table IV.1. Spearman's correlation coefficient between organism densities and environmental variables aggregated by tiles. Only morphospecies with an abundance ≥ 5 are shown. NS = p > 0.05 (not significant).

		Hydrothermal (thiotrophy)				Hydrothermal (iron-oxidation)	Substratum lithology				Terrain characteristics			
Phylum	Morphospecies	Black smoker concentration	White material	*B. azoricus*	Zoanthid	Orange deposit	Sulphide	Slab	Volcanocl. sed.	Basalt	Fractured	Northness	Scree rubbles	TRI
Arthropoda	Alvinocarid	0.29	0.27	0.41	0.23	NS	0.37	-0.26	-0.18	NS	0.16	NS	-0.19	0.17
	Red demersal shrimp	-0.19	-0.20	-0.25	-0.16	NS	-0.29	0.29	NS	NS	NS	NS	NS	NS
	S. mesatlantica	0.48	0.53	0.61	0.53	0.31	0.60	-0.25	-0.18	-0.21	0.32	NS	NS	NS
	Inachidae	NS	NS	NS	NS	NS	NS	NS	NS	NS	NS	-0.15	0.17	NS
	Pycnogonid	NS	NS	NS	NS	NS	NS	NS	NS	NS	NS	NS	NS	-0.20
Chordata	*Cataetyx laticeps*	0.18	NS	NS	NS	-0.18	NS	NS	NS	NS	NS	NS	0.22	NS
	Gadiform	NS	NS	NS	NS	-0.17	NS	NS	0.16	NS	-0.17	NS	NS	NS
	Polycanthonotus rissoanus	NS	NS	NS	NS	NS	NS	NS	NS	NS	NS	NS	NS	NS
Echinodermata	Echinoidae	NS	NS	NS	NS	NS	NS	NS	NS	NS	NS	NS	NS	NS
	Ophiuroidae	NS	NS	0.15	0.19	NS	NS	NS	NS	NS	0.15	NS	NS	NS
Cnidaria	Ceriantharia	NS	NS	NS	NS	NS	NS	NS	-0.15	NS	NS	NS	-0.18	NS
	Actiniidae	0.21	NS	NS	0.30	NS	0.16	NS	NS	NS	NS	NS	NS	NS
	Antipatharia	NS	NS	NS	NS	NS	NS	NS	NS	NS	NS	0.22	NS	NS
	Gorgonacea	NS	NS	NS	NS	-0.16	NS	NS	NS	NS	NS	NS	-0.20	0.20
Porifera	Stick cladorhizid	NS	0.15	0.16	0.15	NS	0.32	-0.21	-0.31	0.30	0.24	NS	NS	0.19
	Arborescent cladorhizid	NS	-0.15	-0.17	-0.27	NS	NS	NS	-0.15	0.48	-0.15	NS	NS	0.29
	Vase hexactinellid	-0.22	-0.25	-0.23	-0.26	NS	-0.34	0.22	NS	0.27	NS	NS	NS	NS
Foraminifera	*Luffamina atlantica*	0.30	0.47	0.44	0.46	0.32	0.54	NS	-0.27	-0.18	0.44	NS	NS	NS

IV.6 Synthèse des résultats

Le développement durant ces dernières années de plates-formes sous-marines et de technologies optiques de plus en plus performantes a permis l'acquisition de données d'imagerie à des niveaux de résolution de plus en plus fins. Celles-ci permettent de cartographier les habitats et la mégafaune épibenthiques sur des échelles de temps et d'espace sans précédents. Malgré des efforts considérables visant l'étude des communautés associées aux sources hydrothermales, la distribution des espèces endémiques et périphériques a rarement été résolue à l'échelle des champs hydrothermaux. Afin d'évaluer la sphère d'influence de l'activité hydrothermale, nous avons annoté l'environnement ainsi que les assemblages biologiques et microbiens sur et autour de quatre édifices actifs du champ hydrothermal Lucky Strike. Des photographies du fond ont été acquises le long de transects parallèles, couvrant une surface totale de ~ 23 340 m². Le développement d'un protocole de traitement et d'analyse d'image innovant a ensuite permis de géoréférencer chaque empreinte d'image pour produire une carte de la faune hydrothermale et non-hydrothermale et identifier les facteurs environnementaux structurants. Pour ce faire, nous avons inclus à nos analyses des données de bathymétrie, position des sources hydrothermales actives et types de substrat ainsi que des données de courant. À l'aide d'analyses multivariées, nous avons évalué l'influence de chaque facteur dans les patrons de distribution spatiale observés. Les édifices du sud-est étaient caractérisés par de larges moulières de *Bathymodiolus azoricus* et des assemblages de zoanthaires situés plus en retrait de l'influence hydrothermale. A l'inverse, la faible couverture de moules et l'absence de zoanthaires au niveau des sites sud-centraux suggèrent l'importance du degré de maturité des édifices sur la distribution des communautés. En plus du "matériel blanc" associé à l'activité hydrothermale, nous avons observé une large distribution de dépôts oranges, témoignant d'une autre source de productivité primaire soutenue par des tapis microbiens oxydants de fer. Leur large couverture suggère leur importance géochimique mais aucun lien écologique avec la faune n'a pu être observé ou identifié à partir de l'imagerie. Les communautés périphériques non-hydrothermales étaient dominées par quelques morpho-espèces suspensivores et microcarnivores, localisées préférentiellement à proximité immédiate des sites ou des zones de sortie des fluides. Cette dépendance aux sources peut s'expliquer par la disponibilité d'une ressource d'origine chimiosynthétique ou la présence d'un substrat dur permettant la fixation des espèces sessiles. De plus, la topographie complexe facilite l'accès à la matière organique d'origine photosynthétique dont l'importance augmente au fur et à mesure que l'on s'éloigne des sources hydrothermales.

Notre étude a mis en évidence le potentiel de l'acquisition d'images du fond marin pour appréhender au mieux la sphère d'influence hydrothermale sur de grandes échelles spatiales. En conséquence, elle ouvre différentes perspectives de recherche quant à la caractérisation du rayon d'influence trophique de l'environnement hydrothermal sur une mégafaune périphérique qui pourra être identifiée par des échantillonnages ciblés. Cette étude a permis de caractériser une plus grande diversité d'habitats et d'assemblages que ce qui avait été permis avec les études temporelles réalisées aux chapitres précédent. Ainsi, elle nous permet de prendre du recul quant à la représentativité des dynamiques et des processus révélés dans les chapitres III et IV. D'autre part, elle nous permet d'étendre notre modèle de compréhension des dynamiques de la faune à de plus grandes échelles spatiales.

Dans le chapitre suivant, nous synthétiserons les résultats principaux de ce travail en les intégrant à différentes échelles spatiales et temporelles. Nous proposerons ensuite quelques perspectives de recherche et de méthodologie pour le futur.

Chapter V

Synthesis and perspectives

BOX 1 - Synthesis of Main Results

Chapter II: Spatio-temporal dynamics of vent assemblages at the assemblage and infra-annual scales using images acquired from 2012 to 2019 (res. ~ 5 cm).

- ✓ Monitoring of the physical habitat depicted high stability despite infra-annual variability in the proximity of the vent fluid due to hydrothermal material accretion. Change in the chemical habitat was predominantly related to tidal modulation.
- ✓ Spatial distribution of *Bathymodiolus azoricus* mussels was highly stable despite a gradual small-scale displacement (~ $dm^2.yr^{-1}$) in the proximity of the vent fluid.
- ✓ Densities of zoanthid assemblages were highly stable through time.
- ✓ Distribution of microbial mats was highly variable and heterogeneous over dm^2 and infra-annual time scales.
- ✓ Biotic interactions were rarely observed and did not appear to be a major driving factor of assemblage changes over time.

Chapter III: Spatio-temporal dynamics of vent assemblages at the edifice and pluri-annual scales using 3D reconstructions from 2015 to 2020 (res. ~ 15 cm).

- ✓ The structure of the edifice remained stable except in areas of emission where repeated collapse of spires and mineralisation of the edifice took place. The global distribution of venting activity remained stable.
- ✓ Spatial distribution of *B. azoricus* mussels was highly stable over 25 years of monitoring despite small-scale variability (< 2 $m^2.yr^{-1}$) in venting areas.
- ✓ Spatial distribution of zoanthid assemblages was highly stable through time.
- ✓ Our updated successional model suggests the presence of a dynamic equilibrium maintaining the climax stage of the vent mussel assemblages.
- ✓ Distribution of microbial mats progressively declined over the whole edifice, probably in response of a magmatic event.

Chapter IV: Spatial distribution of vent assemblages at the vent field scale using high-resolution seabed images acquired along ROV transects (res. ~ 5 cm).

- ✓ Most of vent assemblages remained restricted to vent edifices, with more extensive mussel populations on mature edifices in the south-east of Lucky Strike (i.e. Eiffel Tower and Montségur).
- ✓ Zoanthid assemblages were absent from south-central sites. They formed dense assemblages in the south-east of Lucky Strike.
- ✓ Distinct faunal communities occupied vent and non-vent areas. Peripheral communities displayed distributional differences based on substratum hardness, topographic complexity and proximity to venting areas. However, they remained highly similar among vent sites.
- ✓ The peripheral suspension-feeder and micro-carnivorous assemblages were typical of low-flow current regime and limited food supply conditions.

V.1 Summary of the results

Characterising the variability of natural systems at multiple scales can help to identify the relative influence of biotic and abiotic factors on faunal community structure in order to reach a comprehensive understanding of ecological processes at stake (Levin 1992). This study was designed to aggregate such multi-scale ecological knowledge on vent assemblages at the deep Lucky Strike vent field (LS; -1700 m). The primary objective was to assess if processes driving faunal variability varied across spatio-temporal scales. To do so, we successfully investigated patterns of variability at different nested scales using different imaging techniques (Box 1, Figure V.1A). Firstly, the high-frequency (i.e. daily to monthly) monitoring of biological assemblages over a square metre captured the overall stability of the habitat supporting the high constancy of mussel and zoanthid covers over 7 years. Small environmental modifications at the decimetre scale around the vent exit resulted in the slow migration of vent mussels (~ 10 $cm.yr^{-1}$). Their mobility may allow them to maintain themselves in optimal environmental conditions as previously observed for other mobile vent species in the Pacific (Sen et al. 2014; Lelièvre et al. 2017). For instance, most of the species inhabiting warmer and more variable habitats have high mobility capabilities (e.g. alvinellid worms, Sarrazin et al. 1997; rimicaridid shrimps, Copley et al. 2007; provannid gastropods, Sen et al. 2014). Microbial mats displayed highly heterogeneous patterns of distribution over both space and time. Similarly, at the scale of the vent edifice, most of the habitat variability remained constrained to venting areas were mussel assemblage distribution was more variable (Box 1). Microbial mats displayed a consistent decline over the whole edifice and over 5 years of monitoring coinciding with a slight "cooling" of the assemblages. The previous model of ecological succession proposed by Cuvelier et al. (2014) was revisited to account for the observed dynamic equilibrium of the Eiffel Tower biological assemblages. At the scale of the vent field, we observed higher mussel and zoanthid covers in the south-east while the more recently formed edifices of the south-central area of Lucky Strike may limit colonisation by vent assemblages (Box 1). The non-vent assemblages were dominated by a few morphospecies that colonised areas possibly still under venting influence and with complex topography (Box1; Figure V.1B-C).

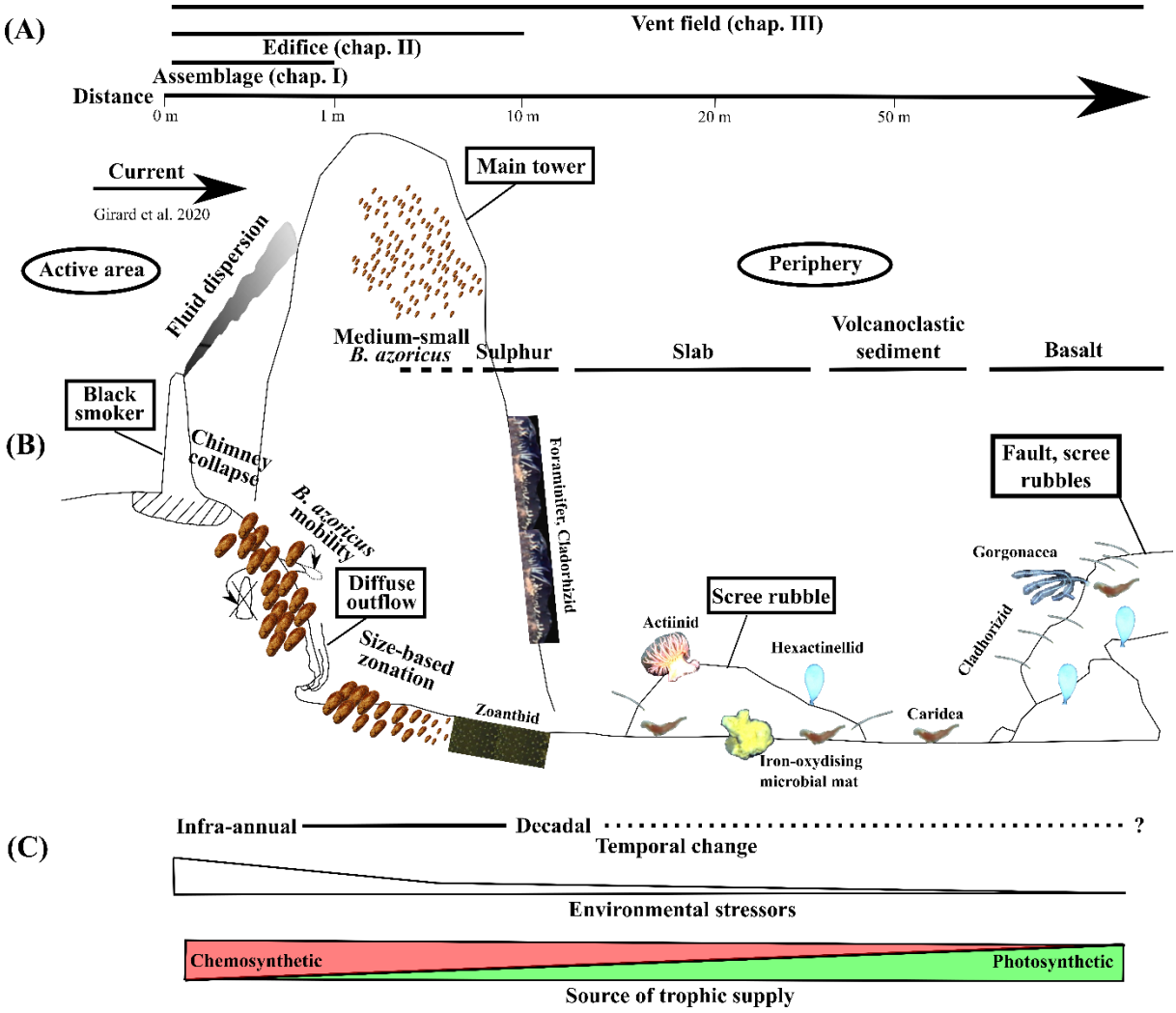

Figure V.1. Conceptual model of benthic assemblages' dynamics at the Lucky Strike vent field. (A) Spatial scale of observation of each study. Note that the distance scale is not linear. (B) Distribution of the vent and non-vent fauna. Ellipses delimit the active and peripheral areas. Rectangles indicate the presence of vents or topographic features. Substrata are represented with black lines. (C) Scale of temporal variation and importance of drivers in the spatial distribution of the benthic fauna.

V.2 Merging the scales

V.2.1 Spatio-temporal dynamics

High-frequency measurements of fluid parameters confirmed that tides strongly influence the variability of the vent chemical habitat (Johnson and Tunnicliffe 1985; Tivey and Johnson 2002; Barreyre et al. 2012). This periodic change conditions the variability of vent exposure of a few degrees (~ 3 °C) in the mussel assemblage. Its effect contrasts from the background environment that remains highly stable with changes of a maximum of ± 0.2 °C. Previous studies showed that *B. azoricus* physiology, transcriptome and behaviour are significantly

influenced by the tidal cycle (Mat et al. 2020). The role of tides was also highlighted in growth of vent mussels from the Pacific (Nedoncelle et al. 2015). Similarly, in the Atlantic and Pacific respectively, Copley et al. (1999) and Lelièvre et al. (2017) correlated tide variability with the micro distribution of motile taxa. In fact, vent shrimps, polynoids and pycnogonids appeared to adapt their position in phase with tidal periodicity, possibly to remain under optimal vent exposure. At Lucky Strike, no tidal variation in the behaviour of mobile non-symbiotic species, including M. *fortunata* and the crab *S. mesatlantica*, was observed (Cuvelier et al. 2017). This could be due to the high mobility of the shrimp and a lack of statistical power related to the low abundances of crabs (Matabos et al. 2015). Therefore, tidal variability should be a factor to consider when characterising the niche daily occupied by vent species (Cuvelier et al. 2011a; Robert et al. 2012). While previous studies conducted at Lucky Strike showed that tidal variability have an impact at the organism level (Mat et al. 2020), we did not further explore its role on species dynamics but rather focused on longer temporal scales.

The lack of observed interspecific biotic interactions within mussel and zoanthid assemblages suggests that they have a limited impact on the structure and dynamics of these assemblages. However, previous successional models established with images highlighted the importance of biotic interactions in structuring vent communities from the Pacific and controlling species realised niche (Sarrazin et al. 1997; Marcus et al. 2009; Podowski et al. 2009, 2010). However, at LS, the absence of other large invertebrates than *B. azoricus* suggests less competition for resources and space compared to what is observed in the Pacific (Sarrazin et al. 1997; Shank et al. 1998; Sen et al. 2014). In retrospect, neither environmental disturbance, nor biotic processes had significant impacts on Eiffel Tower vent assemblages. However, in the absence of observed mortality, the system cannot evolve perpetually towards the accumulation of individuals. Under sustained trophic supply, the availability of suitable habitat conditions (i.e. substratum to anchor with adequate vent exposure) will eventually limit the carrying capacity of the edifice. This thesis results confirmed Cuvelier et al. (2011b) hypothesis stating that the overall mussel assemblages (~ 270 m²) are at their climax stage and may have reached the carrying capacity of the edifice. This implies that other processes may contribute to cap this carrying capacity. They might include competitive mechanisms that cannot be resolved using imaging techniques. In intertidal mussel assemblages, aggregation is an essential trait to cope with the high intensity of natural disturbance (Bertness and Grosholz 1985; Khaitov 2013). In contrast, aggregative behaviour can be detrimental by promoting competition to access resources as the density of the assemblage increases (Bertness and Grosholz 1985; Lehane and Davenport 2004; Khaitov

2013). At Lucky Strike, the sustained stability of vent mussels could lead to competitive processes, such as larviphagy or grazing of small recruits, that may control the mussel population size (Sancho et al. 2005; Lenihan et al. 2008). Although the ecosystem-engineer *B. azoricus* mussel favours the settlement of associated fauna (Sarrazin et al. 2015) and microbial mats, inhibitory interactions are hypothesised to predominate close to the vent exit where the biomass of mussels and grazers increases (Husson et al. 2017). Nevertheless, this hypothesis remains to be tested. In addition to higher temporal variations and environmental stressors characterising large mussel assemblages, competitive inhibition may thus contribute to the lower diversity observed compared to colder habitats (Husson et al. 2017; Sarrazin et al. 2020).

Mapping environmental and faunal changes with image time-series at the scale of the assemblage and edifice (Figure V.1A) showed that sub-annual habitat variability was high in the vicinity of vent exits (Box 1; Figure V.1B). Investigating change in venting activity across the Eiffel Tower edifice allowed classification in three main categories depending on their associated dynamics: infra-annual collapse of venting features, vent exit closure/opening, gradual material accretion (Figure V.1B). Focused venting emanating from spires or chimneys made of friable sulphides repeatedly collapsed between years. Infra-annual repetitive collapse of hydrothermal features appeared to be the main observed factor of disturbance for the fauna with low capacity of mobility such as vent mussels. This could explain their absence on these features as observed in another Pacific study with vent siboglinids (Tunnicliffe et al. 1990; Sarrazin et al. 2002). Decimetre to metre-scale relocation of vent exits resulted from the opening/extinction of a diffusers, without initiating changes in vent activity at larger scales. We also observed that diffusers and flanges can undergo a gradual accretion of hydrothermal minerals up to 1 decimetre per year, possibly contributing to most of the structural build-up of the Eiffel Tower edifice over 5 years (Figure V.1B). Long-term video observations at the metre scale showed that accretion processes result in the displacement of aggregations of large vent mussels (i.e. byssus-bounded), underlining their ability to migrate over distances in the order of ~ 1 dm.yr^{-1} (Box 1). Mobility might allow mussels to maintain themselves into optimal vent exposure conditions suggesting that mobility is a fundamental functional trait ensuring mussels to cope with fine-scale changes of the hydrothermal habitat. Similarly, the importance of mussel mobility in shaping fine-scale temporal dynamics has been reported at Pacific vents (Johnson et al. 1994; Sen et al. 2014) as well as for coastal mussels (Paine 1974; Paine and Levin 1981; Bertness and Grosholz 1985). In the Pacific, mussel displacement remains a means to colonise *Riftia pachyptila* assemblages as vent exposure declines locally (Shank et al. 1998).

The observed scale invariance across Chapters II and III suggests that processes related to venting modification is the predominant driver of *B. azoricus* assemblage dynamics over pluri-annual to multi-decadal scales (Box 1; Figure V.1B). Previous studies at fast-spreading ridges in the Eastern Pacific focusing on post-eruptive recovery of communities have described vent ecosystems as highly dynamic and ephemeral with regular settlement of vent assemblages through recolonisation (Lutz et al. 1994; Tunnicliffe et al. 1997; Shank et al. 1998; Marcus et al. 2009). However, temporal monitoring at slower-spreading features challenged this assumption and described, in the lack of eruptive events, the maintenance of stable communities over a decade (Copley et al. 2007; Gebruk et al. 2010; Cuvelier et al. 2011b; Sen et al. 2014; Du Preez and Fisher 2018). In this work, the high stability of vent communities at Eiffel Tower was confirmed and extended to 25 years (Box 1). The lack of apparent mortality (i.e. empty shell) at the assemblage scale supported the presence of long-lived and stable populations on the edifice. This long-term stability has implications in terms of conservation regulations that are being established in the scope of future deep-sea mining activities (Van Dover 2011; Levin et al. 2016b). Low regime of environmental disturbance suggests that *B. azoricus* mussels might not be able to recover from large-scale disturbance due to SMS mining. This aligns with results provided by a pluri-annual clearance experiment at the Montségur edifice (LS) that showed the lack of recovery of mussels over 2 years (Marticorena et al. 2021). Nonetheless, there remains a lack of knowledge on fundamental ecological traits of *B. azoricus* to infer their recovery potential, such as growth rate or life expectancy (Husson et al. 2018). These latter could not be assessed properly using imagery because of the difficulty to track individuals over several months to years. Experimental approaches could provide such information in the future (e.g. Rhoads et al. 1981; Schöne and Giere 2005; Nedoncelle et al. 2013).

In contrast to mussel assemblages, microbial mats were much more variable in space and time at the scales of the assemblage and edifice. Investigation at the metre scale showed that their dynamics were highly variable at infra-annual scale and heterogeneous in space (Box 1). These variations could result from biotic interactions such as growth facilitation by mussels (i.e. fluid diversion) and their byssus threads (i.e. surface availability) or predation by grazers (Cuvelier et al. 2011a). However, at this scale (< 1 m^2), the rapid development of microbial mats may result from the stochastic growth of a biofilm non-visible in the images until it reaches a certain thickness/size (Guezennec et al. 1998). Those sporadic growths may also occur at the scale of the edifice, but the pluri-annual sampling frequency was inappropriate to observe this process. At the pluri-annual scale, we observed the progressive decline of microbial mats over the edifice

in parallel to a subtle but general "cooling" of vent assemblages, despite apparent stable venting. At LS, the effect of magmatic event on the vent fluid composition can shape microbial communities over time, including in diffuse zones (Rommevaux et al. 2019). Magmatic and tectonic events reported in 2001 and 2015 at Lucky Strike could explain such variations (Dziak et al. 2004; Cuvelier et al. 2011b; Ballu et al. 2019). In the Pacific, a post-eruptive monitoring has shown the rapid development of white filamentous mats (Nees et al. 2008), suggesting the role of large scale geophysical processes on microbial mat development. These mats may develop in response to the modification in the plumbing system that ultimately may affect the composition of the vent fluid (Butterfield et al. 1997; Von Damm 2000). However, we detected no anomalies in the vent fluid physico-chemical characteristics at the scale of the assemblage, although this could be due to the practical difficulty to maintain a single point measurement over time and space as well as due to the lack of replicates. On the other hand, microbial mats may have temporarily benefited from ejecta or particles released during plumbing modification (Juniper et al. 1995), which could explain their growth at Eiffel Tower following the dyke event of 2001 (Dziak et al. 2004; Cuvelier et al. 2011b). Redistribution of ejecta or particles over the structure by black smokers may have provided temporary source of inorganic compounds to support their growth (Girard et al. 2020a).

V.2.2 Spatial distribution

Our results highlighted the strong spatial zonation of vent and non-vent communities at all investigated scales. They confirmed that the dilution gradient of the vent fluid and its sphere of influence are predominant in explaining benthic faunal distribution (Figure V.1B). We considered the role of environmental stressors and derived chemosynthetic material input as drivers of spatial distribution in order to integrate our results together (Figure V.1C).

At fine scales, the arrangement of faunal assemblages in decimetre-scale mosaics is linked to the steep dilution gradient, with large mussels occupying the close vicinity of vent exits characterised by the highest environmental variability while zoanthids occupy more stable habitats with low hydrothermal influence (no temperature anomaly; Cuvelier et al. 2009; Figure V.1B). This is consistent with most ecological studies at vents that highlighted the role of the vent fluid dilution gradient on the distribution of vent faunal assemblages across all vent systems (Copley et al. 1997, 2016; Shank et al. 1998; Sarrazin and Juniper 1999; Podowski et al. 2009; Marsh et al. 2012; Zhou et al. 2018).

Vent edifices remain a particular setting with a high heterogeneity of the habitat. Firstly, their vertical structure allows the upward flow of vent fluid to adequately reach vent assemblages located above (Podowski et al. 2010; Sen et al. 2013; Figure V.1B). In addition to physical disturbance, the fluid outflow heterogeneity over edifices fragments the vent assemblages of the Juan de Fuca Ridge resulting in a mosaic spatial arrangement (Sarrazin et al. 1997, 1999). Furthermore, the complexity of the topography may lead to enhanced hydrodynamics affecting the redistribution of vent fluids and particles (Girard et al. 2020a). This leads to differences of community based on the orientation of the side they colonise (Marsh et al. 2012; Sen et al. 2014). At Eiffel Tower, vent fluid redistribution by current creates heterogeneous patterns of microbial mat and mussel distribution by sides (Cuvelier et al. 2011b; Girard et al. 2020a; Figure V.1B). Comparing edifices across Lucky Strike showed that cover of mussels predominantly dominated vent edifices in the south-east edifices (Eiffel Tower and Montségur) contrasting with the restricted mussel patches at south-central edifices (White Castle, Crystal, South Crystal and Sapin; Box 1). We hypothesise that this pattern could be due to different maturities of the edifices (Hannington et al. 1995). For instance, mature edifices in the south-east would provide large surface areas with extensive diffusion zones available for colonisation and that could sustain large mussel populations. Conversely, we suggest that *B. azoricus* might not have sufficient suitable habitats to colonise the smaller sulphide structures of the south-central sites that harbour a few black smokers. The latters may nonetheless explain the larger cover of microbial mats in the south-east. Although hydrothermal activity has remained relatively stable at these sites (Barreyre et al. 2012), recent observations have also depicted large structural variations of the White Castle edifice within a year (Wheeler et al. in prep.). This demonstrates that, within a single vent field, edifices may not be equivalent in terms of habitat provision and possibly dynamics. Furthermore, mature edifices hosting extensive *B. azoricus* populations may constitute the main source of larvae, therefore contributing to maintain connectivity at the vent field scale.

Peripheral communities dominated by ~ 5 morphospecies remained highly similar among sites despite differences in the end-member fluid composition (Chavagnac et al. 2018; Box 1). In the periphery, we characterised the spatial zonation of a few non-vent species in the sphere of influence of venting areas. A few morpho species (e.g. cladorhizids, foraminifera) densely clustered around active areas (i.e. edifices and cracks; Figure V.1B). Their high density may be supported by the chemosynthesis-based production export (Figure V.1C). The presence of non-vent suspension-feeders community taking advantage of chemosynthetic production in the

close proximity of active areas has been previously described at many vent sites (Hessler et al. 1988; Galkin 1997; Van Dover et al. 2001; Erickson et al. 2009; Podowski et al. 2009, 2010; Fabri et al. 2011; Marsh et al. 2012; Levin et al. 2016a). For instance, some morphotaxa were similar to the peripheral community described from the south-west Pacific vents (Sen et al. 2016). At a distance of ~ 100 m from active sites, Erickson et al. (2009) and Roohi et al. (2022) showed the importance of chemosynthetic-derived food supply in the West Pacific and Atlantic, respectively. Furthermore, hydrothermal active areas not only contribute to the export of trophic supply, but also provides a hard substratum for colonisation by sessile species (i.e. edifices, rubbles or inactive chimneys; Levin et al. 2016a). At LS, we observed the influence of topographic complexity in the distribution of sessile suspension feeders and micro-carnivorous taxa (e.g. basalt; Figure V.1B). Topographic complexity locally enhances current hydrodynamics and, as a result, the resuspension of organic matter. The importance of topographically complex hard substratum away from vent exposure (e.g. basalt at ~ 100 m) in structuring the distribution of suspensivores and micro-carnivores, suggests that food limitation constrain the survival of non-vent fauna to those habitats rather than in soft and flat substratum (e.g. slab or volcanoclastic deposits). Food limitation was also suggested to be the main process explaining the dominance and dynamics of sponge morphotypes typical of food-poor areas (Sen et al. 2016; Schönberg 2021). In fact, at around a hundred metres, photosynthetic-derived organic matter predominantly contributes to the diet of the non-vent fauna (LS: Alfaro-Lucas et al. 2020; Rainbow: Roohi et al. 2022; Figure V.1C). Assuming environmental filtering following recommendation of Alfaro-Lucas et al. (2020), we hypothesise that those peripheral communities may be severely impacted by SMS mining. Furthermore, the panel of functional traits of the peripheral fauna recently suggested their high sensitivity to deep-sea mining activities (Boschen-Rose et al. 2021).

V.3 Methodological developments

The EMSO-Azores deep-sea observatory allowed to revisit the spatio-temporal scales at which ecological investigations are typically performed in the deep sea, thanks to recent advances in underwater platforms and imaging techniques (e.g. Kwasnitschka et al. 2013; Marcon et al. 2013; Robert et al. 2020; Girard et al. 2022). Deep-sea observatories have already been useful for the infra-daily monitoring of an ecosystem, but studies remained often limited to infra-annual duration (e.g. Juniper et al. 2013; Doya et al. 2014; Matabos et al. 2014, 2015; Sarrazin

et al. 2014; Lelièvre et al. 2017; Girard et al. 2020b). The long-term datasets acquisition now allows to disentangle the scales of variability from infra-daily to pluri-annual time scales (e.g. Taylor et al. 2017; Chauvet et al. 2018, 2019; De Leo et al. 2018; Durden et al. 2020). In addition, multidisciplinary monitoring of the environment provides information on habitat variability, essential to identify the drivers of faunal dynamics (Matabos et al. 2022). Nevertheless, the unique and unprecedented characteristics of seabed image sets acquired in this study required the development of new image processing and analytical methodologies (Figure V.2).

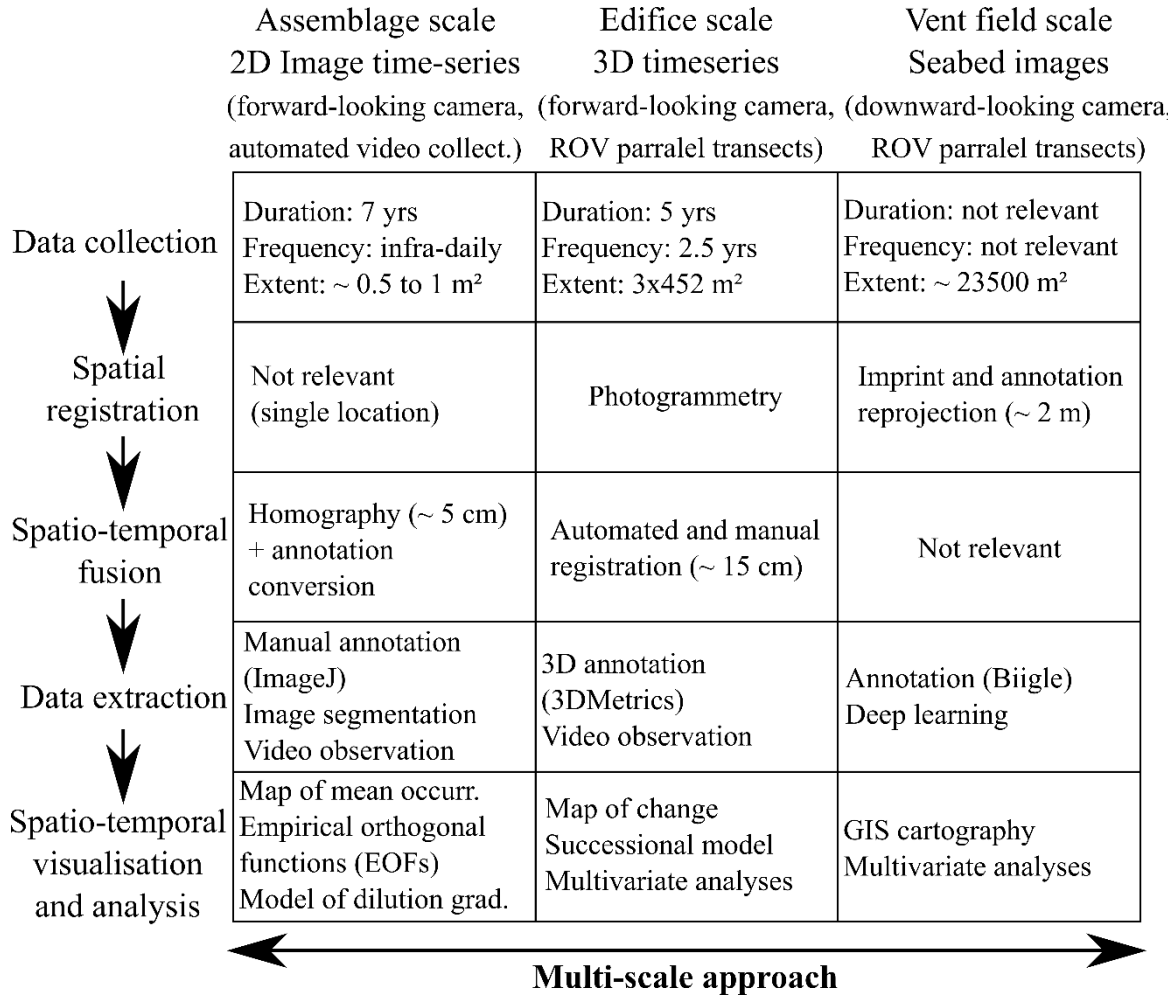

Figure V.2 . General workflow of the three case studies presented in this thesis project from data collection to spatio-temporal visualisation and analyses.

Data collection – In this work, we successfully made use of different imaging techniques to characterise the faunal structure in space and/or time. However, those methods involved different spatial/temporal extents and resolution (Figure V.2). In fact, there remains a compromise between the frequency of sampling and the scale of investigation primarily constrained by the time needed to image the seabed. In this work, we addressed this issue using

a multi-scale approach with studies nested in scales. Methods involved the use of a camera relayed to an observatory infrastructure as well as overlapping transects performed with an underwater vehicle with different configuration of the camera depending on the setting targeted (Figure V.2). As a result, we encountered different challenges and designed different protocols. They followed a similar structure that could be generalised in a workflow (Figure V.2).

Georeferencing - Spatial registration of the images is the first aggregation step and aims to reposition images relatively to each other in space (Figure V.2). Hence, it was not necessary for the camera module as it only recorded one image at a time in the same location. At the edifice scale, the photogrammetry algorithm enabled to rebuild three times and with a high resolution, a georeferenced 3D model of a complex structure (Arnaubec et al. 2015; Figure V.2). Similarly, the parallel transects of seabed images were designed for photogrammetric reconstruction which could have optimised spatial registration of images. Hence, we developed an algorithm capable of ray tracing in order to reproject image imprints over the 3D model, and to calculate an accurate overlap using the optical navigation extracted after photogrammetric reconstructions (Marcillat et al. in prep.). Nevertheless, computer power severely limited the reconstruction of 3D models because of the high number of images of parallel transects (> 4000). The use of a supercomputer could tackle that issue and remains to be explored. Instead, we selected a set of non-overlapping images and reprojected them into a 2D georeferenced system, despite using the less-accurate navigation system of the ROV.

Spatio-temporal fusion – Two of our datasets contained time-series of images which required to aggregate them over time and space (Tang et al. 2020). The TEMPO ecological module was slightly displaced each year during redeployment, creating a set of images with partial overlaps. The spatio-temporal fusion was automated with a routine that automatically repositionned ~ 4000 images using homographies computed with a feature-matching algorithm (Agarwal et al. 2005). Still, we included the possibility to manually match features as changes of camera and light attenuation prevented from any feature matching between certain years. Furthermore, we implemented optional algorithms to extract overlapping areas, to include masks, to provide a metric scale to the images and to convert prior annotations in case the acquisition of the time series continues in the future. This unique workflow developed on Python and specifically designed for handling temporal series of 2D images should be released in the following years. At the edifice scale, 3D overlay of models was performed to reach a residual offset of ~ 15 cm which remains satisfactory compared to resolution acquired in terrestrial investigation with drones (~ 5 cm; Cucchiaro et al. 2018). Because of distortion within the 3D models, we divided

them in sub portions which significantly fastened their manipulation on screen. Despite that considerable effort, we acknowledge that the targeted accuracy of the spatio-temporal fusion should be defined depending on the scales of the research questions. For instance, our investigation with TEMPO had for hypothesis that variability of the vent mussel assemblage occurs at decimetre scales. However, this method may not be relevant in the case of mobile fauna occupying a much larger habitat than the spatial window captured by the camera (e.g. Chauvet et al. 2019; Durden et al. 2020).

Data extraction – As the three image sets came with their own practicalities and panels of targeted organisms, their annotation required the cautious selection of an adequate annotation software. At the scale of the assemblage, ImageJ was selected (Rasband 1997). At the scale of the edifice, 3D metrics enabled to annotate in 3D to avoid overlooking the topographical perspective (Laranjeira et al. 2020). At the scale of the vent field, Biigle eased annotation of a large panel of species with a label tree and fastened annotation re-evaluation with the largo tool (Langenkämper et al. 2017; Figure V.2). However, the use of Biigle comes with the cost of losing the georeferencing of annotations within images. Thus, we developed a feature-matching based algorithm to georeference Biigle annotations on seabed images (Marcillat et al. in prep.). To go further, we considered the use of 3D models to additionally extract descriptors of microtopography which would have be an asset to describe non-vent fauna affinities for specific substratum (e.g. basalt). However, computation of 3D models comes with a loss of quality compared to 2D images, hence erasing small organisms from the models (~ cm; Thornton et al. 2016). Hence, we developed ray-tracing algorithms to project annotations made on 2D images with Biigle over 3D models (repositioning precision: ~ 5 cm; see Marcillat 2022).

As annotation was time consuming (3 to 8 months for each dataset), we identified several ways to fasten that process. In order to optimise annotation time, the use of automated algorithms was tested on a few features and demonstrated high potential for future implementation (e.g. image segmentation on zoanthid in Chapter II; deep learning of image substratum in Chapter IV; Soto Vega et al. in prep.; Figure V.2). They however required specific expertise in order to adapt the image detection algorithms to the particularities of the dataset. Furthermore, in the case of high autocorrelation of the time series (e.g. high stability), we recommend to evaluate if reusing the annotation made at time t-1 could fasten the annotation process at t+1. This will also considerably decrease artefacts arising by independent annotations over time.

Spatio-temporal visualisation and analyses – In this thesis we dissected the scales of spatial and temporal variabilities using a large array of analyses (e.g. uni- or multivariate) and visualisation methods (e.g. mapping). The multidimensionality of the data (TEMPO: 3D, and Eiffel Tower: 4D) does not allow to easily display the results, which led us to employ analyses that aggregate the data over one or more dimensions. Univariate analyses are regularly used to look at general patterns of change by aggregating data over time or over space (e.g. map of change and of mean occurrence; total cover through time, periodograms). Dissecting spatio-temporal patterns or punctual events is a challenge because the size of a high-resolution datasets is rapidly increasing as time steps (i.e. high sampling frequency) and spatial resolution (e.g. tile or pixel) are summed up. We recommend reducing the dimensionality of the dataset with numerical approaches such as variance partitioning over space or time as in the case of univariate dataset (e.g. PCA or also called "empirical orthogonal function" built in the Python homography routine, see Chapter II; Rubio et al. 2020) or using proxies of species composition for multivariate datasets (e.g. assemblage position along a gradient, clustering, trajectory analyses; see Chapter III; De Cáceres et al. 2019; Legendre 2019; Sturbois et al. 2021). The identification of drivers of change can be assessed with multivariate response analyses (e.g. MRT, RDA; Legendre and Legendre 2012; Borcard et al. 2018). Furthermore, RDA offers the possibility to integrate the spatial or temporal relationships inherent to the data (e.g. either time with asymmetric eigenvector maps [AEMs], or space with distance-based Moran's eigenvector maps [dbMEMs]; Blanchet et al. 2008; Legendre and Gauthier 2014).

V.4 Conclusion & perspectives

Theoretically, under stable environmental conditions, a climax equilibrium remains the terminal state of different successional stages (Connell 1978). This probably explains the absence of other stages of succession in vent assemblage at the Eiffel Tower edifice. An induced small-scale disturbance experiment showed that ecological succession at LS transitions first through opportunistic species, including shrimps and gastropods, in the two years following clearance (Marticorena et al. 2021). Therefore there is still a lack of knowledge on the processes shaping successional trajectories to reach a climax vent community at LS. The high-resolution pluri-annual investigation highlighted few areas across Eiffel Tower where transitions between assemblages of mussel of different sizes occurred over a few square metres. Monitoring the natural succession in those areas could confirm or infirm succession patterns proposed by

Marticorena et al. (2021) after disturbance. Infra-daily imagery monitoring in those specific areas of the edifice may also help to discriminate between the role of mussel recruitment and mobility. In addition, monitoring the dynamics of immature edifices being more likely to undergo drastic changes (e.g. Zhou et al. 2018 at Longqi vent field; White Castle edifice of LS in Wheeler et al. in prep.), may provide additional insights on factors driving the spatio-temporal distribution of vent assemblages. Furthermore, monitoring of senescent areas mapped by Barreyre et al. (2012) should be considered to acquire a full understanding of successions under varying venting conditions (e.g. the Sintra edifice of LS being partially inactive). The EMSO-Azores observatory provides the infrastructure and cruise opportunities that could support such studies in the future.

Our vent field-scale study suggested that non-vent communities are not evenly distributed. highlighting the importance of habitat heterogeneity over distances of at least a hundred meter, as observed in other case studies (Arquit 1990; Boschen et al. 2016; Gerdes et al. 2019b). The characterisation of the fauna over larger scales would increase our understanding on the distribution of benthic communities to discriminate the importance of habitat provision vs. vent-derived material along a gradient of hydrothermal influence. The dominance of a few poriferan and cnidarian taxa showed high similarities with peripheral communities observed by Sen et al. (2016). However, as our identification was based on images, taxonomic/genetic identification of morphotaxa is recommended during targeted sampling. In combination, stable isotope or fatty acid analyses will provide insights on the importance of chemosynthetic-derived material in their diet (e.g. for zoanthids, foraminifers or microcarnivorous sponges; Colaço et al. 2007; Erickson et al. 2009; Alfaro-Lucas et al. 2020). Moreover, the trophic link between non-vent assemblages and primary productivity derived from iron-oxidisation should be investigated. It could represent an important new mechanism of hydrothermal influence considering the wide-distribution and extensive cover of orange deposit we observed over LS (Henri et al. 2013). As hydrodynamics and venting locations are well known at LS (Barreyre et al. 2012), we could easily define a sampling design involving faunal collection for stable isotope analyses combined with the deployment of turbidity metres and sediment traps. This design would allow to test if the processes linked to hydrothermal influence are scale-dependent (e.g. microcarnivorous sponge; Arquit 1990; Gerdes et al. 2019; Figure V.1). Much less is known regarding dynamics of peripheral fauna although Sen et al. (2016) described exceptionally fast growth rates and mortality for a few microcarnivorous sponges at vents in the Pacific. Our detailed mapping of

non-vent fauna may be the start for a temporal monitoring combining environmental monitoring performed by the EMSO-Azores observatory.

As deep-sea observatories and mapping technologies (e.g. AUVs) are rapidly developing around the world and image sets are being built up (Delaney et al. 2016; Aguzzi et al. 2019; Durden et al. 2020; Girard et al. 2020b; Rountree et al. 2021; Thornton et al. 2021; Matabos et al. 2022), the international scientific community is gathering to identify future needs and research strategies of imaging (Schoening et al. 2017). For instance, collecting images with the most accurate repositioning in space is important to make the data most useful (Schoening et al. 2017), but it is also a start to build long-term time series that could be reused over decades, notably for defining conservation guidelines as exploitation speculation on deep-sea resources is rising (e.g. Glover and Smith 2003; Simon-Lledó et al. 2019). As we improved the accuracy of spatio-temporal repositioning of images, the workflows developed therein provided adequate protocols to acquire and analyse high-resolution multi-scale data (e.g. homography on 2D images, *Chubacapp*; Figure V.2). Nevertheless, the bottleneck of the annotation task resides in the annotation task. As more extensive datasets are being collected, they come with higher time consumption and cost of annotation (Durden et al. 2016; Schoening et al. 2017). While this task is often left to students, the development of feature segmentation and deep-learning algorithms remains promising for alleviate image annotation (Piechaud et al. 2019; de Oliveira et al. 2021; Yamada et al. 2021; Katija et al. 2022). As an alternative, the engagement of citizens through participative science platforms could provide massive datasets to train algorithms in the coming years (Hoeberechts et al. 2015; Borremans and Matabos 2018).

Chapitre VI

Synthèse et perspectives

ENCADRÉ 1 – Synthèse des principaux résultats

Chapitre II : Dynamique spatio-temporelle des assemblages hydrothermaux à l'échelle de l'assemblage et à l'échelle infra-annuelle à partir d'images acquises de 2012 à 2019 (rés. ~ 5 cm).

✓ Le suivi de l'habitat physique a montré une grande stabilité malgré la variabilité infra-annuelle à proximité de la source de fluide causée par l'accrétion de matériel hydrothermal. Les changements dans l'habitat chimique étaient principalement liés à la modulation par les marées.

✓ La distribution spatiale des moules *Bathymodiolus azoricus* était stable malgré un déplacement graduel à petite échelle (~ $dm^2.an^{-1}$) à proximité de la source de fluide.

✓ Les densités des assemblages de zoanthaires étaient stables dans le temps.

✓ La distribution des tapis microbiens était variable et hétérogène sur des échelles considérant des patchs de l'ordre du ~ dm^2 à l'échelle infra-annuelle.

✓ Les interactions biotiques ont rarement été observées et ne sont pas apparues comme un facteur majeur de changement des assemblages dans le temps.

Chapitre III : Dynamique spatio-temporelle des assemblages hydrothermaux à l'échelle de l'édifice et à l'échelle pluri-annuelle en utilisant des reconstructions 3D de 2015 à 2020 (rés. ~ 15 cm).

✓ La structure de l'édifice Tour Eiffel est restée stable sauf dans les zones d'émission où des effondrements répétés de cheminées et une minéralisation de l'édifice ont eu lieu. La distribution globale de l'activité hydrothermale est restée stable.

✓ La distribution spatiale des moules *B. azoricus* est restée très stable sur 25 ans de suivi malgré une variabilité à petite échelle (< 2 $m^2.an^{-1}$) dans les zones d'émission.

✓ La distribution spatiale des assemblages de zoanthaires était stable dans le temps.

✓ Notre modèle de succession mis à jour suggère la présence d'un équilibre dynamique maintenant le stade climax des assemblages de modioles hydrothermales.

✓ La distribution des tapis microbiens a progressivement diminué sur l'ensemble de l'édifice, probablement suite à un événement magmatique.

Chapitre IV : Distribution spatiale des assemblages benthiques à l'échelle du champ hydrothermal en utilisant des images du fond sous-marin acquises à haute résolution le long de transects réalisés par le ROV (rés. ~ 5 cm).

✓ La plupart des assemblages hydrothermaux sont restés confinés aux édifices, avec des populations de moules plus importantes sur les édifices matures au sud-est de Lucky Strike (i.e. Tour Eiffel et Montségur).

✓ Les assemblages de zoanthaires étaient absents des sites du centre-sud. Ils formaient des assemblages denses dans le sud-est de Lucky Strike.

✓ Des communautés fauniques distinctes occupaient les zones avec et sans apparente activité hydrothermale. Les communautés périphériques présentaient des différences de distribution basées sur la dureté du substrat, la complexité topographique et la proximité des zones d'émission. Cependant, elles sont restées similaires entre les sites hydrothermaux.

✓ Les assemblages périphériques de suspensivores et de microcarnivores étaient typiques d'un régime courantométrique de faible débit et de conditions d'approvisionnement alimentaire limité.

VI.1 Résumé des résultats

La caractérisation de la variabilité des systèmes naturels à plusieurs échelles peut aider à identifier l'influence relative des facteurs biotiques et abiotiques sur la structure des communautés faunistiques, afin d'atteindre une compréhension globale des processus écologiques en jeu (Levin 1992). Cette étude a été conçue pour rassembler de telles connaissances écologiques multi-échelles sur les assemblages hydrothermaux dans le champ hydrothermal profond Lucky Strike (LS; -1700 m). L'objectif principal était d'évaluer si les processus conduisant à la variabilité de la faune variaient selon les échelles spatio-temporelles. Pour ce faire, nous avons étudié avec succès les patrons de variabilité à différentes échelles imbriquées en utilisant différentes techniques d'imagerie (Encadré 1, Figure VI.1A). Tout d'abord, la surveillance à haute fréquence (i.e. quotidienne à mensuelle) des assemblages biologiques sur un mètre carré a permis de caractériser la stabilité globale de l'habitat qui supporte la stabilité observée des couvertures de moules et de zoanthaires sur 7 ans. De petites modifications environnementales à l'échelle décimétrique autour de la sortie de fluide ont entraîné la lente migration des moules hydrothermales (~ 10 $cm.an^{-1}$). En effet, leur mobilité peut leur permettre de se maintenir dans des conditions environnementales optimales, comme cela a été observé précédemment pour d'autres espèces hydrothermales mobiles dans le Pacifique (Sen et al. 2014; Lelièvre et al. 2017). En outre, la plupart des espèces habitant des habitats plus chauds et plus variables ont des capacités de mobilité élevées (par exemple, les vers alvinellidés, Sarrazin et al. 1997; les crevettes rimicaridés, Copley et al. 2007; les gastéropodes provannidés, Sen et al. 2014). Les tapis microbiens présentaient des schémas de distribution très hétérogènes à la fois dans l'espace et dans le temps. Parallèlement, à l'échelle de l'édifice hydrothermal, la plupart de la variabilité de l'habitat est restée cantonée aux zones d'émission, lieu où la distribution de l'assemblage de moules était plus variable (Encadré 1). Les tapis microbiens ont montré un déclin constant sur l'ensemble de l'édifice et sur 5 ans de suivi coïncidant avec un léger "refroidissement" des assemblages. Le précédent modèle de

succession écologique proposé par Cuvelier et al. (2014) a été revisité pour rendre compte de l'équilibre dynamique observé des assemblages biologiques de l'édifice Tour Eiffel. À l'échelle du champ hydrothermal, nous avons observé des couvertures plus élevées de moules et de zoanthaires dans le sud-est, tandis que les édifices plus récemment formés dans la zone centre-sud du champ Lucky Strike peuvent limiter la colonisation par les assemblages hydrothermaux (encadré 1). Les assemblages non hydrothermaux étaient dominés par quelques morpho-espèces colonisant des zones possiblement encore sous l'influence des émissions et présentant une topographie complexe (Encadré 1; Figure VI.1B-C).

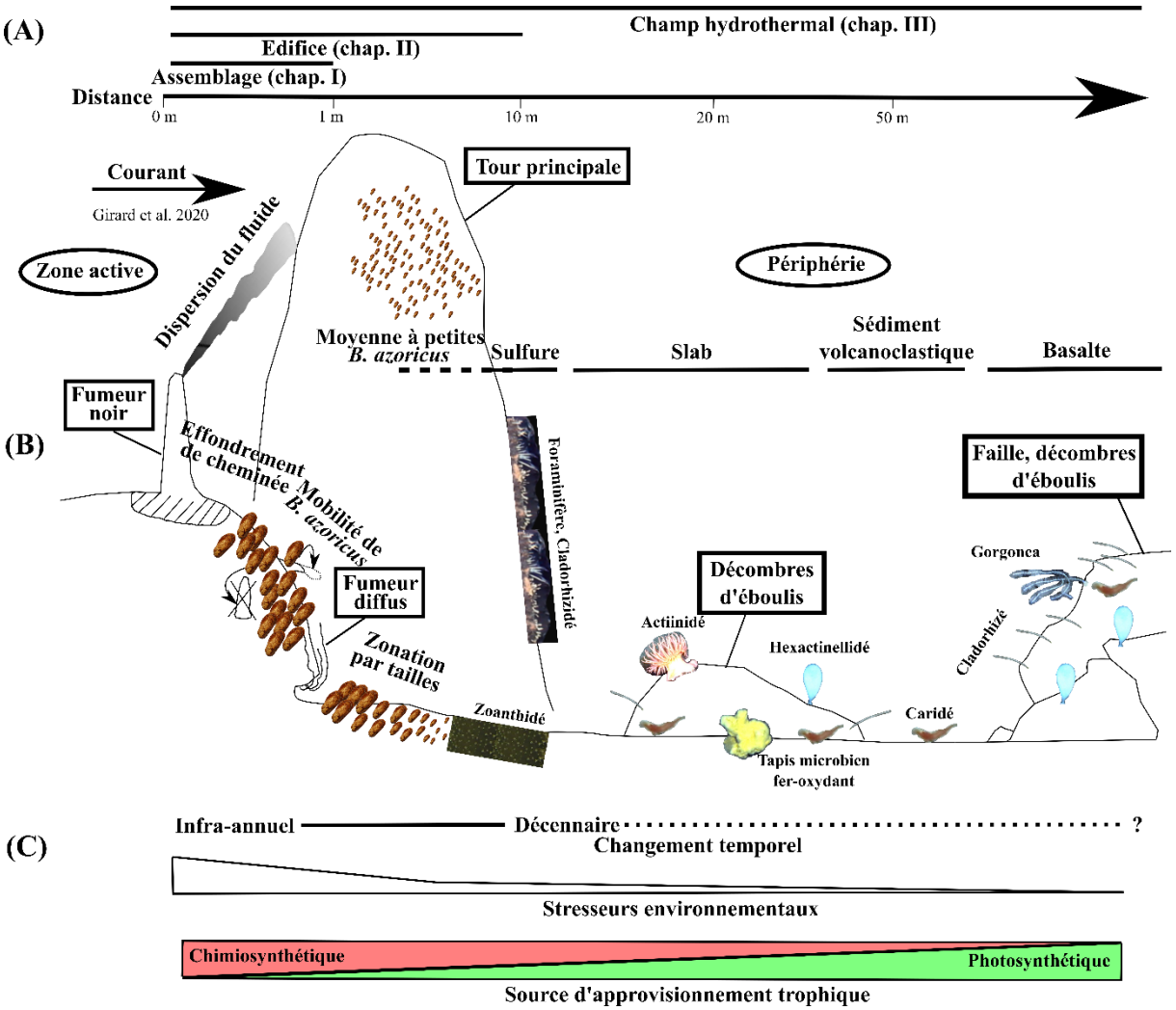

Figure VI.1 Modèle conceptuel de la dynamique des assemblages benthiques dans le champ hydrothermal Lucky Strike. (A) Échelle spatiale d'observation de chaque étude. Notez que l'échelle de distance n'est pas linéaire. (B) Distribution de la faune hydrothermale et non-hydrothermale. Les ellipses délimitent les zones actives et périphériques. Les rectangles indiquent la présence de sorties de fluide ou d'éléments topographiques. Les substrats sont représentés par des lignes noires. (C) Échelle de la variation temporelle et importance des facteurs dans la distribution spatiale de la faune benthique.

VI.2 Intégration des échelles

VI.2.1 Dynamique spatio-temporelle

Les mesures à haute fréquence des paramètres des fluides ont confirmé que les marées influencent fortement la variabilité de l'habitat chimique hydrothermal (Johnson et Tunnicliffe 1985; Tivey et Johnson 2002; Barreyre et al. 2012). Ce changement périodique conditionne la variabilité de l'exposition au fluide de quelques degrés (~ 3 °C) dans l'assemblage de moules. Son effet contraste avec les températures de l'environnement plus froid, restant très stables et ce, malgré des changements d'un maximum de ± 0,2 °C. Des études précédentes ont montré que la physiologie, le transcriptome et le comportement de *B. azoricus* sont significativement influencés par le cycle des marées (Mat et al. 2020). Le rôle des marées a également été mis en évidence dans la croissance des moules hydrothermales du Pacifique (Nedoncelle et al. 2015). De même, dans l'Atlantique et le Pacifique respectivement, Copley et al. (1999) et Lelièvre et al. (2017) ont corrélé la variabilité des marées avec la microdistribution de taxons hydrothermaux mobiles. En effet, les crevettes, les polynoïdes et les pycnogonides semblent adapter leur position en phase avec la périodicité de la marée, peut-être pour rester sous une exposition optimale au fluide hydrothermal. A Lucky Strike, aucune variation de marée dans le comportement des espèces mobiles non symbiotiques, dont la crevette *M. fortunata* et le crabe *S. mesatlantica*, n'a été observée (Cuvelier et al. 2017). Cela pourrait être dû à la grande mobilité des crevettes conjuguée à un manque de puissance statistique lié à la faible abondance des crabes (Matabos et al. 2015). Par conséquent, la variabilité des marées devrait être un facteur à prendre en compte pour caractériser la niche quotidiennement occupée par les espèces hydrothermales (Cuvelier et al. 2011a; Robert et al. 2012). Alors que des études précédentes menées à Lucky Strike ont montré que la variabilité des marées a un impact au niveau de l'organisme (Mat et al. 2020), nous n'avons pas exploré plus loin son rôle sur la dynamique des espèces et nous nous sommes plutôt concentrés sur des échelles temporelles plus longues.

Le manque d'interactions biotiques interspécifiques observées au sein des assemblages de moules et de zoanthaires suggère qu'elles ont un impact limité sur la structure et la dynamique de ces assemblages. Cependant, les précédents modèles de succession établis par imagerie ont souligné l'importance des interactions biotiques dans la structuration des communautés hydrothermales du Pacifique et le contrôle de la niche réalisée par ces espèces (Sarrazin et al. 1997; Marcus et al. 2009; Podowski et al. 2009, 2010). Cependant, à LS, l'absence d'autres grands invertébrés que *B. azoricus* suggère moins de compétition pour les ressources et l'espace par rapport à ce qui a pu être observé dans le Pacifique (Sarrazin et al. 1997; Shank et al. 1998;

Sen et al. 2014). Rétrospectivement, ni les perturbations environnementales, ni les processus biotiques n'ont eu d'impact significatif sur les assemblages hydrothermaux de Tour Eiffel. Cependant, en l'absence de mortalité observée, le système ne peut pas évoluer perpétuellement vers l'accumulation d'individus. Sous une alimentation trophique soutenue, la disponibilité de conditions d'habitat adéquates (i.e. substrat permettant l'attachement et exposition aux fluides) finira par limiter la capacité de charge de l'édifice. Les résultats de cette thèse ont confirmé l'hypothèse de Cuvelier et al. (2011b) selon laquelle l'ensemble des assemblages de moules (~ 270 m²) sont à leur stade climax et ont peut-être atteint la capacité limite de l'édifice. Cela implique cependant que d'autres processus contribueraient à modérer cette capacité limite. Ils pourraient inclure des mécanismes de compétition qui ne peuvent pas être résolus par les techniques d'imagerie. Dans les assemblages de moules intertidales, l'agrégation est un trait essentiel pour faire face à la forte intensité des perturbations naturelles (Bertness et Grosholz 1985; Khaitov 2013). En revanche, le comportement d'agrégation peut être préjudiciable en favorisant la compétition pour l'accès aux ressources lorsque la densité de l'assemblage augmente (Bertness et Grosholz 1985; Lehane et Davenport 2004; Khaitov 2013). À Lucky Strike, la stabilité soutenue des assemblages de modioles pourrait conduire à des processus compétitifs, tels que la larvophagie ou le broutage des petites recrues, qui pourraient ainsi contrôler la taille de la population de moules (Sancho et al. 2005; Lenihan et al. 2008). Bien que la moule *B. azoricus,* espèce ingénieure, favorise l'installation de la faune associée (Sarrazin et al. 2015) et des tapis microbiens, nous pouvons émettre l'hypothèse que les interactions inhibitrices prédominent à proximité de la sortie de fluide, où la biomasse des moules et des brouteurs augmente (Husson et al. 2017). En plus des variations temporelles plus importantes et des facteurs de stress environnementaux caractérisant les grands assemblages de moules, l'inhibition compétitive pourrait donc contribuer à la plus faible diversité observée par rapport aux habitats plus froids (Husson et al. 2017; Sarrazin et al. 2020).

La cartographie des changements environnementaux et fauniques à l'aide de séries chronologiques d'images à l'échelle de l'assemblage et de l'édifice (Figure VI.1A) a montré que la variabilité infra-annuelle de l'habitat était élevée à proximité des sorties de fluides (Encadré 1; Figure VI.1B). L'étude des changements de l'activité hydrothermale sur l'édifice Tour Eiffel a permis la classification en trois catégories principales en fonction de la dynamique qui leur est associée : effondrement infra-annuel d'agrégats hydrothermaux, fermeture/ouverture des sorties de fluide, accrétion progressive de matériaux (Figure VI.1B). Des sources focalisées émanant de sulfures friables et formant notamment des cheminées, se sont effondrées de

manière répétée entre les années. Leur effondrement répétitif infra-annuel semble être le principal facteur de perturbation observé pour la faune peu mobile telle que les moules hydrothermales. Cela pourrait expliquer leur absence à proximité comme cela a été observé dans d'autres études du Pacifique avec les siboglinidés des sources hydrothermales (Tunnicliffe et al. 1990; Sarrazin et al. 2002). De plus, la relocalisation des sorties de fluide à l'échelle du décimètre ou du mètre résulte de l'ouverture/extinction de diffuseurs, sans initier de changements dans l'activité hydrothermale à plus grande échelle. Nous avons également observé que les diffuseurs et les surplombs (flanges) peuvent subir une accrétion progressive de matériel hydrothermal jusqu'à 1 décimètre par an, contribuant possiblement à la majeure partie de la construction structurelle de l'édifice de la Tour Eiffel sur 5 ans (Figure VI.1B). Des observations vidéo à long terme à l'échelle du mètre ont montré que les processus d'accrétion entraînent le déplacement d'agrégations de grandes moules hydrothermales (c'est-à-dire limitées par le byssus), ce qui souligne leur capacité à migrer sur des distances de l'ordre de ~ 1 $dm.an^{-1}$ (Encadré 1). La mobilité pourrait permettre aux moules de se maintenir dans des conditions optimales d'exposition au fluide hydrothermal, suggérant que la mobilité est un trait fonctionnel fondamental assurant aux moules la capacité de faire face aux changements à petite échelle de l'habitat. De même, l'importance de la mobilité des moules dans le façonnement de la dynamique temporelle à petite échelle a été signalée au niveau des sources hydrothermales du Pacifique (Johnson et al. 1994; Sen et al. 2014) ainsi que pour les moules côtières (Paine 1974; Paine et Levin 1981; Bertness et Grosholz 1985). Dans le Pacifique, le déplacement des moules reste un moyen de coloniser les assemblages de *Riftia pachyptila* suite à la diminution locale de l'exposition hydrothermale (Shank et al. 1998).

L'invariance d'échelle observée au travers des chapitres II et III suggère que les processus liés à la modification des sorties de fluide constituent le moteur prédominant de la dynamique des assemblages de *Bathymodiolus azoricus* à des échelles pluriannuelles jusqu'à pluri-décennales (Encadré 1; Figure VI.1B). Des études antérieures menées sur des dorsales à taux d'écartement rapide dans le Pacifique oriental et, axées sur le rétablissement post-éruptif des communautés ont décrit les écosystèmes hydrothermaux comme étant hautement dynamiques et éphémères, avec des reconstitutions régulières des assemblages des sources par recolonisation (Lutz et al. 1994; Tunnicliffe et al. 1997; Shank et al. 1998; Marcus et al. 2009). Cependant, le suivi temporel aux dorsales aux taux d'écartement plus lents a remis en cause cette hypothèse et a décrit, en l'absence d'événements éruptifs, le maintien de communautés stables sur une décennie (Copley et al. 2007; Gebruk et al. 2010; Cuvelier et al. 2011b; Sen et al. 2014; Du Preez et

Fisher 2018). Dans ce travail, la grande stabilité des communautés hydrothermales de Tour Eiffel a été confirmée et étendue à 25 ans (Encadré 1). L'absence de mortalité apparente (c'est-à-dire présence de coquilles vides) à l'échelle de l'assemblage a souligné la présence de populations à longue durée de vie et leur grande stabilité sur l'édifice. Cette stabilité à long terme a des implications en termes de stratégies de conservation qui sont en train d'être établies dans le cadre de futures activités minières en eaux profondes (Van Dover 2011; Levin et al. 2016b). Le faible régime de perturbation environnementale suggère que les moules *B. azoricus* pourraient ne pas être en mesure de récupérer d'une perturbation à grande échelle due à l'exploitation minière des dépôts massifs de sulfures. Cela s'aligne sur les résultats fournis par une expérience de suivi pluriannuel post-perturbation à l'édifice de Montségur (LS) qui a montré l'absence de récupération des moules après 2 ans (Marticorena et al. 2021). Néanmoins, il reste un manque de connaissances sur les traits écologiques fondamentaux de *B. azoricus* pour déduire leur potentiel de récupération, tels que le taux de croissance ou l'espérance de vie (Husson et al. 2018). Ces derniers n'ont pas pu être évalués correctement en utilisant l'imagerie en raison de la difficulté à suivre ces organismes individuellement sur plusieurs mois à années. Des approches expérimentales pourraient fournir de telles informations à l'avenir (ex. Rhoads et al. 1981; Schöne et Giere 2005; Nedoncelle et al. 2013).

Contrairement aux assemblages de moules, les tapis microbiens étaient beaucoup plus variables dans l'espace et le temps aux échelles de l'assemblage et de l'édifice. L'étude à l'échelle du mètre a montré que leur dynamique était très variable à l'échelle infra-annuelle ainsi qu'hétérogène dans l'espace (Encadré 1). Ces variations pourraient être le fruit de l'impact d'interactions biotiques telles que la facilitation de la croissance des tapis par les moules (i.e. détournement de fluide) et leur byssus (i.e. disponibilité de surface) ou la prédation par les brouteurs (Cuvelier et al. 2011a). Cependant, à cette échelle (< 1 m^2), le développement rapide des tapis microbiens peut aussi résulter de la croissance stochastique d'un biofilm non visible sur les images jusqu'à ce qu'il atteigne une épaisseur/taille donnée (Guezennec et al. 1998). Ces croissances sporadiques peuvent également se produire à l'échelle de l'édifice, mais la fréquence d'échantillonnage pluriannuelle était inappropriée pour observer ce processus. A l'échelle pluriannuelle, nous avons observé le déclin progressif des tapis microbiens sur l'édifice en parallèle avec un "refroidissement" subtil mais général des assemblages des sources, malgré une apparente stabilité de l'activité hydrothermale. A LS, l'effet d'un événement magmatique sur la composition du fluide hydrothermal peut façonner les communautés microbiennes au fil du temps, y compris dans les zones diffuses (Rommevaux et al. 2019). Les événements

magmatiques et tectoniques signalés en 2001 et 2015 à Lucky Strike pourraient expliquer de telles variations (Dziak et al. 2004; Cuvelier et al. 2011b; Ballu et al. 2019). Dans le Pacifique, un suivi post-éruptif a montré le développement rapide de tapis filamenteux blancs (Nees et al. 2008), suggérant le rôle des processus géophysiques à grande échelle sur le développement des tapis microbiens. Ces tapis peuvent se développer en réponse à la modification du système de plomberie qui peut finalement affecter la composition du fluide de l'évent (Butterfield et al. 199; Von Damm 2000). Cependant, nous n'avons détecté aucune anomalie dans les caractéristiques physico-chimiques du fluide à l'échelle de l'assemblage, bien que cela puisse être dû à la difficulté pratique de maintenir une mesure en un seul point dans le temps et l'espace ainsi qu'au manque de réplicats. D'autre part, les tapis microbiens pourraient avoir bénéficié temporairement d'éjecta ou de particules libérés lors de la modification du réseau en profondeur de la circulation hydrothermale (Juniper et al. 1995). Cela pourrait notamment expliquer leur croissance à Tour Eiffel suite à l'intrusion de dyke observée en 2001 (Dziak et al. 2004; Cuvelier et al. 2011b). La redistribution des éjectas ou des particules sur la structure par les fumeurs noirs peut avoir fourni une source temporaire de composés inorganiques pour soutenir leur croissance en 2015 (Girard et al. 2020a).

VI.2.2 Distribution spatiale

Nos résultats ont mis en évidence la forte zonation spatiale des communautés hydrothermales et non-hydrothermales à toutes les échelles étudiées. Ils ont confirmé que le gradient de dilution du fluide des sources hydrothermales et leur sphère d'influence sont prédominants pour expliquer la distribution de la faune benthique (Figure VI.1B). Nous avons considéré le rôle des facteurs de stress environnementaux et de l'apport de matières dérivées de la chimiosynthèse comme des moteurs de la distribution spatiale afin d'intégrer nos résultats (Figure VI.1C).

À des échelles fines, la disposition des assemblages fauniques dans des mosaïques à l'échelle décimétrique est liée au gradient de dilution abrupt, les grandes moules occupant le voisinage immédiat des sorties de fluides, caractérisées par la plus grande variabilité environnementale tandis que les zoanthaires occupent des habitats plus stables à faible influence hydrothermale (pas d'anomalie de température; Cuvelier et al. 2009; Figure VI.1B). Ces résultats sont cohérents avec la plupart des études écologiques menées sur les sources hydrothermales. Elles ont mis en évidence le rôle du gradient de dilution du fluide sur la distribution des assemblages dans tous les systèmes hydrothermaux (Copley et al. 1997, 2016; Shank et al. 1998; Sarrazin et Juniper 1999; Podowski et al. 2009; Marsh et al. 2012; Zhou et al. 2018).

Les édifices hydrothermaux présentent une forte hétérogénéité de l'habitat. Tout d'abord, leur verticalité permet au flux ascendant du fluide hydrothermal d'atteindre les assemblages de faune situés au-dessus (Podowski et al. 2010; Sen et al. 2013; Figure VI.1B). Outre les perturbations physiques, l'hétérogénéité des sorties de fluide sur les édifices fragmente les assemblages de la dorsale Juan de Fuca, ce qui entraîne un arrangement spatial en mosaïque (Sarrazin et al. 1997, 1999). De plus, la complexité de la topographie peut conduire à une hydrodynamique accrue affectant la redistribution des fluides et des particules (Girard et al. 2020a). Ceci conduit à des différences de communautés entre les côtés de l'édifice en lien avec leur orientation (Marsh et al. 2012; Sen et al. 2014). Par exemple, à Tour Eiffel, la redistribution du fluide, forcée par le courant, crée des modèles hétérogènes de distribution du tapis microbien et des moules selon les faces de l'édifice (Cuvelier et al. 2011b; Girard et al. 2020a; Figure VI.1B). La comparaison des édifices du champ Lucky Strike a montré que la couverture de moules dominait principalement les édifices du sud-est (Tour Eiffel et Montségur), contrastant avec la couverture restreinte de moules dans les édifices du centre-sud (White Castle, Crystal, South Crystal et Sapin; Encadré 1). Nous supposons que ce schéma pourrait être dû aux différentes maturités des édifices (Hannington et al. 1995). Par exemple, les édifices présumés matures du sud-est offriraient de grandes surfaces colonisable avec des zones de diffusion étendues pouvant soutenir de grandes populations de moules. Inversement, nous suggérons que *B. azoricus* pourrait ne pas avoir suffisamment d'habitats appropriés pour coloniser les structures sulfurées plus petites des sites du centre-sud et arborant quelques fumeurs noirs. Ces derniers pourraient cependant favoriser une plus large couverture de tapis microbien au sud-est. De plus, bien que l'activité hydrothermale soit restée relativement stable sur ces sites (Barreyre et al. 2012), des observations récentes ont montré de grandes variations structurelles de l'édifice de White Castle en l'espace d'un an (Wheeler et al. en prép.). Ceci démontre que, au sein d'un même champ hydrothermal, les édifices ne seraient pas équivalents en termes de disponibilité d'habitats et éventuellement de dynamique. Par conséquent, les édifices matures abritant des populations importantes de *B. azoricus* pourraient constituer la principale source de larves, contribuant ainsi à maintenir la connectivité à l'échelle du champ hydrothermal.

Les communautés périphériques dominées par ~5 morpho espèces sont restées très similaires entre les sites malgré les différences dans la composition des fluides purs (Chavagnac et al. 2018; Encadré 1). En périphérie, nous avons caractérisé la zonation spatiale de quelques espèces non-hydrothermales. Certaines (par exemple, cladorhizidés, foraminifères) se sont densément regroupées autour des zones actives (c'est-à-dire les édifices et les fissures; Figure VI.1B). Leur

densité élevée pourrait être soutenue par l'exportation de la production basée sur la chimiosynthèse (Figure VI.1C). La présence d'une communauté de suspensivores non-hydrothermaux, tirant profit de la production chimiosynthétique à proximité des zones actives, a déjà été décrite à de nombreux sites (Hessler et al. 1988; Galkin 1997; Van Dover et al. 2001; Erickson et al. 2009; Podowski et al. 2009, 2010; Fabri et al. 2011; Marsh et al. 2012; Levin et al. 2016a). Par exemple, certains morphotaxa étaient similaires à la communauté périphérique décrite dans les sites du sud-ouest du Pacifique (Sen et al. 2016). À une distance de ~ 100 m des sites actifs, Erickson et al. (2009) et Roohi et al. (2022) ont montré l'importance de l'approvisionnement en nourriture dérivée de la chimiosynthèse dans le Pacifique Ouest et l'Atlantique, respectivement. De plus, les zones actives hydrothermales contribuent non seulement à l'exportation de matière organique, mais fournissent également un substrat dur pour la colonisation par des espèces sessiles (c'est-à-dire des édifices actifs ou inactifs, ainsi que leurs décombres; Levin et al. 2016a). A LS, nous avons observé l'influence de la complexité topographique dans la distribution des suspensivores sessiles et des taxons microcarnivores (par exemple, le basalte; Figure VI.1B). La complexité topographique accroît localement l'hydrodynamique des courants et favorise ainsi la remise en suspension de la matière organique. L'importance de la complexité topographique et de la dureté du substrat loin de l'exposition hydrothermale (par exemple, basalte à ~ 100 m) dans la structuration de la distribution des suspensivores et des microcarnivores, suggère que la limitation de la nourriture contraint la survie de la faune non-hydrothermale à ces habitats plutôt que dans ceux avec peu d'hétérogénéité de terrain (par exemple, slab ou sédiments volcanoclastiques). La limitation trophique a également été suggérée comme étant le principal processus expliquant la dominance et la dynamique de morphotypes d'éponges typiques de zones pauvres en nourriture (Sen et al. 2016; Schönberg 2021). En fait, à une centaine de mètres, la matière organique dérivée de la photosynthèse devrait contribuer principalement à l'alimentation de la faune non-hydrothermale (LS : Alfaro-Lucas et al. 2020; Rainbow : Roohi et al. 2022; Figure VI.1C). En supposant que l'effet de ce filtre environnemental suive la recommandation d'Alfaro-Lucas et al. (2020), nous supposons que ces communautés périphériques, pourraient être sévèrement affectées par l'exploitation des dépôts massifs de sulfures. De plus, le panel de traits fonctionnels de la faune périphérique a récemment suggéré leur haute sensibilité aux activités minières en milieux marins profonds (Boschen-Rose et al. 2021).

VI.3 Développements méthodologiques

L'observatoire EMSO-Açores a permis de revisiter les échelles spatio-temporelles auxquelles les investigations écologiques sont typiquement réalisées dans les grands fonds, grâce aux progrès récents des plateformes sous-marines et des techniques d'imagerie (ex. Kwasnitschka et al. 2013; Marcon et al. 2013; Robert et al. 2020; Girard et al. 2022). Les observatoires profonds ont déjà été utiles pour le suivi infra-quotidien d'un écosystème, mais les études restaient souvent limitées à des durées infra-annuelles (par exemple, Juniper et al. 2013; Doya et al. 2014; Matabos et al. 2014, 2015; Sarrazin et al. 2014; Lelièvre et al. 2017; Girard et al. 2020b). L'effort d'acquisition de jeux de données à long terme permet désormais de démêler les échelles de variabilité, de l'infra-quotidien au pluri-annuel (par exemple, Taylor et al. 2017; Chauvet et al. 2018, 2019; De Leo et al. 2018; Durden et al. 2020). En outre, le suivi multidisciplinaire de l'environnement fournit des informations sur la variabilité de l'habitat, essentielles pour identifier les moteurs de la dynamique faunique (Matabos et al. 2022). Néanmoins, les caractéristiques uniques et inédites des images de fonds marins acquises dans le cadre de cette étude ont nécessité le développement de nouvelles méthodologies de traitement d'images et de leurs analyses (Figure VI.2).

Collecte de données – Dans ce travail, nous avons utilisé avec succès différentes techniques d'imagerie pour caractériser la structure faunique dans l'espace et/ou dans le temps. Cependant, ces méthodes ont impliqué des étendues et des résolutions spatiales/temporelles différentes (Figure VI.2). En fait, il reste un compromis à trouver entre la fréquence d'échantillonnage et l'échelle d'investigation, principalement limitée par le temps nécessaire à l'acquisition d'images du fond marin. Dans ce travail, nous avons abordé cette question en utilisant une approche multi-échelles avec des études imbriquées dans ces échelles. Les méthodes ont impliqué l'utilisation d'une caméra relayée à une infrastructure d'observatoire ainsi que de transects superposés réalisés avec un véhicule sous-marin et ce, avec une configuration différente de la caméra en fonction du milieu visé (Figure VI.2). Par conséquent, nous avons rencontré différents défis et conçu différents protocoles. Ils ont suivi une structure similaire qui pourrait être généralisée dans un flux méthodologique (Figure VI.2).

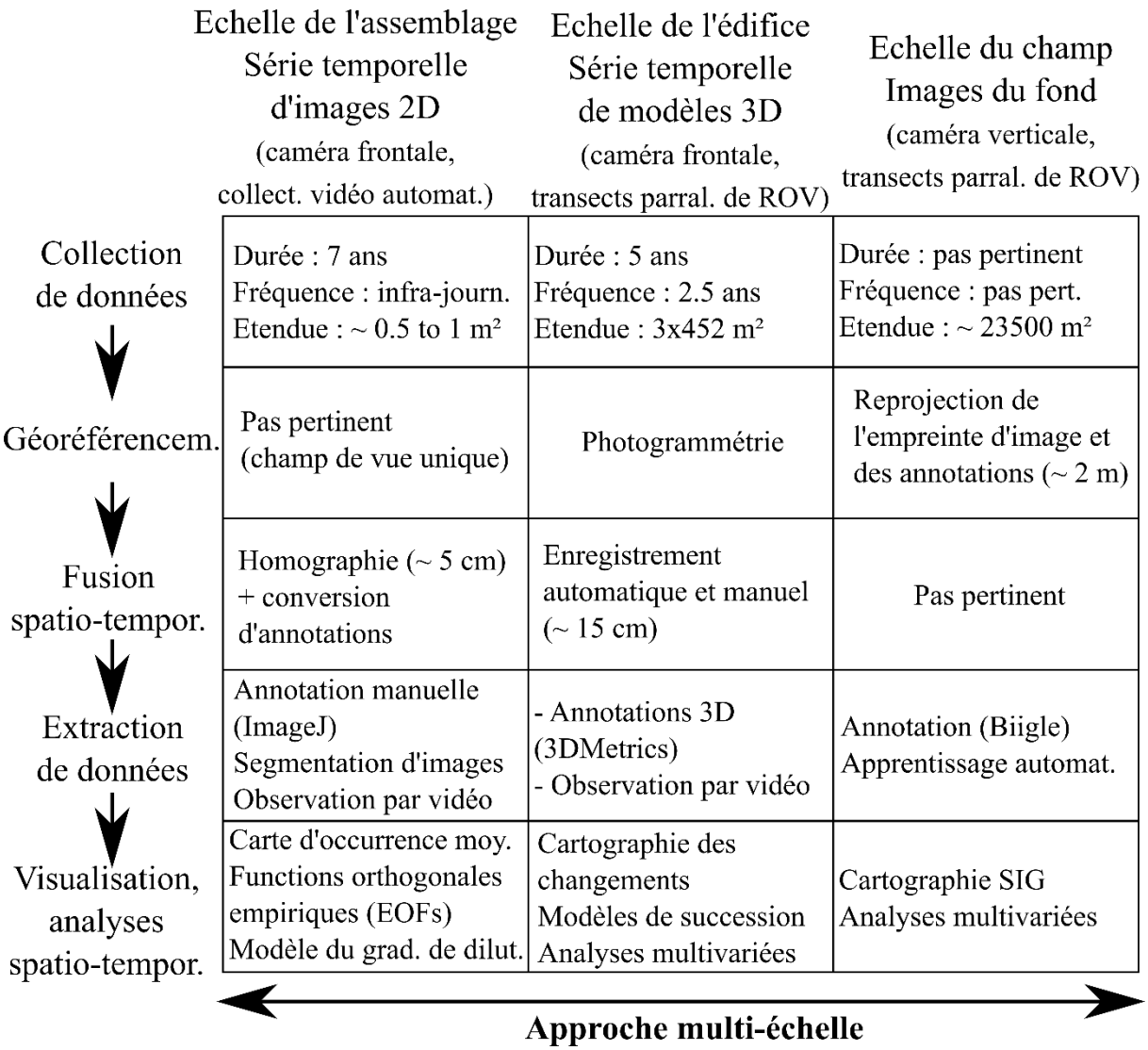

Figure VI.2 Flux méthodologique général des trois études de cas présentées dans ce projet de thèse, de la collecte des données à la visualisation spatio-temporelle et aux analyses.

Géoréférencement – L'enregistrement spatial des images est la première étape d'agrégation et vise à repositionner les images les unes par rapport aux autres dans l'espace (Figure VI.2). Il n'a donc pas été nécessaire pour le module caméra puisqu'il n'a enregistré qu'une seule image à la fois dans la même zone. A l'échelle de l'édifice, l'algorithme de photogrammétrie a permis de reconstruire trois fois et avec une haute résolution, un modèle 3D géoréférencé d'une structure complexe (Arnaubec et al. 2015; Figure VI.2). De même, les transects parallèles d'images du fond marin ont été conçus pour la reconstruction photogrammétrique qui aurait pu optimiser le recalage spatial des images. Nous avons donc développé un algorithme capable de retracer la trajectoire optique afin de reprojeter les empreintes des images sur le modèle 3D, et de calculer un recouvrement précis en utilisant la navigation optique extraite après les reconstructions photogrammétriques (Marcillat et al. en prép.). Néanmoins, la puissance des ordinateurs a fortement limité la reconstruction des modèles 3D en raison du nombre élevé d'images (> 4000).

L'utilisation d'un superordinateur pourrait résoudre ce problème et reste à explorer. Au lieu de cela, nous avons sélectionné un ensemble d'images non chevauchantes et les avons reprojetées dans un système 2D géoréférencé, malgré l'utilisation du système de navigation moins précis du ROV.

Fusion spatio-temporelle – Deux de nos ensembles de données contenaient des séries chronologiques d'images qu'il fallait donc repositionner dans le temps et l'espace (Tang et al. 2020). Le module écologique TEMPO était légèrement déplacé chaque année lors de son redéploiement, créant un ensemble d'images avec des chevauchements partiels. La fusion spatio-temporelle a été automatisée à l'aide d'une routine qui a repositionné automatiquement ~ 4000 images en utilisant des homographies calculées avec un algorithme de *feature matching* (Agarwal et al. 2005). Nous avons néanmoins inclus la possibilité d'apparier manuellement ces *features* entre images, car les changements de caméra et l'atténuation de la lumière ont empêché toute correspondance de caractéristiques entre certaines années. De plus, nous avons implémenté des algorithmes optionnels pour extraire les zones de chevauchement, inclure des masques, fournir une échelle métrique aux images et convertir les annotations antérieures au cas où l'acquisition de la série temporelle se poursuivrait dans le futur. Ce workflow unique développé sur Python et spécifiquement conçu pour la manipulation de séries temporelles d'images 2D devrait être diffusé dans les années à venir. À l'échelle de l'édifice, la superposition 3D des modèles a été réalisée pour atteindre un décalage résiduel de ~ 15 cm qui reste satisfaisant par rapport à une résolution acquise durant une investigation terrestre par drone (~ 5 cm; Cucchiaro et al. 2018). En raison de la distorsion des modèles 3D, nous les avons divisés en sous-portions, ce qui a considérablement accéléré leur manipulation à l'écran. Malgré cet effort considérable, nous reconnaissons que la précision ciblée de la fusion spatio-temporelle doit être définie en fonction de l'échelle des questions de recherche. Par exemple, notre étude avec TEMPO avait pour hypothèse que la variabilité de l'assemblage de moules hydrothermales se produise à des échelles décimétriques. Cependant, cette méthode peut ne pas être pertinente dans le cas d'une faune mobile occupant un habitat beaucoup plus vaste que la fenêtre spatiale capturée par la caméra (par exemple, Chauvet et al. 2019; Durden et al. 2020).

Extraction des données - Les trois ensembles d'images étant accompagnés de leurs propres aspects pratiques et panels d'organismes ciblés, leur annotation a nécessité la sélection prudente d'un logiciel d'annotation adéquat. À l'échelle de l'assemblage, ImageJ a été choisi (Rasband 1997). A l'échelle de l'édifice, le software 3D metrics a permis d'annoter en 3D pour ne pas négliger la perspective topographique (Laranjeira et al. 2020). A l'échelle du champ, Biigle a

facilité l'annotation d'un large panel d'espèces avec un étiquetage suivant une hiérarchie arborescente et a permis la réévaluation des annotations avec l'outil *Largo* (Langenkämper et al. 2017; Figure VI.2). Cependant, l'utilisation de Biigle s'accompagne de la perte des informations de géoréférencement des annotations au sein des images. Ainsi, nous avons développé un algorithme basé sur du *feature matching* pour géoréférencer les annotations Biigle sur les images de fonds marins (Marcillat et al. en prép.). Pour aller plus loin, nous avons envisagé l'utilisation de modèles 3D pour extraire des descripteurs de la microtopographie qui auraient été un atout additionnel pour décrire les affinités de la faune pour des substrats spécifiques (par exemple le basalte pour la faune périphérique). Cependant, le calcul des modèles 3D s'accompagne d'une perte de qualité par rapport aux images 2D, effaçant ainsi les petits organismes des modèles (~ cm; Thornton et al. 2016). Nous avons donc développé des algorithmes de retraçage de rayons (*ray tracing*) pour projeter les annotations faites sur des images 2D avec Biigle sur des modèles 3D (précision de repositionnement : ~ 5 cm; voir Marcillat 2022).

L'annotation prenait du temps (3 à 8 mois pour chaque ensemble de données), nous avons identifié plusieurs moyens d'accélérer ce processus. Afin d'optimiser le temps d'annotation, l'utilisation d'algorithmes automatisés a été testée occasionnellement, mais a démontré un fort potentiel pour de futures implémentations (par exemple, la segmentation d'images sur les zoanthaires au Chapitre II; la labélisation du substrat par apprentissage automatisé au Chapitre IV; Soto Vega et al. in prep.; Figure VI.2). Elles ont cependant nécessité une expertise spécifique afin d'adapter les algorithmes de détection d'images aux particularités du jeu de données. En outre, dans le cas d'une forte autocorrélation des séries temporelles (par exemple, une grande stabilité), nous recommandons d'évaluer si la réutilisation de l'annotation faite au temps t-1 pourrait accélérer le processus d'annotation à t+1. Cela permettra également de réduire considérablement les artefacts résultant d'annotations indépendantes dans le temps.

Visualisation et analyses spatio-temporelles – Dans cette thèse, nous avons disséqué les échelles des variabilités spatiales et temporelles en utilisant un large éventail d'analyses (par exemple uni- ou multivariées) et de méthodes de visualisation (par exemple la cartographie). La multidimensionnalité des données (TEMPO : 3D et Tour Eiffel : 4D) ne permet pas de visualiser facilement les résultats, ce qui nous a conduit à employer des analyses qui agrègent les données sur une ou plusieurs dimensions. Les analyses univariées sont régulièrement utilisées pour examiner les patrons généraux de changement en agrégeant les données dans le temps ou dans l'espace (par exemple, carte de changement et d'occurrence moyenne; couverture

totale dans le temps, périodogrammes). La dissection de schémas spatio-temporels ou d'événements ponctuels est un défi car la taille d'un ensemble de données à haute résolution augmente rapidement au fur et à mesure que l'on additionne les pas de temps (c'est-à-dire une fréquence d'échantillonnage élevée) et la résolution spatiale (c'est-à-dire une cellule ou un pixel). Nous recommandons de réduire la dimensionnalité du jeu de données à l'aide d'approches numériques telles que le partitionnement de la variance dans l'espace ou le temps comme dans le cas d'un ensemble de données univariées (par exemple, l'analyse en composantes principales ou également appelée "fonction orthogonale empirique" construite dans la routine d'homographie Python, voir Chapitre II; Rubio et al. 2020) ou en utilisant des indicateurs de la composition des espèces pour les jeux de données multivariées (par exemple, la position de l'assemblage le long d'un gradient, le regroupement, les analyses de trajectoire; voir le chapitre III; De Cáceres et al. 2019; Legendre 2019; Sturbois et al. 2021). De plus, l'identification des moteurs de changement peut être évaluée à l'aide d'analyses de réponse multivariées (par exemple, MRT, RDA; Legendre et Legendre 2012; Borcard et al. 2018). En outre, la RDA offre la possibilité d'intégrer les relations spatiales ou temporelles inhérentes aux données (par exemple, soit dans le temps avec des cartes de vecteurs propres asymétriques [AEMs], soit dans l'espace avec des cartes de vecteurs propres de Moran basées sur la distance [dbMEMs]; Blanchet et al. 2008; Legendre et Gauthier 2014).

VI.4 Conclusion et perspectives

Théoriquement, dans des conditions environnementales stables, un équilibre climax représente l'état terminal des différents stades de succession (Connell 1978). Ceci explique probablement l'absence des premiers stades de succession sur l'édifice Tour Eiffel. Une expérience de perturbation induite à petite échelle a montré que la succession écologique à LS passe d'abord par des espèces opportunistes, notamment des crevettes et des gastéropodes, dans les deux années qui suivent la défaunation (Marticorena et al. 2021). Par conséquent, nos connaissances sur les processus qui façonnent les trajectoires de succession pour atteindre une communauté hydrothermale climax à LS sont encore incomplètes. L'étude pluriannuelle à haute résolution a mis en évidence quelques zones de Tour Eiffel où des transitions entre des assemblages de moules de différentes tailles se sont produites sur quelques mètres carrés. Le suivi de la succession naturelle dans ces zones pourrait confirmer ou infirmer le modèle de succession proposé par Marticorena et al. (2021) après une perturbation. Le suivi par imagerie infra-quotidienne dans des zones spécifiques de l'édifice pourrait également aider à discriminer le

rôle du recrutement et de la mobilité des moules. En outre, le suivi de la dynamique des édifices immatures davantage susceptibles de subir des changements radicaux (par exemple Zhou et al. 2018 au champ Longqi; l'édifice White Castle de LS dans Wheeler et al. in prep.), pourrait fournir des informations supplémentaires sur les facteurs qui déterminent la distribution spatio-temporelle des assemblages hydrothermaux. En outre, la surveillance des zones sénescentes, cartographiées par Barreyre et al. (2012), devrait être envisagée pour acquérir une compréhension complète des successions dans des conditions variables d'activité (par exemple, l'édifice de Sintra partiellement inactif à LS). L'observatoire EMSO-Açores fournit l'infrastructure et les opportunités de mission en mer qui pourraient soutenir de telles études dans le futur.

Notre étude à l'échelle du champ hydrothermal suggère que les communautés non-hydrothermales ne sont pas distribuées de manière uniforme, ce qui souligne l'importance de l'hétérogénéité de l'habitat sur des distances d'au moins une centaine de mètres, comme cela a été observée dans d'autres études de cas (Arquit 1990; Boschen et al. 2016; Gerdes et al. 2019b). La caractérisation de la faune sur de plus grandes échelles augmenterait notre compréhension sur la distribution des communautés benthiques afin de discriminer l'importance de la disponibilité d'habitats par rapport à celle des apports dérivés de la chimiosynthèse et ce, le long d'un gradient d'influence hydrothermale. La dominance de quelques taxons de porifères et de cnidaires a montré de grandes similitudes avec les communautés périphériques observées par Sen et al. (2016). Cependant, comme notre identification était basée sur des images, l'identification taxonomique/génétique des morphotaxa est recommandée par un échantillonnage ciblé. En combinaison, les analyses d'isotopes stables ou d'acides gras fourniront des informations sur l'importance des apports dérivés de la chimiosynthèse dans leur régime alimentaire (par exemple pour les zoanthaires, les foraminifères ou les éponges microcarnivores; Colaço et al. 2007; Erickson et al. 2009; Alfaro-Lucas et al. 2020). De plus, le lien trophique entre les assemblages non-hydrothermaux et la productivité primaire dérivée de l'oxydation du fer devrait être étudié. Il pourrait représenter un nouveau mécanisme important de l'influence hydrothermale compte tenu de la large distribution et de la couverture étendue des dépôts oranges observés sur LS (Henri et al. 2013). Comme l'hydrodynamique et les emplacements des sources hydrothermales sont bien connus à LS (Barreyre et al. 2012), nous pourrions facilement définir un plan d'échantillonnage comprenant la collecte de la faune pour des analyses d'isotopes stables combinée au déploiement de turbidimètres et de pièges à sédiments. Ce plan permettrait de tester si les processus liés à l'influence hydrothermale sont

dépendants de l'échelle spatiale considérée (par exemple, l'éponge microcarnivore; Arquit 1990; Gerdes et al. 2019; Figure VI.1). On en sait beaucoup moins sur la dynamique de la faune périphérique, bien que Sen et al. (2016) aient décrit des taux de croissance et de mortalité exceptionnellement rapides pour certaines éponges microcarnivores dans les sources hydrothermales du Pacifique. Notre cartographie détaillée de la faune non-hydrothermale peut être le point de départ d'un suivi temporel combinant la surveillance environnemen
par l'observatoire EMSO-Açores.

Alors que les observatoires en eaux profondes et les technologies de cartographie (par exemple, les AUV) se développent rapidement dans le monde entier et que des séries d'images sont constituées (Delaney et al. 2016; Aguzzi et al. 2019; Durden et al. 2020; Girard et al. 2020b; Rountree et al. 2021; Thornton et al. 2021; Matabos et al. 2022), la communauté scientifique internationale se réunit pour identifier les besoins futurs et les stratégies de recherche en matière d'imagerie (Schoening et al. 2017). Par exemple, la collecte d'images avec le repositionnement le plus précis dans l'espace est importante pour rendre les données plus facilement utilisables (Schoening et al. 2017). C'est aussi un début pour construire des séries temporelles à long terme qui pourraient être réutilisées sur des décennies, notamment pour définir des directives de conservation alors que la spéculation sur l'exploitation des ressources des grands fonds augmente (par exemple Glover and Smith 2003; Simon-Lledó et al. 2019). Alors que nous avons amélioré la précision du repositionnement spatio-temporel des images, les flux méthodologiques développés ont fourni des protocoles adéquats pour acquérir et analyser des données multi-échelles à haute résolution (par exemple, homographie sur des images 2D, Chubacapp; Figure VI.2). Néanmoins, le goulot d'étranglement de la tâche de l'analyse d'images réside dans l'annotation. La collecte d'ensembles de données de plus en plus étendus s'accompagne d'une consommation de temps et d'un coût d'annotation plus élevés (Durden et al. 2016; Schoening et al. 2017). Bien que cette tâche soit souvent laissée aux étudiants, le développement de la segmentation des caractéristiques et des algorithmes d'apprentissage profond (*deep learning*) reste prometteur pour alléger l'annotation des images (Piechaud et al. 2019; de Oliveira et al. 2021; Yamada et al. 2021; Katija et al. 2022). Comme alternative, l'engagement des citoyens à travers des plateformes de science participative pourrait fournir des ensembles massifs de données pour entraîner des algorithmes dans les années à venir (Hoeberechts et al. 2015; Borremans et Matabos 2018).

References

A

Agarwal, A., Jawahar, C. V. and Narayanan, P. J. (2005). A survey of planar homography estimation techniques. *Tech. Rep. IIIT/TR/2005/12* 1–25.

Aguzzi, J., Chatzievangelou, D., Marini, S., Fanelli, E., Danovaro, R., Flögel, S., Lebris, N., Juanes, F., De Leo, F. C., Del Rio, J., et al. (2019). New High-Tech Flexible Networks for the Monitoring of Deep-Sea Ecosystems. *Environ. Sci. Technol.* **53**, 6616–6631.

Alfaro-Lucas, J. M., Pradillon, F., Zeppilli, D., Michel, L. N., Martinez-Arbizu, P., Tanaka, H., Foviaux, M. and Sarrazin, J. (2020). High environmental stress and productivity increase functional diversity along a deep-sea hydrothermal vent gradient. *Ecology* **101**, 1–13.

Anderson, M. J. (2001). A new method for non-parametric multivariate analysis of variance. *Austral Ecol.* **26**, 32–46.

Arnaubec, A., Opderbecke, J., Allais, A. G. and Brignone, L. (2015). Optical mapping with the ARIANE HROV at IFREMER: The MATISSE processing tool. *MTS/IEEE Ocean. 2015 - Genova Discov. Sustain. Ocean Energy a New World*.

Aron, M., Cuvelier, D., Aguzzi, J., Costa, C., Doya, C., Sarrazin, J. and Sarradin, P. M. (2013). Preliminary results on automated video-imaging for the study of behavioural rhythms of tubeworms from the TEMPO-mini ecological module (NEPTUNE, Canada). In *Martech 2013 5th International Workshop on Marine Technology. SARTI*, pp. 35–37.

Arquit, A. M. (1990). Geological and hydrothermal controls on the distribution of megafauna in Ashes vent field, Juan de Fuca Ridge. *J. Geophys. Res.* **95**, 12947-12960.

Ayling, A. M. (1981). The role of biological disturbance in temperate subtidal encrusting communities. *Ecology* **62**, 830–847.

B

Baker, E. T. and German, C. R. (2004). On the Global Distribution of Hydrothermal Vent Fields. In *Mid-Ocean Ridges: Hydrothermal Interactions Between the Lithosphere and Oceans* (ed. German, C. R.), Lin, J.), and Parson, L. M.), pp. 245–266. Washington DC, USA: American Geophysical Union.

Baldrighi, E., Zeppilli, D., Crespin, R., Chauvaud, P., Pradillon, F. and Sarrazin, J. (2018). Colonization of synthetic sponges at the deep-sea Lucky Strike hydrothermal vent field (Mid-Atlantic Ridge): a first insight. *Mar. Biodivers.* **48**, 89–103.

Ballu, V., Barreyre, T., Cannat, M., Testut, L., Crawford, W., Escartín, J., Coulombier, T. and Chavagnac, V. (2019). What happened in 2015 at the Lucky Strike volcano? *Geophys. Res. Abstr.* **21**, EGU2019-13294

Barreyre, T., Escartín, J., Garcia, R., Cannat, M., Mittelstaedt, E. and Prados, R. (2012). Structure, temporal evolution, and heat flux estimates from the Lucky Strike deep-sea hydrothermal field derived from seafloor image mosaics. *Geochemistry, Geophys. Geosystems* **13**, 1–29.

Barreyre, T., Escartín, J., Sohn, R. A., Cannat, M., Ballu, V. and Crawford, W. C. (2014). Temporal variability and tidal modulation of hydrothermal exit-fluid temperatures at the Lucky Strike deep-sea vent field, Mid-Atlantic Ridge. *J. Geophys. Res. Solid Earth* **119**, 2543–2566.

Bates, A. E., Tunnicliffe, V. and Lee, R. W. (2005). Role of thermal conditions in habitat selection by hydrothermal vent gastropods. **305**, 1–15.

Bates, A. E., Lee, R. W., Tunnicliffe, V. and Lamare, M. D. (2010). Deep-sea hydrothermal vent animals seek cool fluids in a highly variable thermal environment. *Nat. Commun.* **1**, 1–6.

Bates, A. E., Bird, T. J., Robert, K., Onthank, K. L., Quinn, G. P., Juniper, S. K. and Lee, R. W. (2013) Activity and positioning of eurythermal hydrothermal vent sulphide worms in a variable thermal environment. *J. Exp. Bio. Ecol.* **448**, 149-155.

Bay, H., Tuytelaars, T. and Gool, L. Van (2006). SURF: Speeded Up Robust Features. *Comput. Vision–ECCV 2006* **Part I**, 404–417.

Beaulieu, S. E. and Szafranski, K. (2020). InterRidge Global database of active submarine hydrothermal vent fields, Version 3.4. *World Wide Web Electron. Publ. http//vents-data. interridge.org.*

Bebianno, M. J., Cardoso, C., Gomes, T., Blasco, J., Serrão, R. and Colaço, A. (2018). Metal interactions between the polychaete *Branchipolynoe seepensis* and the mussel *Bathymodiolus azoricus* from Mid-Atlantic-Ridge hydrothermal vent fields. *Mar. Environ. Res.* **135**, 70–81.

Becker, K., Herzen, R. Von, Kirklin, J., Evans, R., Kadko, D., Kinoshita, M., Matsubayashi, O., Mills, R., Schultz, A. and Rona, P. (1996). Conductive heat flow at the TAG active hydrothermal mound : Results from 1993-1995 submersible surveys. *Geophys. Res. Lett.* **23**, 3463–3466.

Bennecke, S., Kwasnitschka, T., Metaxas, A. and Dullo, W. C. (2016). In situ growth rates of deep-water octocorals determined from 3D photogrammetric reconstructions. Coral Reefs **35**, 1227-1239.

Benedetti-Cecchi, L. (2000). Predicting direct and indirect interactions during succession in a mid-littoral rocky shore assemblage. *Ecol. Monogr.* **70**, 45–72.

Benoist, N. M. A., Morris, K. J., Bett, B. J., Durden, J. M., Huvenne, V. A. I., Le Bas, T. P., Wynn, R. B., Ware, S. J. and Ruhl, H. A. (2019). Monitoring mosaic biotopes in a marine conservation zone by autonomous underwater vehicle. *Conserv. Biol.* **33**, 1174–1186.

Bergquist, D. C., Eckner, J. T., Urcuyo, I. A., Cordes, E. E., Hourdez, S., Macko, S. A. and Fisher, C. R. (2007). Using stable isotopes and quantitative community characteristics to determine a local hydrothermal vent food web. *Mar. Ecol. Prog. Ser.* **330**, 49–65.

Bertness, M. D. and Grosholz, E. (1985). Population dynamics of the ribbed mussel, *Geukensia demissa*: The costs and benefits of an aggregated distribution. *Oecologia* **67**, 192–204.

Beukema, J. J. and Dekker, R. (2007). Variability in annual recruitment success as a determinant of long-term and large-scale variation in annual production of intertidal Wadden Sea mussels (*Mytilus edulis*). *Helgol. Mar. Res.* **61**, 71–86.

Bignell, R. D., Tooms, J. S., Cronan, D. S. and Horowitz, A. (1974). An additional location of metalliferous sediments in the Red Sea. *Nature* **248**, 1973–1974.

Blanchet, F. G., Legendre, P. and Borcard, D. (2008). Modelling directional spatial processes in ecological data. *Ecol. Modell.* **215**, 325–336.

Blandin, J., Colaco, A., Legrand, J., Cannat, M., Sarradin, P.-M. and Sarrazin, J. (2010). The MoMAR-D project : a challenge to monitor in real time the Lucky Strike hydrothermal vent field. *ICES J. Mar. Sci.* **68**, 416–424.

Bohidar, S., Crawford, W. and Cannat, M. (2022). Seismic constraints on the hydrothermal circulation and magmato-tectonic interactions beneath Lucky Strike volcano, Mid-Atlantic Ridge. *EGU Gen. Assem. 2022, held 23-27 May 2022 Vienna, Austria, id. 8780*.

Borcard, D., Gillet, F. and Legendre, P. (2018). *Numerical Ecology with R*. 2nd ed. New York: Springer International Publishing AG.

Bormann, F. H. and Likens, G. E. (1979). Catastrophic Disturbance and the Steady State in Northern Hardwood Forests: A new look at the role of disturbance in the development of forest ecosystems suggests important implications for land-use policies. *Am. Sci.* **67**, 660–669.

Borremans, C. and Matabos, M. (2018). The Deep Sea Spy system: building a marine images annotation database from participative science. In *Bollettino di Geofisica teorica ed applicata Bollettino di Geofisica Book of Abstracts* (ed. Giorgetti, A.), Fichaut, M.), and Tosello, V.), pp. 46–48. Barcelona, Spain.

Boschen, R. E., Rowden, A. A., Clark, M. R. and Gardner, J. P. A. (2013). Mining of deep-sea seafloor massive sulfides: A review of the deposits, their benthic communities, impacts from mining, regulatory frameworks and management strategies. *Ocean Coast. Manag.* **84**, 54–67.

Boschen, R. E., Rowden, A. A., Clark, M. R., Barton, S. J., Pallentin, A. and Gardner, J. P. A. (2015). Megabenthic assemblage structure on three New Zealand seamounts : implications for seafloor massive sulfide mining. *Mar. Ecol. Prog. Ser.* **523**, 1–14.

Boschen, R. E., Rowden, A. A., Clark, M. R., Pallentin, A. and Gardner, J. P. A. (2016). Seafloor massive sulfide deposits support unique megafaunal assemblages: Implications for seabed mining and conservation. *Mar. Environ. Res.* **115**, 78–88.

Boschen-Rose, R. E., Clark, M. R., Rowden, A. A. and Gardner, J. P. A. (2021). Assessing the ecological risk to deep-sea megafaunal assemblages from seafloor massive sulfide mining using a functional traits sensitivity approach. *Ocean Coast. Manag.* **210**, 1-21.

Bougerol, M., Boutet, I., LeGuen, D., Jollivet, D. and Tanguy, A. (2015). Transcriptomic response of the hydrothermal mussel *Bathymodiolus azoricus* in experimental exposure to heavy metals is modulated by the Pgm genotype and symbiont content. *Mar. Genomics* **21**, 63–73.

Boutet, I., Tanguy, A., Le Guen, D., Piccino, P., Hourdez, S., Legendre, P. and Jollivet, D. (2009). Global depression in gene expression as a response to rapid thermal changes in vent mussels. *Proc. R. Soc. B Biol. Sci.* **276**, 3071–3079.

Bovbjerg, R. V (1957). Feeding related to mussel activity. *Proc. Iowa Acad. Sci.* **64**, 650–653.

Britayev, T. A., Martin, D., Krylova, E. M., Cosel, R. Von and Aksiuk, T. S. (2007). Life-history traits of the symbiotic scale-worm *Branchipolynoe seepensis* and its relationships with host mussels of the genus *Bathymodiolus* from hydrothermal vents. *Mar. Ecol.* **28**, 36–48.

Brooks, J. L. and Dodson, S. I. (1965). Predation, Body Size, and Composition of Plankton. *Science* **150**, 28–35.

Bruno, J. F. and Bertness, M. D. (2001). Habitat modification and facilitation in benthic marine communities. In *Marine community ecology* (ed. Bertness, M. D.), Gaines, S. D.), and Hay, M. E.), pp. 201–218. Sunderland, MA: Sinauer Associates.

Butler, I. B., Fallick, A. E. and Nesbitt, R. W. (1998). Mineralogy, sulphur isotope geochemistry and the development of sulphide structures at the Broken Spur hydrothermal vent site, 29°10'N, Mid-Atlantic Ridge. *J. Geol. Soc. London.* **155**, 773–785.

Butterfield, D. A., Jonasson, I. R., Massoth, G. J., Feely, R. A., Roe, K. K., Embley, R. E., Holden, J. F., Mcduff, R. E., Lilley, M. D. and Delaney, J. R. (1997). Seafloor eruptions and evolution of hydrothermal fluid chemistry. *Philos. Trans. R. Soc. A Math. Phys. Eng. Sci.* **355**, 369–386.

C

Cannat, M., Briais, A., Deplus, C., Escartı, J., Georgen, J., Lin, J., Mercouriev, S., Meyzen, C., Muller, M., Pouliquen, G., et al. (1999). Mid-Atlantic Ridge –Azores hotspot

interactions: along-axis migration of a hotspot-derived event of enhanced magmatism 10 to 4 Ma ago. *Earth Planet. Sci. Lett.* **173**, 257–269.

Cannat, M. and Sarradin, P.-M. (2010). MOMARSAT : Monitoring the Mid-Atlantic Ridge. *French Oceanogr. Cruises*. 10.18142/130

Cannat, M., Sarradin, P.-M., Blandin, J., Escartín, J. and Colaço, A. (2011). MoMar-Demo at Lucky Strike. A near-real time multidisciplinary observatory of hydrothermal processes and ecosystems at the Mid-Atlantic Ridge. In *In: A.G.U. Fall Meeting, Abstract OS22A-05, San Francisco.*

Cannat, M., Sarradin, P., Blandin, J., Ballu, V., Barreyre, T., Chavagnac, V., Colaco, A., Crawford, W., Daniel, R., Escartín, J., et al. (2016). EMSO-Azores : Monitoring seafloor and water column processes at the Mid-Atlantic Ridge. *Fix03-Project Newsletter. Sevice Act. Spec.* **3**, 16–17.

Cannat, M. (2018). MOMARSAT2018. *French Oceanogr. Cruises*. 10.17600/18000514

Cannon, G. A., Pashinski, D. J. and Lemon, M. R. (1991). Middepth Flow Near Hydrothermal Venting Sites on the Southern Juan de Fuca Ridge. *J. Geophys. Res.* **96**, 12815–12831.

Cannon, G. A. and Thomson, R. E. (1996). Characteristics of 4-day oscillations trapped by the Juan de Fuca Ridge. *Geophys. Res. Lett.* **23**, 1613–1616.

Castilla, J. C., Manríquez, P. H. and Camaño, A. (2010). Effects of rocky shore coseismic uplift and the 2010 Chilean mega-earthquake on intertidal biomarker species. *Mar. Ecol. Prog. Ser.* **418**, 17–23.

Cavanaugh, C. M., McKiness, Z. P., Newton, I. L. G. and Stewart, F. (2006). Marine Chemosynthetic Symbioses. *Prokaryotes* **1**, 475–507.

Chadwick, W. W., Nooner, S. L., Butterfield, D. A. and Lilley, M. D. (2012). Seafloor deformation and forecasts of the April 2011 eruption at Axial Seamount. *Nat. Geosci.* **5**, 474–477.

Charlou, J. L., Donval, J. P., Douville, E., Jean-Baptiste, P., Radford-Knoery, J., Fouquet, Y., Dapoigny, A. and Stievenard, M. (2000). Compared geochemical signatures and the evolution of Menlimnez Gwen (37°50’ N) and Lucky Strike (37°17’ N) hydrothermal fluids, south of the Azores Triple Junction on the Mid-Atlantic Ridge. *Chem. Geol.* **171**, 49–75.

Chauvet, P., Metaxas, A., Hay, A. E. and Matabos, M. (2018). Annual and seasonal dynamics of deep-sea megafaunal epibenthic communities in Barkley Canyon (British Columbia, Canada): A response to climatology, surface productivity and benthic boundary layer variation. *Prog. Oceanogr.* **169**, 89–105.

Chauvet, P., Metaxas, A. and Matabos, M. (2019). Interannual variation in the population dynamics of juveniles of the deep-sea crab *Chionoecetes tanneri*. *Front. Mar. Sci.* **6**, 1–15.

Chavagnac, V., Leleu, T., Fontaine, F., Cannat, M., Ceuleneer, G. and Castillo, A. (2018). Spatial Variations in Vent Chemistry at the Lucky Strike Hydrothermal Field, Mid-Atlantic Ridge (37°N): Updates for Subseafloor Flow Geometry From the Newly Discovered Capelinhos Vent. *Geochemistry, Geophys. Geosystems* **19**, 4444–4458.

Chevaldonné, P., Desbruyères, D. and Le Haître, M. (1991). Time-series of temperature from three deep-sea hydrothermal vent sites. *Deep Sea Res. Part A, Oceanogr. Res. Pap.* **38**, 1417–1430.

Chevaldonné, P. and Jollivet, D. (1993). Videoscopic study of deep-sea hydrothermal vent alvinellid polychaete populations: biomass estimation and behaviour. *Mar. Ecol. Prog. Ser.* **95**, 251–262.

Childress, J. J. (1988). Biology and chemistry of a deep-sea hydrothermal vent on the Galapagos Rift; the Rose Garden in 1985. Introduction. *Deep Sea Res. Part A, Oceanogr. Res. Pap.* **35**, 1677–1680.

Childress, J. J. and Fisher, C. R. (1992). The biology of hydrothermal vent animals: physiology, biochemistry and autotrophic symbioses. In *Oceanography and Marine Biology Annual Review* (ed. Barnes, M.), Ansell, A. D.), and Gibson, R. N.), pp. 337–441. UCL Press.

Clarke, K. R. (1993). Non-parametric multivariate analyses of changes in community. *Aust. J. Ecol.* **18**, 117–143.

Clements, F. E. (1916). *Plant succession: an analysis of the development of vegetation*. Washington, D.C.: Carnergie Institution.

Colaço, A., Desbruyères, D., Comtet, T. and Alayse, A. M. (1998). Ecology of the Menez Gwen hydrothermal vent field (Mid-Atlantic Ridge/Azores Triple Junction). *Cah. Biol. Mar.* **39**, 237–240.

Colaço, A., Dehairs, F. and Desbruyères, D. (2002). Nutritional relations of deep-sea hydrothermal fields at the Mid-Atlantic Ridge: A stable isotope approach. *Deep. Res. Part I Oceanogr. Res. Pap.* **49**, 395–412.

Colaço, A., Martins, I., Laranjo, M., Pires, L., Leal, C., Prieto, C., Costa, V., Lopes, H., Rosa, D., Dando, P. R., et al. (2006). Annual spawning of the hydrothermal vent mussel, *Bathymodiolus azoricus*, under controlled aquarium, conditions at atmospheric pressure. *J. Exp. Mar. Bio. Ecol.* **333**, 166–171.

Colaço, A., Desbruyères, D. and Guezennec, J. (2007). Polar lipid fatty acids as indicators of trophic associations in a deep-sea vent system community. *Mar. Ecol.* **28**, 15–24.

Collins, P. C., Kennedy, R. and Van Dover, C. L. (2012). A biological survey method applied to seafloor massive sulphides (SMS) with contagiously distributed hydrothermal-vent fauna. *Mar. Ecol. Prog. Ser.* **452**, 89–107.

Combier, V., Seher, T., Singh, S. C., Crawford, W. C., Cannat, M., Escartín, J. and Düsünür, D. (2015). Three-dimensional geometry of axial magma chamber roof and

faults at Lucky Strike volcano on the Mid-Atlantic Ridge. *AGU J. Geophys. Res. Solid Earth* **120**, 5379–5400.

Company, R., Serafim, A., Cosson, R., Fiala-Médioni, A., Dixon, D. and João Bebianno, M. (2006). Temporal variation in the antioxidant defence system and lipid peroxidation in the gills and mantle of hydrothermal vent mussel *Bathymodiolus azoricus*. *Deep. Res. Part I Oceanogr. Res. Pap.* **53**, 1101–1116.

Comtet, T. and Desbruyères, D. (1998). Population structure and recruitment in mytilid bivalves from the Lucky Strike and Menez Gwen hydrothermal vent fields (37°17' N and 37°50' N on the Mid-Atlantic Ridge). *Ecology* **163**, 165–177.

Connell, J. H. (1961). The influence of interspecific competition and other factors on the distribution of the barnacle *Chthamalus stellatus*. *Ecology* **42**, 710–723.

Connell, J. H. and Slatyer, R. O. (1977). Mechanisms of succession in natural communities and their role in community stability and organization. *Am. Nat.* **111**, 1119–1144.

Connell, J. H. (1978). Diversity in Tropical Rain Forests and Coral Reefs. *Science* **199**, 1302–1310.

Connell, J. H. (1985). The consequences of variation in initial settlement vs. post-settlement mortality in rocky intertidal communities. *J. Exp. Mar. Bio. Ecol.* **93**, 11–45.

Cooper, M. J., Elderfield, H. and Schultz, A. (2000). Diffuse hydrothermal fluids from Lucky Strike hydrothermal vent field: Evidence for a shallow conductively heated system. *J. Geophys. Res. Solid Earth* **105**, 19369–19375.

Copley, J. T. P., Tyler, P. A., Murton, B. J. and Van Dover, C. L. (1997). Spatial and interannual variation in the faunal distribution at Broken Spur vent field (29°N, Mid-Atlantic Ridge). *Mar. Biol.* **129**, 723–733.

Copley, J. T. P., Tyler, P. A., Van Dover, C. L., Schultz, A., Dickson, P., Singh, S. and Sulanowska, M. (1999). Subannual temporal variation in faunal distributions at the TAG hydrothermal mound (26°N, Mid-Atlantic Ridge). *Mar. Ecol.* **20**, 291–306.

Copley, J. T. P., Jorgensen, P. B. K. and Sohn, R. A. (2007). Assessment of decadal-scale ecological change at a deep Mid-Atlantic hydrothermal vent and reproductive time-series in the shrimp *Rimicaris exoculata*. *J. Mar. Biol. Assoc. United Kingdom* **95**, 1–3.

Copley, J. T. P., Marsh, L., Glover, A. G., Hühnerbach, V., Nye, V. E. and Reid, W. D. K. (2016). Ecology and biogeography of megafauna and macrofauna at the first known deep-sea hydrothermal vents on the ultraslow-spreading Southwest Indian Ridge. *Nat. Publ. Gr.* **6**, 1–13.

Corliss, J. B. and Ballard, R. (1977). Oases of life in tbe cold abyss. *Natl. Geogr. Mag.* **152**, 441–454.

Cotte, L., Chavagnac, V., Pelleter, E., Laës-Huon, A., Cathalot, C., Dulaquais, G., Riso, R. D., Sarradin, P. M. and Waeles, M. (2020). Metal partitioning after in situ filtration

at deep-sea vents of the Lucky Strike hydrothermal field (EMSO-Azores, Mid-Atlantic Ridge, 37°N). *Deep. Res. Part I Oceanogr. Res. Pap.* **157**, 1-12.

Coumou, D., Driesner, T. and Heinrich, C. A. (2008). The Structure and Dynamics of Mid-Ocean Ridge Hydrothermal Systems. *Science* **321**, 1825–1828.

Cowart, D. A., Matabos, M., Brandt, M. I., Marticorena, J. and Sarrazin, J. (2020). Exploring Environmental DNA (eDNA) to Assess Biodiversity of Hard Substratum Faunal Communities on the Lucky Strike Vent Field (Mid-Atlantic Ridge) and Investigate Recolonization Dynamics After an Induced Disturbance. *Front. Mar. Sci.* **6**, 1–21.

Crawford, W. C., Rai, A., Singh, S. C., Cannat, M., Escartín, J., Wang, H., Daniel, R. and Combier, V. (2013). Hydrothermal seismicity beneath the summit of Lucky Strike volcano, Mid-Atlantic Ridge. *Earth Planet. Sci. Lett.* **373**, 118–128.

Crépeau, V., Cambon Bonavita, M. A., Lesongeur, F., Randrianalivelo, H., Sarradin, P. M., Sarrazin, J. and Godfroy, A. (2011). Diversity and function in microbial mats from the Lucky Strike hydrothermal vent field. *FEMS Microbiol. Ecol.* **76**, 524–540.

Crone, T. J. and Wilcock, W. S. D. (2005). Modeling the effects of tidal loading on mid-ocean ridge hydrothermal systems. *Geochemistry, Geophys. Geosystems* **6**, 25.

Cucchiaro, S., Cavalli, M., Vericat, D., Crema, S., Llena, M., Beinat, A., Marchi, L. and Cazorzi, F. (2018). Monitoring topographic changes through 4D-structure-from-motion photogrammetry: application to a debris-flow channel. *Environ. Earth Sci.* **77**, 1–21.

Cuvelier, D., Sarrazin, J., Colaço, A., Copley, J., Desbruyères, D., Glover, A. G., Tyler, P. and Serrão Santos, R. (2009). Distribution and spatial variation of hydrothermal faunal assemblages at Lucky Strike (Mid-Atlantic Ridge) revealed by high-resolution video image analysis. *Deep. Res. Part I Oceanogr. Res. Pap.* **56**, 2026–2040.

Cuvelier, D., Sarrazin, J., Colaço, A., Copley, J. T., Glover, A. G., Tyler, P. A., Santos, R. S. and Desbruyères, D. (2011a). Community dynamics over 14 years at the Eiffel Tower hydrothermal edifice on the Mid-Atlantic Ridge. *Limnol. Oceanogr.* **56**, 1624–1640.

Cuvelier, D., Sarradin, P.-M., Sarrazin, J., Colaço, A., Copley, J. T., Desbruyères, D., Glover, A. G., Santos, R. S. and Tyler, P. A. (2011b). Hydrothermal faunal assemblages and habitat characterisation at the Eiffel Tower edifice (Lucky Strike, Mid-Atlantic Ridge). *Mar. Ecol.* **32**, 243–255.

Cuvelier, D., de Busserolles, F., Lavaud, R., Floc'h, E., Fabri, M. C., Sarradin, P. M. and Sarrazin, J. (2012). Biological data extraction from imagery - How far can we go? A case study from the Mid-Atlantic Ridge. *Mar. Environ. Res.* **82**, 15–27.

Cuvelier, D., Legendre, P., Laes, A., Sarradin, P.-M. and Sarrazin, J. (2014a). Rhythms and community dynamics of a hydrothermal tubeworm assemblage at main endeavour field - A multidisciplinary deep-sea observatory approach. *PLoS One* **9**, 1-16.

Cuvelier, D., Beesau, J., Ivanenko, V. N., Zeppilli, D., Sarradin, P. M. and Sarrazin, J. (2014b). First insights into macro- and meiofaunal colonisation patterns on paired

wood/slate substrata at Atlantic deep-sea hydrothermal vents. *Deep. Res. Part I Oceanogr. Res. Pap.* **87**, 70–81.

Cuvelier, D., Legendre, P., Laës-Huon, A., Sarradin, P. M. and Sarrazin, J. (2017). Biological and environmental rhythms in (dark) deep-sea hydrothermal ecosystems. *Biogeosciences* **14**, 2955–2977.

D

d'Angelo, P. (2005). Hugin-Panorama photo stitcher. *Open Source Software, Sourceforge Community*.

D'Urban Jackson, T., Williams, G. J., Walker-Springett, G. and Davies, A. J. (2020). Three-dimensional digital mapping of ecosystems: A new era in spatial ecology. *Proc. R. Soc. B Biol. Sci.* **287**, 1–10.

Davis, E. and Becker, K. (1999). Tidal pumping of fluids within and from the oceanic crust: New observations and opportunities for sampling the crustal hydrosphere. *Earth Planet. Sci. Lett.* **172**, 141–149.

Dayton, P. K. (1971). Competition, disturbance, and community organization: the provision and subsequent utilization of space in a rocky intertidal community. *Ecol. Monogr.* **41**, 351–389.

Dayton, P. K. and Hessler, R. R. (1972). Role of biological disturbance in maintaining diversity in the deep sea. *Deep. Res. Oceanogr. Abstr.* **19**, 199-208.

Dayton, P. K., Tegner, M. J., Seymour, R. J. and Parnell, P. E. (1989). Unusual Marine Erosion in San Diego County from a Single Storm. *Estuar. Coast. Shelf Sci.* **29**, 151–160.

De'ath, G. (2002). Multivariate regression trees: a new technique for modeling species–environment relationships. *Ecology* **83**, 1105–1117.

De Busserolles, F., Sarrazin, J., Gauthier, O., Gélinas, Y., Fabri, M. C., Sarradin, P. M. and Desbruyères, D. (2009). Are spatial variations in the diets of hydrothermal fauna linked to local environmental conditions? *Deep. Res. Part II Top. Stud. Oceanogr.* **56**, 1649–1664.

De Cáceres, M., Coll, L., Legendre, P., Allen, R. B., Wiser, S. K., Fortin, M. J., Condit, R. and Hubbell, S. (2019). Trajectory analysis in community ecology. *Ecol. Monogr.* **89**, 1-15.

De Leo, F. C., Ogata, B., Sastri, A. R., Heesemann, M., Mihály, S., Galbraith, M. and Morley, M. G. (2018). High-frequency observations from a deep-sea cabled observatory reveal seasonal overwintering of *Neocalanus* spp. in Barkley Canyon, NE Pacific: Insights into particulate organic carbon flux. *Prog. Oceanogr.* **169**, 120–137.

de Oliveira, L. M. C., Lim, A., Conti, L. A. and Wheeler, A. J. (2021). 3D Classification of Cold-Water Coral Reefs: A Comparison of Classification Techniques for 3D Reconstructions of Cold-Water Coral Reefs and Seabed. *Front. Mar. Sci.* **8**, 1–19.

Delaney, J. R., Mogk, D. W. and Mottl, M. J. (1987). Quartz-cemented breccias from the Mid- Atlantic Ridge: samples of a high-salinity hydrothermal upflow zone. *J. Geophys. Res.* **92**, 9175–9192.

Delaney, J. R., Kelley, D. S., Marburg, A., Stoermer, M., Hadaway, H., Juniper, K. and Knuth, F. (2016). AXIAL SEAMOUNT - WIRED AND RESTLESS: A Cabled Submarine Network Enables Real-time, Tracking of a Mid-Ocean Ridge Eruption and Live Video of an Active Hydrothermal System Juan de Fuca Ridge, NE Pacific. In *OCEANS 2016 MTS/IEEE Proceedings*, pp. 1–8. Monterey: IEEE.

Demina, L. L. and Galkin, S. V. (2008). On the role of abiogenic factors in the bioaccumulation of heavy metals by the hydrothermal fauna of the Mid-Atlantic Ridge. *Oceanology* **48**, 784–797.

Denny, M. W. (1987). Lift as a mechanism of patch initiation in mussel beds. *J. Exp. Mar. Bio. Ecol.* **113**, 231–245.

Denny, M. W. and Paine, R. T. (1998). Celestial mechanics, sea-level changes, and intertidal ecology. *Biol. Bull.* **194**, 108–115.

Denny, M. W. and Wethey, D. (2001). Physical processes that generate patterns in marine communities. *Mar. Community Ecol.* 3–37.

Desbruyères, D. (1998). Temporal variations in the vent communities on the East Pacific Rise and Galapagos Spreading Centre: A review of present knowledge. *Cah. Biol. Mar.* **39**, 241–244.

Desbruyères, D., Biscoito, M., Caprais, J. C., Colaço, A., Comtet, T., Crassous, P., Fouquet, Y., Khripounoff, A., Le Bris, N., Olu, K., et al. (2001). Variations in deep-sea hydrothermal vent communities on the Mid-Atlantic Ridge near the Azores plateau. *Deep. Res. Part I Oceanogr. Res. Pap.* **48**, 1325–1346.

Desbruyères, D., Segonzac, M., Bright, M. and Decapoda, A. (2006). *Handbook of Deep-Sea Hydrothermal*. Second completely revised edition. *Denisia*, 18. *Biologiezentrum der Oberösterreischischen Landesmuseen. Linz, Austria*, pp. 544

Dethier, M. N. (1984). Disturbance and recovery in intertidal pools: maintenance of mosaic patterns. *Ecol. Monogr.* **54**, 99–118.

Detrick, R. S., Buhl, P., Vera, E., Mutter, J., Orcutt, J., Madsen, J. and Brocher, T. (1987). Multi-channel seismic imaging of a crustal magma chamber along the East Pacific Rise. *Nature* **326**, 2–8.

Dick, G. J. (2019). The microbiomes of deep-sea hydrothermal vents: distributed globally, shaped locally. *Nat. Rev. Microbiol.* **17**, 271–283.

Dixon, D. R., Lowe, D. M. O., Miller, P. I. O., Villemin, G. R., Colac, A. and Serra, R. (2006). Evidence of seasonal reproduction in the Atlantic vent mussel *Bathymodiolus azoricus*, and an apparent link with the timing of photosynthetic primary production. *J. Mar. Biol. Assoc. United Kingdom* **86**, 1363–1371.

Dolch, T. and Reise, K. (2010). Long-term displacement of intertidal seagrass and mussel beds by expanding large sandy bedforms in the northern Wadden Sea. *J. Sea Res.* **63**, 93–101.

Douville, E., Charlou, J. L., Oelkers, E. H., Bienvenu, P. and Colon, C. F. J. (2002). The rainbow vent fluids (36°14'N, MAR): the influence of ultramafic rocks and phase separation on trace metal content in Mid-Atlantic Ridge hydrothermal fluids. *Chem. Geol.* **184**, 37–48.

Doya, C., Aguzzi, J., Pardo, M., Matabos, M., Company, J. B., Costa, C., Mihaly, S. and Canals, M. (2014). Diel behavioral rhythms in sablefish (*Anoplopoma fimbria*) and other benthic species, as recorded by the Deep-sea cabled observatories in Barkley canyon (NEPTUNE-Canada). *J. Mar. Syst.* **130**, 69–78.

Du Preez, C. and Fisher, C. R. (2018). Long-term stability of back-arc basin hydrothermal vents. *Front. Mar. Sci.* **5**, 1–10.

Dubilier, N., Bergin, C. and Lott, C. (2008). Symbiotic diversity in marine animals: The art of harnessing chemosynthesis. *Nat. Rev. Microbiol.* **6**, 725–740.

Duperron, S., Bergin, C., Zielinski, F., Blazejak, A., Pernthaler, A., McKiness, Z. P., DeChaine, E., Cavanaugh, C. M. and Dubilier, N. (2006). A dual symbiosis shared by two mussel species, *Bathymodiolus azoricus* and *Bathymodiolus puteoserpentis* (Bivalvia: Mytilidae), from hydrothermal vents along the northern Mid-Atlantic Ridge. *Environ. Microbiol.* **8**, 1441–1447.

Duperron, S. (2010). The Diversity of Deep-Sea Mussels and Their Bacterial Symbioses. In *The Vent and Seep Biota* (ed. Kiel, S.), pp. 137–167. Dordrecht: Springer.

Durden, J. M., Schoening, T., Althaus, F., Friedman, A., Garcia, R., Glover, A. G., Greinert, J., Stout, N. J., Jones, D. O. B., Jordt, A., et al. (2016). Perspectives in visual imaging for biology and ecology: from acquisition to understanding. *Oceanogr. Mar. Biol. An Annu. Rev.* **54**, 1–72.

Durden, J. M., Bett, B. J., Huffard, C. L., Pebody, C., Ruhl, H. A. and Smith, K. L. (2020). Response of deep-sea deposit-feeders to detrital inputs: A comparison of two abyssal time-series sites. *Deep. Res. Part II Top. Stud. Oceanogr.* **173**, 104677.

Dziak, R. P., Smith, D. K., Bohnenstiehl, D. W. R., Fox, C. G., Desbruyères, D., Matsumoto, H., Tolstoy, M. and Fornari, D. J. (2004). Evidence of a recent magma dike intrusion at the slow spreading Lucky Strike segment, Mid-Atlantic Ridge. *J. Geophys. Res. Solid Earth* **109**, 1–15.

E

Embley, R. W., Chadwick, W. W., Clague, D. A. and Stakes, D. (1999). 1998 Eruption of Axial Volcano: Multibeam anomalies and seafloor observations. *Geophys. Res. Lett.* **26**, 3425–3428.

Emerson, D. (2007). Iron Cycling at Loihi Seamount. In *AGU Fall Meeting*, pp. B23G-03.

Emerson, D., Rentz, J. A., Lilburn, T. G., Davis, R. E., Aldrich, H., Chan, C. and Moyer, C. L. (2007). A Novel Lineage of Proteobacteria Involved in Formation of Marine Fe-Oxidizing Microbial Mat Communities. *PLoS One* **2**, 1–9.

Erickson, K. L., Macko, S. A. and Dover, C. L. Van (2009). Evidence for a chemoautotrophically based food web at inactive hydrothermal vents (Manus Basin). *Deep. Res. Part II* **56**, 1577–1585.

Escartín, J., Soule, S. A., Cannat, M., Fornari, D. J., Düsünür, D. and Garcia, R. (2014). Lucky Strike seamount: Implications for the emplacement and rifting of segment-centered volcanoes at slow spreading mid-ocean ridges. *Geochemistry, Geophys. Geosystems* **15**, 4157–4179.

Escartín, J., Barreyre, T., Cannat, M., Garcia, R., Gracias, N., Deschamps, A., Salocchi, A., Sarradin, P. M. and Ballu, V. (2015). Hydrothermal activity along the slow-spreading Lucky Strike ridge segment (Mid-Atlantic Ridge): Distribution, heatflux, and geological controls. *Earth Planet. Sci. Lett.* **431**, 173–185.

F

Fabri, M. C., Bargain, A., Briand, P., Gebruk, A., Fouquet, Y., Morineaux, M. and Desbruyères, D. (2011). The hydrothermal vent community of a new deep-sea field, Ashadze-1, 12°58′N on the Mid-Atlantic Ridge. *J. Mar. Biol. Assoc. United Kingdom* **91**, 1–18.

Fabri, M., Dugornay, O., De, X., Guerin, C., Sanchez, P., Arnaubec, A., Autin, T., Piasco, R. and Puig, P. (2022). 3D-Representations for studying deep-sea coral habitats in the Lacaze-Duthiers Canyon, from geological settings to individual specimens. *Deep. Res. Part I* **187**, 103831.

Farnsworth, K. D., Thygesen, U. H., Ditlevsen, S. and King, N. J. (2007). How to estimate scavenger fish abundance using baited camera data. *Mar. Ecol. Prog. Ser.* **350**, 223–234.

Favali, P., Person, R., Barnes, C. R., Kaneda, Y., Delaney, J. R. and Hsu, S. (2010). Seafloor observatory science. *Proc. Ocean.* **9**, 21–25.

Feng, J. C., Liang, J., Cai, Y., Zhang, S., Xue, J. and Yang, Z. (2022). Deep-sea organisms research oriented by deep-sea technologies development. *Sci. Bull.* **67**, 1802–1816.

Ferreira, T. and Rasband, W. (2012). The ImageJ 1.44 User Guide. *ImageJ/Fiji* 131–134.

Fiala-Médioni, A., McKiness, Z. P., Dando, P., Boulegue, J., Mariotti, A., Alayse-Danet, A. M., Robinson, J. J. and Cavanaugh, C. M. (2002). Ultrastructural, biochemical, and immunological characterization of two populations of the mytilid mussel *Bathymodiolus azoricus* from the Mid-Atlantic Ridge: Evidence for a dual symbiosis. *Mar. Biol.* **141**, 1035–1043.

Fisher, C. R., Childress, J. J., Arp, A. J., Brooks, J. M., Distel, D., Favuzzi, J. A., Felbeck, H., Hessler, R., Johnson, K. S., Kennicutt, M. C., et al. (1988). Microhabitat variation in the hydrothermal vent mussel, *Bathymodiolus thermophilus*, at the Rose Garden vent on the Galapagos Rift. *Deep Sea Res. Part A, Oceanogr. Res. Pap.* **35**, 1769–1791.

Fisher, C. R., Childress, J. J., Macko, S. A., Brooks, J. M., Fisher, C. R. and Childress, J. J. (1994). Nutritional interactions in Galapagos Rift hydrothermal vent communities: inferences from stable carbon and nitrogen isotope analyses. *Mar. Ecol. Prog. Ser.* **103**, 45–55.

Fisher, C. R. (1995). Toward an appreciation of hydrothermal-vent animals: Their environment, physiological ecology, and tissue stable isotope values. In *Geophysical Monograph Series* (ed. Humphris, S. E.), Zierenberg, R. A.), Mullineaux, L. S.), and Thomson, R. E.), pp. 297–316.

Fontaine, F. J. and Wilcock, W. S. D. (2006). Dynamics and storage of Brine in mid-ocean ridge hydrothermal systems. *J. Geophys. Res. Solid Earth* **111**, 1–16.

Fontaine, F. J., Cannat, M., Escartín, J. and Crawford, W. C. (2014). Along-axis hydrothermal flow at the axis of slow spreading Mid-Ocean Ridges: Insights from numerical models of the Lucky Strike vent field (MAR). *Geochemistry, Geophys. Geosystems* **15**, 2918–2931.

Fornari, D. J., Shank, T., Von Damm, K. L., Gregg, T. K. P., Lilley, M., Levai, G., Bray, A., Haymon, R. M., Perfit, M. R. and Lutz, R. (1998). Time-series temperature measurements at high-temperature hydrothermal vents, East Pacific Rise 9°49’-51’N: Evidence for monitoring a crustal cracking event. *Earth Planet. Sci. Lett.* **160**, 419–431.

Fouquet, Y., Charlou, J.-L., Costa, I., Donval, J.-P., Radford-Knoery, J., Pellé, H., Ondreas, H., Lourenco, N., Segonzac, M. and Tivey, M. K. (1994). A detailed study of the Lucky Strike hydrothermal site discovery of a new hydrothermal site: Menez Gwen; preliminary results of the DIVA1 cruise [5–29 May 1994]. *InterRidge News* **3**, 14–17.

François, D. X., Godfroy, A., Mathien, C., Aubé, J., Cathalot, C., Lesongeur, F., L’Haridon, S., Philippon, X. and Roussel, E. G. (2021). *Persephonella atlantica* sp. nov.: How to adapt to physico-chemical gradients in high temperature hydrothermal habitats. *Syst. Appl. Microbiol.* **44**, 1-10.

Fraser, D., Soul, L. C., Tóth, A. B., Balk, M. A., Eronen, J. T., Pineda-Munoz, S., Shupinski, A. B., Villaseñor, A., Barr, W. A., Behrensmeyer, A. K., et al. (2021). Investigating Biotic Interactions in Deep Time. *Trends Ecol. Evol.* **36**, 61–75.

Früh-Green, G. L., Kelley, D. S., Lilley, M. D., Cannat, M., Chavagnac, V. and Baross, J. A. (2022). Diversity of magmatism, hydrothermal processes and microbial interactions at mid-ocean ridges. *Nat. Rev. Earth Environ.* 1-22.

Fugazza, D., Scaioni, M., Corti, M., D'Agata, C., Azzoni, R. S., Cernuschi, M., Smiraglia, C. and Adele Diolaiuti, G. (2018). Combination of UAV and terrestrial photogrammetry to assess rapid glacier evolution and map glacier hazards. *Nat. Hazards Earth Syst. Sci.* **18**, 1055–1071.

Fustec, A., Desbruyères, D. and Juniper, S. K. (1987). Deep-Sea Hydrothermal Vent Communities at 13 ° N on the East Pacific Rise : Microdistribution and Temporal Variations. *Biol. Oceanogr.* **4**, 121–164.

G

Galkin, S. V. (1997). Megafauna associated with hydrothermal vents in the Manus Back-Arc Basin (Bismarck Sea). *Mar. Geol.* **142**, 197–206.

Gauthier, O., Sarrazin, J. and Desbruyères, D. (2010). Measure and mis-measure of species diversity in deep-sea chemosynthetic communities. *Mar. Ecol. Prog. Ser.* **402**, 285–302.

Gebruk, A. V., Chevaldonné, P., Shank, T., Lutz, R. A. and Vrijenhoek, R. C. (2000). Deep-sea hydrothermal vent communities of the Logatchev area (14°45'N, Mid-Atlantic Ridge): Diverse biotopes and high biomass. *J. Mar. Biol. Assoc. United Kingdom* **80**, 383–393.

Gebruk, A., Fabri, M. C., Briand, P. and Desbruyères, D. (2010). Community dynamics over a decadal scale at Logatchev, 14°45'N, Mid-Atlantic Ridge. *Cah. Biol. Mar.* **51**, 383–388.

Georgieva, M., Taboada, S., Riesgo, A., Díez-vives, C., De Leo, Fabio, C., Jeffreys, R. M., Copley, J. T., Little, C. T. S., Ríos, P., Cristobo, J., Hestetun, J. T. and Glover, A. G. (2020). Evidence of Vent-Adaptation in Sponges Living at Periphery of Hydrothermal Vent Environment: Ecological and Evolutionary Implications. Front. Microbiol. **11**, 1-15.

Gerdes, K., Arbizu, P. M., Schwarz-Schampera, U., Schwentner, M. and Kihara, T. C. (2019a). Detailed mapping of hydrothermal vent fauna: A 3D reconstruction approach based on video imagery. *Front. Mar. Sci.* **6**, 1-21.

Gerdes, K. H., Arbizu, P. M., Schwentner, M., Freitag, R. and Schwarz-schampera, U. (2019b). Megabenthic assemblages at the southern Central Indian Ridge – Spatial segregation of inactive hydrothermal vents from active- , periphery- and non- vent sites. *Mar. Environ. Res.* **151**, 104776.

Girard, F., Sarrazin, J., Arnaubec, A., Cannat, M., Sarradin, P.-M., Wheeler, B. and Matabos, M. (2020a). Currents and topography drive assemblage distribution on an active hydrothermal edifice. *Prog. Oceanogr.* **187**, 102397.

Girard, F., Sarrazin, J. and Olu, K. (2020b). Impacts of an Eruption on Cold-Seep Microbial and Faunal Dynamics at a Mud Volcano. *Front. Mar. Sci.* **7**, 1–15.

Girard, F., Litvin, S. Y., Sherman, A., McGill, P., Gannon, A., Lovera, C., DeVogelaere, A., Burton, E., Graves, D., Schnittger, A., et al. (2022). Phenology in the deep sea: Seasonal and tidal feeding rhythms in a keystone octocoral. *Proc. R. Soc. B.* **289**, 1-10

Glover, A. G. and Smith, C. R. (2003). The deep-sea floor ecosystem: Current status and prospects of anthropogenic change by the year 2025. *Environ. Conserv.* **30**, 219–241.

Glover, A. G., Gooday, A. J., Bailey, D. M., Billett, D. S. M., Chevaldonné, P., Colaço, A., Copley, J., Cuvelier, D., Desbruyères, D., Kalogeropoulou, V., et al. (2010). Temporal Change in Deep-Sea Benthic Ecosystems. A Review of the Evidence From Recent Time-Series Studies. *Advances in marine biology* **58**, 1-95.

Goffredi, S. K. (2010). Indigenous ectosymbiotic bacteria associated with diverse hydrothermal vent invertebrates. *Environ. Microbiol. Rep.* **2**, 479–488.

Goffredi, S. K., Motooka, C., Fike, D. A., Gusmão, L. C., Tilic, E., Rouse, G. W. and Rodríguez, E. (2021). Mixotrophic chemosynthesis in a deep-sea anemone from hydrothermal vents in the Pescadero Basin, Gulf of California. *BMC Biol.* **19**, 1–18.

Gollner, S., Govenar, B., Martinez Arbizu, P., Mullineaux, L. S., Mills, S., Le Bris, N., Weinbauer, M., Shank, T. M. and Bright, M. (2020). Animal Community Dynamics at Senescent and Active Vents at the 9°N East Pacific Rise After a Volcanic Eruption. *Front. Mar. Sci.* **6**, 1-18.

Gonzalez, A., Germain, R. M., Srivastava, D. S., Filotas, E., Dee, L. E., Gravel, D., Thompson, P. L., Isbell, F., Wang, S., Kéfi, S., et al. (2020). Scaling-up biodiversity-ecosystem functioning research. *Ecol. Lett.* **23**, 757–776.

Govenar, B., Freeman, M., Bergquist, D. C., Johnson, G. A. and Fisher, C. R. (2004). Composition of a one-year-old *Riftia pachyptila* community following a clearance experiment: Insight to succession patterns at deep-sea hydrothermal vents. *Biol. Bull.* **207**, 177–182.

Govenar, B., Bris, N. Le, Gollner, S., Glanville, J., Aperghis, A. B., Hourdez, S. and Fisher, C. R. (2005). Epifaunal community structure associated with *Riftia pachyptila* aggregations in chemically different hydrothermal vent habitats. *Mar. Ecol. Prog. Ser.* **305**, 67–77.

Govenar, B. and Fisher, C. R. (2007). Experimental evidence of habitat provision by aggregations of *Riftia pachyptila* at hydrothermal vents on the East Pacific Rise. *Mar. Ecol.* **28**, 3–14.

Govenar, B. (2010). Shaping Vent and Seep Communities: Habitat Provision and Modification by Foundation Species. In *The Vent and Seep Biota* (ed. Kiel, S.), pp. 403–432. Dordrecht: Springer.

Govenar, B. (2012). Energy transfer through food webs at hydrothermal vents linking the lithosphere to the biosphere. *Oceanography* **25**, 246–255.

Graber, S., Petersen, S., Yeo, I., Szitkar, F., Klischies, M., Jamieson, J., Hannington, M., Rothenbeck, M., Wenzlaff, E., Augustin, N., et al. (2020). Structural Control, Evolution, and Accumulation Rates of Massive Sulfides in the TAG Hydrothermal Field. *Geochemistry, Geophys. Geosystems* **21**, 1-25.

Grassle, J. F., Berg, C. J., Childress, J. J., Hessler, R. R., Jannasch, H. J., Karl, D. M., Lutz, R. A., Mickel, T. J., Rhoads, D. C., Sanders, H. L., et al. (1979). Galápagos '79: initial findings of a deep-sea biological quest. *Oceanus* **22**, 1–10.

Gray, A. P., Seed, R. and Richardson, C. A. (1997). Reproduction and growth of *Mytilus edulis chilensis* from the Falkland Islands. *Sci. Mar.* **61**, 39–48.

Grelon, D., Morineaux, M., Desrosiers, G. and Juniper, S. K. (2006). Feeding and territorial behavior of *Paralvinella sulfincola*, a polychaete worm at deep-sea hydrothermal vents of the Northeast Pacific Ocean. *J. Exp. Mar. Bio. Ecol.* **329**, 174–186.

Gripp, A. E. and Gordon, R. G. (2002). Young tracks of hotspots and current plate velocities. *Geophys. J. Int.* **150**, 321–361.

Guezennec, J., Ortega-Morales, O., Raguenes, G. and Geesey, G. (1998). Bacterial colonization of artificial substrate in the vicinity of deep-sea hydrothermal vents. *FEMS Microbiol. Ecol.* **26**, 89–99.

H

Hannachi, A., Jolliffe, I. T. and Stephenson, D. B. (2007). Empirical orthogonal functions and related techniques in atmospheric science: A review. *Int. J. Climatol.* **27**, 1119–1152.

Hannington, M. D., Jonasson, I., Herzig, P. M. and Petersen, S. (1995). Physical and Chemical Processes of Seafloor Mineralization at Mid-Ocean Ridges. In *Seafloor hydrothermal systems: Physical, chemical, biological, and geological interactions* (ed. Humphris, S. E.), Zierenberg, R. A.), Mullineaux, L. S.), and Thomson, R. E.), pp. 115–157. American Geophysical Union, Geophysical Monograph Series.

Harger, J. R. W. (1972). Competitive coexistence: maintenance of interacting associations of the sea *Mytilus edulis* and *Mytilus californianus*. *Veliger* **14**, 387–410.

Haymon, R. M., Fornari, D. J., Von Damm, K. J., Lilley, M. D., Perfit, M. R., Edmond, J. M., Shanks, W. C., Lutz, R. A., Grebmeier, S. C., Wright, D., et al. (1993). Volcanic eruption of the mid-ocean ridge along the East Pacific Rise crest at 9 45–52′ N: Direct

submersible observations of seafloor phenomena associated with an eruption event in April, 1991. *Earth Planet. Sci. Lett.* **119**, 85–101.

Henri, P. A., Rommevaux, C., Menez, B., Lesongeur, A. and Godfroy, A. (2013). Study of microorganisms/basaltic crust interactions at hydrothermal vents and abyssal environments by an in situ experimental approach. *AGU Fall Meet. Abstr.* **B13J-08**.

Henry, M. S., Childress, J. J. and Figueroa, D. (2008). Metabolic rates and thermal tolerances of chemoautotrophic symbioses from Lau Basin hydrothermal vents and their implications for species distributions. *Deep. Res. Part I Oceanogr. Res. Pap.* **55**, 679–695.

Hessler, R. R., Smithey, W. M. and Keller, C. H. (1985). Spatial and temporal variation of giant clams, tube worms and mussels at deep-sea hydrothermal vents. *Bull. Biol. Soc. Washingt.* **6**, 411–428.

Hessler, R. R., Smithey, W. M., Boudrias, M. A., Keller, C. H., Lutz, R. A. and Childress, J. J. (1988). Temporal change in megafauna at the Rose Garden hydrothermal vent (Galapagos Rift; eastern tropical Pacific). *Deep Sea Res. Part A, Oceanogr. Res. Pap.* **35**, 1681–1709.

Hilgerloh, G., Herlyn, M. and Michaelis, H. (1997). The influence of predation by herring gulls *Larus argentatus* and oystercatchers *Haematopus ostralegus* on a newly established mussel *Mytilus edulis* bed in autumn and winter. *Helgolander Meeresuntersuchungen* **51**, 173–189.

Hoagland, P., Beaulieu, S., Tivey, M. A., Eggert, R. G., German, C., Glowka, L. and Lin, J. (2010). Deep-sea mining of seafloor massive sulfides. *Mar. Policy* **34**, 728–732.

Hoeberechts, M., Owens, D., Riddell, D. J. and Robertson, A. D. (2015). The power of Seeing: Experiences using vidoe as a deep-sea engagement and education tool. In *OCEANS 2015 - MTS/IEEE Proceedings*, pp. 1–9. Washington.

Hollander, M. and Wolfe, D. (1999). *Nonparametric statistical methods*. New York: John Wiley & Sons.

Honkavaara, E., Litkey, P. and Nurminen, K. (2013). Automatic storm damage detection in forests using high-altitude photogrammetric imagery. *Remote Sens.* **5**, 1405–1424.

Horn, H. S. (1976). Succession. In *Theoretical ecology. Principles and applications* (ed. May, R. M.), pp. 187–204. Philadelphia: WB Saunders.

Hourdez, S. and Jollivet, D. (2020). Metazoan adaptation to deep-sea hydrothermal vents. *Life Extrem. Environ.* 42–67.

Hourdez, S. and Lallier, F. H. (2007). Adaptations to hypoxia in hydrothermal-vent and cold-seep invertebrates. *Rev. Environ. Sci. Biotechnol.* **6**, 143–159.

Howse, J. (2013). *OpenCV Computer Vision with Python*. Packt Publishing Ltd.

Humphris, S. E. and McCollum, T. (1998). The cauldron beneath the seafloor. *Ocean. Mag.* **41**, 18–21.

Humphris, S. E., Herzic, P. M., Miller, D. J., Alt, J. C., Brown, D., Becker, K., Briigmann, G., Chiba, H., Fouquet, Y., Gemmell, J. B., et al. (1995). The internal structure of an active sea-floor massive sulphide deposit. *Lett. to Nat.* **377**, 713–716.

Humphris, S. E., Fornari, D. J., Scheirer, D. S., German, C. R. and Parson, L. M. (2002). Geotectonic setting of hydrothermal activity on the summit of Lucky Strike Seamount (37°17'N, Mid-Atlantic Ridge). *Geochemistry, Geophys. Geosystems* **3**, 1-24.

Hunt, H. L. and Scheibling, R. E. (1998). Effects of whelk (*Nucella lapillus* (L.)) predation on mussel (*Mytilus trossulus* (Gould), *M. edulis* (L.)) assemblages in tidepools and on emergent rock on a wave-exposed rocky shore in Nova Scotia, Canada. *J. Exp. Mar. Bio. Ecol.* **226**, 87–113.

Hunt, H. L. and Scheibling, R. E. (2001). Patch dynamics of mussels on rocky shores: integrating process to understand pattern. *Ecology* **82**, 3213–3231.

Husson, B., Sarradin, P. M., Zeppilli, D. and Sarrazin, J. (2017). Picturing thermal niches and biomass of hydrothermal vent species. *Deep. Res. Part II* **137**, 6–25.

Husson, B., Sarrazin, J., van Oevelen, D., Sarradin, P. M., Soetaert, K. and Menesguen, A. (2018). Modelling the interactions of the hydrothermal mussel *Bathymodiolus azoricus* with vent fluid. *Ecol. Modell.* **377**, 35–50.

Hutchinson, G. E. (1957). Concluding remarks. *Cold Spring Harb. Symp. Quant. Biol.* **22**, 415–427.

Huvenne, V. A. I., Robert, K., Marsh, L., Lo Iacono, C., Le Bas, T. and Wynn, R. B. (2018). ROVs and AUVs. In *Springer Geology*, pp. 93–108. Springer US.

ISA (2022). Minerals: Polymetallic Sulphides. https://www.isa.org.jm/exploration-contracts/polymetallic-sulphides, consulted the 27th August 2022.

Ivanenko, V. N., Ferrari, F. D., Defaye, D., Sarradin, P. M. and Sarrazin, J. (2011). Description, distribution and microhabitats of a new species of Tisbe (Copepoda: Harpacticoida: Tisbidae) from a deep-sea hydrothermal vent field at the Mid-Atlantic Ridge (37°N, Lucky Strike). *Cah. Biol. Mar.* **52**, 89–106.

J

James, M. R., Robson, S. and Smith, M. W. (2017). 3-D uncertainty-based topographic change detection with structure-from-motion photogrammetry: precision maps for ground control and directly georeferenced surveys. *Earth Surf. Process. Landforms* **42**, 1769–1788.

Jamieson, J. W., Clague, D. A. and Hannington, M. D. (2014). Hydrothermal sulfide accumulation along the Endeavour Segment, Juan de Fuca Ridge. *Earth Planet. Sci. Lett.* **395**, 136–148.

Jamieson, J. W., Petersen, S. and Bach, W. (2016a). Hydrothermalism. In *Encyclopedia of Marine Geosciences.* (ed. Harff, J.), Meschede, M.), and Petersen, S.), p. Dordrecht: Springer.

Jamieson, J. W., Hannington, M. D., Tivey, M. K., Hansteen, T., Williamson, N. M. B., Stewart, M., Fietzke, J., Butterfield, D., Frische, M., Allen, L., et al. (2016b). Precipitation and growth of barite within hydrothermal vent deposits from the Endeavour Segment, Juan de Fuca Ridge. *Geochim. Cosmochim. Acta* **173**, 64–85.

Jannasch, H. W. (1985). The chemosynthetic support of life and the microbial diversity at deep-sea hydrothermal vents. *Proc. R. Soc. London. Ser. B. Biol. Sci.* **225**, 277–297.

Jannasch, H. J. (1995). Microbial interaction with hydrothermal fluids. In *Seafloor Hydrothermal Systems:Physical, Chemical, Biological, and Geological Interactions* (ed. Humphris, S. E.), pp. 273–296.

Johnson, H. P. and Tunnicliffe, V. (1985). Time-series measurements of hydrothermal activity on northern juan de fuca ridge. *Geophys. Res. Lett.* **12**, 685–688.

Johnson, K. S., Childress, J. J. and Hessler, R. R. (1988a). Chemical and biological interactions in the Rose Garden hydrothermal vent field, Galapagos spreading center. *Deep Sea Res.* **35**, 1723–1744.

Johnson, K. S., Childress, J. J. and Beehler, C. L. (1988b). Short-term temperature variability in the Rose Garden hydrothermal vent field : an unstable deep-sea environment. *Deep Sea Res.* **35**, 1711–1721.

Johnson, K. S., Childress, J. J., Beehler, C. L. and Sakamoto, C. M. (1994). Biogeochemistry of hydrothermal vent mussel communities : the deep-sea analogue to the intertidal zone. *Deep. Res. I* **4**, 993–1011.

Juniper, S. K. and Tunnicliffe, V. (1997). Crustal accretion and the hot vent ecosystem. *Philos. Trans. R. Soc. A Math. Phys. Eng. Sci.* **355**, 459–474.

Juniper, S. K., Jonasson, I. R., Tunnicliffe, V. and Southward, A. J. (1992). Influence of a tube-building polychaete on hydrothermal chimney mineralization. *Geology* **20**, 895–898.

Juniper, S. K., Martineu, P., Sarrazin, J. and Gélinas, Y. (1995). Microbial-mineral floc associated with nascent hydrothermal activity on CoAxial Segment, Juan de Fuca Ridge. *Geophys. Res. Lett.* **22**, 179–182.

Juniper, S. K. and Sarrazin, J. (1995). Interaction of Vent Biota and Hydrothermal Deposits:Past Evidence and Future Experimentation. In *Seafloor Hydrothermal Systems:Physical, Chemical, Biological, and Geological Interactions*, pp. 178–193. American Geophysical Union.

Juniper, S. K., Sarrazin, J. and Grehan, A. (1998). Remote sensing of organism density and biomass at hydrothermal vents. *Cah. Biol. Mar.* **39**, 245–247.

Juniper, S. K., Matabos, M., Mihály, S., Ajayamohan, R. S., Gervais, F. and Bui, A. O. V. (2013). A year in Barkley Canyon: A time-series observatory study of mid-slope benthos and habitat dynamics using the NEPTUNE Canada network. *Deep. Res. Part II Top. Stud. Oceanogr.* **92**, 114–123.

Juniper, S. K., Thornborough, K., Douglas, K. and Hillier, J. (2019). Remote monitoring of a deep-sea marine protected area: The Endeavour Hydrothermal. *Aquat. Conserv. Mar. Freshw. Ecosyst.* **29**, 84–102.

K

Karl, D. M. (1995). Ecology of free-living, hydrothermal vent microbial communities. In *The microbiology of deep-sea hydrothermal vents* (ed. Karl, D. M.), pp. 35–125. Boca Raton: FL: Chemical Rubber Company.

Katija, K., Orenstein, E., Schlining, B., Lundsten, L., Barnard, K., Sainz, G., Boulais, O., Cromwell, M., Butler, E., Woodward, B., et al. (2022). FathomNet: A global image database for enabling artificial intelligence in the ocean. *Sci. Rep.* **12**, 1–14.

Kato, S., Takano, Y., Kakegawa, T., Oba, H., Inoue, K., Kobayashi, C., Utsumi, M., Marumo, K., Kobayashi, K., Ito, Y., et al. (2010). Biogeography and biodiversity in sulfide structures of active and inactive vents at deep-sea hydrothermal fields of the southern mariana trough. *Appl. Environ. Microbiol.* **76**, 2968–2979.

Khaitov, V. (2013). Life in an unstable house : community dynamics in changing mussel beds. *Hydrobiologia* **706**, 139–158.

Khripounoff, A., Vangriesheim, A., Crassous, P., Segonzac, M., Lafon, V. and Warén, A. (2008). Temporal variation of currents, particulate flux and organism supply at two deep-sea hydrothermal fields of the Azores Triple Junction. *Deep. Res. Part I Oceanogr. Res. Pap.* **55**, 532–551.

Kim, S. and Hammerstrom, K. (2012). Hydrothermal vent community zonation along environmental gradients at the Lau back-arc spreading center. *Deep. Res. Part I Oceanogr. Res. Pap.* **62**, 10–19.

Kwasnitschka, T., Hansteen, T. H., Devey, C. W. and Kutterolf, S. (2013). Doing fieldwork on the seafloor: Photogrammetric techniques to yield 3D visual models from ROV video. *Comput. Geosci.* **52**, 218–226.

L

Laës-Huon, A., Cathalot, C., Legrand, J., Tanguy, V. and Sarradin, P. M. (2016). Long-Term in situ survey of reactive iron concentrations at the Emso-Azores observatory. *IEEE J. Ocean. Eng.* **41**, 744–752.

Lague, D., Brodu, N. and Leroux, J. (2013). Accurate 3D comparison of complex topography with terrestrial laser scanner: Application to the Rangitikei canyon (N-Z). *ISPRS J. Photogramm. Remote Sens.* **82**, 10–26.

Laming, S. R., Gaudron, S. M., Duperron, S. and Rogers, A. D. (2018). Lifecycle Ecology of Deep-Sea Chemosymbiotic Mussels : A Review. *Front. Mar. Sci.* **5**, 1-15.

Langenkämper, D., Zurowietz, M., Schoening, T. and Nattkemper, T. W. (2017). BIIGLE 2.0 - Browsing and Annotating Large Marine Image Collections. *Front. Mar. Sci.* **4**, 1–10.

Langmuir, C. L., Charlou, J. L., Colodner, D., Corey, S., Costa, J., Desbruyères, D., Desonie, D., Emerson, T., Fornari, D., Fouquet, Y., et al. (1993). Lucky Strike-A newly discovered hydrothermal site on the Azores platform. *RIDGE Events* **4**, 3–5.

Langmuir, C., Humphris, S., Fornari, D., Van Dover, C., Von Damm, K., Tivey, M. K., Colodner, D., Charlou, J. L., Desonie, D., Wilson, C., et al. (1997). Hydrothermal vents near a mantle hot spot: The Lucky Strike vent field at 37°N on the Mid-Atlantic Ridge. *Earth Planet. Sci. Lett.* **148**, 69–91.

Lantéri, N., Ruhl, H. A., Gates, A., Martínez, E., del Rio Fernandez, J., Aguzzi, J., Cannat, M., Delory, E., Embriaco, D., Huber, R., et al. (2022). The EMSO Generic Instrument Module (EGIM): Standardized and Interoperable Instrumentation for Ocean Observation. *Front. Mar. Sci.* **9**, 1–17.

Laranjeira, M., Arnaubec, A., Brignone, L., Dune, C. and Opderbecke, J. (2020). 3D Perception and Augmented Reality Developments in Underwater Robotics for Ocean Sciences. *Curr. Robot. Reports* **1**, 123–130.

Le Bris, N., Rodier, P., Sarradin, P. M. and Le Gall, C. (2006a). Is temperature a good proxy for sulfide in hydrothermal vent habitats? *Cah. Biol. Mar.* **47**, 465–470.

Le Bris, N., Govenar, B., Le Gall, C. and Fisher, C. R. (2006b). Variability of physico-chemical conditions in 9°50′N EPR diffuse flow vent habitats. *Mar. Chem.* **98**, 167–182.

Le Bris, N. and Duperron, S. (2010). Chemosynthetic Communities and Biogeochemical Energy Pathways Along the Mid-Atlantic Ridge: The Case of *Bathymodiolus azoricus*. *Geophys. Monogr. Ser.* **188**, 409–429.

Le Layec, V. and Hourdez, S. (2021). Oxygen consumption rates in deep-sea hydrothermal vent scale worms: Effect of life-style, oxygen concentration, and temperature sensitivity. *Deep. Res. Part I Oceanogr. Res. Pap.* **172**, 1-9.

Lee, R. W., Robert, K., Matabos, M., Bates, A. E. and Juniper, S. K. (2015). Temporal and spatial variation in temperature experienced by macrofauna at Main Endeavour hydrothermal vent field. *Deep. Res. Part I Oceanogr. Res. Pap.* **106**, 154–166.

Legendre, P. (2012). Whittaker-Robinson periodogram. *R Progr. Doc.*

Legendre, P. and Legendre, L. (2012). *Numerical ecology*. Elsevier.

Legendre, P. and De Cáceres, M. (2013). Beta diversity as the variance of community data: Dissimilarity coefficients and partitioning. *Ecol. Lett.* **16**, 951–963.

Legendre, P. and Gauthier, O. (2014). Statistical methods for temporal and space-time analysis of community composition data. *Proc. R. Soc. B Biol. Sci.* **281**, 1-9.

Legendre, P. and Borcard, D. (2018). Box Cox-chord transformations for community composition data prior to beta diversity analysis. *Ecography (Cop.).* **41**, 1820–1824.

Legendre, P. (2019). A temporal beta-diversity index to identify sites that have changed in exceptional ways in space–time surveys. *Ecol. Evol.* **9**, 3500–3514.

Lehane, C. and Davenport, J. (2004). Ingestion of bivalve larvae by *Mytilus edulis*: Experimental and field demonstrations of larviphagy in farmed blue mussels. *Mar. Biol.* **145**, 101–107.

Leleu, T., Chavagnac, V., Cannat, M., Ceuleneer, G., Castillo, A. and Menjot, L. (2015). Fluid geochemistry of the Capelinhos Vent Site. A Key to Understand the Lucky Strike Hydrothermal Vent Field (37° N, MAR). *Am. Geophys. Union, Fall Meet. Abstr.* **OS43A-2025**.

Lelièvre, Y., Legendre, P., Matabos, M., Mihály, S., Lee, R. W., Sarradin, P. M., Arango, C. P. and Sarrazin, J. (2017). Astronomical and atmospheric impacts on deep-sea hydrothermal vent invertebrates. *Proc. R. Soc. B Biol. Sci.* **284**, 10.

Lelièvre, Y., Sarrazin, J., Marticorena, J., Schaal, G., Day, T., Legendre, P., Hourdez, S. and Matabos, M. (2018). Biodiversity and trophic ecology of hydrothermal vent fauna associated with tubeworm assemblages on the Juan de Fuca Ridge. *Biogeosciences* **15**, 2629–2647.

Lenihan, H. S., Mills, S. W., Mullineaux, L. S., Peterson, C. H., Fisher, C. R. and Micheli, F. (2008). Biotic interactions at hydrothermal vents : Recruitment inhibition by the mussel *Bathymodiolus thermophilus*. *Deep. Res. I* **55**, 1707–1717.

Léveillé, R. J., Levesque, C. and Juniper, S. K. (2005). Biotic Interactions and Feedback Processes in Deep-Sea Hydrothermal Vent Ecosystems. In *Interactions Between Macro and Microorganisms in Marine Sediments* (ed. Kristensen, E.), Haese, R. R.), and Kostka, J. E.), pp. 299–321. American Geophysical Union.

Levesque, C., Juniper, S. K. and Marcus, J. (2003). Food resource partitioning and competition among alvinellid polychaetes of Juan de Fuca Ridge hydrothermal vents. *Mar. Ecol. Prog. Ser.* **246**, 173–182.

Levesque, C., K., J. and Limén, H. (2006). Spatial organization of food webs along habitat gradients at deep-sea hydrothermal vents on Axial Volcano, Northeast Pacific. *Deep. Res. Part I* **53**, 726–739.

Levin, S. A. (1992). The problem of pattern and scale in ecology. *Ecology* **73**, 1943–1967.

Levin, S. A. and Paine, R. T. (1974). Disturbance, patch formation, and community structure. *Proc. Natl. Acad. Sci. U. S. A.* **71**, 2744–2747.

Levin, L. A., Baco, A. R., Bowden, D. A., Colaco, A., Cordes, E. E., Cunha, M. R., Demopoulos, A. W. J., Gobin, J., Grupe, B. M., Le, J., et al. (2016a). Hydrothermal vents and methane seeps: Rethinking the sphere of influence. *Front. Mar. Sci.* **3**, 1–23.

Levin, L. A., Mengerink, K., Gjerde, K. M., Rowden, A. A., Van Dover, C. L., Clark, M. R., Ramirez-Llodra, E., Currie, B., Smith, C. R., Sato, K. N., et al. (2016b). Defining "serious harm" to the marine environment in the context of deep-seabed mining. *Mar. Policy* **74**, 245–259.

Li, J., Zhou, H., Peng, X., Wu, Z., Chen, S. and Fang, J. (2012). Microbial diversity and biomineralization in low-temperature hydrothermal iron-silica-rich precipitates of the Lau Basin hydrothermal field. *FEMS Microbiol. Ecol.* **81**, 205–216.

Lim, A., Wheeler, A. J., Price, D. M., O'Reilly, L., Harris, K. and Conti, L. (2020). Influence of benthic currents on cold-water coral habitats: a combined benthic monitoring and 3D photogrammetric investigation. *Sci. Rep.* **10**, 1–15.

Limén, H., Levesque, C. and Kim Juniper, S. (2007). POM in macro-/meiofaunal food webs associated with three flow regimes at deep-sea hydrothermal vents on Axial Volcano, Juan de Fuca Ridge. *Mar. Biol.* **153**, 129–139.

Limén, H., Stevens, C. J., Bourass, Z. and Juniper, S. K. (2008). Trophic ecology of siphonostomatoid copepods at deep-sea hydrothermal vents in the northeast Pacific. *Mar. Ecol. Prog. Ser.* **359**, 161–170.

Lonsdale, P. J. (1977). Clustering of suspension-feeding macrobenthos near abyssal hydrothermal vents at oceanic spreading centers. *Deep. Res.* **24**, 857–863.

Lopez-Gonzalez, P. J., Rodriguez, E., Gili, J. M. and Segonzac, M. (2003). New records on sea anemones (Anthozoa: Actiniaria) from hydrothermal vents and cold seeps. *Zool. Verh.* 215–243.

Loucks, O. L. (1970). Evolution of diversity, efficiency, and community stability. *Integr. Comp. Biol.* **10**, 17–25.

Lowell, R. P. and Yao, Y. (2002). Anhydrite precipitation and the extent of hydrothermal recharge zones at ocean ridge crests. *J. Geophys. Res.* **107**, 1–9.

Lutz, R. A., Shank, T. M., Fornari, D. J., Haymon, R. M., Lilley, M. D., Von Damm, K. L. and Desbruyères, D. (1994). Rapid growth at deep-sea vents. *Nature* **371**, 663–664.

Lutz, R. A., Shank, T. M. and Evans, R. (2001). Life after death in the deep sea. *Am. Sci.* **89**, 422–431.

Lutz, R., Shank, T., Rona, P., Reed, A., Allen, C., Lange, W., Low, S. and Kristof, E. (2002). Recent advances in imaging deep-sea hydrothermal vents. *Cah. Biol. Mar.* **43**, 267–269.

Lutz, R. A., Shank, T. M., Luther, G. W., Vetriani, C., Tolstoy, M., Nuzzio, D. B., Moore, T. S., Waldhauser, F., Crespo-Medina, M., Chatziefthimiou, A. D., et al. (2008). Interrelationships between vent fluid chemistry, temperature, seismic activity, and biological community structure at a mussel-dominated, deep-sea hydrothermal vent along the east pacific rise. *J. Shellfish Res.* **27**, 177–190.

M

MacArthur, R. H. and Wilson, E. O. (1967). The theory of island biogeography. *Princet. Univ. Press* **1**.

Mack, G. A. and Skillings, J. H. (1980). A Friedman-Type Rank Test for Main Effects in a Two Factor ANOVA. *J. Am. Stat. Assoc.* **75**, 947–951.

Malanson, G. P., Westman, W. E. and Yan, Y. L. (1992). Realized versus fundamental niche functions in a model of chaparral response to climatic change. *Ecol. Modell.* **64**, 261–277.

Marcillat, M. (2022). Distribution spatiale, structure et composition des assemblages de mégafaune dans les bassins d'arrière-arc du Pacifique sud-ouest. *Univ. Sorbonne* 1–36.

Marcillat, M., Van Audenhaege, L., Ramière, A., Borremans, C., Arnaubec, A. and Menot, L. (in prep.). 3D reprojection for optimal 2D annotation georeferencing.

Marcon, Y., Sahling, H., Borowski, C., dos Santos Ferreira, C., Thal, J. and Bohrmann, G. (2013). Megafaunal distribution and assessment of total methane and sulfide consumption by mussel beds at Menez Gwen hydrothermal vent, based on geo-referenced photomosaics. *Deep. Res. Part I Oceanogr. Res. Pap.* **75**, 93–109.

Marcus, J. and Tunnicliffe, V. (2002). Living on the edges of diffuse vents on the Juan de Fuca Ridge. *Cah. Biol. Mar.* **43**, 263–266.

Marcus, J., Tunnicliffe, V. and Butterfield, D. A. (2009). Post-eruption succession of macrofaunal communities at diffuse flow hydrothermal vents on Axial Volcano , Juan de Fuca Ridge , Northeast Pacific. *Deep. Res. Part II* **56**, 1586–1598.

Marsh, L., Copley, J. T., Huvenne, V. A. I., Linse, K., Reid, W. D. K., Rogers, A. D., Sweeting, C. J. and Tyler, P. A. (2012). Microdistribution of Faunal Assemblages at Deep-Sea Hydrothermal Vents in the Southern Ocean. *PLoS One* **7**, 1–19.

Marsh, L., Copley, J. T., Huvenne, V. A. I., Tyler, P. A. and the Isis ROV Facility (2013). Getting the bigger picture: Using precision Remotely Operated Vehicle (ROV) videography to acquire high-definition mosaic images of newly discovered hydrothermal vents in the Southern Ocean. *Deep. Res. Part II Top. Stud. Oceanogr.* **92**, 124–135.

Marticorena, J., Matabos, M., Ramirez-Llodra, E., Cathalot, C., Laes-Huon, A., Leroux, R., Hourdez, S., Donval, J.-P. and Sarrazin, J. (2021). Recovery of hydrothermal vent communities in response to an induced disturbance at the Lucky Strike vent field (Mid-Atlantic Ridge). *Mar. Environ. Res.* **168**, 1–14.

Martins, I., Colaço, A., Dando, P. R., Martins, I., Desbruyères, D., Sarradin, P. M., Marques, J. C. and Serrão-Santos, R. (2008). Size-dependent variations on the nutritional pathway of *Bathymodiolus azoricus* demonstrated by a C-flux model. *Ecol. Modell.* **217**, 59–71.

Martins, I., Colaço, A., Santos, R. S., Lesongeur, F., Godfroy, A., Sarradin, P. M. and Cosson, R. P. (2009). Relationship between the occurrence of filamentous bacteria on *Bathymodiolus azoricus* shell and the physiological and toxicological status of the vent mussel. *J. Exp. Mar. Bio. Ecol.* **376**, 1–6.

Martins, I., Cosson, R. P., Riou, V., Sarradin, P. M., Sarrazin, J., Santos, R. S. and Colaço, A. (2011). Relationship between metal levels in the vent mussel *Bathymodiolus azoricus* and local microhabitat chemical characteristics of Eiffel Tower (Lucky Strike). *Deep. Res. Part I Oceanogr. Res. Pap.* **58**, 306–315.

Mat, A., Sarrazin, J., Markov, G., Apremont, V., Dubreuil, C., Eché, C., Fabioux, C., Klopp, C., Sarradin, P. M., Tanguy, A., et al. (2020). Biological rhythms in the deep-sea hydrothermal mussel *Bathymodiolus azoricus*. *Nat. Commun.* **11**, 1–12.

Matabos, M., Le Bris, N., Pendlebury, S. and Thiébaut, E. (2008). Role of physico-chemical environment on gastropod assemblages at hydrothermal vents on the East Pacific Rise (13°N/EPR). *J. Mar. Biol. Assoc. United Kingdom* **88**, 995–1008.

Matabos, M., Bui, A. O. V., Mihály, S., Aguzzi, J., Juniper, S. K. and Ajayamohan, R. S. (2014). High-frequency study of epibenthic megafaunal community dynamics in Barkley Canyon: A multi-disciplinary approach using the NEPTUNE Canada network. *J. Mar. Syst.* **130**, 56–68.

Matabos, M., Cuvelier, D., Brouard, J., Shillito, B., Ravaux, J., Zbinden, M., Barthelemy, D., Sarradin, P. M. and Sarrazin, J. (2015). Behavioural study of two hydrothermal crustacean decapods: *Mirocaris fortunata* and *Segonzacia mesatlantica*, from the Lucky Strike vent field (Mid-Atlantic Ridge). *Deep. Res. Part II Top. Stud. Oceanogr.* **121**, 146–158.

Matabos, M. and Arnaubec, A. (2015). Eiffel Tower hydrothermal chimney (Lucky Strike Hydrothermal Field, Mid Atlantic Ridge): 3D scene and imagery. *SEANOE*.

Matabos, M., Best, M., Blandin, J., Hoeberechts, M., Juniper, S. K., Pirenne, B., Robert, K., Ruhl, H. A., Sarrazin, J. and Vardaro, M. (2016). Seafloor Observatories. In *Biological Sampling in the Deep Sea* (ed. Clark, M. R.), Consalvey, M.), and Rowden, A. A.), pp. 306–337. John Wiley & Sons, Ltd.

Matabos, M., Barreyre, T., Juniper, S. K., Cannat, M., Colaço, A., Kelley, D., Alfaro-lucas, J. M., Levin, L. A., Mihaly, S. and Mittelstaedt, E. (2022). Integrating Multidisciplinary Observations in Vent Environments (IMOVE): Decadal Progress in Deep-Sea Observatories at Hydrothermal Vents. *Front. Mar. Sci.* **9**, 1–32.

McCook, L. J. and Chapman, A. R. O. (1997). Patterns and variations in natural succession following massive ice- scour of a rocky intertidal seashore. *J. Exp. Mar. Bio. Ecol.* **214**, 121–147.

McGrorty, S. and Goss-Custard, J. D. (1993). Population dynamics of the mussel *Mytilus edulis* along environmental gradients : spatial variations in density-dependent mortalities. *J. Anim. Ecol.* **62**, 415–427.

McIntosh, R. P. (1981). Succession and Ecological Theory. In *Forest Succession*, pp. 10–23.

McMahon, B. R. (1988a). Physiological responses to oxygen depletion in intertidal animals. *Integr. Comp. Biol.* **28**, 39–53.

McMahon, R. F. (1988b). Respiratory response to periodic emergence in intertidal molluscs. *Integr. Comp. Biol.* **28**, 97–114.

Menge, B. A. and Sutherland, J. P. (1976). Species diversity gradients: synthesis of the roles of predation, competition, and temporal heterogeneity. *Am. Nat.* **110**, 351–369.

Menge, B. A. (1978). Predation Intensity in a Rocky Intertidal Community - Relation between Predator Foraging Activity and Environmental Harshness. *Oecologia* **34**, 1–16.

Micheli, F., Peterson, C. H., Mullineaux, L. S., Fisher, C. R., Mills, S. W., Sancho, G., Johnson, G. A. and Lenihan, H. S. (2002). Predation structures communities at deep-sea hydrothermal vents. *Ecol. Monogr.* **72**, 365–382.

Milligan, B. N. and Tunnicliffe, V. (1994). Vent and nonvent faunas of Cleft segment, Juan de Fuca Ridge, and their relations to lava age. *J. Geophys. Res. Solid Earth* **99**, 4777–4786.

Minchinton, T. E., Scheibling, R. E. and Hunt, H. L. (1997). Recovery of an intertidal assemblage following a rare occurrence of scouring by Sea Ice in Nova Scotia, Canada. *Bot. Mar.* **40**, 139–148.

Mitchell, E. G. and Harris, S. (2020). Mortality, Population and Community Dynamics of the Glass Sponge Dominated Community "The Forest of the Weird" From the Ridge Seamount, Johnston Atoll, Pacific Ocean. *Front. Mar. Sci.* **7**, 1–21.

Mittelstaedt, E., Escartín, J., Gracias, N., Olive, J. A., Barreyre, T., Davaille, A., Cannat, M. and Garcia, R. (2012). Quantifying diffuse and discrete venting at the Tour Eiffel vent site, Lucky Strike hydrothermal field. *Geochemistry, Geophys. Geosystems* **13**, 1-18.

Moore, T. S., Shank, T. M., Nuzzio, D. B. and Luther, G. W. (2009). Time-series chemical and temperature habitat characterization of diffuse flow hydrothermal sites at 9°50′N East Pacific Rise. *Deep. Res. Part II Top. Stud. Oceanogr.* **56**, 1616–1621.

Moulon, P., Monasse, P., Perrot, R. and Marlet, R. (2017). OpenMVG: Open multiple view geometry. *Lect. Notes Comput. Sci. (including Subser. Lect. Notes Artif. Intell. Lect. Notes Bioinformatics)* **10214 LNCS**, 60–74.

Mullineaux, L. S., Peterson, C. H., Micheli, F. and Mills, S. W. (2003). Successional mechanism varies along a gradient in hydrothermal fluid flux at deep-sea vents. *Ecol. Monogr.* **73**, 523–542.

Mullineaux, L. S., Micheli, F., Peterson, C. H., Lenihan, H. S. and Markus, N. (2009). Imprint of past environmental regimes on structure and succession of a deep-sea hydrothermal vent community. *Oecologia* **161**, 387–400.

Mullineaux, L. S., Le Bris, N., Mills, S. W., Henri, P., Bayer, S. R., Secrist, R. G. and Siu, N. (2012). Detecting the Influence of Initial Pioneers on Succession at Deep-Sea Vents. *PLoS One* **7**, 1-14.

Mullineaux, L. S., Mills, S. W., Bris, N. Le, Beaulieu, S. E., Sievert, S. M. and Dykman, L. N. (2020). Prolonged recovery time after eruptive disturbance of a deep-sea hydrothermal vent community. *Proc. R. Soc. B Biol. Sci.* **287**, 1-8.

Murton, B. J., Lehrmann, B., Dutrieux, A. M., Martins, S., de la Iglesia, A. G., Stobbs, I. J., Barriga, F. J. A. S., Bialas, J., Dannowski, A., Vardy, M. E., et al. (2019). Geological fate of seafloor massive sulphides at the TAG hydrothermal field (Mid-Atlantic Ridge). *Ore Geol. Rev.* **107**, 903–925.

N

Nakamura, R. (1976). Temperature and the Vertical Distribution of Two Tidepool Fishes (*Oligocottus maculosus, O. snyderi*). *Am. Soc. Ichthyol. Herpetol.* 143–152.

Nedoncelle, K., Lartaud, F., de Rafelis, M., Boulila, S. and Le Bris, N. (2013). A new method for high-resolution bivalve growth rate studies in hydrothermal environments. *Mar. Biol.* **160**, 1427–1439.

Nedoncelle, K., Lartaud, F., Contreira Pereira, L., Yücel, M., Thurnherr, A. M., Mullineaux, L. and Le Bris, N. (2015). *Bathymodiolus growth* dynamics in relation to environmental fluctuations in vent habitats. *Deep. Res. Part I Oceanogr. Res. Pap.* **106**, 183–193.

Nees, H. A., Moore, T. S., Mullaugh, K. M., Holyoke, R. R., Janzen, C. P., Ma, S., Metzger, E., Waite, T. J., Yücel, M., Lutz, R. A., et al. (2008). Hydrothermal Vent Mussel Habitat Chemistry, Pre- and Post-Eruption at 9°50′North on the East Pacific Rise. *J. Shellfish Res.* **27**, 169–175.

Nehls, G. and Thiel, M. (1993). Large-scale distribution patterns of the mussel *Mytilus edulis* in the Wadden Sea of Schleswig-Holstein: Do storms structure the ecosystem? *Netherlands J. Sea Res.* **31**, 181–187.

Nehls, G., Hertzler, I. and Scheiffarth, G. (1997). Stable mussel *Mytilus edulis* beds in the Wadden Sea - They’re just for the birds. *Helgolander Meeresuntersuchungen* **51**, 361–372.

Neufeld, M., Metaxas, A. and Jamieson, J. W. (2022). Non-Vent Megafaunal Communities on the Endeavour and Middle Valley Segments of the Juan de Fuca Ridge, Northeast Pacific Ocean. *Front. Mar. Sci.* **9**, 1–16.

Newell, R. C. (1973). Factors affecting the respiration of intertidal invertebrates. *Integr. Comp. Biol.* **13**, 513–528.

O

Odum, E. P. (1969). The Strategy of Ecosystem Development. *Science* **164**, 262–270.

Okamoto, N., Igarashi, Y., Matsui, T. and Fukushima, T. (2019). Preliminary Results of Environmental Monitoring of Seafloor Massive Sulphide Excavation and Lifting Tests in the Okinawa Trough. In *29th International Ocean and Polar Engineering Conference*, pp. 78–84. Honolulu, Hawaii, USA, June 16-21, 2019.

Okamura, B. (1986). Group living and the effects of spatial position in aggregations of Mytilus edulis. *Oecologia* **69**, 341–347.

Oksanen, J., Legendre, P., O'Hara, B., Stevens, M. H. H., Oksanen, M. J. and Suggests, M. (2007). The vegan package. *Community Ecol. Packag.* **10**, 631–637.

Ondréas, H., Fouquet, Y., Voisset, M. and Radford-Knoery, J. (1997). Detailed Study of Three Contiguous Segments of the Mid-Atlantic Ridge, South of the Azores (37° N to 38°30′ N), Using Acoustic Imaging Coupled with Submersible Observations. *Mar. Geophys. Res.* **19**, 231–255.

Ondréas, H., Cannat, M., Fouquet, Y., Normand, A., Sarradin, P. M. and Sarrazin, J. (2009). Recent volcanic events and the distribution of hydrothermal venting at the Lucky Strike hydrothermal field, Mid-Atlantic Ridge. *Geochemistry, Geophys. Geosystems* **10**, 1-18.

P

Paine, R. T. (1974). Intertidal community structure - Experimental studies on the relationship between a dominant competitor and its principal predator. *Oecologia* **15**, 93–120.

Paine, R. T. (1976). Size-limited predation: an observational and experimental approach with the *Mytilus-Pisaster* interaction. *Ecology* **57**, 858–873.

Paine, R. T. and Levin, S. A. (1981). Intertidal landscapes: disturbance and the dynamics of pattern. *Ecol. Monogr.* **51**, 145–178.

Parr, C. L. and Andersen, A. N. (2006). Patch mosaic burning for biodiversity conservation: A critique of the pyrodiversity paradigm. *Conserv. Biol.* **20**, 1610–1619.

Parr, C. L. and Brockett, B. H. (1999). Patch-mosaic burning: A new paradigm for savanna fire management in protected areas? *Koedoe* **42**, 117–130.

Pebesma, E. (2018). Simple features for R: Standardized support for spatial vector data. *R J.* **10**, 439–446.

Perfit, M. R. and Chadwick, W. W. (1998). Magmatism at Mid-Ocean Ridges: Constraints from Volcanological and Geochemical Investigations. *Geophys. Monogr. Union* **106**, 59–116.

Pester, N. J., Reeves, E. P., Rough, M. E., Ding, K., Seewald, J. S. and Seyfried, W. E. (2012). Subseafloor phase equilibria in high-temperature hydrothermal fluids of the Lucky Strike Seamount (Mid-Atlantic Ridge, 37°17'N). *Geochim. Cosmochim. Acta* **90**, 303–322.

Petraitis, P. S. (1995). The role of growth in maintaining spatial dominance by mussels (*Mytilus edulis*). *Ecology* **76**, 1337–1346.

Pickett, S. T. A. and Thompson, J. N. (1978). Patch dynamics and the design of nature reserves. *Biol. Conserv.* **13**, 27–37.

Pickett, S. T. A. and White, P. S. (1985). The ecology of natural disturbance and patch dynamics: An introduction. In *The ecology of natural disturbance and patch dynamics*, pp. 1–13. Orlando.

Pickett, S. T. A., Collins, S. L. and Armesto, J. J. (1987). A hierarchical consideration of causes and mechanisms of succession. In *Theory and models in vegetation science*, pp. 109–114. Dordrecht: Springer.

Pickett, A. S. T. A., Kolasa, J., Armesto, J. J. and Collins, S. L. (1989). The Ecological Concept of Disturbance and Its Expression at Various Hierarchical Levels. *Wiley behalf Nord. Soc. Oikos* **54**, 129–136.

Piechaud, N., Hunt, C., Culverhouse, P. F., Foster, N. L. and Howell, K. L. (2019). Automated identification of benthic epifauna with computer vision. *Mar. Ecol. Prog. Ser.* **615**, 15–30.

Pieters, H., Kluytmans, J. H., Zandee, D. I. and Cadée, G. C. (1980). Tissue composition and reproduction of *Mytilus edulis* in relation to food availability. *Netherlands J. Sea Res.* **14**, 349–361.

Platt, W. J. and Connell, J. H. (2003). Natural disturbances and directional replacement of species. *Ecol. Monogr.* **73**, 507–522.

Plum, C., Pradillon, F., Fujiwara, Y. and Sarrazin, J. (2017). Copepod colonization of organic and inorganic substrata at a deep-sea hydrothermal vent site on the Mid-Atlantic Ridge. *Deep. Res. Part II Top. Stud. Oceanogr.* **137**, 335–348.

Podowski, E. L., Moore, T. S., Zelnio, K. A., Luther, G. W. and Fisher, C. R. (2009). Distribution of diffuse flow megafauna in two sites on the Eastern Lau Spreading Center, Tonga. *Deep. Res. Part I Oceanogr. Res. Pap.* **56**, 2041–2056.

Podowski, E. L., Ma, S., Luther, G. W., Wardrop, D. and Fisher, C. R. (2010). Biotic and abiotic factors affecting distributions of megafauna in diffuse flow on andesite and basalt along the Eastern Lau Spreading Center, Tonga. *Mar. Ecol. Prog. Ser.* **418**, 25–45.

Portail, M., Brandily, C., Cathalot, C., Colaço, A., Gélinas, Y., Husson, B., Sarradin, P. M. and Sarrazin, J. (2018). Food-web complexity across hydrothermal vents on the Azores triple junction. *Deep. Res. Part I Oceanogr. Res. Pap.* **131**, 101–120.

Preisendorfer, R. W. and Mobley, C. D. (1988). Principal component analysis in meteorology and oceanography. *Dev. Atmos. Sci.* **17**.

Price, D. M., Robert, K., Callaway, A., Lo lacono, C., Hall, R. A. and Huvenne, V. A. I. (2019). Using 3D photogrammetry from ROV video to quantify cold-water coral reef structural complexity and investigate its influence on biodiversity and community assemblage. *Coral Reefs* **38**, 1007–1021.

Pruis, M. J. and Johnson, H. P. (2004). Tapping into the sub-seafloor: Examining diffuse flow and temperature from an active seamount on the Juan de Fuca Ridge. *Earth Planet. Sci. Lett.* **217**, 379–388.

R

R Core Team (2016). R: A language and environment for statistical computing.

Rasband, W. S. (1997). ImageJ. https://imagej.nih.gov/ij/download.html

Raymond, E. H. and Widder, E. A. (2007). Behavioral responses of two deep-sea fish species to red, far-red, and white light. *Mar. Ecol. Prog. Ser.* **350**, 291–298.

Rhoads, D. C., Lutz, R. A., Revelas, E. C. and Cerrato, R. M. (1981). Growth of Bivalves at Deep-Sea Hydrothermal Vents along the Galápagos Rift. *Science.* **214**, 911–913.

Rigaud, V. (2007). Innovation and Operation With Robotized Underwater Systems. *J. F. Robot.* **24**, 449–459.

Riou, V., Colaço, A., Bouillon, S., Khripounoff, A., Dando, P., Mangion, P., Chevalier, E., Korntheuer, M., Santos, R. S. and Dehairs, F. (2010). Mixotrophy in the deep sea: A dual endosymbiotic hydrothermal mytilid assimilates dissolved and particulate organic matter. *Mar. Ecol. Prog. Ser.* **405**, 187–201.

Robert, K., Onthank, K. L., Juniper, S. K. and Lee, R. W. (2012). Small-scale thermal responses of hydrothermal vent polynoid polychaetes: Preliminary in situ experiments and methodological development. *J. Exp. Mar. Bio. Ecol.* **420**–**421**, 69–76.

Robert, K., Huvenne, V. A. I., Georgiopoulou, A., Jones, D. O. B., Marsh, L., Carter, D. O. G. and Chaumillon, L. (2017). New approaches to high-resolution mapping of marine vertical structures. *Sci. Rep.* **7**, 1–14.

Robert, K., Jones, D. O. B., Georgiopoulou, A. and Huvenne, V. A. I. (2020). Cold-water coral assemblages on vertical walls from the Northeast Atlantic. *Divers. Distrib.* **26**, 284–298.

Robigou, V., Delaney, J. R. and Stakes, D. S. (1993). Large massive sulfide deposits in a newly discovered active hydrothermal system, the High-Rise field, Endeavour Segment, Juan de Fuca Ridge. *Geophys. Res. Lett.* **20**, 1887–1890.

Rogers, A. D., Tyler, P. A., Connelly, D. P., Copley, J. T., James, R., Larter, R. D., Linse, K., Mills, R. A., Garabato, A. N., Pancost, R. D., et al. (2012). The discovery of new deep-sea hydrothermal vent communities in the Southern ocean and implications for biogeography. *PLoS Biol.* **10**, 1-17.

Rommevaux, C., Henri, P., Degboe, J., Chavagnac, V., Lesongeur, F., Godfroy, A., Boulart, C., Destrigneville, C. and Castillo, A. (2019). Prokaryote Communities at Active Chimney and In Situ Colonization Devices After a Magmatic Degassing Event (37°N MAR, EMSO-Azores Deep-Sea Observatory). *Geochemistry, Geophys. Geosystems* **20**, 3065–3089.

Roohi, R., Hoogenboom, R., Van Bommel, R., Van Der Meer, M. T. J., Mienis, F. and Gollner, S. (2022). Influence of Chemoautotrophic Organic Carbon on Sediment and Its Infauna in the Vicinity of the Rainbow Vent Field. *Front. Mar. Sci.* **9**, 1–11.

Rosenberg, D. B. and Freedman, S. M. (1994). Temporal heterogeneity and ecological community structure. *Int. J. Environ. Stud.* **46**, 97–102.

Rossi, P., Castagnetti, C., Capra, A., Brooks, A. J. and Mancini, F. (2020). Detecting change in coral reef 3D structure using underwater photogrammetry: critical issues and performance metrics. *Appl. Geomatics* **12**, 3–17.

Rountree, R. A., Aguzzi, J., Marini, S., Fanelli, E., De Leo, F. C., Del Rio, J. and Juanes, F. (2021). Oceanography and Marine Biology. In *Oceanography and Marine Biology: An Annual Review* (ed. Hawkins, S. J., Allcock, A. L., Bates, A. E., Evans, A. J., Firth, L. B., McQuaid, C. D., Russell, B. D., Smith, I. P., Swearer, S. E., and Todd, P. A.), pp. 79–106. Taylor & Francis.

Rubin, K. H., Soule, S. A., Chadwick, W. W., Fornari, D. J., Clague, D. A., Embley, R. W., Baker, E. T., Perfit, M. R., Caress, D. W. and Dziak, R. P. (2012). Volcanic eruptions in the deep sea. *Oceanography* **25**, 143–157.

Rubio, I., Ganzedo, U., Hobday, A. J. and Ojea, E. (2020). Southward re-distribution of tropical tuna fisheries activity can be explained by technological and management change. *Fish Fish.* **21**, 511–521.

Rybakova, E. and Galkin, S. (2015). Hydrothermal assemblages associated with different foundation species on the East Pacific Rise and Mid-Atlantic Ridge, with a special focus on mytilids. *Mar. Ecol.* **36**, 45–61.

S

Salmi, M. S., Johnson, P. H., Tivey, M. A. and Hutnak, M. (2014). Quantitative estimate of heat flow from a mid-ocean ridge axial valley Raven field Juan de Fuca Ridge: Observations and inferences. *J. Geophys. Res. Solid Earth* **119**, 6841–6854.

Sánchez-Mora, D., Jamieson, J., Cannat, M., Escartín, J. and Barreyre, T. (2022). Age and Rate of Accumulation of Metal-Rich Hydrothermal Deposits on the Seafloor: The Lucky Strike Vent Field, Mid-Atlantic Ridge. *J. Geophys. Res. Solid Earth* **127**, 1-16.

Sancho, G., Fisher, C. R., Mills, S., Micheli, F., Johnson, G. A., Lenihan, H. S., Peterson, C. H. and Mullineaux, L. S. (2005). Selective predation by the zoarcid fish *Thermarces cerberus* at hydrothermal vents. *Deep. Res. Part I Oceanogr. Res. Pap.* **52**, 837–844.

Sanders, H. L., Hessler, R. R. and Hampson, G. R. (1972). An introduction to the study of deep-sea benthic faunal assemblages along the Gay Head-Bermuda transect. *Deep. Res.* **12**, 845–867.

Sarradin, P.-M., Caprais, J.-C., Riso, R., Kerouel, R. and Aminot, A. (1999). Chemical environment of the hydrothermal mussel communities in the Lucky Strike and Menez Gwen vent fields, Mid Atlantic Ridge. *Cah. Biol. Mar.* **40**, 93–104.

Sarradin, P. M., Waeles, M., Bernagout, S., Le Gall, C., Sarrazin, J. and Riso, R. (2009). Speciation of dissolved copper within an active hydrothermal edifice on the Lucky Strike vent field (MAR, 37°N). *Sci. Total Environ.* **407**, 869–878.

Sarradin, P.-M. and Cannat, M. (2015). MOMARSAT2015. *French Oceanogr. Cruises*. 10.17600/15000200

Sarradin, P.-M. and Legrand, J. (2020). MOMARSAT2020. *French Oceanogr. Cruises*. 10.17600/18000684

Sarrazin, J., Robigou, V., Juniper, S. K. and Delaney, J. R. (1997). Biological and geological dynamics over four years on a high-temperature sulfide structure at the Juan de Fuca Ridge hydrothermal observatory. *Mar. Ecol. Prog. Ser.* **153**, 5–24.

Sarrazin, J. and Juniper, K. S. (1998). The use of video imagery to gather biological information at deep-sea hydrothermal vents. *Cah. Biol. Mar.* **39**, 255–258.

Sarrazin, J. and Juniper, S. K. (1999). Biological characteristics of a hydrothermal edifice mosaic community. *Mar. Ecol. Prog. Ser.* **185**, 1–19.

Sarrazin, J., Juniper, S. K., Massoth, G. and Legendre, P. (1999). Physical and chemical factors influencing species distributions on hydrothermal sulfide edifices of the Juan de Fuca Ridge, northeast Pacific. *Mar. Ecol. Prog. Ser.* **190**, 89–112.

Sarrazin, J., Levesque, C., Juniper, S. K. and Tivey, M. K. (2002). Mosaic community dynamics on Juan de Fuca Ridge sulphide edifices: Substratum, temperature and implications for trophic structure. *Cah. Biol. Mar.* **43**, 275–279.

Sarrazin, J. and Sarradin, P. M. (2006). MoMARETO: A cruise dedicated to the spatio-temporal dynamics and the adaptations of hydrothermal vent fauna on the mid-Atlantic Ridge. *InterRidge News* **15**, 24–33.

Sarrazin, J., Walter, C., Sarradin, P. M., Brind'Amour, A., Desbruyères, D., Briand, P., Fabri, M. C., Van Gaever, S., Vanreusel, A., Bachraty, C., et al. (2006). Community structure and temperature dynamics within a mussel assemblage on the Southern East Pacific Rise. *Cah. Biol. Mar.* **47**, 483–490.

Sarrazin, J., Blandin, J., Delauney, L., Dentrecolas, S., Dorval, P., Dupont, J., Legrand, J., Leroux, D., Léon, P., Lévèque, J. P., et al. (2007). TEMPO: A new ecological module for studying deep-sea community dynamics at hydrothermal vents. *Ocean. 2007 - Eur.* 1–4.

Sarrazin, J., Cuvelier, D., Peton, L., Legendre, P. and Sarradin, P.-M. (2014). High-resolution dynamics of a deep-sea hydrothermal mussel assemblage monitored by the EMSO-Açores MoMAR observatory. *Deep. Res. Part I Oceanogr. Res. Pap.* **90**, 62–75.

Sarrazin, J., Legendre, P., de Busserolles, F., Fabri, M. C., Guilini, K., Ivanenko, V. N., Morineaux, M., Vanreusel, A. and Sarradin, P. M. (2015). Biodiversity patterns, environmental drivers and indicator species on a high-temperature hydrothermal edifice, Mid-Atlantic Ridge. *Deep. Res. Part II Top. Stud. Oceanogr.* **121**, 177–192.

Sarrazin, J., Portail, M., Legrand, E., Cathalot, C., Laes, A., Lahaye, N., Sarradin, P. M. and Husson, B. (2020). Endogenous versus exogenous factors: What matters for vent mussel communities? *Deep. Res. Part I Oceanogr. Res. Pap.* **160**, 1-19.

Sarrazin, J., Cathalot, C., Laes, A., Marticorena, J., Michel, L. N. and Matabos, M. (2022). Integrated Study of New Faunal Assemblages Dominated by Gastropods at Three Vent Fields Along the Mid-Atlantic Ridge : Diversity, Structure, Composition and Trophic Interactions. *Front. Mar. Sci.* **9**, 1–15.

Scheirer, D. S., Shank, T. M. and Fornari, D. J. (2006). Temperature variations at diffuse and focused flow hydrothermal vent sites along the northern East Pacific Rise. *Geochemistry, Geophys. Geosystems* **7**, 1-23.

Schoening, T., Osterloff, J. and Nattkemper, T. W. (2016). RecoMIA-recommendations for marine image annotation: Lessons learned and future directions. *Front. Mar. Sci.* **3**, 1-11.

Schoening, T., Durden, J., Preuss, I., Branzan Albu, A., Purser, A., De Smet, B., Dominguez-Carrió, C., Yesson, C., de Jonge, D., Lindsay, D., et al. (2017). Report on the Marine Imaging Workshop 2017. *Res. Ideas Outcomes* **3**, 1–16.

Schönberg, C. H. L. (2021). No taxonomy needed: Sponge functional morphologies inform about environmental conditions. *Ecol. Indic.* **129**, 1-30.

Schöne, B. R. and Giere, O. (2005). Growth increments and stable isotope variation in shells of the deep-sea hydrothermal vent bivalve mollusk *Bathymodiolus brevior* from the North Fiji Basin, Pacific Ocean. *Deep. Res. Part I Oceanogr. Res. Pap.* **52**, 1896–1910.

Sen, A., Becker, E. L., Podowski, E. L., Wickes, L. N., Ma, S., Mullaugh, K. M., Hourdez, S., Luther, G. W. and Fisher, C. R. (2013). Distribution of mega fauna on sulfide edifices on the Eastern Lau Spreading Center and Valu Fa Ridge. *Deep. Res. Part I Oceanogr. Res. Pap.* **72**, 48–60.

Sen, A., Podowski, E. L., Becker, E. L., Shearer, E. A., Gartman, A., Yücel, M., Hourdez, S., Luther, G. W. and Fisher, C. R. (2014). Community succession in hydrothermal vent habitats of the Eastern Lau Spreading Center and Valu Fa Ridge, Tonga. *Limnol. Oceanogr.* **59**, 1510–1528.

Sen, A., Kim, S., Miller, A. J., Hovey, K. J., Hourdez, S., Luther, G. W. and Fisher, C. R. (2016). Peripheral communities of the Eastern Lau Spreading Center and Valu Fa Ridge: community composition, temporal change and comparison to near-vent communities. *Mar. Ecol.* **37**, 599–617.

Shank, T. M., Fornari, D. J., Von Damm, K. L., Lilley, M. D., Haymon, R. M. and Lutz, R. A. (1998). Temporal and spatial patterns of biological community development at nascent deep-sea hydrothermal vents (9°50'N, East Pacific Rise). *Deep. Res. Part II Top. Stud. Oceanogr.* **45**, 465–515.

Shank, T., Fornari, D., Yoerger, D., Humphris, S., Bradley, A., Hammond, S., Lupton, J., Scheirer, D., Collier, R., Reysenbach, A.-L., et al. (2003). Deep Submergence Synergy: Alvin and ABE Explore the Galapagos Rift at 86°W. *Eos, Trans. Am. Geophys. Union* **84**, 425–440.

Shurin, J. B., Allen, E. G., Shurin, J. B. and Allen, E. G. (2001). Effects of Competition, Predation, and Dispersal on Species Richness at Local and Regional Scales. *Am. Nat.* **158**, 624–637.

Sigwart, J. D. and Chen, C. (2018). Comparative Oxygen Consumption of Gastropod Holobionts from Deep-Sea Hydrothermal Vents in the Indian Ocean. *Biol. Bull.* **235**, 102–112.

Simeoni, P., Sarrazin, J., Nouze, H., Sarradin, P. M., Ondreas, H., Scalabrin, C. and Sinquin, J. M. (2007). Victor 6000: New high resolution tools for deep sea research. « Module de mesures en route ». *Ocean. 2007 - Eur.* 0–5.

Simon-Lledó, E., Bett, B. J., Huvenne, V. A. I., Köser, K., Schoening, T., Greinert, J. and Jones, D. O. B. (2019). Biological effects 26 years after simulated deep-sea mining. *Sci. Rep.* **9**, 1–13.

Singh, S. C., Crawford, W. C., Carton, H., Seher, T., Combier, V., Cannat, M., Canales, J. P., Düsünür, D., Escartín, J. and Miranda, J. M. (2006). Discovery of a magma chamber and faults beneath a Mid-Atlantic Ridge hydrothermal field. *Nature* **442**, 1029–1032.

Sogin, E. M., Leisch, N. and Dubilier, N. (2020). Chemosynthetic symbioses. *Curr. Biol.* **30**, R1137–R1142.

Soto, K. J. and Kim, S. (2022). Hydrothermal vent periphery invertebrate community habitat preferences of the Lau Basin. *J. Exp. Mar. Bio. Ecol.* **552**, 151741.

Soto Vega, P. J., Papadakis, P., Matabos, M., Van Audenhaege, L., Ramière, A., Sarrazin, J. and da Costa, G. A. O. P. (in prep.). Hydrothermal Vents Substrate Classification using Convolutional Neural Networks.

Sousa, W. P. (1979). Disturbance in marine intertidal boulder fields: the nonequilibrium maintenance of species diversity. *Ecology* **60**, 1225–1239.

Sousa, W. P. (1984a). The role of disturbance in natural communities. *Annu. Rev. Ecol. Syst.* **15**, 353–391.

Sousa, W. P. (1984b). Intertidal mosaics: patch size, propagule availability, and spatially variable patterns of succession. *Ecology* **65**, 1918–1935.

Spiess, F. N., Macdonald, K. C., Atwater, T., Ballard, R., Carranza, A., Cordoba, D., Cox, V., Diaz Garcia, V. M., Francheteau, J., Guerrero, J., et al. (1980). East Pacific Rise: Hot Springs and Geophysical Experiments. *Science* **207**, 1421–1433.

Steele, J. H. (1978). Some comments on plankton patches. In *Spatial pattern in plankton communities* (ed. Springer), pp. 1–20. Boston, MA: Plenum.

Steenbergen, J., Baars, J. M. D. D., Van Stralen, M. R. and Craeymeersch, J. A. (2006). Winter survival of mussel beds in the intertidal part of the Dutch Wadden Sea. *NERI Tech. Rep.* 107–111.

Steinke, D. M. and Buckham, B. J. (2005). A Kalman filter for the navigation of remotely operated vehicles. *Proc. Ocean. 2005 MTS/IEEE* 581–588.

Strasser, M., Reinwald, T. and Reise, T. (2001). Differential effects of the severe winter of 1995/96 on the intertidal bivalves *Mytilus edulis*, *Cerastoderma edule* and *Mya arenaria* in the Northern Wadden Sea. *Helgol. Mar. Res.* **55**, 190–197.

Sturbois, A., De Cáceres, M., Sánchez-Pinillos, M., Schaal, G., Gauthier, O., Mao, P. Le, Ponsero, A. and Desroy, N. (2021). Extending community trajectory analysis: New metrics and representation. *Ecol. Modell.* **440**, 1-15.

Suchanek, T. H. (1978). The ecology of *Mytilus edulis* L. in exposed rocky intertidal communities. *J. Exp. Mar. Bio. Ecol.* **31**, 105–120.

Suchanek, T. H. (1981). The role of disturbance in the evolution of life history strategies in the intertidal mussels *Mytilus edulis* and *Mytilus californianus*. *Oecologia* **50**, 143–152.

T

Tang, Y., Wang, Q., Zhang, K. and Atkinson, P. M. (2020). Quantifying the Effect of Registration Error on Spatio-Temporal Fusion. *IEEE J. Sel. Top. Appl. Earth Obs. Remote Sens.* **13**, 487–503.

Taylor, C. D., Wirsen, C. O. and Gaill, F. (1999). Rapid microbial production of filamentous sulfur mats at hydrothermal vents. *Appl. Environ. Microbiol.* **65**, 2253–2255.

Taylor, J., Krumpen, T., Soltwedel, T., Gutt, J. and Bergmann, M. (2017). Dynamic benthic megafaunal communities: Assessing temporal variations in structure, composition and diversity at the Arctic deep-sea observatory HAUSGARTEN between 2004 and 2015. *Deep. Res. Part I Oceanogr. Res. Pap.* **122**, 81–94.

Tempera, F., Henriques, A. B., Porteiro, F. and Morato, T. (2012). Cataloguing deep-sea biological facies of the Azores. In *Revista de Investigación Marina* (ed. Borja, Á.) and Galparsoro, I.), pp. 21–70. Unidad de Investigación Marina de Tecnalia.

Tews, J., Brose, U., Grimm, V., Tielbörger, K., Wichmann, M. C., Schwager, M. and Jeltsch, F. (2004). Animal species diversity driven by habitat heterogeneity/diversity: The importance of keystone structures. *J. Biogeogr.* **31**, 79–92.

Thomson, R. E., Roth, S. E. and Dymond, J. (1990). Near-Inertial Motions Over a Mid-Ocean Ridge: Effects of Topography and Hydrothermal Plumes. *J. Geophys. Res.* **95**, 7261.

Thornton, B., Bodenmann, A., Pizarro, O., Williams, S. B., Friedman, A., Nakajima, R., Takai, K., Motoki, K., Watsuji, T. o., Hirayama, H., et al. (2016). Biometric assessment of deep-sea vent megabenthic communities using multi-resolution 3D image reconstructions. *Deep. Res. Part I Oceanogr. Res. Pap.* **116**, 200–219.

Thornton, B., Bodenmann, A., Yamada, T., Stanley, D., Massot-Campos, M., Huvenne, V., Durden, J., Bett, B., Ruhl, H. and Newborough, D. (2021). Visualizing Multi-Hectare Seafloor Habitats with BioCam. *Oceanography* **34**, 92–93.

Tivey, M. K. (1995). Modeling chimney growth and associated fluid flow at seafloor hydrothermal vent sites. *Geophys. Monogr. Ser.* **91**, 158–177.

Tivey, M. K. (2007). Generation of seafloor hydrothermal vent fluids and associated mineral deposits. *Oceanography* **20**, 50–65.

Tivey, M. A. and Johnson, H. P. (2002). Crustal magnetization reveals subsurface structure of Juan de Fuca Ridge hydrothermal vent fields. *Geology* **30**, 979–982.

Tokeshi, M. (2011). Spatial structures of hydrothermal vents and vent-associated megafauna in the back-arc basin system of the Okinawa Trough, western Pacific. *J. Oceanogr.* **67**, 651–665.

Tolstoy, M., Cowen, J. P., Baker, E. T., Fornari, D. J., Rubin, K. H., Shank, T. M., Waldhauser, F., Bohnenstiehl, D. R., Forsyth, D. W., Holmes, R. C., et al. (2006). A sea-floor spreading event captured by seismometers. *Science* **314**, 1920–1922.

Tooms, J. S. (1970). Metal deposits in the Red Sea - their nature, origin and economic worth. *Underw. Sci. Technol. J.* **2**, 28–33.

Trask, J. L. and Van Dover, C. L. (1999). Site-specific and ontogenetic variations in nutrition of mussels (*Bathymodiolus* sp.) from the Lucky Strike hydrothermal vent field, Mid-Atlantic Ridge. *Limnol. Oceanogr.* **44**, 334–343.

Tsuchiya, M. (1983). Mass mortality in a population of the mussel *mytilus edulis* l. caused by high temperature on rocky shores. *J. Exp. Mar. Bio. Ecol.* **66**, 101–111.

Tsurumi, M. and Tunnicliffe, V. (2001). Characteristics of a hydrothermal vent assemblage on a volcanically active segment of Juan de Fuca Ridge, northeast Pacific. *Can. J. Fish. Aquat. Sci.* **58**, 530–542.

Tsurumi, M. and Tunnicliffe, V. (2003). Tubeworm-associated communities at hydrothermal vents on the Juan de Fuca Ridge, northeast Pacific. *Deep. Res. I* **50**, 611–629.

Tunnicliffe, V. (1990). Observations on the Effects of Sampling on Hydrothermal Vent Habitat and Fauna of Axial Seamount, Juan de Fuca Ridge. *J. Geophys. Res.* **95**, 12961–12966.

Tunnicliffe, V. (1991). The biology of hydrothermal vents: ecology and evolution. In *Oceanography and Marine Biology Annual Review* (ed. Barnes, H.), Barnes, M.), Ansell, A. D.), and Gibson, R. N.), pp. 319–407. Aberdeen University Press.

Tunnicliffe, V. and Jensen, R. G. (1987). Distribution and behaviour of the spider crab *Macroregonia macrochira* Sakai (Brachyura) around the hydrothermal vents of the northeast Pacific. *Can. J. Zool.* **65**, 2443–2449.

Tunnicliffe, V. and Juniper, K. S. (1990). Dynamic character of the hydrothermal vent habitat and the nature of sulphide chimney fauna. *Prog. Oceanogr.* **24**, 1–13.

Tunnicliffe, V., Garrett, J. F. and Paul Johnson, H. (1990). Physical and biological factors affecting the behaviour and mortality of hydrothermal vent tubeworms (vestimentiferans). *Deep. Res.* **37**, 103–125.

Tunnicliffe, V., Holden, J. F., Butterfield, D. A. and Juniper, S. K. (1997). Biological colonization of new hydrothermal vents following an eruption on Juan de Fuca Ridge. *Deep. Res. I* **44**, 1627–1644.

Turner, P. J., Thaler, A. D., Freitag, A. and Colman, P. (2019). Deep-sea hydrothermal vent ecosystem principles : Identification of ecosystem processes, services and communication of value. *Mar. Policy* **101**, 118–124.

Tyler, P. A. and Young, C. M. (1999). Reproduction and dispersal at vents and cold seeps. *J. Mar. Biol. Assoc. United Kingdom* **79**, 193–208.

Tyler, P., German, C. and Tunnicliffe, V. (2005). Biologists do not pose a threat to deep-sea vents. *Nature* **434**, 18–18.

U

Underwood, N., Hambäck, P. and Inouye, B. D. (2005). Large-scale questions and small-scale data: Empirical and theoretical methods for scaling up in ecology. *Oecologia* **145**, 177–178.

Urcuyo, I. A., Massoth, G. J., Julian, D. and Fisher, C. R. (2003). Habitat, growth and physiological ecology of a basaltic community of *Ridgeia piscesae* from the Juan de Fuca Ridge. *Deep. Res. Part I Oceanogr. Res. Pap.* **50**, 763–780.

V

Van Audenhaege, L., Fariñas-Bermejo, A., Schultz, T. and Lee Van Dover, C. (2019). An environmental baseline for food webs at deep-sea hydrothermal vents in Manus Basin (Papua New Guinea). *Deep. Res. Part I Oceanogr. Res. Pap.* **148**, 88–99.

Van Audenhaege, L., Matabos, M., Brind'Amour, A., Drugmand, J., Laës-Huon, A., Sarradin, P.-M. and Sarrazin, J. (2022). Long-term monitoring reveals unprecedented stability of a vent mussel assemblage on the Mid-Atlantic Ridge. *Prog. Oceanogr.* **204**, 1-23.

van de Koppel, J., Gascoigne, J. C., Theraulaz, G., Rietkerk, M., Mooij, W. M. and Herman, P. M. J. (2008). Experimental evidence for spatial self-organization and its emergent effects in mussel bed ecosystems. *Science* **322**, 739–742.

Van Dover, C. (1986). A comparison of stable isotope ratios ($^{18}O/^{16}O$ and $^{13}C/^{12}C$) between two species of hydrothermal vent decapods (*Alvinocaris lusca* and *Munidopsis subsquamosa*). *Mar. Ecol. Prog. Ser.* **31**, 295–299.

Van Dover, C. L. and Fry, B. (1994). Microorganisms as food resources at deep-sea hydrothermal vents. *Limnol. Oceanogr.* **39**, 51–57.

Van Dover, C. L., Desbruyères, D., Segonzac, M., Comtet, T., Saldanha, L., Fiala-Médioni, A. and Langmuir, C. (1996). Biology of the Lucky Strike hydrothermal field. *Deep. Res. Part I Oceanogr. Res. Pap.* **43**, 1509–1529.

Van Dover, C. L. and Trask, J. L. (2000). Diversity at deep-sea hydrothermal vent and intertidal mussel beds. *Mar. Ecol. Prog. Ser.* **195**, 169–178.

Van Dover, C. L., Humphris, S. E., Fornari, D., Cavanaugh, C. M., Collier, R., Goffredi, S. K., Hashimoto, J., Littey, M. D., Reysenbach, A. L., Shank, T. M., et al. (2001). Biogeography and ecological setting of Indian Ocean hydrothermal vents. *Science* **294**, 818–823.

Van Dover, C. L. and Doerries, M. B. (2005). Community structure in mussel beds at Logatchev hydrothermal vents and a comparison of macrofaunal species richness on slow- and fast-spreading mid-ocean ridges. *Mar. Ecol.* **26**, 110–120.

Van Dover, C. L. (2011). Mining seafloor massive sulphides and biodiversity: What is at risk? *ICES J. Mar. Sci.* **68**, 341–348.

Van Dover, C. L. (2014). Impacts of anthropogenic disturbances at deep-sea hydrothermal vent ecosystems: A review. *Mar. Environ. Res.* **102**, 59–72.

Van Dover, C. L. (2019). Inactive sulfide ecosystems in the deep sea: A review. *Front. Mar. Sci.* **6**, 1–19.

Vismann, B. (1991). Sulfide tolerance: physiological mechanisms and ecological implications. *Ophelia* **34**, 1–27.

Vohsen, S. A., Gruber-Vodicka, H. R., Osman, E. O., Saxton, M. A., Joye, S. B., Dubilier, N., Fisher, C. R. and Baums, I. B. (2020). Deep-sea corals near cold seeps associate with chemoautotrophic bacteria that are related to the symbionts of cold seep and hydrothermal vent mussels. *bioRxiv* **968453**, 1–37.

Von Cosel, R., Comtet, T. and Krylova, E. (1999). *Bathymodiolus* (Bivalvia: Mytilidae) from Hydrothermal Vents on the Azores Triple Junction and the Logatchev Hydrothermal Field, Mid-Atlantic Ridge. *The Veliger* **42**, 218–248.

Von Damm, K. L. (1988). Systematics of and Postulated Controls on Submarine Hydrothermal Solution Chemistry. *J. Geophys. Res.* **93**, 4551–4561.

Von Damm, K. L., Bray, A. M., Buttermore, L. G. and Oosting, S. E. (1998). The geochemical controls on vent fluids from the Lucky Strike vent field, Mid-Atlantic Ridge. *Earth Planet. Sci. Lett.* **160**, 521–536.

Von Damm, K. L. (2000). Chemistry of hydrothermal vent fluids from 9°-10°N, East Pacific Rise: "Time zero," the immediate posteruptive period. *J. Geophys. Res. Solid Earth* **105**, 11203–11222.

Vuillemin, R., Le Roux, D., Dorval, P., Bucas, K., Sudreau, J. P., Hamon, M., Le Gall, C. and Sarradin, P. M. (2009). CHEMINI: A new in situ CHEmical MINIaturized analyzer. *Deep. Res. Part I Oceanogr. Res. Pap.* **56**, 1391–1399.

W

Warwick, P., Clarke, R. M. and Somerfield P. J. (2008). *k*-Dominance Curves. In *Encyclopedia of Ecology* (ed. Jørgensen, S. E., Fath, B. D.), pp. 2055-2057. Academic Press

Watt, A. S. (1947). Pattern and process in the plant community. *Br. Ecol. Soc.* **35**, 1–22.

Wheeler, B., Cannat, M., Chavagnac, V. and Fontaine, F. (in prep.). Near seafloor hydrothermal circulations at Lucky Strike vent field from geological mapping and time series of fluid temperature and chemistry, Mid-Atlantic Ridge.

Wiens, J. A. (1976). Population responses to patchy environments. *Annu. Rev. Ecol. Syst.* **7**, 81–120.

Wiens, J. A., Stenseth, N. C., Horne, B. Van and Ims, R. A. (1993). Ecological Mechanisms and Landscape Ecology. *Oikos* **66**, 369–380.

Wiens, J. A. (1997). The Emerging Role of Patchiness in Conservation Biology. *Ecol. Basis Conserv.* 93–107.

Wilcock, W. S. D. and Delaney, J. R. (1996). Mid-ocean ridge sulfide deposits : Evidence for heat extraction from magma chambers or cracking fronts? *Earth Planet. Sci. Lett.* **145**, 49–64.

Wilcock, W. S. D., Tolstoy, M., Waldhauser, F., Garcia, C., Tan, Y. J., Bohnenstiehl, D. W. R., Caplan-Auerbach, J., Dziak, R. P., Arnulf, A. F. and Mann, M. E. (2016). Seismic constraints on caldera dynamics from the 2015 Axial Seamount eruption. *Science* **354**, 1395–1399.

Wilson, J. H. and Seed, R. (1974). Reproduction in *Mytilus edulis* L. (Mollusca: Bivalvia) in Carlingford Lough, Northern Ireland. *Irish Fish. Investig.* **SERIES B**, 1–31.

Wilson, M. F. J., O'Connell, B., Brown, C., Guinan, J. C. and Grehan, A. J. (2007). Multiscale terrain analysis of multibeam bathymetry data for habitat mapping on the continental slope. *Mar. Geod.* **30**, 3–35.

Witman, J. D. (1987). Subtidal coexistence: storms, grazing, mutualism, and the zonation of kelps and mussels. *Ecol. Monogr.* **57**, 167–187.

Won, Y. J., Hallam, S. J., O'Mullan, G. D., Pan, I. L., Buck, K. R. and Vrijenhoek, R. C. (2003). Environmental Acquisition of Thiotrophic Endosymbionts by Deep-Sea Mussels of the Genus *Bathymodiolus*. *Appl. Environ. Microbiol.* **69**, 6785–6792.

Woodin, S. A. (1974). Adult-larval interactions in dense infaunal assemblages: patterns of abundance. *J. Mar. Res.* **44**, 171–187.

Wootton, J. T. (1993). Size-dependent competition: effects on the dynamics vs. the end point of mussel bed succession. *Ecology* **74**, 195–206.

Wootton, J. T. (2001). Local interactions predict large-scale pattern in empirically derived cellular automata. *Nature* **413**, 841–844.

X

Xu, G., Jackson, D. R., Bemis, K. G. and Rona, P. A. (2013). Observations of the volume flux of a seafloor hydrothermal plume using an acoustic imaging sonar. *Geochemistry, Geophys. Geosystems* **14**, 2369–2382.

Y

Yamada, T., Prügel-Bennett, A. and Thornton, B. (2021). Learning features from georeferenced seafloor imagery with location guided autoencoders. *J. F. Robot.* **38**, 52–67.

Z

Zajac, R. N., Whitlatch, R. B. and Thrush, S. F. (1998). Recolonization and succession in soft-sediment infaunal communities: The spatial scale of controlling factors. *Hydrobiologia* **375**–**376**, 227–240.

Zeppilli, D., Vanreusel, A., Pradillon, F., Fuchs, S., Mandon, P., James, T. and Sarrazin, J. (2015). Rapid colonisation by nematodes on organic and inorganic substrata deployed at the deep-sea Lucky Strike hydrothermal vent field (Mid-Atlantic Ridge). *Mar. Biodivers.* **45**, 489–504.

Zhang, Z. (1994). Iterative point matching for registration of free-form curves and surfaces. *Int. J. Comput. Vis.* **13**, 119–152.

Zhang, T., Tang, J., Qin, S. and Wang, X. (2019). Review of Navigation and Positioning of Deep-sea Manned Submersibles. *J. Navig.* **72**, 1021–1034.

Zhou, Y., Zhang, D., Zhang, R., Liu, Z., Tao, C., Lu, B., Sun, D., Xu, P., Lin, R., Wang, J., et al. (2018). Characterization of vent fauna at three hydrothermal vent fields on the Southwest Indian Ridge: Implications for biogeography and interannual dynamics on ultraslow-spreading ridges. *Deep. Res. Part I Oceanogr. Res. Pap.* **137**, 1–12.

Zhou, Y., Chen, C., Zhang, D., Wang, Y., Watanabe, H. K., Sun, J., Bissessur, D., Zhang, R., Han, Y., Sun, D., et al. (2022). Delineating biogeographic regions in Indian Ocean deep-sea vents and implications for conservation. *Divers. Distrib.* **00**, 1–13.

COLLEGE SCIENCES DOCTORAL DE LA MER BRETAGNE ET DU LITTORAL

Université de Bretagne Occidentale

Titre : Étude par l'imagerie de la distribution spatio-temporelle multi-échelles des communautés benthiques associées au champ hydrothermal Lucky Strike

Mots clés : sources hydrothermales, dynamique de communautés, assemblages benthiques, multi-échelles, imagerie sous-marine, écologie spatio-temporelle

Résumé : La caractérisation multi-échelle de la variabilité d'un écosystème est fondamentale à la conceptualisation de modèles de dynamique. Depuis sa découverte en 1993, le champ hydrothermal profond Lucky Strike a fait l'objet d'un grand nombre d'études, ce qui en fait l'une des zones hydrothermales les mieux connues. La difficulté d'accès a toutefois limité la compréhension intégrée de l'écosystème dans le temps et l'espace. A l'aide de nouvelles technologies d'observation, cette thèse vise à comprendre l'influence des processus régissant la dynamique des communautés de Lucky Strike à différentes échelles spatiales : l'assemblage, l'édifice et le champ. Les suivis d'assemblages de faune de l'édifice Tour Eiffel ont été effectués aux échelles infra-annuelle grâce à l'observatoire EMSO Açores pluri-annuelle à partir de reconstructions photogrammétriques. Ils ont révélé l'intensité et le nombre limités des perturbations auxquelles est soumise la faune hydrothermale. La variabilité décimétrique restreinte aux zones d'émissions a peu d'impact sur l'espèce dominante *Bathymodiolus azoricus*, de par sa mobilité. La distribution des espèces n'ayant pas changé sur une décennie, cette invariance d'échelle (du m² à l'édifice) expliquerait que cette communauté ait atteint un stade de climax depuis au moins 25 ans. Enfin, à l'échelle du champ, l'analyse de la distribution préférentielle de la faune hydrothermale et périphérique a rendu compte de l'importante hétérogénéité de l'habitat sur une centaine de mètres. Ces résultats suggèrent une forte structuration et une faible résilience des écosystèmes hydrothermaux à de potentielles perturbations d'envergure sur la dorsale médio-Atlantique.

Title: Imaging study of the multi-scale spatio-temporal distribution of benthic communities associated with the Lucky Strike hydrothermal field

Keywords: hydrothermal vent, community dynamics, benthic assemblages, multiscale, underwater imaging, spatio-temporal ecology

Summary: The multi-scale characterisation of ecosystem variability is fundamental to the conceptualisation of dynamic models. Since its discovery in 1993, the Lucky Strike vent field has been extensively studied, making it one of the most well-known hydrothermal area of the World's ocean. However, remote access has limited -in space and time- the scope of the studies, preventing an integrated understanding of the ecosystem. Using new technologies, this thesis aims to unravel the relative role of processes driving the dynamics of biological communities at Lucky Strike over different spatial scales: at the assemblage, the edifice and the field scales. The monitoring of the faunal assemblages of the Eiffel Tower hydrothermal edifice were carried out at sub-annual scales through the EMSO Azores observatory and pluri-annually based on photogrammetric reconstructions. These surveys have revealed a limited intensity and number of disturbances to which the hydrothermal fauna is subjected. Decadal variability restricted to emission areas had little impact on the dominant engineer species *Bathymodiolus azoricus*, because of its mobility. Considering the stable distribution of species over a decade, the remarkable scale invariance (from m² to the edifice) could explain why this community has reached a climax stage maintained for at least 25 years. Finally, analysis of the factors controlling the distribution of benthic vent and peripheral communities at the scale of the field showed the importance of habitat heterogeneity over a hundred of metres. These results suggest a strong structuring and a low resilience of hydrothermal ecosystems to any potential large-scale disturbance on the Mid-Atlantic Ridge.